



HAL
open science

Etude translationnelle des phénomènes neuroinflammatoires précoces et tardifs post-traumatisme crânien

Alice Jacquens

► **To cite this version:**

Alice Jacquens. Etude translationnelle des phénomènes neuroinflammatoires précoces et tardifs post-traumatisme crânien. Neurobiologie. Université Paris Cité, 2021. Français. NNT : 2021UNIP7287 . tel-04062569

HAL Id: tel-04062569

<https://theses.hal.science/tel-04062569>

Submitted on 7 Apr 2023

HAL is a multi-disciplinary open access archive for the deposit and dissemination of scientific research documents, whether they are published or not. The documents may come from teaching and research institutions in France or abroad, or from public or private research centers.

L'archive ouverte pluridisciplinaire **HAL**, est destinée au dépôt et à la diffusion de documents scientifiques de niveau recherche, publiés ou non, émanant des établissements d'enseignement et de recherche français ou étrangers, des laboratoires publics ou privés.



Thèse de doctorat de l'Université de Paris

Préparée à l'Université de Paris

École doctorale BioSPC 562

Institut Jacques Monod - Équipe Polarité cellulaire dans le développement et l'évolution

Étude des mécanismes associés à la polarité rotationnelle des centrioles dans les cellules animales

Par Noémie Gaudin

Thèse de doctorat de Biologie Cellulaire

Dirigée par Juliette Azimzadeh

Présentée et soutenue publiquement à Paris le 21 Septembre 2021

Rapporteuse : Dr Anne-Marie Tassin, Université Paris-Saclay

Rapporteur : Dr Paul Guichard, Université de Genève

Examinatrice : Dr Alice Meunier, École normale supérieure

Examinatrice : Dr Christine Vesque, Sorbonne Université

Examineur : Dr Alexandre Benmerah, Université de Paris

Directrice de thèse : Dr Juliette Azimzadeh, Université de Paris



Except where otherwise noted, this work is licensed under
<http://creativecommons.org/licenses/by-nc-nd/3.0/>

Noémie Gaudin – Thèse de doctorat – 2021

« *La symétrie, c'est l'ennui.* » *Victor Hugo, Les Misérables*

Résumé :

Les centrioles sont des structures cellulaires conservées au cours de l'évolution. Ils sont formés par des triplets de microtubules organisés selon une symétrie en 9. Chez les animaux, les centrioles forment le cœur du centrosome, le principal centre d'organisation des microtubules. Les centrosomes sont des acteurs clés de l'organisation cellulaire, essentiels à des processus fondamentaux tels que la division et la polarité cellulaires. Le plus âgé des centrioles au sein du centrosome permet aussi l'assemblage du cil primaire, un organite sensoriel important pour de nombreuses voies de signalisation. Des dysfonctionnements des cils sont impliqués dans une classe de maladies génétiques appelées ciliopathies. Les centrioles sont présents dans tous les principaux groupes eucaryotes, ce qui indique qu'ils ont une origine évolutive commune. Chez nombre d'organismes unicellulaires, les centrioles présentent une asymétrie rotationnelle due à des structures accessoires associées à des triplets spécifiques. Chez l'algue flagellée *Chlamydomonas reinhardtii*, la protéine Vfl1p contrôle l'asymétrie rotationnelle des centrioles. Dans cette thèse, nous montrons qu'un orthologue de Vfl1p est aussi nécessaire à la polarisation rotationnelle des centrioles dans les cellules multiciliées de la planaire *Schmidtea mediterranea*. C'est aussi le cas pour VFL3, l'orthologue d'une autre protéine contrôlant la polarité rotationnelle des centrioles chez *C. reinhardtii*. Chez la planaire, les centrioles sont arrangés en un réseau présentant une asymétrie chirale. Nous avons identifié VFL1 et VFL3 comme étant des composants des centrioles nécessaires à l'établissement de connexions asymétriques entre les centrioles. En effet, ces protéines affectent l'assemblage des appendices centriolaires responsables de l'ancrage des éléments de cytosquelette qui contrôlent la position des centrioles. Nous montrons également que l'orthologue humain de VFL3 est présent au niveau d'appendices centriolaires nécessaires à l'ancrage des microtubules et est nécessaire à cette fonction. Nous réalisons ensuite l'analyse fonctionnelle de l'orthologue humain de VFL1, aussi appelé LRRCC1. Dans le contexte du centrosome humain, les centrioles ne présentent pas d'asymétrie rotationnelle évidente. Le plus âgé des deux centrioles qui composent le centrosome possède des appendices organisés selon une symétrie en neuf comme le centriole lui-même. En utilisant une technique d'imagerie super-résolutive appelée expansion microscopy, nous montrons que l'orthologue humain de VFL1 s'associe préférentiellement à deux triplets consécutifs à l'extrémité distale des centrioles, comme cela avait été observé chez *C. reinhardtii*. VFL1 co-localise partiellement et affecte le recrutement d'un autre composant distal, C2CD3, dont nous montrons qu'il est également localisé de manière asymétrique dans la lumière du centriole. La localisation de VFL1 et C2CD3 dans les centrioles humains rappelle la forme d'une structure filamenteuse présente au même niveau dans les centrioles des flagellés. De plus, la déplétion de VFL1 dans les cellules humaines induit des défauts dans la structure du centriole, l'assemblage du cil primaire et la signalisation par le cil. Ces résultats indiquent que VFL1 coopère avec C2CD3 pour organiser la région distale des centrioles, et confirment le lien entre VFL1 et les ciliopathies suggéré par l'identification il y a quelques années d'une mutation dans le gène LRRCC1 chez deux patients atteints du syndrome de Joubert. Ainsi, nous mettons en évidence que l'asymétrie rotationnelle des centrioles, une propriété ancienne chez les eucaryotes, est conservée au sein du centrosome humain, et est liée à la fonction du cil primaire. L'ensemble de ces résultats apporte un éclairage nouveau sur les bases moléculaires et les fonctions de la polarité rotationnelle des centrioles dans différents contextes biologiques et au cours de l'évolution.

Mots clés : VFL1, C2CD3, centriole, centrosome, cil primaire, polarité rotationnel, ciliopathies, VFL3, acorn, microtubules

Investigating the molecular mechanisms associated with centriole rotational polarity in animal cells

Abstract:

Centrioles are evolutionarily conserved cellular structures. In animals, centrioles form the structural core of the centrosome, the main center of microtubule organization. Centrosomes are key players in cell organization, essential for fundamental cellular processes such as division and polarity. The oldest centriole within the centrosome also enables the assembly of the primary cilium, a sensory organelle important for the transduction of many signaling pathways. Cilia dysfunction is implicated in a class of genetic diseases called ciliopathies. Centrioles are present in all major eukaryotic groups, indicating that they have a common evolutionary origin. In many organisms, centrioles exhibit rotational asymmetry due to accessory structures associated with specific triplets. In the flagellated alga *Chlamydomonas reinhardtii*, the protein Vfl1p (Variable flagella number 1) controls the rotational asymmetry of centrioles. In this thesis, we show that an ortholog of Vfl1p called SMED-VFL1 is also required for rotational polarization of centrioles in multiciliated cells of the planarian *Schmidtea mediterranea*. This is also the case for VFL3, the ortholog of another protein controlling centriole rotational polarity in *C. reinhardtii*. In planarians, centrioles are arranged in a pattern generated by a network of centrioles with asymmetric properties. We identified VFL1 and VFL3 as components of centrioles required for the establishment of asymmetric connections between centrioles. These proteins affect the assembly of centriolar appendages responsible for anchoring cytoskeletal elements that control centriole position. We also show that the human orthologue of VFL3 is present at centriolar appendages required for microtubule anchoring and is necessary for this function. We then undertake a functional analysis of the human ortholog of VFL1, also called LRRCC1 (Leucine Rich Repeat and Coiled-Coil containing 1). A mutation in the gene encoding this protein has been linked to a specific ciliopathy, indicating its possible role in primary cilium function. In the context of the human centrosome, the centrioles do not show obvious rotational asymmetry. The older of the two centrioles that make up the centrosome has appendages organized in ninefold symmetry like the centriole itself. Using a super-resolution imaging technique called expansion microscopy, we show that the human ortholog of VFL1 preferentially associates with two consecutive triplets at the distal end of the centrioles, as previously observed in *C. reinhardtii*. VFL1 partially co-localizes and affects the recruitment of another distal component, C2CD3, which we show is also asymmetrically localized in the centriole lumen. The localization of VFL1 and C2CD3 in human centrioles is reminiscent of the shape of a filamentous structure present at the same level in flagellate centrioles. Furthermore, depletion of VFL1 in human cells induces defects in centriole structure, primary cilium assembly and cilium signaling. These results support that VFL1 cooperates with C2CD3 to organize the distal region of centrioles and confirm the involvement of VFL1 in ciliopathies. Thus, we demonstrate that rotational asymmetry of centrioles, an ancient property in eukaryotes, is conserved within the human centrosome, and is related to primary cilium function. Our results in planarian multiciliated cells also led us to analyze the role of human VFL1 in microtubule anchoring. We observed that VFL1 depletion induces a decrease in microtubule anchoring to the centrosome, in interphase and in mitosis. Together, these results shed new light on the molecular basis and functions of centriole rotational polarity in different biological contexts and during evolution.

Keywords: VFL1, LRRCC1, Centriole, Centrosome, Primary Cilium, Polarity, VFL3, CCDC61, C2CD3, Multiciliated cells

Remerciements

Juliette, merci pour tout, pour m’avoir pris dans l’équipe, m’avoir formée, m’avoir fait confiance, pour ton excellence scientifique, ta bienveillance et ton humanité. J’ai été très chanceuse que tu sois ma directrice de thèse.

Je remercie mes rapporteurs, Anne-Marie Tassin et Paul Guichard pour avoir accepté avec enthousiasme d’apporter leur relecture et leurs critiques scientifiques à mon manuscrit de thèse.

Je remercie les examinateurs de ma soutenance de thèse, Alice Meunier, Christine Vesque et Alexandre Benmerah pour leur expertise scientifique et l’évaluation de mon travail.

Paula, je te remercie tout particulièrement pour m’avoir accompagné durant ces deux dernières années dans la réalisation de mon projet de thèse, pour ton soutien, ton aide et ton professionnalisme. Merci pour tes traits d’esprit, ton humour et ton relativisme. Tu m’as apporté beaucoup de sérénité et je te fais toute confiance pour réaliser une thèse exceptionnelle dans l’équipe.

Cyril, je te remercie tout particulièrement pour avoir supporté mes questions incessantes pendant mes deux premières années de thèse, pour avoir fait augmenter mon taux de glycémie par l’apport régulier de bonbons Haribo, pour ton enthousiasme et tes coups de gueules justifiés.

Meriem, Manon, Quentin, Lucia, Ngan, Marion, Roland, Simon, Juliane et Inès, merci d’avoir participé aux résultats de ma thèse et à la vie du laboratoire.

Line, mon soutien inconditionnel depuis le début, je te remercie pour ta bienveillance et ton opiniâtreté. Tu m’impressionnes tous les jours.

Laetitia, Jeremy, merci d’avoir été mes modèles. Merci d’avoir pris soin de moi dès le premier jour. Merci pour votre amitié depuis bientôt 5 ans.

Youcef merci pour les cafés et les rires partagés. Nicolas merci pour ta vexation à mes remarques objectives et pour m’avoir aidé pour les ES. Anne-Laure, merci pour ta bienveillance et l’ambiance conviviale que tu sais apporter. Thomas, merci pour ton humour et tes initiatives pour la vie sociale de l’institut. Vanessa, merci pour ton **ENTHOUSIASME** et ta passion pour la

science. Gaël, merci pour m’ avoir accompagné courir même quand je me trainais. Eslande, merci pour ta flamboyance à l’ institut. Et merci au reste du cinquième étage de faire et d’ avoir fait de cet étage le meilleur de l’ institut.

Merci au laboratoire des Ladoux-Mège pour m’ avoir permis d’ utiliser leurs équipements et merci à Joseph, Alison, Alexandros, Olivia et le reste des collègues pour les moments conviviaux partagés ensemble.

Merci à la plateforme ImagoSeine en particulier Xavier, Nicolas, Paul, Catherine et Rémi pour votre aide et pour la qualité du matériel mis à ma disposition pour la réalisation de ma thèse.

Merci Norry pour ton hospitalité incomparable, pour tes blagues souvent hilarantes et par-dessus tout pour ta gentillesse. Merci Jonathan pour ton humour et ta bonne humeur incontestable, je ne te remercie pas pour les pichenettes. Merci Laurent de faire tenir ce bâtiment à bout de bras, l’ institut ne pourrait fonctionner sans toi.

Merci au personnel administratif de l’ institut pour votre soutien au travail scientifique de l’ institut. Merci en particulier à Nathalie et Lindsay pour les commandes.

Je souhaite remercier tout particulièrement Paul Guichard et Virginie Hamel. Merci de m’ avoir ouvert les portes de votre laboratoire et pour le travail scientifique de qualité que vous faites. Merci Marine pour ton hospitalité et de m’ avoir appris la technique qui a fait passer mon travail au niveau supérieur.

Merci Dmitry, pour le programme qui me manquait cruellement.

Merci Ferdinand et Camille, mes correcteurs de l’ extrême.

Papa, Maman, merci pour votre éducation et votre soutien durant mes études. Je vous aime <3.

Merci Sci hub.

Abbreviations

AU	Airy Unit	PTCH1	Patched
BB	Basal Body	PALM	PhotoActivated Localization Microscopy
BBS	Bardet-Biedl Syndrome	pbb	Probasal bodies
CCDC61	Coiled-Coil Domain-Containing protein 61	PCD	Primary Ciliary Dyskinesia
CDKs	Cyclin-Dependent Kinases	PCM	PeriCentriolar Material
CKIs	CDK Inhibitors	PCM1	PeriCentriolar-Material 1
CLERC	Centrosomal LEucine-Rich repeat and Coiled-coil containing protein	PCNT	Pericentrin
CPAP	Centrosomal P4.1-Associated Protein	PCP	Planar Cell Polarity
CS	Centriolar Satellites	PI	PhosphoInositides
DAs	Distal Appendages	PKD	Polycystic Kidney Disease
dcf	Distal connecting Fiber	PLK1	Polo-Like Kinase 1
DCPs	Daughter Centriole-specific/enriched Proteins	PLK4	Polo-Like Kinase 4
EM	Electron Microscopy	SMO	Smoothened
ExM	Expansion Microscopy	SPB	Spindle Pole Body
Ft/Ds	Fat/Dachsous	SAP2	Sodium channel Associated Protein 2
Hh	hedgehog	SDAs	SubDistal Appendages
IFT	IntraFlagellar Transport	SIM	Structured Illumination Microscopy

JBTS	JouBerT syndrome	SMAF	Striated Microtubule-Associated Fibers
LECA	Last Eukaryotic Common Ancestor	STIL	SCL-interrupting locus protein
LRR	Leucine-Rich Repeat	STORM	STochastic Optical Reconstruction Microscopy
MAP	Magnified Analysis of the Proteome	TEM	Transmission Electron Microscopy
MKS	Meckel-Gruber Syndrome	tfs	Transition fibers
MTOC	MicroTubule Organizing Center	TZ	Transition Zone
MTs	MicroTubules	U-ExM	Ultrastructure Expansion Microscopy
MTS	Molar Tooth Sign	<i>vfl</i>	variable flagella number
NPHP	Nephronophthisis	Vfl1	Variable FLagellar number 1
NuMA	Nuclear Mitotic Apparatus	Wnt/PCP	Wnt/Planar Cell Polarity
OFD	OroFacioDigital syndrome	γ -TuRC	γ -Tubulin Rings Complexes

Remerciements	1
Abbreviations	3
1. Introduction.....	9
1.1. Centrosome general introduction.....	9
1.1.1. History.....	9
1.1.2. Centriole structure.....	11
1.1.2.1. Centriole core and appendages.....	11
1.1.2.2. The pericentriolar material.....	17
1.1.2.3. Centriolar satellites.....	19
1.1.2.4. Cilia.....	20
1.1.3. Evolution.....	24
1.2. The centrosome through the cell cycle	27
1.2.1. The cell cycle.....	27
1.2.2. Centriole duplication initiation, elongation and maturation.....	29
1.2.3. Mitosis.....	32
1.2.4. The primary cilium	33
1.2.4.1. Early steps of ciliary assembly.....	33
1.2.4.2. Intraflagellar transport	35
1.2.4.3. Ciliary signaling	37
1.3. Polarity	38
1.3.1. The centrosome as a microtubule organizing center	38
1.3.2. Migration.....	41
1.3.3. Polarity in multiciliated cells.....	43
1.3.4. Establishing and maintaining asymmetry in cells, tissue and organisms	45
1.4. Ciliopathies and microtubules related diseases	46
1.4.1. Introduction	46
1.4.2. Joubert syndrome.....	48
1.4.3. Microcephaly.....	50
1.5. hVFL1 and hVFL3.....	52
1.5.1. In Chlamydomonas	52

1.5.2.	In human.....	54
1.5.2.1.	hVFL1/LRRCC1	54
1.5.2.2.	hVFL3/CCD61	55
1.6.	A resolution revolution	55
1.6.1.	The resolution limit.....	55
1.6.2.	Electron microscopy	56
1.6.3.	Super resolution microscopy	57
1.6.4.	Expansion microscopy	60
1.7.	Hypothesis	62
2.	Results.....	65
2.1.	Evolutionary conservation of centriole rotational asymmetry in the human centrosome (Article 1)	65
2.2.	hVFL3/CCDC61 is a component of mother centriole subdistal appendages required for centrosome cohesion and positioning (Article 2).....	123
2.3.	Emergence of a bilaterally symmetric pattern from chiral components in Planarian epidermis (Article 3).....	140
2.4.	hVFL1 impacts microtubules organization in mitosis and interphase	157
2.4.1.	Introduction	157
2.4.2.	Methods.....	159
2.4.3.	Results	162
2.4.3.1.	hVFL1 impacts microtubules during interphase	162
2.4.3.2.	hVFL1 impacts microtubules during mitosis	166
2.4.4.	Preliminary conclusions and perspectives	170
3.	Discussion and Perspectives.....	171
3.1.	Centriole inherent asymmetry.....	171
3.2.	Centriole rotational asymmetry and the primary cilium	178
3.3.	Rotational asymmetry in centriole duplication.....	179
3.4.	MT anchoring, polarity, development and cancer.....	180
4.	References.....	181

Preface

My thesis project aimed to better understand the function of an evolutionarily conserved protein, called VFL1, and a second protein with no sequence homology to the first, but often involved in similar processes, called VFL3. Our team's interest in these proteins was initially sparked by a genetic screen in the planarian *Schmidtea mediterranea* performed by my thesis supervisor (Azimzadeh et al., 2012). The observed defects suggested that these proteins originally characterized in the flagellated green alga *Chlamydomonas reinhardtii* could perform similar roles in animal cells. The main contribution of my thesis work was to characterize the function of human VFL1 at the centrosome. I also contributed to the study of human VFL3, as well as planarian VFL1 and VFL3. For a better understanding of my thesis work, I will first detail the structure of the centrosome, its involvement in the cell cycle and cell polarity, centrosome-related diseases, the VFL1 and VFL3 proteins, and the microscopy techniques used in my study.

The centrosome is a non-membrane organelle composed of two centrioles embedded in a pericentriolar material (PCM). It is found in animals, fungi, and several other eukaryotic lineages. In animal cells, it serves as the main Microtubule organizing center (MTOC), as microtubules (MTs) are nucleated from the PCM. In cells that do not divide, only one copy of the centrosome is present, and it duplicates with each cell cycle to ensure that each daughter cell inherits a complete centrosome. During this process, the centrosome contributes to the formation of the mitotic spindle that separates the chromosomes. In quiescent cells, the older centriole within the centrosome, called mother centriole, templates the formation of the cilium, a slender sensory and/or motile organelle that projects to the periphery of the cell surface. In this context, the centriole is called basal body (BB).

Centrioles are one of the most recognizable structures in electron microscopy. Their elegant 9-fold symmetrical organization contrasts with the chaotic appearance of the cytoplasm (Figure 1). Centrioles allow the formation of the centrosome, a key player in cell organization. Therefore, centrioles are epitomes of clarity and order in their structure, but also in their function (Uzbekov R.E. & Alieva I.B., 2013).

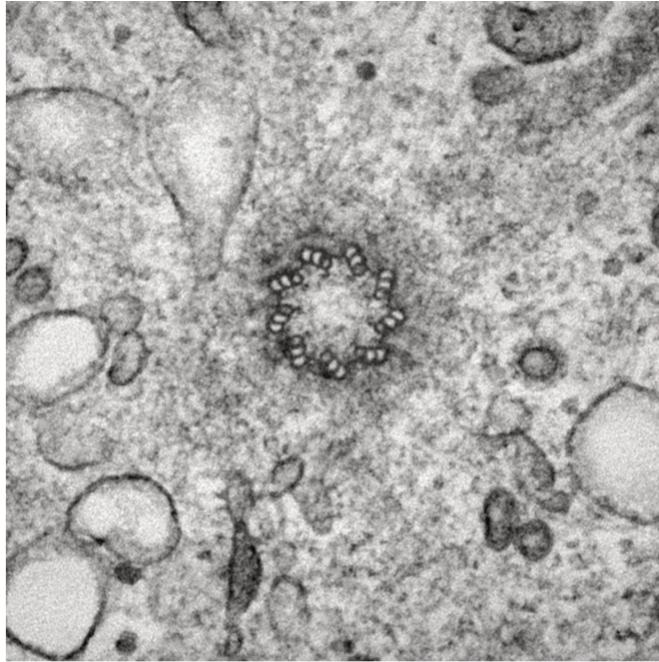


Figure 1: Transversal view of a centriole observed by electron microscopy in Human Umbilical Vein Endothelial Cell by Ian White (unpublished).

1. Introduction

1.1. Centrosome general introduction

1.1.1. History

Before the discovery of the centrosome, the cell, chromosomes and the mitotic spindle had already been observed and described. The mitotic spindle was named so from its resemblance to a spinning spindle, driving the passive chromosome to specific parts of the cytoplasm, the spindle poles. In the 1870s, the poles of the mitotic spindle were first described as two symmetric structures in dividing cells. Edouard Van Beneden is considered the first to have discovered the centrosome, when in 1876 he described the anatomy and development of a mesozoan parasite belonging to the phylum *Dicyemidae*. He identified granules at the poles of the mitotic spindle and called them “polar corpuscles”. In 1887, he studied the fertilization in *Ascaris megalocephala*, a parasitic nematode worm. He speculated that centrosomes, which by then he called “central corpuscles”, were permanent self-replicating cellular organelles (Figure 2). The same year, Theodore Boveri independently studied the centrosome in *Ascaris* eggs. He described a differentiated sphere of cytoplasm at spindle poles from which astral and spindle fibers emanated (Figure 2). It is Boveri that in 1895 coined the name centrosome and later, centriole. Boveri confirmed Van Beneden’s observation that polar corpuscles do not disappear completely at the end of mitosis, but are preserved in interphase, during which they are often located near the geometric center of the cell. This discovery led both Van Beneden and Boveri to conclude that these structures have an autonomous reproduction cycle (Gall, 2004).

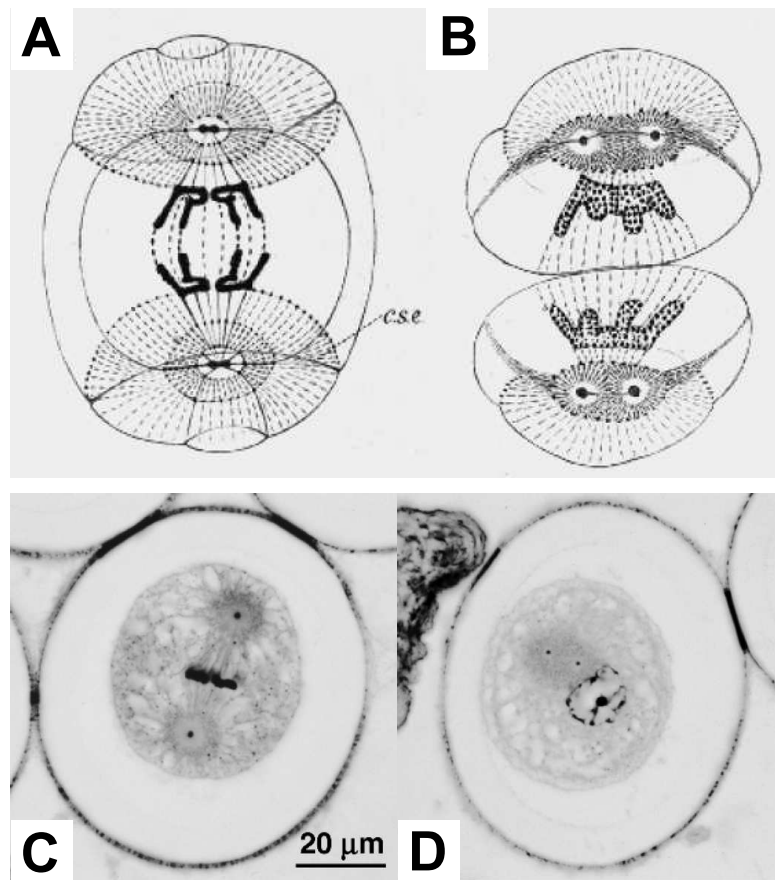


Figure 2: First studies of the centrosome, in the first cleavage division in the egg of the nematode worm *Ascaris megalocephala*. (A)(B) Van Beneden's drawings of *Ascaris* Eggs, taken from (Gall, 2004). (A) The doubling of centrioles in anaphase (B) and their separation during early interphase are represented. (C)(D) Photographs taken by Joseph G. Gall from Boveri's slide of *Ascaris* eggs, taken from (Gall, 2004). (C) Metaphase of the first cleavage, to be compared with A. (D) End of the first cleavage division, where the two centrioles are separated from one another and situated next to the nucleus, to be compared with B.

They both made the hypothesis that the centrosome is a permanent organelle that can only arise via self-replication. To challenge this conclusion, other researchers later sought evidence of *de novo* assembly of centrosomes. In 1925, E. B. Wilson studied marine invertebrate eggs induced for parthenogenesis. The activated eggs contained distinct centrioles, which therefore could not have been provided by sperm. But because he could not rigorously establish that the eggs did not contain centrioles before activation, his conclusion that centrioles can be formed *de novo* was insufficiently supported. *De novo* formation of centrioles was then documented in plants in a more convincing manner. Unlike in animal cells, centrioles are not present at the spindle poles of

dividing plant cells. Nevertheless, during the last divisions of the male gametophyte of some plant species, giant centrosome-like structures, called blepharoblasts, can be observed at the spindle poles. These structures can then form multiple centrioles at their surface, which then template the assembly of motile cilia (Gall, 2004). Historically, cilia were actually discovered first, before centrioles. They were identified by Antonie van Leeuwenhoek in 1676, who described them as “incredibly thin feet, or little legs” (Choksi et al., 2014).

In parallel with the study of *de novo* centriole formation, about 50 years ago, researchers considered the hypothesis that centrioles would contain their own DNA to explain their ability to self-replicate. This assumption was based on the parallel with other organelles such as mitochondria and chloroplasts, which self-replicate and contain their own DNA. Thus, DNA was searched for by different methods in centrioles, such as Feulgen staining or incorporation of DNA precursors during replication. In the end, these studies did not provide any tangible evidence for the presence of DNA in centrioles (Sluder, 2014).

The hypothesis that the BBs, from which the cilia emanate, and the centrioles present in the centrosome are in fact equivalent structures, was formulated very early on. However, it was with the advent of electron microscopy (EM) in the 1950s that it became clear that their structures were indeed very similar. This technical revolution allowed to describe with great precision the structure of centrioles and BBs in many species, thus highlighting the high conservation of their architecture. Nevertheless, to understand the replication of these organelles, it is also necessary to elucidate their composition and to determine how each component is incorporated into the structure. The remarkable technical advances of the last decades have given us a much more complete view of these mechanisms, which will be presented in the following section.

1.1.2. Centriole structure

1.1.2.1. Centriole core and appendages

The centrosome is composed of two centrioles embedded in the PCM. Centrioles have the shape of a cylinder composed of 9 blades and are polarized along their proximo-distal axis (Figure 3). In EM, this gigantic protein complex is easily recognized by the symmetrical nine-fold arrangement of the MTs triplets that compose it. The triplets are twisted counterclockwise when viewed from the proximal end, making the centriole a chiral structure. The centriole measures

about 450 nm in length and its outer diameter is about 250 nm, which is below the resolution limit of conventional light microscopy. MTs triplets (Figure 3) are composed of only one complete MT, the A-MT, which is composed of 13 protofilaments of linearly arranged α/β -tubulin dimers. The B-MT and C-MT are composed of only 10 protofilaments and form on the wall of the A-MT and the B-MT, respectively. The C-MT is only present from the proximal part to about the half of the centrioles, but the exact area where the C-MT stops is variable from one triplet to another. The distal part is thus composed of doublets of MTs. It is worth noting that the orientation of the MT doublets/triplets is not the same in the distal and proximal part of the centriole. The angle formed by the doublets/triplets to the center of the centriole is about 120° in the proximal region and 100° in the distal region, revealing that the triplets are tilted along their length. The MT triplets act as a scaffold for the other proteins that compose the centrioles. The centriole is one of the largest protein-based structures, containing over 100 different proteins associated along the triplet wall. MT triplets are linked to the other by the A-C linker, a protein-based structure connecting the A-MT of one triplet to the C-MT of the following triplet (LeGuenec et al., 2020).

Within the centriole, the best characterized region is the cartwheel, a 9-fold symmetric structure located in the lumen of the proximal region. The cartwheel is 100 nm long and consists of a stack of circular elements surrounded by 9 spokes connected to the MTs wall by a pinhead. The circular part and the spokes are formed by 9 homodimers of the SAS-6 protein. It has been clearly established in models ranging from flagellate protists to animals that the self-assembling properties of SAS-6 are responsible for the centriole 9-fold symmetry (Kitagawa et al., 2011) (van Breugel et al., 2011). In the centrosome of vertebrate cells, proteins that connect the two centrioles are also found in the proximal region. C-NAP1, a large protein located near the cartwheel, serves as a platform to recruit other components of the inter-centriolar linker such as rootletin. The inner scaffold, located distal to the cartwheel and up to the region where the MT triplets become doublets, is another key centriolar structure that was only recently uncovered. It consists of a ring-like structure bound to the luminal side of the MT triplets, and is composed of at least five proteins: FAM161A, POC1B, POC5, Centrin-2, WDR90. The inner scaffold was shown to provide mechanical strength to the centriole and contributes to regulating centriole length (Le Guennec et al., 2020) (Le Guennec et al., 2020).

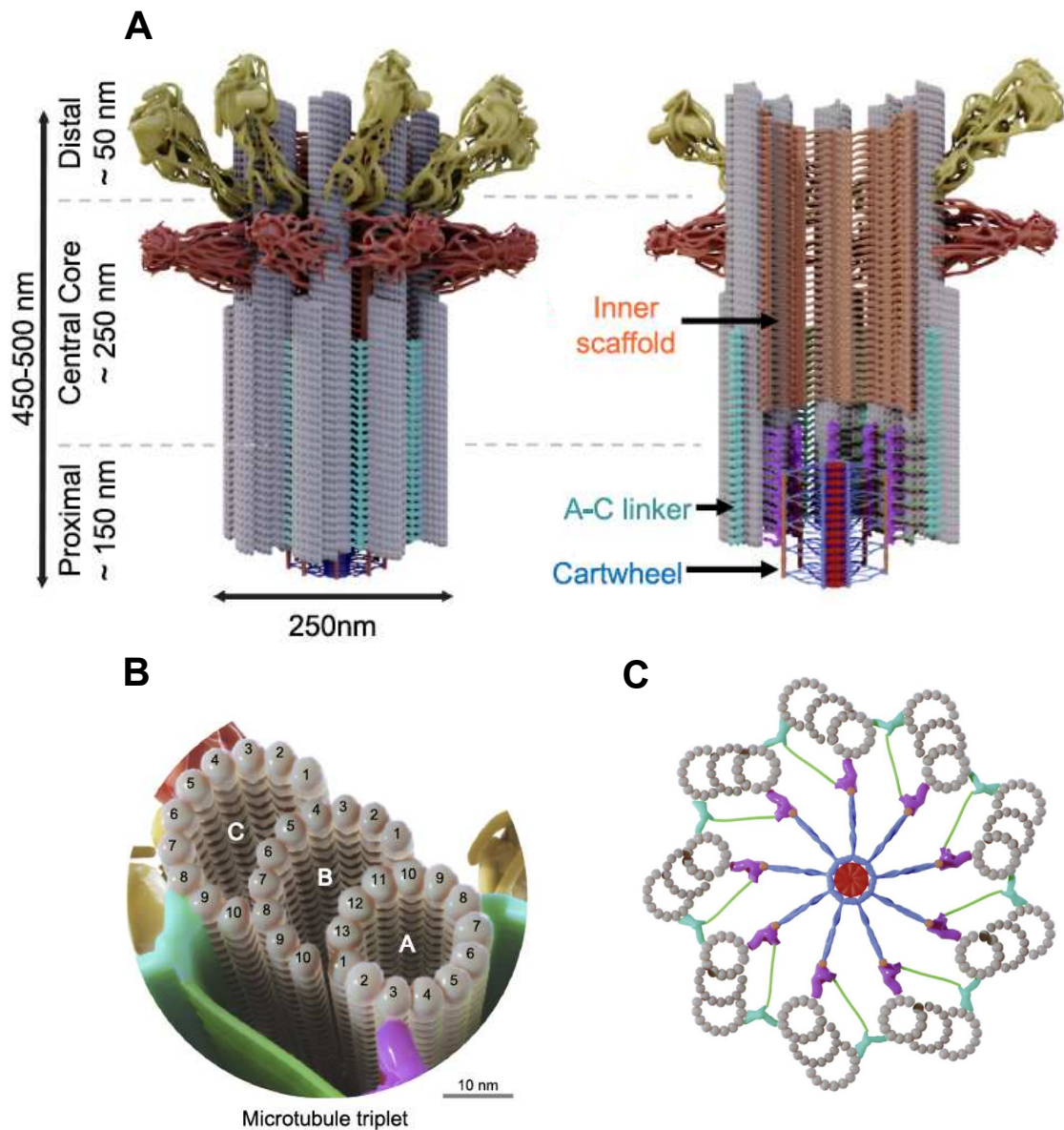


Figure 3: Structural view of the mother centriole, taken from (LeGuennec et al., 2020). (A) Model of centrioles, complete and longitudinal cross section. Three regions can be differentiated: the proximal region, the central core and the distal region. Known structural elements in the lumen are highlighted in the cross section. The sub-distal appendages (SDAs) are represented in red, and the distal appendages (DAs) in yellow. (B) Detailed view of a triplet showing the individual protofilaments that compose the A, B and C-MTs. (C) Transversal view of the proximal region of the centriole showing the AC linker connecting consecutive triplets (cyan), and the cartwheel, with the central tube and spokes formed by SAS-6 (blue), and the pinheads connecting the MT triplets (magenta).

Continuing the journey towards the distal centriole end, there are two sets of fibrous appendages, which are carried only by the mother centriole. First, the subdistal appendages (SDAs) are conical structures that emerge from the MT triplet at a 90° angle. Reflecting centriolar symmetry, up to 9 SDAs can assemble, but in reality, the number of SDAs is often less than 9 (Uzbekov & Alieva, 2018). The outer diameter of the ring formed by the SDAs is approximately 600 nm (Figure 3). Known SDA components include, from closest to the centriole wall to the tip of the appendages: ODF2, CEP128, centriolin, ninein, and CEP170 (Figure 4). Ninein has been shown to be capable of retaining γ -Tubulin Rings Complexes (γ -TuRC) that cap the minus end of MTs. Part of the MTs formed and released in the cytoplasm are then stably anchored at the SDAs. Directly after the SDAs are the distal appendages (DAs). The DAs, which are essential for ciliogenesis, are tilted conical structures with a bulbous end, arranged in a 9-fold symmetry. The outer diameter of the DA ring is about 550 nm, and each DA connects a pair of MT-doublets/triplets. The DAs are not orthogonal to the centriole in longitudinal view but form a 34° angle, with the tips pointing towards the distal extremity of the centriole. Protein known to compose DAs are from the closer to the MT wall to the periphery: CEP83, CEP89, SCLT1, FBF1, and CEP164 and ANKRD26 (LeGuennec et al., 2020) (Winey & O'Toole, 2014). At the distal end of the centriole are several proteins specific to this region including C2CD3, CP110, OFD1, Talpid3, CEP290 (Figure 4). CP110 forms a sort of “cap” completely at the end of the centriole, while C2CD3 is localized a little further inside the lumen, and OFD1, Talpid3, and CEP290 are localized near the MT doublets (Thauvin-Robinet et al., 2014) (Kumar & Reiter, 2021) (L. Wang et al., 2018) (Tsai et al., 2019) (Kim et al., 2008).

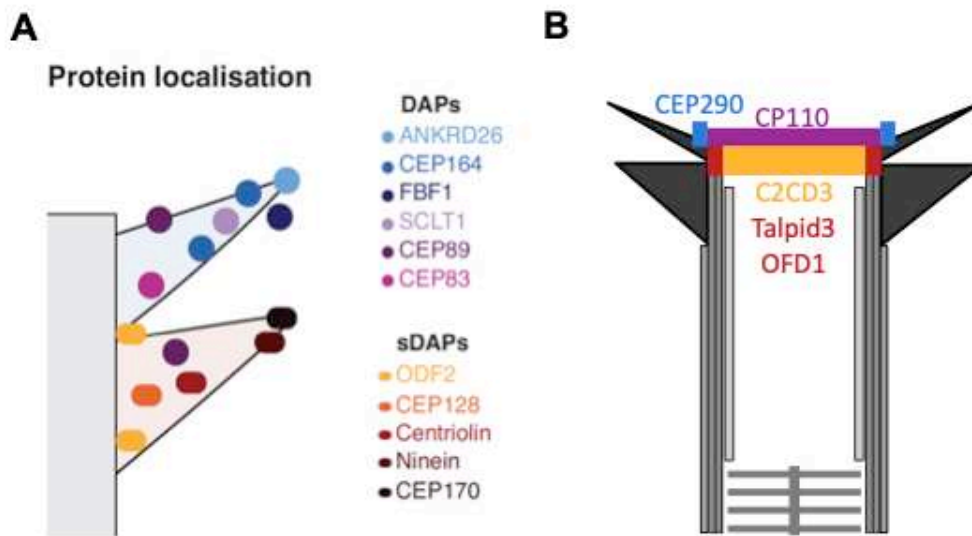


Figure 4: Localization of components of the distal region of the mother centriole. (A) Distal appendages and subdistal appendages components, from (Tischer et al., 2020). (B) Distal cap components.

While some aspects of centriole structure are highly conserved across species, such as the MT triplets, the cartwheel or the DAs, others, such as the SDAs, are only found in vertebrates. Within the eukaryotic tree of life, a variety of appendages or fibers associated with centrioles are indeed observed. The unicellular green alga *Chlamydomonas reinhardtii* is one of the species in which the structure of centrioles has been the best characterized. In *C. reinhardtii*, two centrioles (or BBs) support the assembly of two motile flagella necessary for locomotion. A set of fibers and microtubular roots links the centrioles to each other and to other cellular structures (Figure 5A). These fibers and roots are attached to specific MT triplets, which provide the centriole an inherent circumferential, or rotational asymmetry. In two studies published in 2004 and 2005, Geimer and Melkonian described these structures in detail, and also uncovered structures located asymmetrically within centrioles (Geimer & Melkonian, 2004) (Geimer & Melkonian, 2005). First, they described a 10-nm diameter filament forming an annular structure associated to 5 consecutive doublets in the distal centriole lumen, which they called the “acorn” (Figure 5B and A). Second, they observed a V-shaped filament linking the acorn to two triplets located opposite to it. These two structures are situated at the same level as the transitional fibers (tf), which are equivalent to the DAs. The acorn and V-shaped filament are early markers of rotational polarity in *C. reinhardtii* centrioles since they are already found in procentrioles (or probasal bodies (pbb)). The V-shape filament contains Centrin, but the composition of the acorn has not been

elucidated. However, in their 2004 study, Geimer and Melkonian suggested that a protein named Vfl1p might be a component of the acorn, as Vfl1p is located near the acorn on the triplets facing the distal connecting fiber (dcf) (*i.e.*, triplets 1, 2 and 9) (Silflow et al., 2001). The authors also stated that structures resembling the acorn can be seen on electron micrographs obtained from several other eukaryotic species, although these observations are nowhere near as conclusive as their own data. Recently, however, an acorn-like structure was described in a more convincing manner in *Trypanosoma brucei* centrioles (Vaughan & Gull, 2016). These findings therefore suggest that, despite the variability of appendages associated with centrioles in different species, there may be conserved structures within centrioles that generate molecular asymmetry between the MT triplets (Kloc, 2019).

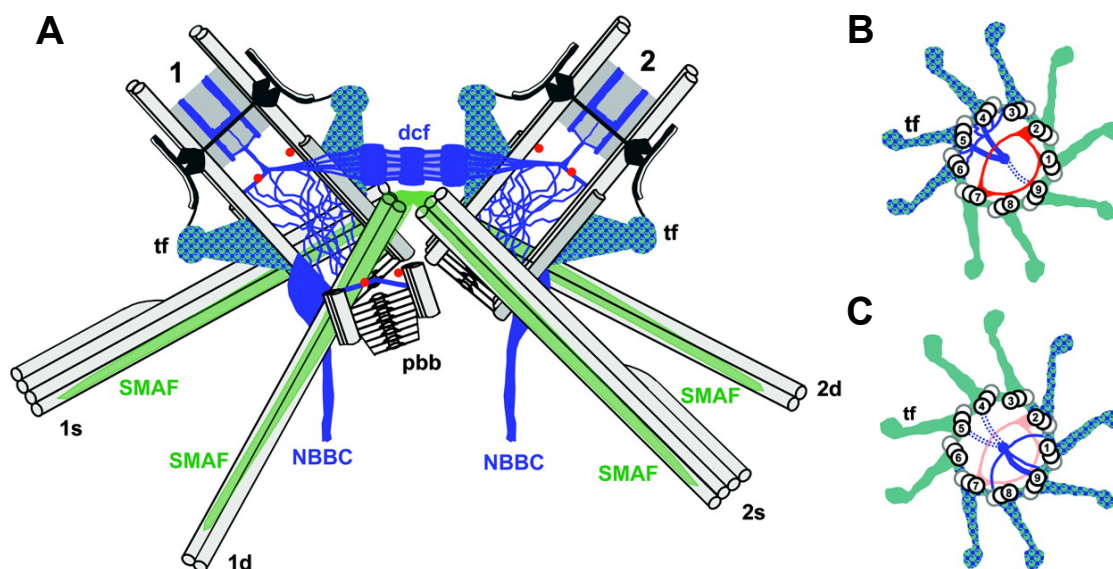


Figure 5: : Schematic representation of the basal apparatus of *Chlamydomonas reinhardtii*, from (Geimer & Melkonian, 2005). The two basal bodies (BBs) are shown in longitudinal section (1 is the older, 2 is the younger), including the transition region of the axoneme. Also shown are the two probasal bodies (pbb), the distal connecting fiber (dcf) that connects the BBs, the four flagellar roots with their microtubular and fibrous components (Striated Microtubule-Associated Fibers (SMAF)), and the transition fibers (tf), which are equivalent to the distal appendages and connect the centriole to the ciliary membrane. Centrin-containing structures form a continuous filamentous scaffold (shown in blue) that extends from the two nuclear basal body connectors (NBBCs) to the transition zone (TZ). Among them, the V-shaped filament is located at the distal end of the basal and pbb, at the same level as the acorn (shown in red). (B)(C) Cross sections in the distal part of the centriole at the level of the transition between triplets and doublets (B) or slightly below (C). The acorn (in red) connects triplets 7, 8, 9, 1, and 2, and the V-shaped filament (in blue) connects triplets 4 and 5 to the acorn and to other centrin-containing elements.

1.1.2.2. The pericentriolar material

The second major component of the centrosome after the centrioles is the PCM, also called the centromatrix, which surrounds the centrioles. The PCM is a dense and dynamic collection of proteins often described as filamentous and insoluble. The major components of the PCM in the human centrosome are pericentrin (PCNT), CEP192, CDK5RAP2, CEP152, centrosomal p4.1-associated protein (CPAP) and γ -tubulin. One shared feature among most of these different proteins is the abundance of coiled-coil domains. These domains consist of intertwined α -helices that mediate protein-protein interactions, creating a porous structural scaffold on which key regulators of centrosome function are loaded. A well-known function of PCM is MT nucleation, *i.e.*, the initiation of *de novo* MT assembly. MTs nucleation is mediated by large protein complexes called γ -tubulin ring complexes (γ -TuRCs), which are recruited by PCM components (Figure 6A). The γ -TuRC, which exhibits 13-fold symmetry and is approximately 25 nm in diameter like MTs, allows the assembly of the first α/β -tubulin dimers to form the 13 protofilaments characteristic of *in vivo* MTs. In addition, the γ -TuRC caps and stabilizes the minus end of MTs. Once the limiting step of nucleation has been catalyzed by the γ -TuRC, MTs extend towards the periphery of the cytoplasm by addition of tubulin dimers at their + end.

The centrosome is a membrane-less organelle, implying that its shape and size are not delimited by a clear boundary. PCM components are not dense to electrons, and thus little structural information on the organization of the PCM could be provided by EM. Recent advances in super-resolution optical microscopy have allowed significant progress in the understanding of this organization. Unlike what was originally proposed, it was discovered that the PCM is in fact well-organized. In interphase, the PCM is ordered in compact layers around the centrioles. PCNT and CEP152 are polarized around the centrioles and serve as molecular rulers to set the size of the PCM inner layer. CEP192, CDK5RAP2 and γ -Tubulin then accumulate within this layer. The size and composition of the PCM vary with the cell cycle. Most strikingly, the PCM massively expands prior to mitosis to ensure the formation of the mitotic spindle and the numerous MTs it requires. PCM expansion is triggered by the phosphorylation of several PCM components by Polo-Like Kinase 1 (PLK1). This process, called centrosome maturation, involves a massive recruitment of PCM proteins, creating an outer PCM layer and thus increasing PCM diameter. This gel-like condensate, which unlike the inner layer appears to lack a uniform organization,

serves as a scaffold to load the γ -TuRC and assemble mitotic MTs. At the end of mitosis, PLK1 is inactivated, inducing dephosphorylation of PCM components and PCM disassembly. One proposed model to explain the timely disassembly of the mitotic PCM is that it also involves cortical forces exerted by MT motors, which tear the PCM apart (Figure 6B) (Fry et al., 2017) (Woodruff et al., 2014).

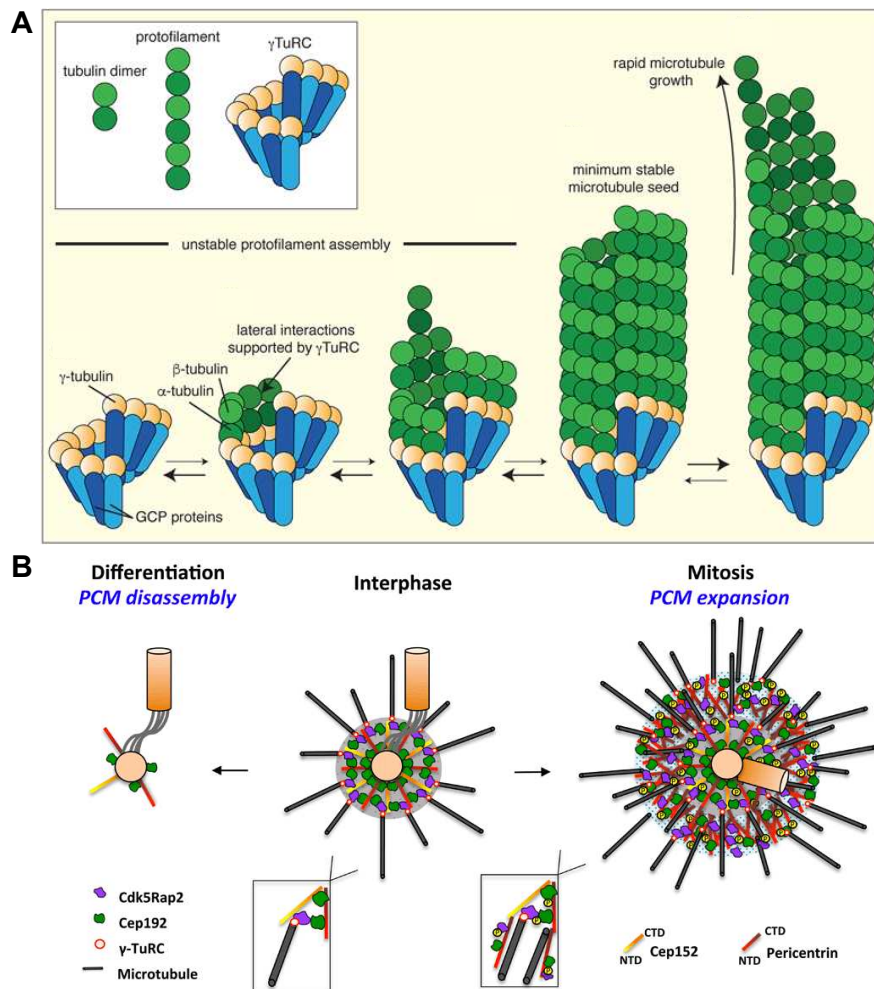


Figure 6: Nucleation of microtubules (MTs) by the γ -TuRC and PCM structure during cell cycle progression. (A) Schematic representation of MTs nucleation within the γ -TuRC. The γ -tubulin (yellow) and GCP proteins (blue) that compose the γ -TuRC are assembled in a single-turn helix. The γ -tubulin molecules recruit α/β -tubulin dimers, thereby promoting lateral interactions between α/β -tubulin dimers as they grow into protofilaments. From (Tovey & Conduit, 2018). Changes in PCM structure during PCM maturation and disassembly. In interphase, the PCM is associated with the mother centriole. The size of the PCM is defined by PCTN and CEP152 that form the inner layer (in gray). Within this layer, CDK5RAP2 and CEP192 form a branched matrix that provides binding sites for the γ -TuRC. In mitosis, PCM expansion is triggered by

PLK1-phosphorylation of PCTN, CDK5RAP2 and CEP192. The outer expansion layer (in blue) has gel-like properties and is less organized than the interphase PCM but has a greater capacity to nucleate MTs. At the end of mitosis, PCM disassembly is triggered by PLK1-phosphorylation and motor-driven cortical forces. From (Fry et al., 2017)

1.1.2.3. Centriolar satellites

Centriolar satellites (CS), non-membranous cytoplasmic granules that concentrate near the centrosome, are often considered the third compartment of the centrosome. They are very large electron-dense protein assemblies ranging in size from 70 to 100 nm. CS disperse upon entry into mitosis and reassemble upon exit from mitosis. They are associated with MTs and some of them move along the MTs thanks to molecular motors, in particular dynein. However, the majority of CS exhibit non-directional diffusive movement. CS are important regulators of centrosome and cilia functions because they act as storage containers for centrosomal and ciliary components, allowing either their delivery to the centrosome or conversely their sequestration. The Pericentriolar-Material 1 protein (PCM1) acts as a scaffolding protein for CS. This large protein, rich in coiled-coil domains, performs its function by self-oligomerizing and physically interacting with other components of the CS. Other proteins are important for maintaining and forming the CS, such as BBS4 and OFD1, but unlike PCM1, they also localize to the centrosome. The CS perform many roles: they are involved in ciliogenesis through ciliary vesicle assembly, axoneme extension, and ciliary signaling, functions that will be discussed in more details later in this manuscript. CS have also been shown to be involved in the ubiquitin-proteasome system and autophagy, among others (Tischer et al., 2020) (Hori & Toda, 2017) (Prosser & Pelletier, 2020).

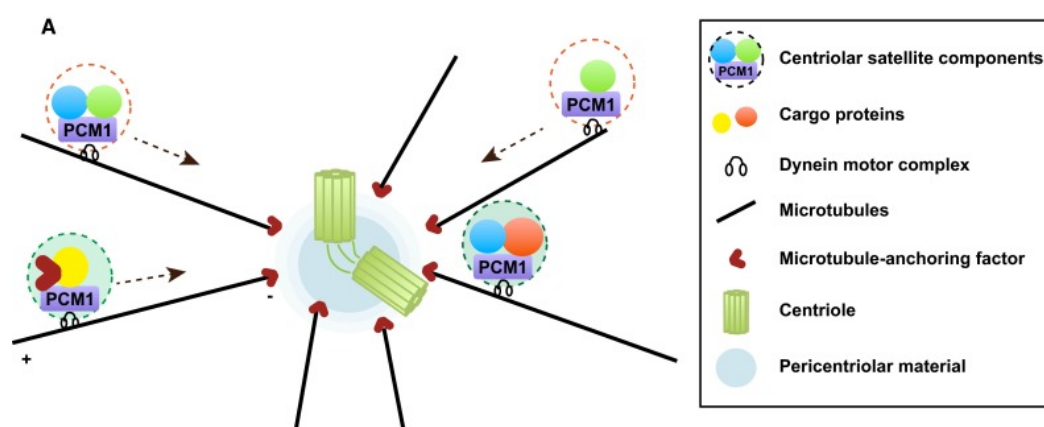


Figure 7: Schematic representation of the centriolar satellites (CS), from (Hori & Toda, 2017). The protein PCM1 serves as a platform for CS assembly. CS localize along MTs and can accumulate around the centrosome in a dynein-dependent manner.

1.1.2.4. Cilia

Centrioles are not only important for the organization of the MTOC, but also provide an essential template for cilia formation. When associated with a cilium, the centriole is called a BB, but in vertebrates at least, the overall structure of the BB is not markedly different from that of the mother centriole. The axoneme, formed by elongation of the doublets present at BB distal end, retain for at least part of its length the 9-fold symmetry inherited from the BB (Figure 8). The distal end of the axoneme, however, usually does not maintain this organization, as some of the MTs terminate before the others. There is a great variety in the architecture of the distal domain of cilia, which appears to be adapted to the specific functions of cilia (Soares et al., 2019). The axoneme is ensheathed in the ciliary membrane, which is in continuity with the plasma membrane of the cell. This continuity of the membranes does not imply that they share the same composition. Phosphoinositides (PI) are phosphorylated lipids that confer distinct molecular identities to the different cell membranes and indeed, the ciliary membrane maintains a distinct PI composition with a high level of PI(4)P and a low level of PI(4,5)P₂. This is due to inositol polyphosphate-5-phosphatase E which hydrolyzes PI(4,5)P₂ to PI(4)P in the ciliary membrane. At the base of some cilia, in particular the primary cilia, there is the ciliary pocket. The ciliary pocket is a membrane invagination separating the ciliary membrane from the plasma membrane, and it also has a distinct composition from those of the other two membranes (Garcia et al., 2018).

The limit between the plasma membrane, or the ciliary pocket, and the ciliary membrane is delimited by the *tf*, which connect the BB to the plasma membrane (Figure 8). The transition zone (TZ) is the domain at the base of the cilium, after the *tf*, that serves as a diffusion barrier to control the protein composition of the ciliary compartment. At this level, several rows of so-called Y-links (Figure 8) are present, ranging from one in some fibroblasts to around 40 in retinal rod cells (Garcia-Gonzalo & Reiter, 2017). Those Y-shaped linkers connect the MTs of the axoneme by the rod of the “Y” to the ciliary membrane with their two arms. At the ciliary membrane, the rings formed by transmembrane proteins of the “arms”, which are visible by EM, form the so-called ciliary necklace. The TZ consists of three main modules: the MKS, NPHP and CEP290 complexes, named after one of their components. Proteins of the same complex are interdependent for their localization in the TZ. The CEP290 module is composed of CEP290 and

NPHP5. It is localized above the tf to the level where the Y-links begin, in a circular localization associated with the wall of the MT doublets. The NPHP1 module is composed of NPHP1, NPHP4, and RPGRIP1L, and the MKS module is composed of TCTN1, TCTN2, TCTN3, MKS1, B9D1, B9D2, CC2D2A, TMEM17, TMEM67, TMEM107, TMEM216, TMEM231 and TMEM237. These two modules are thought to be components of the Y-links. Indeed, it has been shown that several proteins composing these 2 modules exhibit a 9-fold doublet distribution that fits the distribution of the “arms” of the Y. The TZ and tf act as a gate that controls the composition of the cilium by facilitating, restricting or preventing the entry of proteins from the cytoplasm or the plasma membrane (Shi et al., 2017) (Yang et al., 2015) (Gonçalves & Pelletier, 2017). The intraflagellar transport (IFT) is a highly conserved process in animals that need to pass this gate. It is based on the kinesin and dynein motor that navigate up and down through the axoneme, important for cilia function and assembly (see 1.2.4.2 The intraflagellar transport).

This basic structure of the cilium is conserved among eukaryotes, but cilia nevertheless exhibit considerable variations in terms of shape, size, presence of associated structures, number per cell, motility patterns, and sensory abilities (Figure 8). This structural variability reflects the diversity of their functions. Indeed, cilia appear to be adapted to specific biological functions, from fluid transport and cellular locomotion to sensory sites for various signal transduction pathways. Moreover, a variety of proteins are required in different kinds of cilia, and hundreds of components are implied in their structure, function and assembly. Cilia can be separated in two major group: immotile or motile, with numerous subtypes. Those cilia can be arbored as one per cell, or multiple cilia can be formed in so-called multiciliated cells. Sensory function is more associated with immotile cilia even though motile cilia can also have this function.

Immotile cilia, also called sensory cilia, can be specialized to sense fluid flow, light, odorants or signaling molecules. The most studied immotile cilium, which is present on most quiescent cells within the vertebrate body, is a solitary signaling cilium called the primary cilium. It is composed of nine MT doublets but lacks central MTs, a configuration referred to as 9+0. The primary cilium is required for signal transduction of different signaling pathways acting principally during development, in particular the hedgehog (Hh) pathway. Another type of immotile cilia is found in the epithelial cells lining the mammalian kidney tubules. It projects into the tubular lumen, and has a mechano-sensory role in perceiving urine flow. In the embryonic node of many vertebrate

species, sensory cilia have been shown to trigger the establishment of left-right asymmetry by detecting (by flow sensing or chemo sensing) the leftward fluid flow generated by another type of cilia within the node cavity (Tajhya & Delling, 2020). Immotile cilia are also an essential part of the sensory apparatus of the nose, eyes and ears.

Motile cilia are usually longer than immotile ones. They are organized in a so-called 9+2 MTs organization, which results from the presence of two central MT singlets in addition to the nine peripheral doublets. Between MTs doublets, motile cilia have inner and outer dynein arms that use energy from ATP hydrolysis to power their movement. Their rhythmic motion can vary due to the nexin-dynein regulatory complex, which regulates the activity of the dynein arms. Motile monocilia, such as the prototypical flagella on protozoans and sperm cells, beat generally in a wavelike or rotational fashion in order to generate cellular locomotion. In contrast, the motile cilia that generate a leftward flow in the embryonic node display a 9+0 configuration and move in a rotational manner. Finally, multiple motile cilia such as those carried by multiciliated cells lining the respiratory tract, the brain ventricles, and the oviducts, can move fluids of higher viscosity. Multiciliated cells form up to several hundreds of motile cilia, which display a 9+2 configuration. These cilia beat in a planar fashion, forming synchronous waves that induce a directional movement to clear the mucus in the airways, circulate cerebrospinal fluid or move oocytes, respectively within the brain, the spinal cord and the oviducts in humans (Choksi et al., 2014). Cilia in multiciliated cells possess a striated rootlet at the proximal part of the BB to anchor them, as well as an appendage called the basal foot, which is aligned with the direction of the ciliary beat. A similar cell type is present in the epidermis of some invertebrates such as the flatworm *Schmidtea mediterranea*. This freshwater planarian uses ciliary beating for locomotion. Like in vertebrates, BBs in planarian multiciliated cells possess a basal foot pointing in the direction of the effective stroke, and a striated ciliary rootlet pointing in the opposite direction. These appendages are linked to different cytoskeletal arrays that control BB anchoring and polarization (Basquin et al., 2015).

Planar ciliary beating is also observed in unicellular eukaryotes. For instance, the two flagella of *C. reinhardtii* beat planarly and in opposite direction, performing a breaststroke type of swimming. The two BBs at the base of these flagella do not possess a structure clearly

homologous to the basal foot, but they are also associated to various accessory structures that decorate the BBs in a rotationally asymmetric manner (Figure 5).

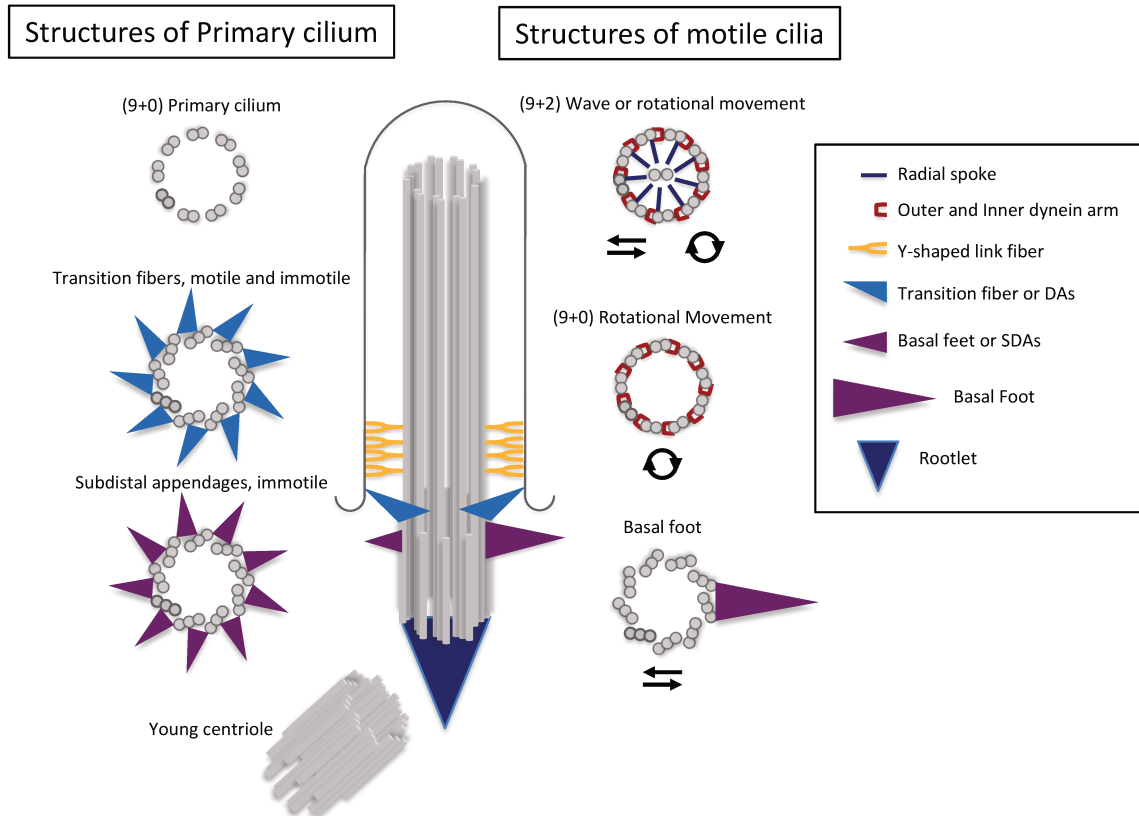


Figure 8: Most common ciliary architectures, adapted from (Soares et al., 2019). The axoneme is composed of nine microtubules (MTs) doublets (gray) that extend from the basal body (BB). In the distal part of the BB, transition fibers (tf) are arranged in a 9-fold symmetry (light blue). The Y-shaped links (yellow), along with the tf, form the transition zone. (Left) The primary cilium is a non-motile (9+0) structure. Subdistal appendages (purple) are found below the tf and are not always in a 9-fold symmetry. The young centriole, usually placed next to the BB, does not support an axoneme. (Right) The motile cilium possesses motor proteins positioned between the MTs doublets, the outer and the inner dynein arms (red), that drive ciliary movement. In the (9+2) cilium, a central pair of MTs is present in the middle of the axoneme. It is surrounded by 9 radial spokes linking the central pair to the peripheral MTs doublets. (9+0) motile cilia like the nodal cilia exhibit a rotational beating pattern. In animal multiciliated cells, cilia beating in a planar fashion are assembled from BBs possessing a unique basal foot (purple), which is aligned with the direction of the ciliary beat.

1.1.3. Evolution

Over millions of years, mutations and selection have favored the occurrence of changes at all scales within living organisms, giving rise to a wide range of species, each with its own solution for survival. The centrosome as a MTOC is found in animals, higher fungi and several other related eukaryotic lineages. In these different lineages, the structure of the centrosome is highly variable. For instance, the centrosomes of higher fungi and dictyostelids do not contain centrioles. Nevertheless, centrosomes in these different lineages perform similar functions and share some of their molecular components. The basic properties associated with the centrosome are to maintain itself to the cell center due to its MT nucleation activity, to duplicate itself once during each cell cycle and to be physically associated with the nucleus. One likely hypothesis is that the centriole-based centrosome evolved from a flagellate ancestor by internalization of the BBs, which provided the core of the centrosome. Centrioles and cilia are among the most conserved structures in eukaryotes. Every major branch of the eukaryotic tree of life includes organisms with motile cilia, composed of MTs doublets connected by dynein arms, associated to a centriole formed by MT triplets in a nine-fold symmetrical arrangement organized around a cartwheel. The conservation of such a complex structure both within and between divergent lineages suggest that centrioles and cilia were already present in the Last Eukaryotic Common Ancestor (LECA), which gave rise to all extant eukaryotes. Based on the ancient association between these structures, it seems likely that centrioles evolved for the primary purpose of growing cilia and flagella. Further supporting a common origin, key molecular components of centrioles were conserved throughout eukaryotic evolution. There is no fossil record to account for the cellular organization of the LECA, but it can be to some extent inferred by comparing the cellular and cytoskeletal architecture of present-day eukaryotes. By carefully comparing the organization of the BBs and their associated connectors and cytoskeletal arrays in flagellates from divergent eukaryotic lineages, it is indeed possible to identify homologies between these different elements. Based on these analyses, the LECA was probably a biflagellate cell resembling modern organisms referred to as ‘typical excavates’. According to this model, the LECA thus possessed a complex cytoskeleton, with two flagella, one for motility and the other for feeding through a ventral groove. The oldest BB (BB1) at the base of the posterior flagellum was associated with microtubular roots delineating the ventral groove, in which the posterior flagellum was encased. The youngest BB (BB2), at the base of the anterior flagellum, was

associated with two other microtubular roots, one of them organizing an array of superficial MTs supporting the dorsal part of the cell. After cell division, BB2 moved to the posterior position and acquired the same roots as BB1, a process called flagellar transformation that is observed in extant biflagellates. Like these organisms, the LECA thus had fibers and MT roots decorating its BBs in a rotationally asymmetric manner. Therefore, centriole rotational asymmetry is likely to be an ancestral property of centrioles.

Whereas centrioles are clearly conserved across the eukaryotes tree of life, this is less clear for the centrosome. Centrosomes with diverse structures but similar functions and shared molecular components can be found in animals, higher fungi and several related eukaryotic lineages belonging to a lineage called Amorphea, which is estimated to have appeared ~300 million years after the LECA. The main function of the centrosome, which is to organize MTs, resides in the PCM. Major PCM proteins can be traced back to the origin of Amorphea (CEP192, CDK5RAP2), or at least to the last common ancestor of opisthokonts, which encompasses fungi, animals and several unicellular lineages (PCNT). In some Amorphea, the centrosome diverged and the centrioles were lost, like in yeasts that possess spindle pole body (SPB) and some amoebozoan like *Dictyostelium* that have a nucleus-associated body (NAB), both playing the role of a MTOC. The NAB and SPBs share key molecular components with the animal centrosome, supporting a common evolutionary origin. Further evolution in Metazoa (animals) was also linked to multicellularity in this lineage. For instance, in organisms like *Drosophila*, centrosome functions are clearly more important for the survival of the organism than for the survival of individual cells (Basto et al., 2006). In planarians, the centrosome was lost during evolution and centrioles only retained for ciliary assembly (Azimzadeh et al., 2012).

Instead of the fibrous and microtubular roots associated asymmetrically to the BBs of flagellates, animal centrioles either carry a basal foot – in multiciliated cells – or symmetrical SDAs. In mouse and planarian flatworms, basal foot assembly requires the conserved protein ODF2, which is also present in the genome of early branching animals. In addition, ODF2 is required for the assembly of SDAs that decorate the mother centriole in vertebrate cells. SDAs share additional components with basal feet and also serve as anchoring sites for MTs. The basal foot and its associated MTs are possibly derived from the microtubular root of earlier-branching opisthokonts, which itself might be homologous to one of the posterior roots of the excavate-like

cytoskeleton. Interestingly, conserved proteins of the VFL1 (Variable FLagella number 1) and VFL3 families are required for centriole polarization and proper assembly of microtubular roots in *Chlamydomonas* and *Paramecium*, basal foot assembly in planarian multiciliated cells, and SDA function at the mammalian centrosome. This suggests that some molecular aspects underlying MT anchorage at centrioles/BBs are ancient and conserved between the microtubular roots of flagellates and centriole appendages of vertebrate cells. Furthermore, centriole rotational asymmetry, which was likely inherited from the LECA, is shared between flagellates such as *Chlamydomonas* and animal multiciliated cells. In contrast, centrioles within the centrosome show no structural rotational asymmetry. One could thus expect that molecular mechanisms establishing centriole rotational polarity in flagellates and multiciliated cells would not be conserved at the centrosome (Azimzadeh, 2021) (Azimzadeh, 2014) (Nabais et al., 2020) (Geimer & Melkonian, 2005).

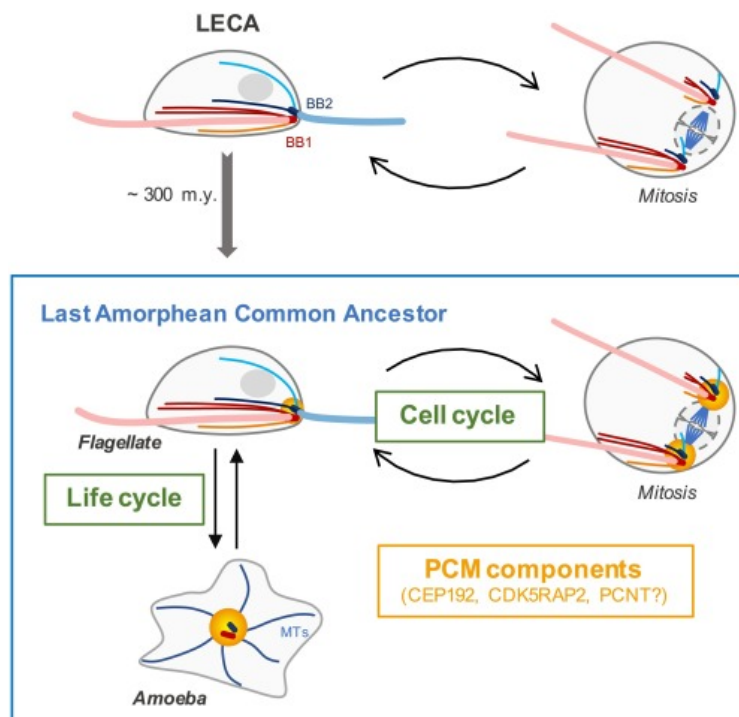


Figure 9: Possible scenarios for the evolutionary origin of the centrosome, from (Azimzadeh, 2021). The last common ancestor of Amorphea, which is estimated to have lived ~300 million years after the LECA, was still sharing most traits of the excavate-like cytoskeleton present in the LECA. Key centrosome matrix proteins can be traced back to the origin of Amorphea (CEP192, CDK5RAP2), or at least to the last common ancestor of apusomonads and opisthokonts (PCNT). PCM components might have had first evolved for organizing mitotic microtubules, even though basal bodies were possibly also connected to the spindle poles of the LECA.

1.2. The centrosome through the cell cycle

1.2.1. The cell cycle

After cell division, each daughter cell inherits a mature centrosome containing two centrioles. For this, the existing centrosome in the mother cell needs to duplicate its centrioles, a process that is tightly linked to cell cycle progression. The cell cycle is a series of events through which a cell duplicates its genome, grows and divides. The eukaryotic cell cycle is typically divided into four phases, the G1 phase (Gap 1) in which cells grow, the S phase (synthesis) in which the nuclear DNA is replicated, the G2 phase (Gap 2) in which cells also grow and the M phase (mitosis) when sister chromatids are separated and distributed to the newly formed daughter cells. At the end of mitosis, cytokinesis occurs to complete the cell division by forming two daughter cells separated by a plasma membrane. The cell cycle progression and the transitions between phases are driven by a sequential activation and deactivation of cyclin-dependent kinases (CDKs). The control on this system is provided through the availability of partner cyclins (cyc) and by phosphorylation/dephosphorylation events. CDK inhibitors (CKIs) provide a third level of CDK regulation by binding to and inactivating CDK–cyc complexes. p53 family members and other proteins transcriptionally regulate CKI levels. The progression through the cell cycle is controlled at specific checkpoints, where the cycle can stop if certain conditions are not respected. For instance, activation of the G1-S and G2-M checkpoints can arrest the cell cycle in response to DNA damage. Activation of the spindle checkpoint during anaphase prevents the separation of sister chromatids until each one of them is properly attached by their kinetochore to the spindle. Disruption of centrosome integrity by removal of centrosome components has also been shown to arrest the cells in G1 in a p53-dependent manner. Deactivating the p53 checkpoint has since been used as a tool for the functional study of centrosomal proteins beyond the G1-phase in mammalian cells (Srsen et al., 2006).

Cells begin the cell cycle in G1 with only one centrosome, and centriole biogenesis is initiated at the G1/S transition with the formation of a procentriole orthogonally to the proximal part of each preexisting centriole. This event is followed by the elongation of the procentrioles during S and G2 phases. In late G2, the two pairs of centrioles separate to form the opposite spindle poles for mitotic spindle assembly. In mitosis, the procentrioles are complete but still attached to the parental centrioles. At the end of mitosis, the young centrioles disengage from their parent

centriole and remain linked by a fibrous and more flexible linker (Figure 10). The newly formed centrioles become the new daughter centrioles, and the preexisting centrioles remain (old mother) or become (old daughter) the new mother centrioles. As a result of this duplication mechanism, the two centrioles differ in age and maturity, and have different functions (Sullenberger et al., 2020).

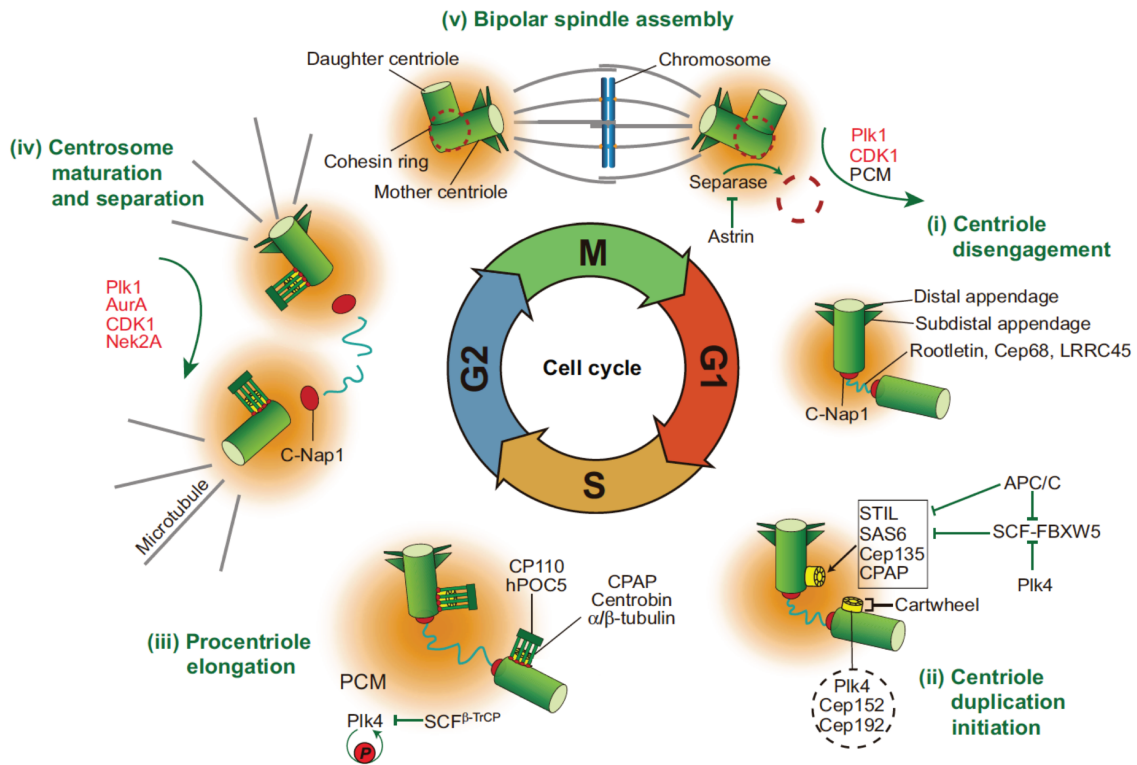


Figure 10: The centrosome cycle is linked to the cell cycle (inner circle). Mitotic kinases are shown in red. (i) Centriole disengagement occurs by the removal of the cohesin ring at the end of mitosis to early G1 phase. This process is regulated by the PCM, PLK1, CDK1, separase and astrin. After centriole disengagement, a proteinaceous linker is established, composed mainly of C-Nap1, rootletin, CEP68 and LRRC45. (ii) To initiate centriole duplication at the G1/S transition, CEP152 and CEP192 recruit PLK4. CEP135, SAS6, SCL-interrupting locus protein (STIL) and CPAP form afterwards the structural basis of the cartwheel, a process strongly regulated by APC/C, SCF-FBXW5 and PLK4. (iii) Procentriole elongation happens subsequently as centrin stabilizes α/β -tubulin dimers that nucleate from γ -tubulin complexes. CP110 and CPAP have antagonist roles to regulate procentriole length, whereas hPOC5 is a component of an inner scaffold that stabilizes the elongated centrioles. To prevent centriole reduplication, PLK4 induces its own degradation by autophosphorylation mediated by SCF β -TrCP. (iv) Maturation and separation happen before mitosis as the newly formed mother centriole starts assembling distal appendages and subdistal appendages, and both centrosomes separate and recruit additional PCM components (orange). This process is regulated by AurA, PLK1, CDK1 and Nek2A. (v) A bipolar spindle assembles as the separated centrosomes act as strong MTOCs. From (G. Wang et al., 2014).

1.2.2. Centriole duplication initiation, elongation and maturation

The initiation of centriole biogenesis is driven by the sequential action of three highly evolutionarily conserved proteins: Polo-like kinase 4 (PLK4), a serine-threonine kinase, SCL-interrupting locus protein (STIL), a scaffold protein and SAS6, the structural component of the cartwheel that acts as building block to institute the nine-fold symmetry of the centriole.

PLK4 is a master regulator of centriole duplication as loss of its activity leads to failure of centriole duplication and its over-expression leads to formation of supernumerary centrioles. In early G1 phase, PLK4 binds the proximal periphery of centrioles, a process mediated by CEP63, CEP192, and CEP152. The PCM protein CEP152 is hypothesized to act as a scaffold for PLK4, allowing it to initially form a discrete ring-like pattern composed of randomly distributed seeds (Takao et al., 2019). PLK4 can self-assemble and when present in condensates, its dissociation rate is attenuated and it auto-phosphorylates, which changes its condensation properties. PLK4 then condensates to form aggregates, thus the aggregate that recruits the greatest quantity of PLK4 prevents neighboring aggregates from recruiting more PLK4 by lateral inhibition. As well, STIL and SAS-6 preferentially bind to the largest PLK4 focus and lead to its stabilization. Consequently, the position containing the most PLK4 tends then to be the only site of centriole duplication, creating a bias that breaks the symmetry of the initial ring pattern and leading to the formation of a unique procentriole for each parent centriole (Yamamoto & Kitagawa, 2019).

PLK4 then phosphorylates STIL, which triggers STIL binding to SAS-6 and initiates centriole formation. SAS-6 self-organizes into a nine-fold symmetrical cartwheel structure, which represents the initial step of procentriole formation at the morphological level. Structurally, in humans, the cartwheel is linked to the parental centriole via a stalk of 110 nm (Guichard et al., 2010). After cartwheel formation, MT walls are formed by MTs polymerization around the cartwheel, a process that requires CPAP (Loncarek & Bettencourt-Dias, 2018). The A-MTs are first nucleated by the γ -TuRC and grow at their + end to form nine MT singlets connected to the cartwheel. Before completion of the nine A-MTs, B-MTs start growing from the wall of A-MTs, and then C-MTs grow on B-MTs to form the triplets. In contrast to A-MTs, B- and C-MTs grow bidirectionally (Guichard et al., 2010) (Loncarek & Bettencourt-Dias, 2018). Procentrioles will eventually lose their cartwheel in mitosis.

Procentrioles then elongate throughout the S and G2 phases. The dimensions of centrioles are remarkably constant in most cells of a given organism, indicating the existence of a regulation mechanism. Indeed, centriole length depends on several positive regulators of elongation like CPAP, CEP295, CEP120, Centrobin, SPICE1, C2CD3 and Talpid3, or negative regulators such as CP110, OFD1, CEP290 and Centrin-2 (Nigg & Holland, 2018) (Sharma et al., 2021). CP110 is recruited early and caps the distal end of growing pro-centrioles to limit MT extension. Other distal centriole proteins are recruited at an early stage of centriole biogenesis like C2CD3, Talpid3, OFD1 and CEP290 (Sullenberger et al., 2020). Like CP110, they are also important for cilium formation (Thauvin-Robinet et al., 2014) (Kumar & Reiter, 2021) (L. Wang et al., 2018) (Tsai et al., 2019) (Kim et al., 2008). In addition, Centrin-2 and -3 are recruited very early to assembly sites of procentrioles and are found within the distal lumen of full-length centrioles. Centrin-2 was shown to be a component of the inner scaffold of the centriole. Other proteins of the scaffold are recruited during centriole elongation, including hPOC5, POC1, FAM161A and WDR90 (Azimzadeh et al., 2009) (Le Guennec et al., 2020). However, a lot remains to be discovered regarding how these different proteins are incorporated during centriole elongation.

Posttranslational modifications of centriole MTs are also required for providing their extremely long-term stability. Indeed, centriolar tubulins are heavily modified by acetylation and glutamylation, among others. Procentriole MTs begin to be acetylated at their earliest stages and mature human centrioles are highly acetylated along the entire length of MTs. Acetylation is also prominent on stabilized cytosolic MTs and in the ciliary axoneme. Centrioles are also heavily glutamylated, a modification of tubulin that is more concentrated around the centriole's proximal ends, as polyglutamylated signal is localized at the outer C-MT, which is absent from distal ends (Hamel et al., 2017) (Sullenberger et al., 2020).

The elongation process ends when the cell reaches mitosis, and the end product is a daughter centriole. Maturation of the daughter centriole into a mother centriole will occur in the next cell cycle. Indeed, the centrosome is an asymmetric organelle because its two centrioles differ by at least one cell cycle in age and protein composition. The younger centriole is characterized by daughter centriole-specific/enriched proteins (DCPs) and the older by its appendages. DCPs, which include CEP120, Centrobin, and Neurl4, are recruited to nascent daughter centrioles after centriole duplication initiation and are involved in the regulation of centriole elongation. DCPs

are removed at the G1/S transition of the next cell cycle during mother centriole maturation. Then, SDAs and DAs are respectively assembled during the G2 phase and at the G2/M transition. DAs assemble through the sequential recruitment of CEP83, CEP89, SCLT1, CEP164, and FBF1 proteins. The assembly of SDAs is initiated by the recruitment of ODF2, a protein that is also present at the base of DAs and required for the assembly of both types of appendages (Ishikawa et al., 2005) (Nigg & Stearns, 2011). Other SDA components include CEP128, centriolin, ninein and CEP170 (Mazo et al., 2016). The distal proteins Talpid3, C2CD3 and OFD1 form a network important for centriole maturation, as DCP removal requires Talpid3 and C2CD3, DAs assembly requires all 3 proteins, and SDAs assembly requires Talpid3 and OFD1. Mature mother centrioles also have an associated PCM, which new centrioles acquire during a process termed “centriole-to-centrosome conversion”. It involves the recruitment of CEP295 to the proximal centriole wall, which then triggers the recruitment of CEP152, a critical factor for centriole duplication and PCM organization (Loncarek & Bettencourt-Dias, 2018) (see section 1.1.2.2).

At the beginning of G2, there is a transient remodeling of both types of appendages present on mother centrioles. SDAs and DAs become undetectable and less conspicuous, respectively, in G2 and throughout mitosis, and reappear in G1. It was shown that SDA and DA proteins localized near the centriole remain associated with centrioles during the entire cell cycle, whereas proteins at the periphery of appendages are relocated to the adjacent PCM. The current model is that the inner appendage proteins may serve as a permanent scaffold for recruitment of more functional and dynamic components at their end. However, the two mother centrioles obtained at the end of mitosis still have functional asymmetries. For example, cells that inherit the older mother centriole grow a primary cilium earlier than those with the younger mother centriole. It has been proposed that appendage remodeling could help reduce the effects of age asymmetry between the old and the new mother centriole (Sullenberger et al., 2020) (Bowler et al., 2019).

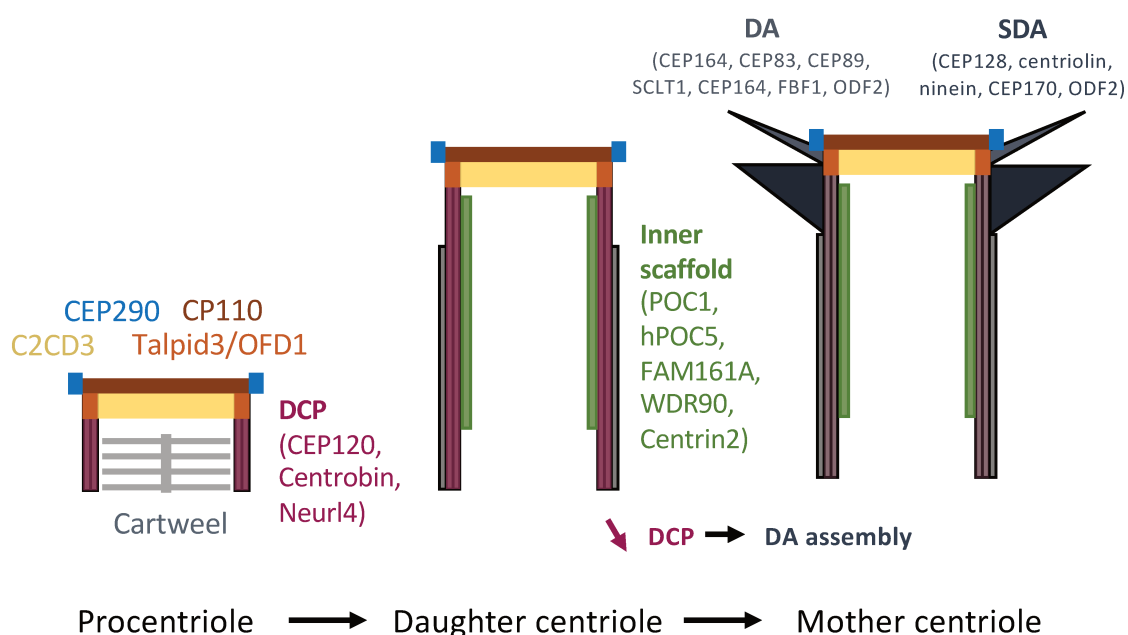


Figure 11: Centriole assembly and maturation. Distal proteins are already present in procentrioles prior to elongation. The Inner scaffold appears to be incorporated during centriole elongation. Maturation of a daughter centriole into a mother centriole requires DCP removal to induce DAs and SDAs formation.

1.2.3. Mitosis

Even though the centrosome is not strictly required for mitosis, it still actively participates in this final step of the cell cycle. At G2–M, the two newly formed centrosomes, with their procentriole still engaged, progressively go apart from one another and orchestrate the formation of the mitotic spindle. The PCM of both centrosomes expands in size in a process called centrosome maturation, which increases centrosome MT-nucleation capacity and thereby promotes the formation of the mitotic spindle.

Besides spindle MTs, mitotic centrosomes also nucleate astral MTs required for positioning the spindle. Spindle position depends on MTs-nucleating factors and proteins stabilizing MT minus ends, on the one hand, and on protein complexes localized at the cortical surface or in the cytoplasm that capture MT plus ends, on the other hand. Dynein, a minus-end directed motor, generates forces that are crucial for correct spindle positioning. Dynein anchored at the cell cortex pulls on astral MT plus ends to move the centrosomes closer to the cortex. The protein NuMA (Nuclear Mitotic Apparatus) provides the cortical anchor for dynein to generate these

pulling forces. NuMA localization is controlled by the planar cell polarity (PCP) pathway, which determines the orientation of the mitotic spindle in certain cell types (Elric & Etienne-Manneville, 2014). Although centrosomes are not strictly required for the formation of a bipolar spindle, they are required for the assembly of astral MTs. In the absence of centrosomes, bipolar spindles form, but are not attached to the cell cortex and are randomly oriented. Because the spindle dictates the position and orientation of the cleavage furrow during cytokinesis, centrosome position ultimately determines the orientation of cell division (Elric & Etienne-Manneville, 2014).

During mitosis, newly formed daughter centrioles are still connected in a perpendicular orientation to mother centrioles. It is in telophase/G1 that the two pairs of centrioles separate in a process called centriole disengagement. This process occurs when the ring of cohesin between the two centrioles is degraded by the protease separase (Figure 10). After their disengagement, a proteinaceous linker forms between mother and daughter centrioles to maintain centrosome cohesion. This linker is composed mainly of C-Nap1 and Rootletin. C-Nap1 is located at the proximal part of both centrioles and recruits Rootletin, which form fibers connecting the two centrioles. The linker remains until late G2, when it disassembles to allow the assembly of the mitotic spindle. Centrosome separation is triggered by the Serine/threonine-protein kinase Nek2, which phosphorylates C-Nap1 and rootletin to allow their displacement from the centrosomes (Agircean et al., 2014)

1.2.4. The primary cilium

1.2.4.1. Early steps of ciliary assembly

At the end of mitosis, when appendages are fully (re)assembled, cells can trigger the formation of a primary cilium. Ciliogenesis happens either in G1 or in G0 as cells exit the cell cycle. It starts by the docking of pre-ciliary vesicles, presumably derived from the Golgi, to the DAs. DAs, or tf in this context, are crucial for this process. At the periphery of the tf, CEP164 interacts with Rab8 and Rabin8, and anchors the pre-ciliary vesicles. These vesicles then fuse into a larger ciliary vesicle that extends over the DAs following membrane remodeling orchestrated by EHD1 and EHD3, which are membrane-shaping proteins, and their partners, PACSIN1 and PACSIN2. After ciliary vesicle assembly, the distal centriole components CP110 and CEP97 are removed from the mother centriole. This step is fundamental as these proteins are inhibitors of cilium assembly.

Additional interactors of CP110 have been shown to play a role, such as the kinase TTBK2 whose recruitment depends on the lipid composition of the ciliary vesicle. Removal of the inhibitory proteins triggers the elongation of MT doublets at the distal end of the mother centriole, and simultaneously, the elongation of the ciliary membrane. IFT proteins such as IFT88 and IFT20 are recruited to the ciliary base and mediate axoneme elongation, with components of the TZ complex that ensure selective protein entry into the cilium. The coordination of ciliary membrane elongation is managed by components of the vesicular trafficking machinery such as Rabin8 and Rab8 (Kumar & Reiter, 2021). TZ assembly is a complex process involving multimeric protein modules that are subject to a strict assembly hierarchy. In most eukaryotes, three protein complexes (CEP290, NPHP, and MKS) cooperate to build the TZ. CEP290 has been shown to coordinate the early formation of TZ (Z. Wu et al., 2020), but variations exist between organisms and even cell types (Wiegering et al., 2018). The ciliary membrane expands concomitantly to axoneme elongation, forming a sheath that encloses it. The ciliary sheath will then fuse to the plasma membrane to expose the primary cilium to the external environment. When the cell re-enters the cell cycle, the cilium is generally resorbed at the G1/S transition or in S phase, but this process is depending on the cell type.

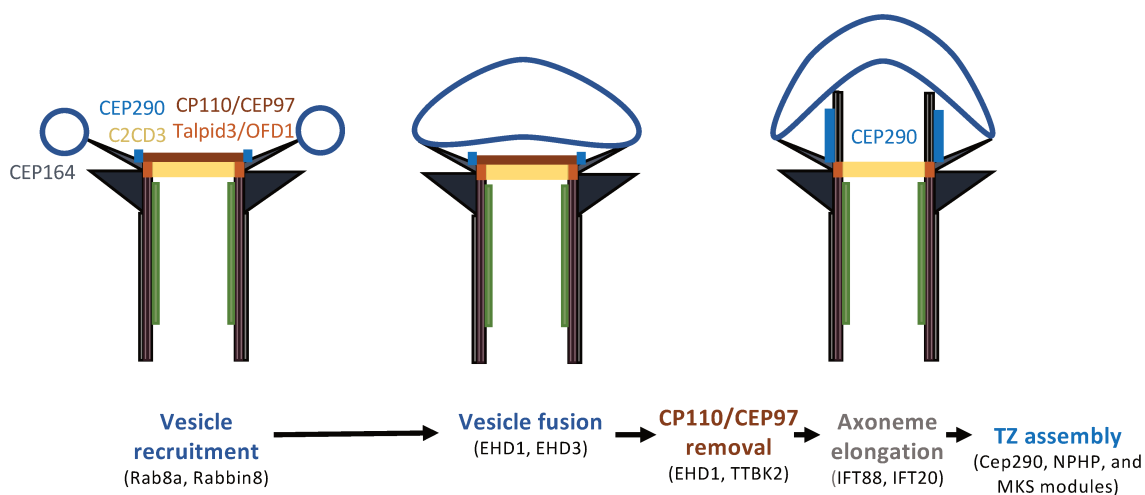


Figure 12: Early steps of ciliogenesis. C2CD3, Talpid3 and OFD1 are positive regulators of ciliogenesis as they help form the distal appendages (DAs). CEP290 is a transition zone component, already present in the distal part of centrioles prior to the initiation of ciliogenesis. CP110 and CEP97 are inhibitors of ciliogenesis. Cilium formation begins with the recruitment of pre-ciliary vesicles by the DAs mediated by Rab8a and Rabin8. These vesicles fuse under the action of EHD1 and EHD3 to form a ciliary vesicle. CP110/CEP97 removal, mediated by EHD1 and TTBK2, uncaps mother centriole microtubules, allowing the formation of axoneme doublets. The transition zone is then assembled, accompanied by an extension of the CEP290 domain.

1.2.4.2. Intraflagellar transport

In order to elongate, the axoneme relies on the recruitment of tubulin dimers and other axoneme components transported by the IFT machinery. IFT particles, which are large multiprotein complexes, assemble into IFT trains that move bidirectionally along the axoneme. Inhibition of the IFT prevents the assembly of most cilia, and perturbations of IFT components can impair ciliary architecture and function as observed in multiple ciliopathies. In transmission electron microscopy (TEM), IFT trains are linear arrays of electron-opaque particles sandwiched between the ciliary membrane and the MTs doublets. The detailed ultrastructure of IFT trains was analyzed by electron tomography and two types were reported: long IFT trains of 700 nm that contribute to anterograde transport, and shorter ones, about 250 nm in length, for the retrograde transport. The movement along the MTs relies on motor proteins and is remarkably fast (0,5-5µm/s) (Bertiaux et al., 2018). IFT trains are carried to the ciliary tip (anterograde) by kinesin-2 and returned to the cell body (retrograde) by dynein 2. IFT trains are fairly large complexes of at least 20 or more proteins, which are organized in two subcomplexes, the IFT-A and IFT-B complexes, which function together in both retrograde and anterograde transport (Taschner & Lorentzen, 2016). In *C. reinhardtii*, anterograde trains were found to travel along the B-MT, whereas retrograde trains were restricted to the A-MT (Stepanek & Pigino, 2016). Considering the relatively large size of the IFT trains, and the limited space available in the cilium, the question of the spatial organization of IFT is not trivial. In agreement, a recent study showed that IFT is restricted to certain MT doublets in the flagella of *T. brucei*. The authors show that IFT trains are found almost exclusively along doublets 3-4 and doublets 7-8, the doublets on the prolongation of the central pair, indicating an asymmetric distribution of IFT in these flagella (Bertiaux et al., 2018). When anterograde trains reach the distal end, they are converted into usually smaller retrograde trains while remaining on the same MTs doublets (Buisson et al., 2013). Indeed, IFT trains are not the only molecules navigating in the cilium, and restricting IFT to specific doublets could provide better spatial organization for all the trafficking occurring in the cilium. For instance, proteins small enough to pass the ciliary gate can diffuse in the cilia without the IFT and membrane trafficking can occur by lateral diffusion. In addition to the axoneme building blocks, the IFT trains transport another complex called the BBSome. BBSome proteins are the products of genes whose mutations have been linked to Bardet–Biedl syndrome.

The BBSome is thought to function as an IFT adaptor for the trafficking of membrane proteins to and out of the primary cilium.

To enable ciliary maintenance and function, IFT particles and their cargoes must pass through the gate formed by the TZ and the tf at the base of the cilia. The ciliary lumen and the ciliary membrane are contiguous with the cytosol and the plasma membrane, respectively, and the ciliary gate is thus crucial to maintain a distinct composition between the cilium and the rest of the cell. This leads to the concentration of specific proteins in the cilium and the exclusion of others, which is critical to the proper function and maintenance of the cilium. To enter or exit the lumen of the cilium, soluble proteins can diffuse or be actively transported. Only small proteins can cross the barrier by diffusion because the ciliary gate behaves as a sieve with a size-exclusion filter. The pore size of the sieve is smaller than the distances between adjacent electron-dense structures (Y links or tf), revealing the possible presence of a non-electron dense meshwork between them. In contrast to the diffusion of small proteins, larger ones require active transport dependent on MT motors. In the case of membrane proteins, lateral exchange between plasma and ciliary membrane is prevented by a septin-based diffusion barrier localized at the TZ. Trafficking complexes are required for membrane proteins to cross this barrier. The mechanisms by which large proteins complexes, whether associated to the membrane or not, are able to cross the tf, the ciliary necklace, the Y-links, the septin barrier, and other obstacles they may encounter along the way is still unknown (Garcia-Gonzalo & Reiter, 2017) (Breslow et al., 2013).

1.2.4.3. Ciliary signaling

Primary cilia play essential roles in many signaling pathways, including Hh, GPCR, WNT, RTK, TGF β /BMP, Notch, ECM receptor, Hippo, mTOR and NF- κ B signaling pathways. The Hh pathway is a conserved signaling cascade whose activation in vertebrates depends strictly on the presence of a cilium. Hh signaling plays crucial roles in many fundamental processes such as embryonic development, stem cell maintenance, and tissue homeostasis. Deregulation of the Hh pathway is associated with cell transformation and tumorigenesis. First identified in *Drosophila*, the main components of the Hh pathway are overall conserved in animals, although the precise intracellular organization of the cascade can vary between species. Notably, the Hh pathway functions independently of the cilium in *Drosophila*.

In the absence of Hh ligand, PTCH1, the transmembrane receptor for Hh, is located at the base of a primary cilium and inhibits the activity of the transmembrane protein smoothed (SMO) (Figure 13). At the same time, the key intracellular Hh pathway regulator, SUFU, and the kinesin Kif7, sequester the transcriptional factors Gli1, Gli2, and Gli3, allowing for Gli proteins to be phosphorylated by the kinases PKA, GSK-3 β and CK1. They are then processed into transcriptional repressors or targeted for degradation. This leads to the formation of the transcriptional repressor Gli3, which cannot activate target gene transcription upon binding to DNA in the nucleus.

Hh signaling pathway requires the regulated production, processing, secretion and trafficking of Hh ligands, which in vertebrates include Sonic Hh, Indian Hh and Desert Hh. These Hh ligands initiate the signaling cascade by binding to their canonical receptor Patched (PTCH1), and to the co-receptors CDON and BOC. This triggers PTCH1 to move out of the cilium and to release the inhibition of SMO, allowing SMO translocation into the cilium and phosphorylation of its cytoplasmic tail. In the cilium, activated SMO mediates the dissociation of GLI proteins from Kif7 and SUFU. GLI proteins are then differentially phosphorylated and processed into Gli1 and Gli2 transcriptional activators. Gli activators are transported to the nucleus to activate the expression of Hh target genes, which include many components of the pathway, such as PTCH1 and GLI1, leading to feedback mechanisms (Pala et al., 2017).

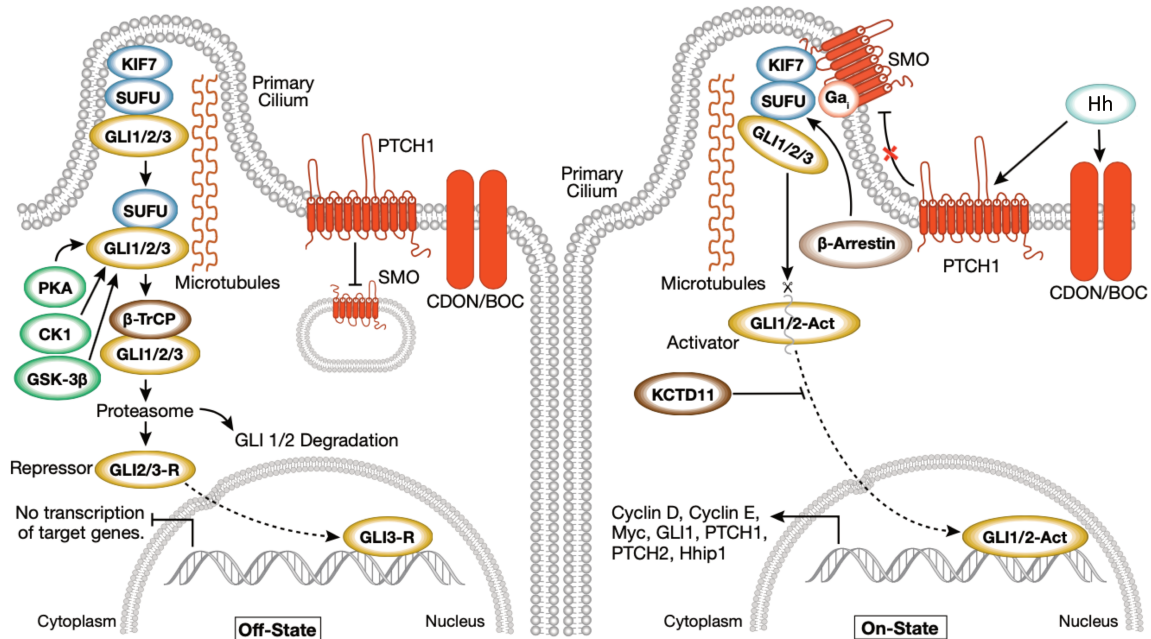


Figure 13: The mammalian Hh signaling pathway. Comparison between the off-state in the absence of Hh ligand, left, and the on-state, right. The ciliary axoneme is represented by orange waves enclosed by the ciliary membrane. The signaling cascade involves the ligand Hh, in light blue; the transmembrane receptor PTCH1, SMO and co-receptors CDON and BOC, in orange; the transcriptional factors GLI1/2/3, in yellow; the kinases PKA, CK1 and GSK-3β, in green; and the pathway regulator Kif7 and SUFU, in dark blue. From Cell Signaling Technology.

1.3. Polarity

1.3.1. The centrosome as a microtubule organizing center

The centrosome mediates a plethora of cell functions and is specifically involved in MT organization. This MTOC nucleates an aster of MTs that radiates towards the cell cortex. Some of these MTs are anchored via their minus end at the centrosome, either by the mother centriole SDAs or by other anchoring complexes, while other MTs are released into the cytoplasm. All centrosomal MTs are capped at their minus end by the γ -TuRC or other capping factors. MT anchoring at SDAs involves Ninein, a coiled-coil protein also found at the proximal end of both mother and daughter centrioles. MT minus ends are thus stably anchored to the extremities of SDAs. Increased expression of ninein can inhibit the release of MTs from the centrosome. The anchoring of MTs is essential for the maintenance of the radial network of MTs in interphase. However, nucleation and anchoring of MTs are mechanistically distinct processes. MTs can be rapidly released from their nucleation sites to serve other functions in the cell. Retention of MTs

at the centrosome is important for delivery of proteins to the centrosome and to the cilium. This process is mediated by cytoplasmic dynein, as many centrosome and cilium proteins are delivered to the centrosome via the CS (J. Wu & Akhmanova, 2017).

The MT network is involved in centering the centrosome. Indeed, the centrosome was named after the fact that it is usually located near the centroid of the cell, which is even more obvious in cells from which the nucleus has been removed - the nucleus otherwise occupies the centroid region, slightly displacing the centrosome (Piel et al., 2000). The nucleus is tightly bound to the centrosome in very diverse organisms, suggesting an ancient association (Azimzadeh, 2021). The connection between the nucleoskeleton and the cytoskeleton through the nuclear envelope links the centrosome to the nucleus and participates in the control of nuclear movement. Similarly, the Golgi apparatus and the centrosome are closely associated, with the Golgi often located adjacent to the centrosome. Control of centrosome position occurs in coordination with these other organelles, and thus centrosome movements cannot be considered isolated (Barker et al., 2016). Yet, multiple factors exert forces on the aster and mediate centrosome centering (Figure 14):

- pushing forces from MT polymerization;
- pulling and pushing forces from MT motors;
- pulling and pushing forces from MT interactions with actomyosin;
- pulling and pushing forces from actomyosin itself.

It has been shown that the central position of centrosomes is mainly due to the MT pulling forces developed by dynein located on the cell cortex and intracellular vesicles. Indeed, the role of dynein in centrosome centering has been repeatedly demonstrated, as inhibition of dynein activity induces a clear centrosome displacement from the center. The forces developed by actomyosin also play a role but are not yet fully understood. Otherwise, under certain circumstances, the centrosome can be relocated from its centered position.

For example, the centrosome is usually localized in the apical part of epithelial cells. Thus, centrosome positioning can be roughly classified in three types:

- when the centrosome is located close to the centroid of the cell, which is characteristic of non-motile and non-polarized cultured cells;
- when it moves to an edge of the cell during cell polarization, as it happens in epithelial differentiation or immune synapse formation;

- when it moves into the apical part of the cell, this phenomenon being often associated with the growth of a cilium (Burakov & Nadezhdina, 2020).

Indeed, ciliogenesis requires the relocation of centriole to the cell cortex and its docking to the cortical cytoskeleton. During this process, the centrosome remains intact as the mother and daughter centrioles migrate together and remain associated throughout ciliogenesis (Barker et al., 2016).

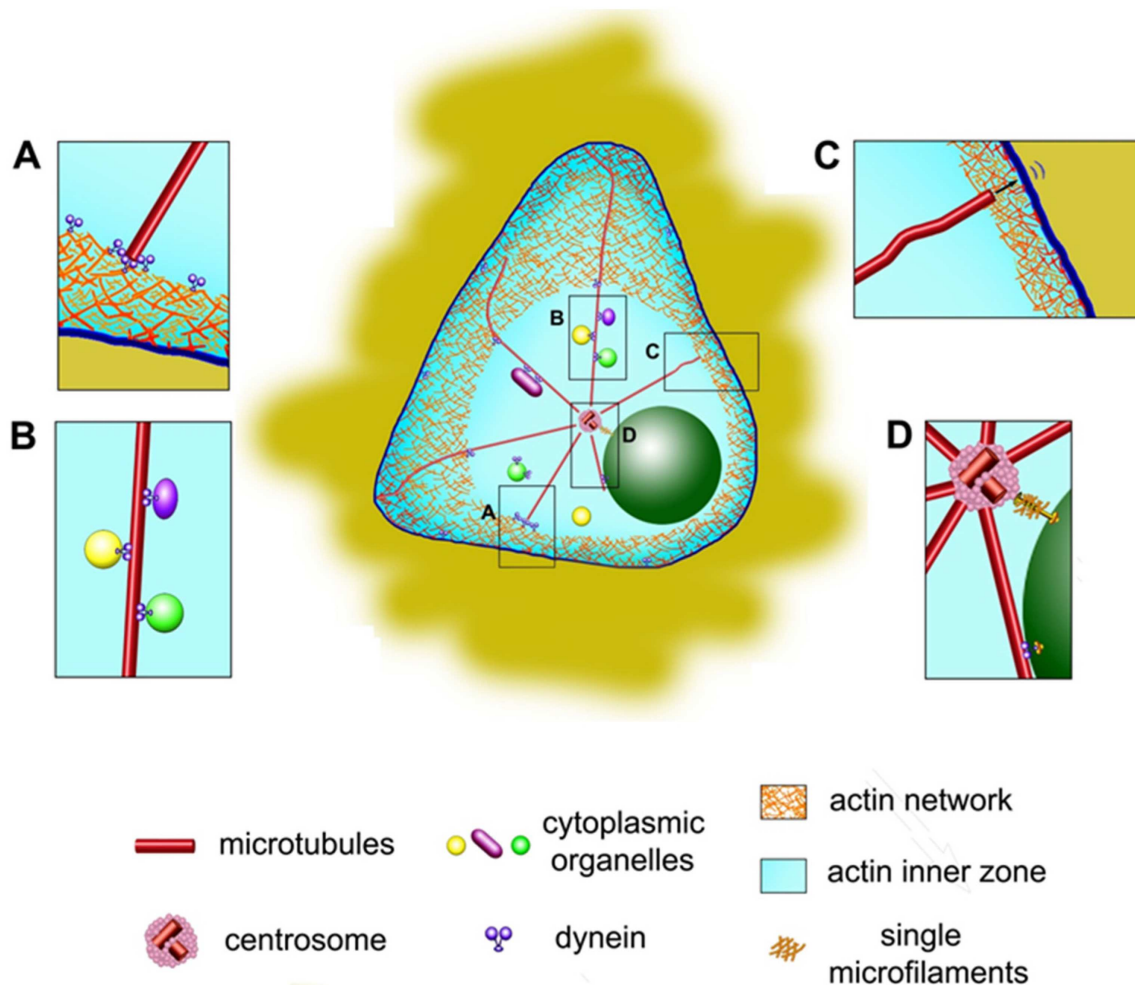


Figure 14: Mechanisms involved in centrosome centering, from (Burakov & Nadezhdina, 2020). (A) At the cell periphery, multiple dynein molecules pull microtubules (MTs). (B) Along the MTs, pulling forces are applied by dynein molecules anchored at the surface of cytoplasmic organelles. (C) Plus ends of growing MTs generate pushing forces. The forces applied to MTs by the actin cortical flow are not shown. (D) The centrosome and the nucleus are connected to each other. Middle panel: pulling forces are applied in the inner actin zone only; curved MTs outside of this zone do not contribute to centering.

1.3.2. Migration

Cell migration occurs in many processes, like development, immune response or wound healing. For this purpose, cells need to orchestrate their movements in a particular direction and towards a specific location. To this end, cells acquire a specific polarity that determines the direction of their movement. The anteroposterior axis of migrating cells is generally determined by the nucleus-centrosome axis. Indeed, on 2D substrates, the centrosome constantly shifts as the lamellipodium changes direction to follow the direction of migration. The polarity axis is thought to promote persistent directional migration by ensuring a continuous intracellular trafficking to the leading edge. Generally, the centrosome is localized between the nucleus and the leading edge, but the position of the centrosome during migration is dependent on the cell type and the cellular context.

For example, in 2D, fibroblasts position their centrosome in front of the nucleus, but in 1D (*i.e.*, in a microfluidic channel) and 3D, the centrosome is located at the back of the cell (Barker et al., 2016). In all cases, centrosome localization is actively controlled and centrosome positioning requires the integrity of the MT network (Figure 15). The association of dynein with MTs has been implicated in centrosome positioning in migrating cells. At the leading edge or at cell-cell contacts, dynein generates MT-mediated pulling forces on the centrosome, which are likely coupled to the simultaneous depolymerization of pulled MTs. The movement of the nucleus towards the back of the cell is linked to the retrograde flow of actin fibers accompanying cell migration. Once coupled to actin cables, the nucleus moves with the actin flow to the back of the cell, behind the centrosome. Actomyosin contractions are also required for centrosome positioning. The impact of the nucleus on centrosome position depends on the nucleus-centrosome link. Despite cell type specificities, molecular pathways acting on MT motors and on actomyosin contractility lead to a balance between forces exerted on the centrosome and the nucleus. Thus, these pathways define and maintain a nucleus-centrosome axis parallel to the front-to-rear polarity axis of migrating cells. In this context, small G proteins of the Rho family have an essential role. Indeed, they coordinate the regulation of dynein and myosin that generate the forces required for the orientation of the centrosome-nucleus axis in migrating cells (Elric & Etienne-Manneville, 2014).

Cell migration can be experimentally mimicked in 2D with immotile cells. This involves the use of single cell micropatterns coated with fibronectin. In a crossbow-shaped oriented pattern, cells adopt a stereotypical polarity that mimicks migrating cells. They arbore a pseudo-lamellipodium at the front, and polarize their internal constituents, with the centrosome in front of the nucleus and the Golgi in between. These micropatterns can be used to verify cell polarization, using the nucleus-centrosome axis as a marker.

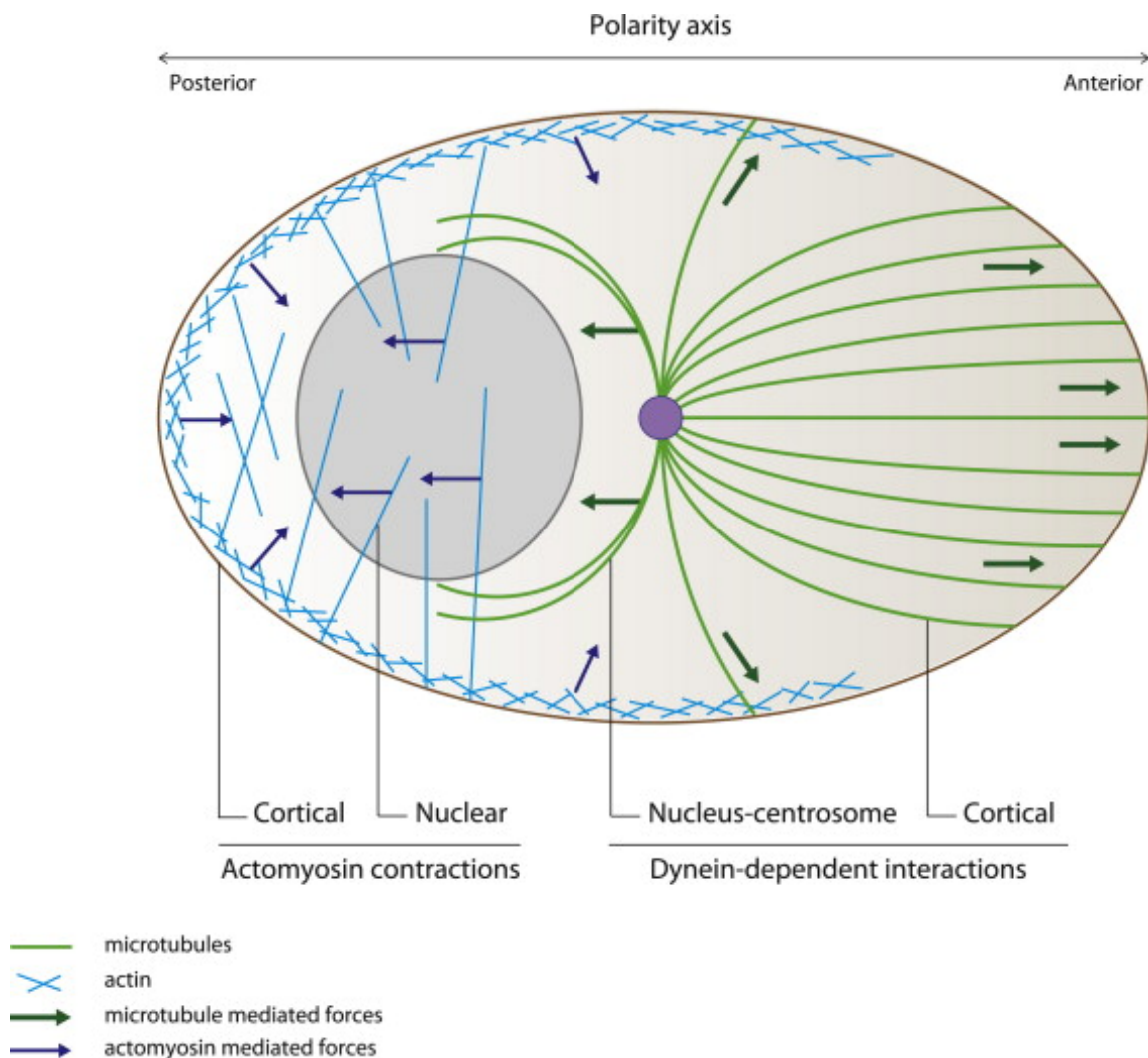


Figure 15: The orientation of the nucleus-centrosome axis results from a balance of actin- and MT-mediated forces, from (Elric & Etienne-Manneville, 2014). The centrosome, in purple, is connected to the MT network, in green, which exerts dynein-mediated pulling forces from the cell cortex and the nucleus. The actomyosin network, in blue, generates pushing forces from the cell cortex and onto the nucleus, contributing to the orientation of the nucleus-centrosome axis.

1.3.3. Polarity in multiciliated cells

Multiciliated cells are a specialized population of post-mitotic cells that generates directional fluid flows. Their motile cilia beat in a polarized and synchronized way, which is important for the physiological functions of these cells. Ciliary beating is driven by the action of axonemal outer and inner dynein arms, causing adjacent MT doublets to slide over each other. Combined with the basal anchoring of the axoneme, this results in the bending of the cilium. In multiciliated cells, the ciliary beat cycle has a stereotypical planar waveform and consists of a fast and effective stroke and a slower recovery stroke. The former propels fluid by extending the cilium through an arc; the latter brings the cilium back to its initial position. The central pair of MTs, nexin-dynein regulatory complex and the radial spoke are primordial for correct ciliary beating. During their differentiation, multiciliated cells produce simultaneously from 30 to 300 BBs, and as many cilia beating in the same direction. Centriole amplification is organized in three consecutive phases. The first one is the amplification phase during which procentrioles form. Two pathways have been shown to contribute to this massive BB amplification:

- The centriolar pathway, comparable to centriole duplication, but with two to six procentrioles forming orthogonally to the centrosomal centrioles instead of one. This pathway forms about 10% of the centrioles of the final multiciliated cell. This pathway has been shown to be initiated by CEP63.
- The deuterosome pathway, by which multiple procentrioles form around spherical structures called deuterosomes. This pathway is initiated by DEUP1 and is responsible for the formation of around 90% of centrioles.

Both pathways are active simultaneously and involve the same downstream molecular cascade as centrosome duplication during the cell cycle. Deuterosomes are formed by an electron dense core composed of centrosome elements. Deuterosomes sequentially form coming from the proximal wall of the youngest centriole within the centrosome, or daughter centriole. The second phase is the centriole growth step. It occurs when the final number of centrioles has been reached and the deuterosomes stops forming. Then, all procentrioles grow and mature concomitantly, both from the centrosome and deuterosome platforms. At the molecular level, procentrioles become positive for POC5, a marker of later stages of centriole assembly. The third phase is disengagement, during which all centrioles detach at the same time, migrate to the apical membrane and nucleate motile cilia. It is not known by which process deuterosomes ultimately disappear.

Once docked to the apical plasma membrane, the BBs acquire a rotational polarity that determines the direction of planar cilia beating (Spassky & Meunier, 2017). For *Schmidtea mediterranea*, epidermal multiciliated cells are required for locomotion. These flatworms lack centrosomes and thus amplify centrioles *de novo*. The DEUP1 gene and a key upstream regulator of centriole amplification in vertebrate multiciliated cells called Multicilin, are lacking in the planarian genome. This suggests that centrioles are amplified through a *de novo* pathway that is distinct from the transcriptional cascade described in vertebrates. Nevertheless, downstream centriole duplication factors are conserved and essential for BB assembly in planarians (Azimzadeh et al., 2012).

BBs are closely associated with both actin and MT networks. Experiments perturbing cytoskeletal arrays showed that BB migration and docking depends on actin filament assembly, but not MT polymerization. Multiciliated cell differentiation next involves the polarization of cilia in the plane of the apical membrane, or rotational polarization, which is primordial for generating directional fluid flows. During the final stages of multiciliated cell differentiation, cilia are progressively reoriented until all of them beat in a mostly unidirectional fashion. Cytoskeleton disruption experiments established that both actin and MT networks are required for establishing centriole rotational polarity, which determines ciliary beat direction, but also established that these networks play distinct roles in this process (Brooks & Wallingford, 2014).

The rotational polarity of the BBs is revealed by the orientation of their appendages, the basal foot and the ciliary rootlet. The basal foot is aligned with the axis of the ciliary beat, in the direction of the effective stroke. A ciliary rootlet usually points in the opposite direction. Both the basal foot and the ciliary rootlet anchor cytoskeletal networks, which connect the BBs to each other and to apical cell junctions, providing stability to the BB network. Polarity proteins localize at the BBs and cellular junctions to connect BB rotational polarity to the planar polarity of the epithelium. As well, in multiciliated cells, apical actin assembly and BB docking are orchestrated by the PCP pathway. Originally identified in the *Drosophila* wing, this pathway is a conserved signaling pathway that governs a range of developmental processes. In vertebrates, it regulates both intracellular and tissue-level planar polarities. Its establishment at the tissue-level involves the asymmetric partitioning of its components at the cell cortex. It also requires intercellular communication to coordinate polarity between neighboring cells (Meunier & Azimzadeh, 2016).

1.3.4. Establishing and maintaining asymmetry in cells, tissue and organisms

Vertebrate animals are asymmetric along three axes: anterior-posterior, dorsal-ventral, and left-right. These polarities appear within the developing embryo through a combination of different processes:

- asymmetric cell division, in which two daughter cells receive different amounts of cellular material, like proteins;
- asymmetric localization of specific proteins within cells, often mediated by the cytoskeleton;
- concentration gradients of secreted proteins such as Wnt or Nodal across the embryo;
- differential expression of membrane receptors and ligands that cause lateral inhibition, in which the receptor-expressing cell adopts one fate and its neighbors another.

All of these processes rely on cell polarity, which is tightly coupled to the cytoskeletal machinery. Cytoskeleton-mediated feedback interactions within the cell and these processes can guide cell fate specification during development (Yamashita et al., 2010).

The establishment of body polarity is the design that will form biological systems. Polarity can be found at all scales, from end-to-end polarity of cytoskeletal fibers, to the distribution of polarization proteins within cells, or across tissues or whole organisms. Coordination of polarity vectors across scales has been shown in the *Drosophila* wing or the *Xenopus* larval multiciliated epidermis, but the mechanisms that coordinate polarity at the tissue or organismal scale are not completely understood. The polarity proteins involved in these processes are localized at the cell junctions and centrioles. These proteins regulate cytoskeleton architecture to coordinate centriole rotational polarity with the planar polarity of the epithelium. A first conserved pathway controlling cell planar polarization in animals is the Wnt/planar cell polarity (Wnt/PCP) pathway. In *S. mediterranea*, the Wnt/PCP pathway controls the alignment of BBs along the anteroposterior axis. A second conserved pathway, the Fat/Dachsous (Ft/Ds) pathway, aligns the BBs towards the edges of the animal. The combined effect of these two pathways generates a symmetrical organization pattern of BBs on either side of the midline (Vu et al., 2019)

In addition to defining body axes, cell polarity also regulates many different morphogenetic processes including asymmetric stem cell division. This process results in the production of one

stem cell and one differentiating cell. For self-renewal of the dividing stem cell, one daughter cell must retain stem cell characteristics. Before the division, mother centrioles accumulate comparable levels of PCM components. This step is primordial for the symmetric organization of the mitotic spindle and thus the proper segregation of genetic material. Nevertheless, functional asymmetries between the two centrosomes exist and are exploited in the asymmetric division of some types of stem cells. These asymmetries result from the age difference between the parental centrioles, which give the two centrosomes different properties, for example in terms of MT nucleation. Such stem cell divisions in which centrosome age plays a role are found during embryonic development, tissue regeneration, morphogenesis as are also important to maintain homeostasis. These asymmetric divisions depend on cell polarity and tissue architecture. For example, many stem cells are polarized in their microenvironment, in order to keep the daughter stem cell close to the niche from which the stemness signals are emitted (Yamashita et al., 2010).

1.4. Ciliopathies and microtubules related diseases

1.4.1. Introduction

Ciliopathies are a group of severe, often fatal genetic diseases associated with mutations leading to cilia dysgenesis or dysfunction. As cilia can be found in almost all human cells, both motile or non-motile, their malfunction leads to a wide range of diverse ciliopathies usually associated with multiple symptoms. Common features associated with ciliopathies include renal disease, cerebral anomalies, liver fibrosis, retinal degeneration, and skeletal anomalies. Ciliopathies are termed motile, sensory, or both, depending on the type of cilia affected by the mutation (figure 16). The most common motile ciliopathy is the primary ciliary dyskinesia (PCD). PCD is a clinically heterogeneous group of disorders that may include respiratory problems, subfertility, hydrocephalus, situs defects and hearing problems. Non-motile, or sensory, ciliopathies can be roughly classified in subgroups:

- neurodevelopmental ciliopathies, like Joubert syndrome (JBTS) and Meckel-Gruber syndrome (MKS);
- kidney ciliopathies, like nephronophthisis (NPHP) and polycystic kidney disease (PKD);
- skeletal ciliopathies, like orofaciodigital syndrome (OFD);
- obesity ciliopathies, like Bardet-Biedl syndrome (BBS).

Currently, 35 different ciliopathies have been reported, a number that is likely to increase. These diseases form a group because of their genetic and phenotypic overlap. Indeed, different mutations in the same gene can give rise to distinct ciliopathies, the phenotypes associated with one specific ciliopathy are often shared with others, and there is a heterogeneity of phenotypes within the same syndrome. This complexity leads to delays in diagnosis and patient care, and there is currently no cure for these diseases, although new therapeutic approaches based on a better understanding of the primary cilium are under investigation. The current number of ciliopathy-associated genes is about 187, and candidate genes are 241 (Reiter & Leroux, 2017). The vast majority of these conditions are inherited in an autosomal recessive manner. Still, the single most common ciliopathy is the autosomal dominant PKD, mainly caused by mutations in PKD1. It is the most common cause of end-stage renal failure and one of the most common genetic diseases in humans. The individual incidence of the other ciliopathies is low, but taken together they represent relatively frequent genetic diseases and the number of diseases identified as ciliopathies or suspected to be ciliopathies is continually rising.

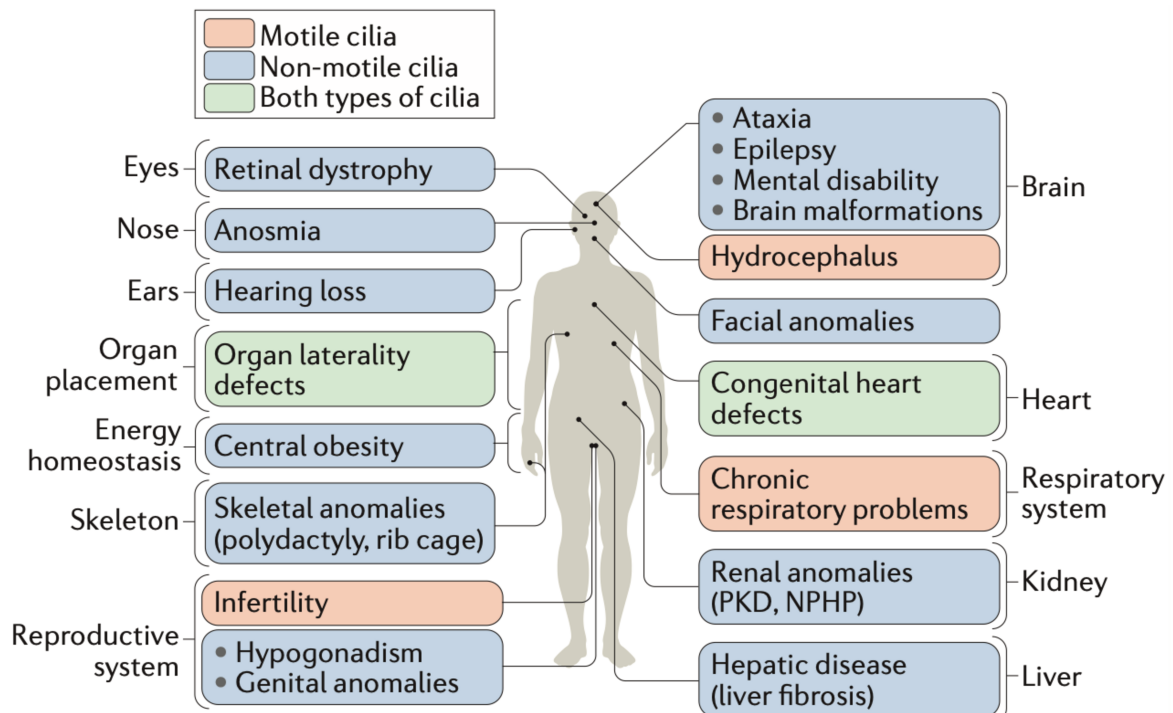


Figure 16: Organ or systems affected in diverse ciliopathies and their main phenotypic manifestations. Dysfunctions of motile and/or non-motile cilia cause ciliopathies that affect most human organs and functions. Ciliopathies caused by defects in motile cilia are shown in orange, those that result from defects in primary cilia are shown in blue, and those associated with defects in both types of cilia are shown in green. From (Reiter & Leroux, 2017).

1.4.2. Joubert syndrome

The JBTS is a rare recessive genetic disorder that affects most visibly the cerebellum, an area of the brain that controls balance and coordination. The incidence is about 1/100 000 but it is probably underestimated. JBTS is characterized by three primary findings: a distinctive cerebellar and brain stem malformation on brain MRI called the molar tooth sign (MTS) (figure 17), hypotonia and developmental delays. Clinical diagnosis is based on the presence of these 3 features, which makes it easier compared with other ciliopathies, as an MRI is sufficient to identify the syndrome. MTS allows for diagnostic uniformity of cohorts, which is an essential parameter for the discovery of the responsible genes. The MTS is frequently accompanied by apnea and/or atypical eye movements. Cognitive abilities are variable, ranging from normal to severe intellectual disability. In addition to this central nervous system malformation, other clinical signs characteristic of ciliopathies can be present in a variable manner: retinal degeneration, renal disease, hepatic fibrosis and polydactyly. Variations can be observed both intra- and interfamilial. To date, pathogenic variants in 34 genes are known to cause JBTS, including CEP164, CEP290, MKS1, NPHP1, RPGRIP1L, C2CD3, Talpid3 and OFD1. JBTS is perfectly representative of the ciliopathy group, due to the phenotypic and genetic overlap with other ciliopathies. Mutations in a number of genes can cause either JBTS or MKS, depending on the precise mutation, suggesting that JBTS and MKS are caused by genes that affect the same essential ciliary functions (Parisi & Glass, 1993).

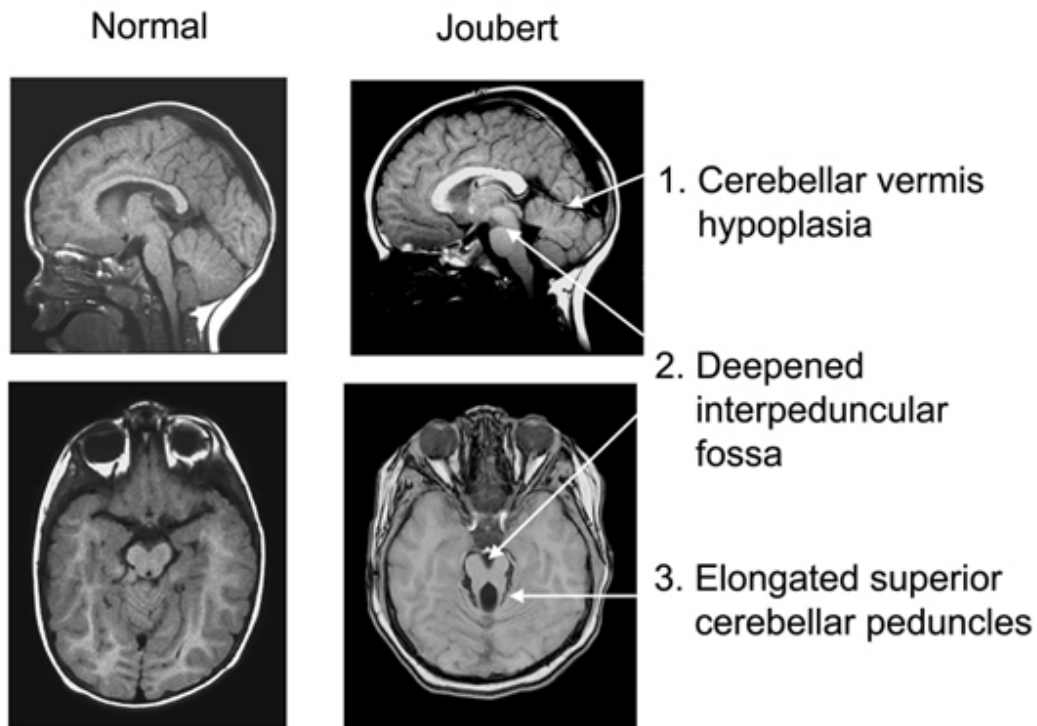


Figure 17: The molar tooth sign (MTS) in Joubert syndrome (JBTS). Comparison of MRI images between a normal individual showing intact cerebellar vermis and brain stem, and a child with JBTS. Arrows indicate the three key components of the MTS. (*Joubert Syndrome - UW Hindbrain Malformation Research Program*, s. d.).

MKS represents the most severe condition among ciliopathies as it is lethal *in utero* or immediately after birth. MKS is characterized by central nervous system defects, most frequently occipital encephalocele, with cystic kidneys, hepatic fibrosis, and polydactyly (C.-P. Chen, 2007).

Many genes that are mutated in MKS and JBTS encode proteins that localize to the ciliary TZ. Specific JBTS-associated mutations in TZ components have been shown to disrupt SMO accumulation in the TZ and ciliary localization, supporting that disruption of TZ architecture in JBTS leads to disruption of developmental signaling (Shi et al., 2017). NPHP is also caused by defects in TZ components and genetically overlaps with MKS and JBTS, but it is less severe than MKS and JBTS. It is likely that the severity of the TZ impairment is related to the severity of the associated syndrome. Indeed, the syndromic diagnosis of ciliopathies is not straightforward. Classifying them by syndrome masks the overlap between mutated genes and pathological

mechanisms among the different ciliopathies. A descriptive diagnosis based on multi-organ involvement and genome sequencing is needed to better describe the complex phenotypes related to ciliopathy mutations (Mitchison & Valente, 2017). The overlap between JBTS and MKS produces a continuous spectrum of phenotypes between these two pathologies.

Some of the proteins mutated in JBTS or other sensory ciliopathies are not TZ components but are found in distal part of the centriole, involved in centriole biogenesis and maturation. These include C2CD3, OFD1, Talpid3, CEP164, CEP83 and CEP120. (Thauvin-Robinet et al., 2014) CEP120 (Reiter & Leroux, 2017) (Sakakibara et al., 2019) (Shamseldin et al., 2020) (Fraser & Davey, 2019) (Failler et al., 2014)

1.4.3. Microcephaly

Microcephaly is a disorder in which the brain fails to achieve a normal size. It is defined by an occipitofrontal head circumference that is below the mean by at least 2 standard deviations. Brain size is influenced by several developmental processes and controlled by both genetic and environmental factors. The causes of microcephaly are highly heterogeneous and also include environmental and genetic factors. The mechanisms involved in genetic microcephaly can affect all the important processes of brain development, such as progenitor cell proliferation, cell differentiation, and cell death. Syndromic microcephaly is when microcephaly is associated with malformations in the rest of the body.

Microcephaly can be primary when it is detectable at birth, as a static developmental anomaly, or progressive, when the size of the brain is normal at birth but will be reduced postnatally, as a progressive neurodegenerative condition. Therefore, progressive (also called secondary, or postnatal onset) microcephaly refers to a diffuse brain atrophy that occurs postnatally, within the first years of life. Patients with progressive microcephaly frequently show progressive motor degeneration, cognitive deterioration, and seizures, but their symptoms may also appear to be stable over time. Ongoing neurodegeneration does not imply a failure of neurogenesis but an increased neuronal death. It can be associated in rare case with metabolic disorders such as serine deficiency or thiamine pyrophosphate transporter deficiency. Other causes of genetic progressive microcephaly are often syndrome-related and have been linked to defects in gene transcription, DNA repair, or insufficient formation of myelin (Nakayama et al., 2015). The

causes of genetic progressive microcephaly remain mostly unsolved, and cases of primary microcephaly are described in a more mechanistic manner. In some cases, primary microcephaly can resemble progressive microcephaly, as the brain size can still be small or normal at birth and only fall within the range of microcephaly during the first year of life (Passemar et al., 2013).

Genetic primary microcephaly is a severe disorder caused by reduced proliferation of neuronal and glia progenitors during embryonic development. Defects in mitotic spindles, centrosomes, and DNA repair are commonly associated with this disorder. Most of the genes mutated in primary microcephaly code for centrosomal proteins, some of which have a role in centriole duplication such as PLK4 or STIL. There is evidence that defects in centriole biogenesis may be an underlying cause of neurogenesis defects. To self-renew during brain development, neural progenitors undergo symmetric proliferative divisions. Because centrosomes are important for mitotic spindle orientation, defects in the centrosome number or structure can impair symmetric divisions, leading to premature depletion of neural progenitors. While there is evidence to support this hypothesis, defects in mitotic spindle orientation were not observed in the microcephalic brains of some mouse models, and randomizing spindle orientation in mouse neuroepithelial progenitors showed no influence on the rate of neuron production. Another scenario is that cells with abnormal centriole numbers or centriolar defects exhibit delayed spindle assembly, and therefore increased mitosis duration. In support of this idea, in the developing mouse brain, extending mitosis was shown to promote both differentiation and death of neural progenitors. The current data support the model that centrosomal defects lead to mitotic delays in the developing brain, inducing activation of the mitotic surveillance pathway (Nigg & Holland, 2018).

Primary microcephaly has been linked to only one confirmed ciliopathy gene, which encodes the CENPF protein (Reiter & Leroux, 2017). In addition, a candidate gene for ciliopathies, a mutation of which appears to cause JBTS, has also been linked to progressive microcephaly (Shaheen et al., 2016). This is the *LRCC1* gene coding for a poorly characterized centrosome component called hVFL1/LRCC1.

1.5. hVFL1 and hVFL3

1.5.1. In *Chlamydomonas*

The *vfl* (variable flagella number) mutants, which exhibit defects in the number and location of flagella, were identified in the early 1980s in *C. reinhardtii*. Detailed characterization of the ultrastructure of the *vfl1* mutant revealed that dcf are absent or defective, and SMAFs (Striated microtubules-associated fibers) are present in reduced numbers (Figure 5, page 16). In the wild type, these structures are necessary to connect BBs to each other and control their rotational polarity, which is crucial for efficient swimming in this organism. In the *vfl1* mutant, defective assembly of the dcf and other fibrous structures connecting the BBs leads to a defect in BB segregation during mitosis, and thus an abnormal number of BBs and flagella. The BBs are also aberrantly positioned and oriented (Adams et al., 1985). The Vfl1 protein (Vfl1p) was subsequently identified in 2001. The Vfl1p protein was found to exhibit a rotationally asymmetric localization pattern at the distal ends of BBs (Figure 18). By analyzing serial immuno-EM sections, the authors were able to show that Vfl1p localizes within the BB lumen, near the three triplets (2, 1, and 9) that face the dcf (Figure 5, page 16). The model they proposed is that Vfl1p controls the rotational asymmetry of the BBs, allowing for the correct establishment of BBs connectors and thus proper BB orientation in the plane of the membrane (Silflow et al., 2001).

A second *vfl* mutant was also analyzed by the authors of the *vfl1* first study. The *vfl3* mutant exhibits a phenotype closely resembling that of *vfl1*, with a variable number of improperly positioned flagella. The *vfl3* mutant lacks normal dcf and SMAFs. In the same manner, an analysis of structural polarity markers in the proximal portion of flagella shows that the rotational orientation of these flagella is abnormal, consistent with their aberrant beating direction (Wright et al., 1983) (Hoops et al., 1984). The sequence of the gene mutated in the *vfl3* mutants has been available in genome databases for a long time, but it is only recently that the Vfl3p protein was confirmed to be a BB component in *C. reinhardtii* (Ochi et al., 2020). Orthologs of Vfl3p had however been characterized earlier in another unicellular eukaryote, *Paramecium tetraurelia*. In these species, VFL3 proteins play a crucial role in BB docking and orientation, suggesting that the VFL3 function is conserved between *C. reinhardtii* and *P. tetraurelia*. In *P. tetraurelia*, BBs are associated with one striated rootlet and two microtubular ribbons, which are required for

defining the site of new BB assembly and for organizing the BB rows characteristic of ciliates. VFL3-1, a member of one of the two VFL3 subfamilies present in *P. tetraurelia*, was shown to localize transiently at the interface between the BBs and their associated striated rootlet at an early step of their duplication. Depletion of VFL3 can result in multiple striated rootlets associated with individual BBs. This suggests that VFL3 may be required for the acquisition of triplet specification for the establishment of rotational asymmetry. (Bengueddach et al., 2017).

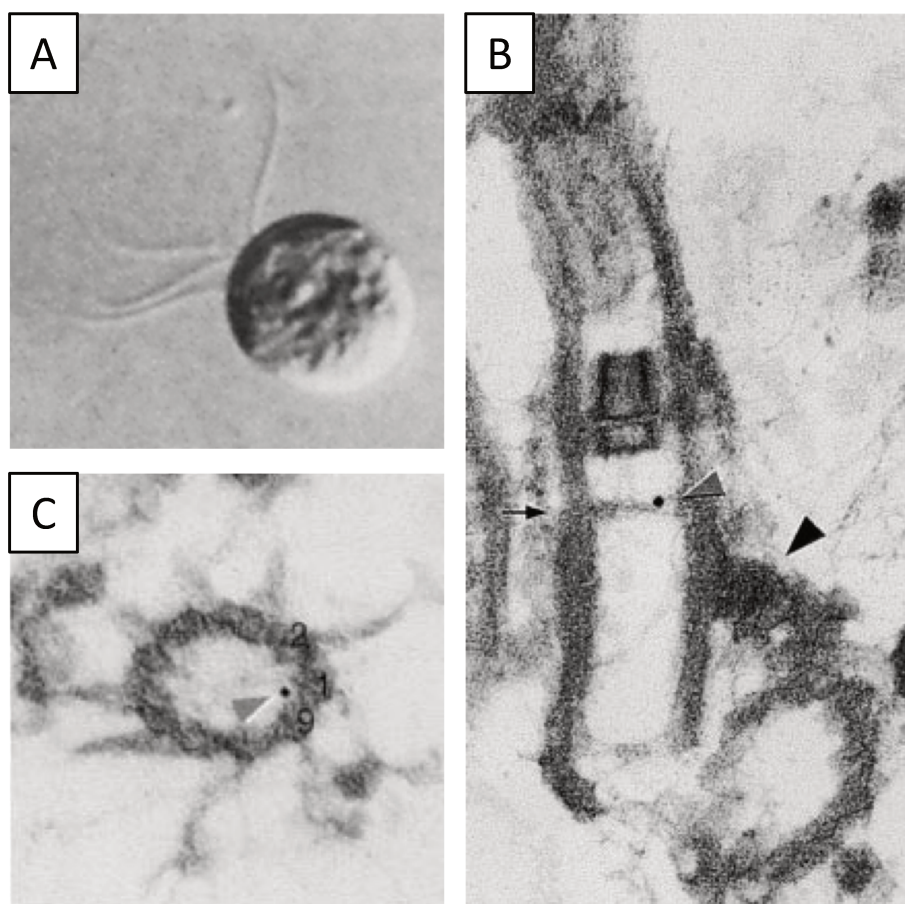


Figure 18: Characterization of Vfl1p in *C. reinhardtii*. (A) Micrograph showing a *vfl1* mutant cell with 4 flagella, the number of flagella in this mutant ranging from 0 to 5, from (Adams et al., 1985). (B, C) Vfl1p localization by pre-embedding immunogold labeling, from (Silflow et al., 2001) (B) Longitudinal section of a basal body (BB), the arrow indicate the region of the BB where the C tubules end and the doublet MTs of the axoneme begin. The black arrowhead indicates the distal connecting fiber (dcf). Gold particles are indicated by a grey arrowhead. (C) Transverse section of a BB, viewed from the distal end. Triplets number 9, 1, and 2 are identified based on their association with the distal dcf. A gold particle is indicated by the grey arrowhead. Note the transition fibers in the same plane as the gold particle.

1.5.2. In human

1.5.2.1. hVFL1/LRRCC1

The human ortholog of Vfl1p was originally found in a proteomic analysis of human centrosome components (Andersen et al., 2003) and was later confirmed to be a centrosome component (Muto et al., 2008). hVFL1 has been also termed CLERC (Centrosomal LEucine-Rich repeat and Coiled-coil containing protein), KIAA1764, SAP2 (Sodium channel Associated Protein 2), and LRRCC1 (Leucine Rich Repeat and Coiled-Coil containing 1). In the article relating to my main work, hVFL1 is termed LRRCC1, the name approved by the HUGO (HUMAN Genome Organization) gene nomenclature committee (Page 67). The gene *LRRCC1* maps to 8q21.2. Database analyses suggest the existence of potential isoforms. The longest isoform, which is also the most closely related to *C. reinhardtii* Vfl1p, consists of 19 exons encoding a predicted open reading frame of 1032 amino acids (GenBank Accession number NP_208325) with a predicted molecular mass of 119,589 Da. *C. reinhardtii* Vfl1p and human VFL1 sequences are 22% identical, and both proteins share five leucine-rich repeat (LRR) sequences near the N-terminus and an α -helical coiled-coil domain distributed over its C-terminal two-thirds (Figure 19). Four shorter isoforms lacking part or the entire LRR domain are also predicted to be expressed. The protein is evolutionarily conserved amongst ciliated eukaryotes, the LRR domain in particular being highly conserved, and the VFL1 protein family has an ancient origin. In their 2008 study, Muto et al. found that the inactivation of hVFL1 by RNAi leads to the formation of multipolar mitotic spindles. They proposed a model postulating that hVFL1-depletion provokes premature centriole disengagement during interphase, leading to the formation of additional spindle poles (Muto et al., 2008).

Later, in 2016, Shaheen *et al.* identified a putative loss-of-function mutation in *LRRCC1* in two siblings with JBTS (Shaheen et al., 2016). Both siblings exhibit typical JBTS features on MRI associated with hepatomegaly, hypotonia, echogenic kidneys, retinal dystrophy on ERG and a global developmental delay, all of which are symptoms commonly found in JBTS patients. In addition, these patients exhibit progressive microcephaly, a clinical feature that is not usually part of the ciliopathy spectrum. The microcephaly of the youngest sibling is described as progressive, but it is not specified whether the microcephaly of the older sibling is primary or progressive. The mutation (NM_033402.4:c.105-1G>C: p.(Ser35Argfs*17)) is homozygous for the two

siblings and affects the splice acceptor site of exon 2. This mutation is the only segregating variant in the exome, and it is proposed by the authors to be a loss of function mutation. However, it is not clear how many isoforms of the protein exists in humans. Gene banks lists 5 possible isoforms and the *Chlamydomonas* orthologue of LRRCC1 is most closely related to isoform 1. Isoform 2 has a shorter and distinct N-terminus compared to isoform 1 that would not be affected by the mutation. It is thus possible that the two siblings affected by this mutation still express at least one isoform of the protein.

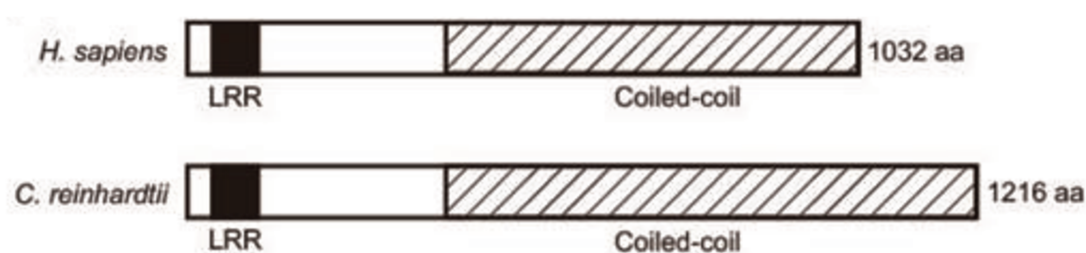


Figure 19: Schematic representation of the human CLERC protein and the *C. reinhardtii* Vfl1 protein. The LRR region (black bar) is located near the N terminus, and the coiled-coil region (hatched bar) is at the C terminus. From (Muto et al., 2008).

1.5.2.2. hVFL3/CCD61

hVFL3, also a highly conserved protein in ciliated eukaryotes (Bengueddach et al., 2017), is encoded in humans by the *CCDC61* gene (Coiled-Coil Domain-Containing protein 61; NM_001096129). The longest isoform consists of 512 amino acids and has a molar mass of 57 kDa. Apart from two short coiled-coil domains located in the central region, hVFL3 contains no conserved motifs. At the time the study included in this manuscript was initiated, no data were available on the function of hVFL3. Since then, two studies, in addition to ours, have been published, which will be discussed in more detail at the end of this manuscript (Bärenz et al., 2018) (Ochi et al., 2020).

1.6. A resolution revolution

1.6.1. The resolution limit

Over the centuries, successive technological advances in microscopy have allowed scientists to better understand the biological processes they were studying, from the invention of the microscope to recent technological advances in EM pushing resolution limits. The resolution

power of an optical system is its capacity to distinguish details. It is defined by the minimum resolvable distance which is the smallest distance from which two points can be distinguished. This distance is called d and depends on the wavelength λ of the light used in the optical system, the refractive index of the medium n , and the half-angle converging to the spot θ .

$$d = \frac{\lambda}{2n \sin \theta}$$

The value of $2n \sin\theta$ depends on the physical characteristics of the microscope optics (numerical aperture of the objective and condenser) and is limited to about 2,8 for modern optics. The wavelength λ depends on the fluorochrome used in fluorescent microscopy. In confocal microscopy, this allows a lateral resolution of about 180 nm and a Z resolution of about 600 nm. The size of a centriole being about 250 nm in diameter and 450 nm in length, the details of centriole ultrastructure cannot be distinguished with conventional confocal microscopy. Optical systems with a greater resolution power must be used for this purpose.

1.6.2. Electron microscopy

One way to decrease d is to work with particles with wavelengths shorter than the photons, which is the case of electrons. EM allows to reach a resolution lower than 1 ångström (0.1 nm), but the average resolution obtained by this approach is of the order of a few ångströms. The resolution is indeed limited by the imperfections of the magnetic lens used to focus the electron beam. If the magnetic lens had no aberrations, the technical resolution could be measured in picometers. Among the different types of EM, the one commonly used for centrioles is TEM. In TEM, electrons are accelerated by an electron gun, focused on an ultra-thin sample by magnetic lenses and an electron detector is used to obtain an image of the sample previously fixed and contrasted. The images obtained highlight dense electronic structures, and specific proteins can be localized using gold or silver beads coupled to antibodies (Figure 18: localization of hVFL1 in *C. reinhardtii*). Thanks to its resolution power, TEM can resolve the ultrastructure of the centriole and allow the observation of its chirality (Figure 20). Although centriole structure analysis has traditionally been performed by TEM, this technique is laborious, requires specific training and equipment not always available, and is often not suitable for collecting a quantity of data compatible with robust statistical analyses.

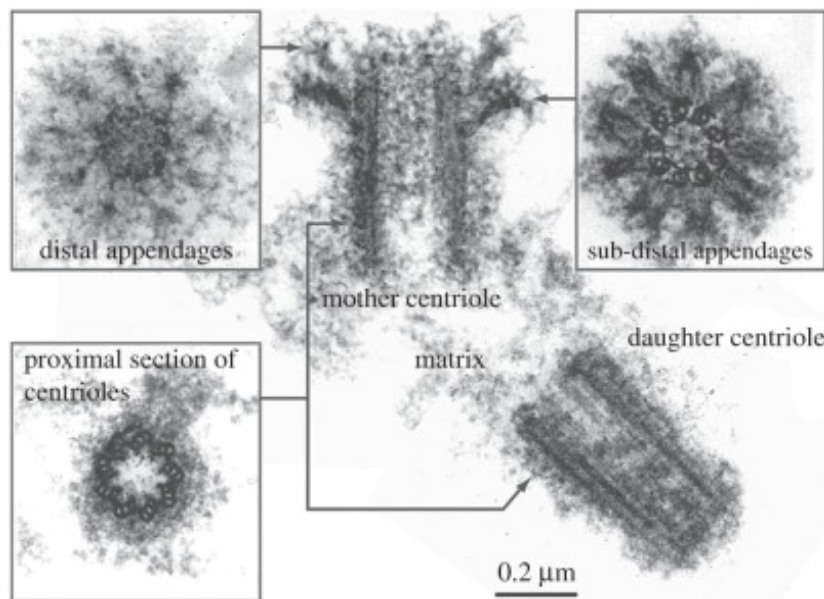


Figure 20: Transmission electron micrographs of centrioles in isolated centrosomes shown in longitudinal section. The boxed images show cross sections corresponding to the regions indicated by arrows and highlighting in particular the distal appendages and subdistal appendages of the parent centriole. From (Winey & O'Toole, 2014).

1.6.3. Super resolution microscopy

In parallel to EM, super-resolution optical microscopy, which allows the localization of proteins of interest with a greater accuracy than confocal microscopy, has experienced a very important development in recent years. The principle of super-resolution microscopy is to acquire not a single image, but several, and then to reconstruct an image from the information obtained from multiple images. There are different approaches to acquire these images. Photoactivated localization microscopy (PALM) and stochastic optical reconstruction microscopy (STORM) allow to separate in time, points that are spaced at a distance lower than the resolvable distance. To do so, these techniques use the property of fluorochromes to blink in the presence of excitation light, so that only one fluorophore will emit at a given time within a perimeter greater than the resolution distance. Each fluorophore can then be located separately, allowing it to be located with greater accuracy. By performing several acquisitions of the same region separated in time, it is possible to determine the precise location of all the fluorophores and to then generate a single reconstructed image. The STORM approach has been used, for example, to determine the organization of the rings of MKS and NPHP complexes along the TZ. The reconstructed images

need to be averaged most of the time, because a single reconstructed image is not totally faithful to the observed structure, some regions being incomplete (figure 21). The main advantage of STORM is its high lateral and axial resolution: 20 nm and 50 nm respectively. However, this approach requires a specific photo-switchable fluorochrome, is not suitable for thick samples and is not easily accessible to non-experts.

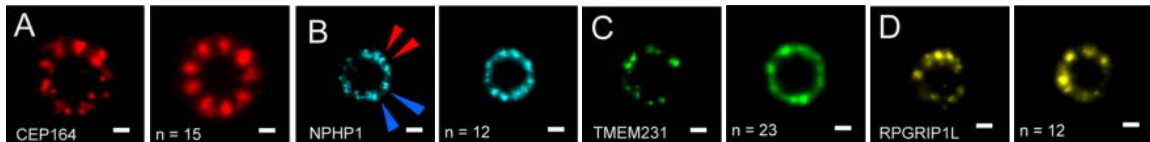


Figure 21: STORM images of mother centriole distal appendages (DAs) and ciliary transition zone (TZ) in medullary thymic epithelial cells. CEP164 is used as a DA marker, and NPHP1, TMEM231 and RPKGRI1L as markers of TZ complexes. For each marker, an individual reconstructed image (left) or an average view of multiple images aligned by cross correlation (right) are shown. NPHP and MKS complexes form nine-fold symmetric doublets, whereas DAs appear as nine-fold symmetric singlets. From (Shi et al., 2017).

Structured illumination microscopy (SIM) is a super-resolution technique that improves resolution by collecting information in frequency space outside the observable region. It is based on the excitation of the sample with a spatially structured light pattern and depends on the generation of interference patterns called the Moiré effect. The interference signals of the different images acquired are mathematically deconvolved and a super-resolution image is obtained. SIM allows to obtain a resolution twice as high as confocal microscopy (~ 120 nm).

This technique requires a specific microscope and non-bleaching antibodies, as the acquisition takes time. Also, it is prone to creating artefacts, as image reconstruction highly depends on the selected parameters.

Alternatively, Airyscan is a super-resolution technique developed by Zeiss that uses a specific detector. Confocal microscopes only detect the light passing by a pinhole that has the diameter of one Airy Unit (1 AU). Light coming from planes above or below the focal plane is thus out of focus when it reaches the pinhole. Consequently, most of the light generated by the fluorophores does not contribute to the image formation. In contrast, Zeiss Airyscan detectors use the light outside the 1 AU area to allow reconstruction of an image using not just 1 pinhole, but 32 pinhole-sized detectors. This technique improves the resolution by 1,7-fold and has the advantage

of being sensitive, resolutive and allowing a fast acquisition, as the 32 detectors work simultaneously.

Airyscan and SIM achieve better resolution than confocal microscopy and are easier to use than PALM and STORM. Yohei and collaborators compared these 2 techniques combined or not with expansion microscopy (see next section) to the study of primary cilia and centrioles (Figure 22) (Katoh et al., 2020). The difference in resolution between SIM and Airyscan microscopy is described by the authors as negligible when combined with expansion microscopy. Therefore, they recommend Airyscan microscopy for its convenience of use.

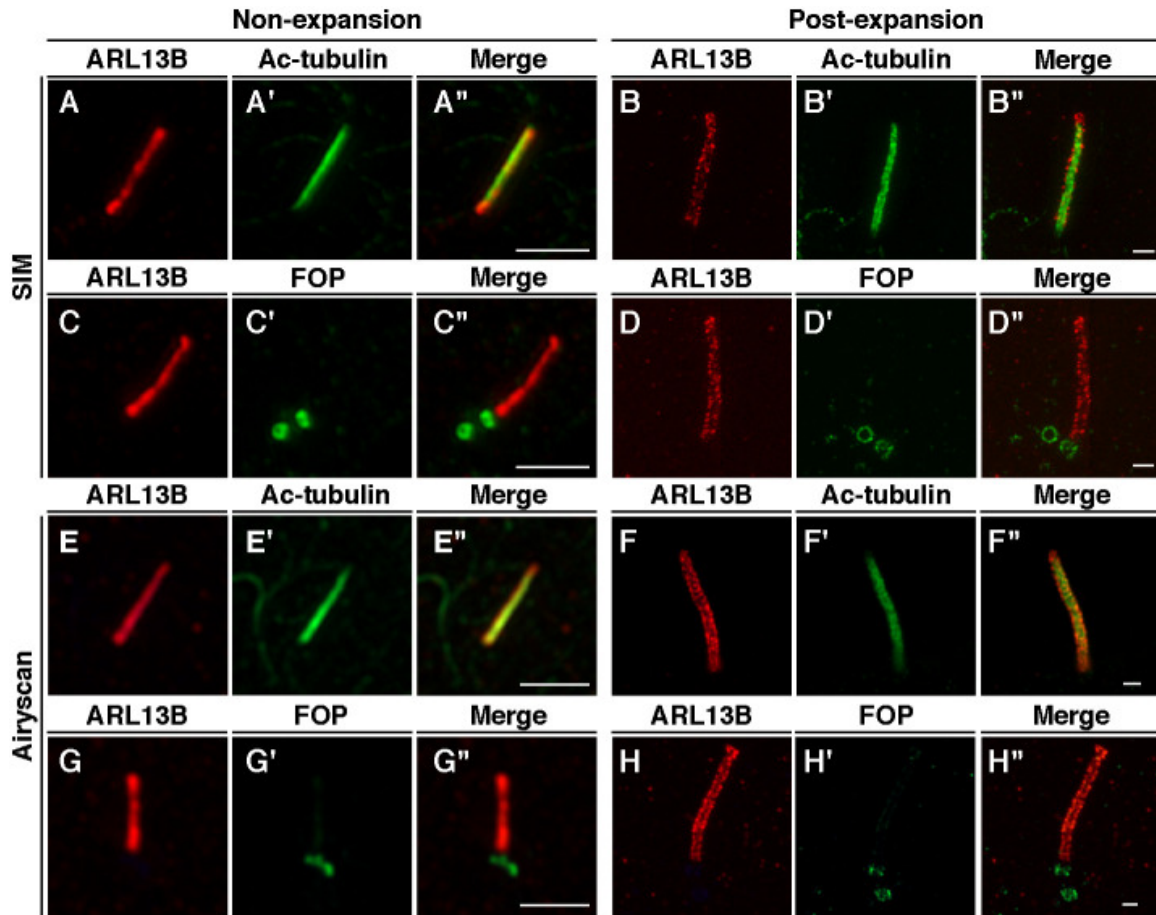


Figure 22: Comparison of centrioles and cilia in RPE1 cells observed directly or after treatment for expansion microscopy (ExM), by SIM or Airyscan microscopy, from (Katoh et al., 2020). Scale bar 2 μ m.

1.6.4. Expansion microscopy

To increase the capacity to distinguish details in another way than by exploiting optical properties, techniques that increase the sample size have been developed. The first protocol was developed by Chen *et al.* in 2015 and called expansion microscopy (ExM). It consists of expanding a sample that is previously fixed and submitted to immunofluorescence by inclusion in a gel composed in part of a superabsorbent polymer, sodium acrylate. A second protocol called ‘Magnified Analysis of the Proteome’ (MAP) protocol was developed in 2016 by Ku *et al.*, which differs from the ExM protocol in that the sample is cross-linked by a fixative and included in an expandable gel prior to performing immunofluorescence. The protocol called ‘Ultrastructure Expansion Microscopy’ (U-ExM), developed by Gambarotto *et al.* in 2018, is an improved version of the previous protocols. The sample is first incubated in a cross-link prevention solution composed of acrylamide and paraformaldehyde at concentrations that preserve the geometry of the sample after expansion. The sample is then embedded in the expandable gel and submitted to immunofluorescence. The authors showed that the U-ExM protocol leads to a perfectly isotropic macromolecular expansion of centrioles compared to MAP and ExM (Figure 23). Also, U-ExM allows for better labeling efficiency, as antibodies can better access the macromolecular superstructure of the centriole. This technique was used to resolve the localization of the inner scaffold of centriole (Figure 3). An alternative version of this protocol exists which also preserves the cytoplasmic MTs. U-ExM coupled with STORM allows not only to distinguish individual centriole triplets, but also to visualize their chirality (Gambarotto *et al.*, 2019).

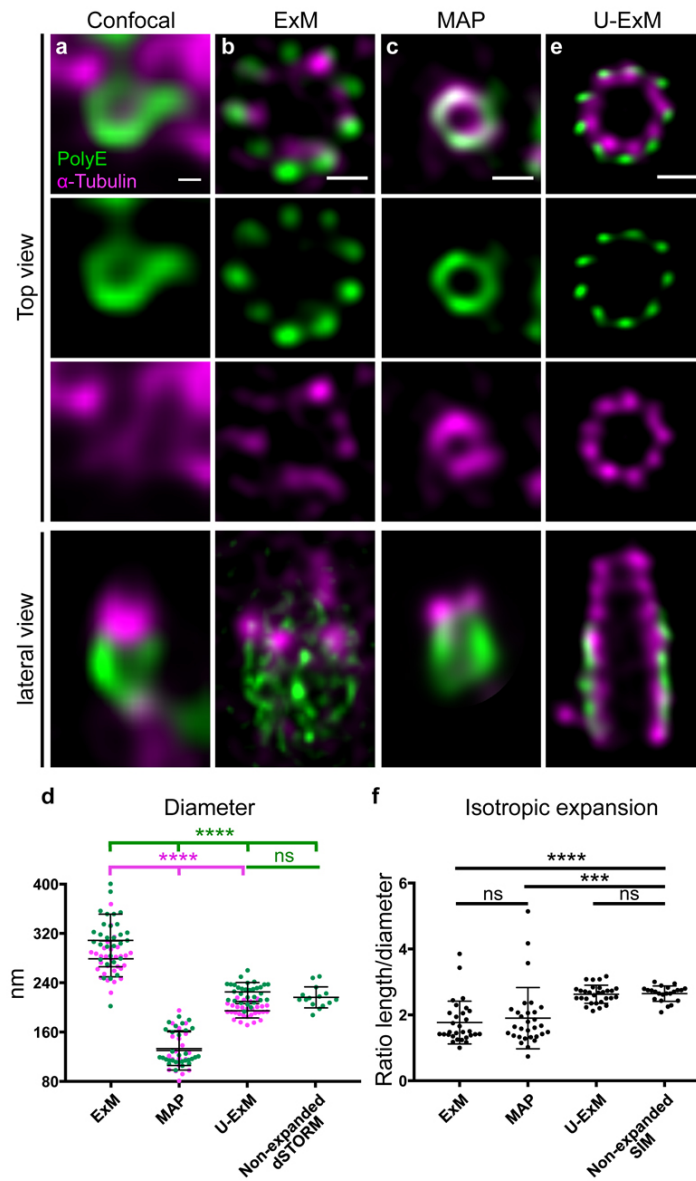


Figure 23: Comparison of different protocols for the expansion of centrioles, from (Gambarotto et al., 2019). (a) non-expanded, or expanded with (b) ExM, (c) MAP and (e) U-ExM. Samples were stained for poly-glutamylated tubulin (PolyE), in green, and α -tubulin, in magenta, and imaged by confocal microscopy followed by HyVolution image processing. Scale bar (a), 100 nm and (b, c, e), 450 nm. (d) Diameter of centrioles measured from PolyE and α -tubulin labeling (green and magenta dots, respectively). (f) Evaluation of expansion isotropy from the ratio between centriole length and diameter.

1.7. Hypothesis

Interest in the VFL1 and VFL3 protein families began in our laboratory because of their involvement in controlling the direction of locomotion in *S. mediterranea*, uncovered by a genetic screen performed by my thesis supervisor. The abnormal direction of locomotion was expected to result from aberrant ciliary beat orientation in epidermal multiciliated cells, itself controlled by BB rotational polarity. Our team thus undertook to study the role of these proteins in *S. mediterranea* multiciliated cells. To determine the localization of SMED-VFL1 and SMED-VFL3, I developed and tested antibodies against these proteins. This allowed to establish that SMED-VFL1 and -VFL3 are localized to the BBs in multiciliated cells. Overall, the work published by our team demonstrated the involvement of these two proteins in the assembly of centriolar appendages and the organization of cytoskeleton networks that control the rotational polarity of BBs. Remarkably, these results revealed that the network formed by the BBs and the associated cytoskeleton networks possess chiral asymmetry, which appears to arise from asymmetries within the BBs themselves, *i.e.* from asymmetries between the MT triplets. These results are presented in section 2.3 (Article 2).

In parallel to this work, I undertook to study the role of hVFL1, and contributed to the study of hVFL3 in human cells, a context where centrioles do not show visible rotational asymmetry. By analogy with the results obtained in planarian, our hypothesis was that these proteins might be involved in the assembly or function of centriolar appendages. In particular, SDAs share many similarities with the basal foot in terms of both structure and function, and the inter-centriolar linker is composed mainly of rootletin like the ciliary rootlet. First, I studied the effect of hVFL1 inactivation on the anchoring of MTs to the centrosome, in order to identify possible defects in the function of SDAs. To do so, I analyzed the impact of hVFL1 depletion on MT regrowth and release from the centrosome following depolymerization. I observed a greater release of MTs upon depletion of hVFL1, which indeed suggests that MT anchoring is perturbed in hVFL1-depleted cells.

Since MT anchoring to SDAs has been implicated in the control of centrosome position, I studied afterwards the impact of depletion of hVFL1, as well as hVFL3, on centrosome positioning. Using adhesive micropatterns that allow to generate a stereotyped cellular organization, I found

that both hVFL1 and hVFL3 are required for the proper positioning of the centrosome. The team studied in detail the function of hVFL3, and my results analyzing the position of the centrosome using micropatterning in hVFL3-depleted cells are presented in section 2.2 (Article 3). I also developed and tested an anti-hVFL3 antibody for this study. As part of the study of the role of hVFL1 in anchoring MTs to the centrosome, I also studied the context of mitotic cells. During mitosis, the spindle is oriented through the anchoring of astral MTs to the cell cortex. After depletion of hVFL1, I observed a wider distribution of mitosis angles, suggesting abnormalities in the organization or function of astral MTs. Indeed, a detailed analysis of astral MTs in hVFL1-depleted cells confirmed that they are fewer and longer than in control cells. These results, presented in section 2.4, support that hVFL1 is required for the organization of MTs in interphase and mitosis.

Because a mutation in *LRRCCI* had been found in JBTS patients (Shaheen et al., 2016), I decided to explore the role of hVFL1 in ciliogenesis. I analyzed ciliary assembly and signaling in RPE1 cells depleted from hVFL1 either by CRISPR/Cas9 genome editing or by RNAi. This allowed me to identify defects in these two processes and thus to confirm the link between hVFL1 and JBTS. I then developed antibodies against hVFL1 which allowed me to show that it localizes to the distal end of the centrioles, which concentrates many proteins related to JBST and sensory ciliopathies in general. To determine the localization of hVFL1 with greater precision, I turned to U-ExM for which I trained in the laboratory of Paul Guichard and Virginie Hamel at the University of Geneva. This approach allowed me to show that hVFL1 is localized in a rotationally asymmetric manner within the centrioles distal lumen of the centrosome. This property was reminiscent of Vfl1p localization in *C. reinhardtii*, but it was unprecedented among centrosome components. I then analyzed the localization of other distal centriole components in hVFL1-depleted cells to identify proteins that could cooperate with hVFL1 and contribute to ciliary phenotypes. Using U-ExM, I first showed that the morphology of DAs, analyzed using CEP164, is abnormal in hVFL1-deficient cells, which likely contributes to the ciliary phenotypes observed in these cells. Next, I identified another protein whose recruitment is disrupted by depletion, the C2CD3 protein. Unexpectedly, my results showed that C2CD3 is itself asymmetrically localized within the distal lumen of centrioles. Taken together, my results suggest that hVFL1 and C2CD3 form a structure that may be homologous to the one formed by Vfl1p and the acorn in *C. reinhardtii*, suggesting a conservation of molecular mechanisms controlling

rotational polarity in eukaryotes, including within the human centrosome. These results, which represent the main contribution of my thesis work, are presented in section 2.1 (Article 1).

My thesis work is therefore presented in the form of three articles and a chapter of unpublished data on the role of hVFL1 in the anchoring of MTs to the centrosome. These are followed by a general conclusion and future perspectives.

2. Results

2.1. Evolutionary conservation of centriole rotational asymmetry in the human centrosome (Article 1)

In this article, hVFL1 is referred to as LRRCC1, the name approved by the HUMAN Genome Organization (HUGO) gene nomenclature committee.

The highlights of this work are:

- LRRCC1 is required for proper ciliary assembly and signaling, confirming its implication in JBTS.
- LRRCC1 localizes asymmetrically at the distal end of human centrioles.
- LRRCC1 partially co-localizes and affects the recruitment of another distal component, C2CD3, which itself exhibits a rotationally asymmetric localization pattern.
- Rotational asymmetry is a conserved property of centrioles.
- Centriole asymmetry influences the position where new centrioles form

My participation in this work includes:

Performing most of the experiments, from design to interpretation of results. Training and supervising Paula Martin Gil (research technician), and Meriem Boumendjel, Manon Bouix, Quentin Delobelle, Lucia Maniscalco, and Thanh Bich Ngan Phan (Bachelor or Master students) to perform the experiments described in this article. Contributing to writing the manuscript.

Foreword

AiryScan microscopy being simpler to use than SIM or other super resolution techniques, I used this approach in association with U-ExM in my thesis work. This combination of approaches allowed me to increase the resolution by a factor of 1.7 x for AiryScan microscopy and of 4.5 x on average for U-ExM, *i.e.*, a factor of about 8 in total compared to conventional confocal microscopy. This corresponds to a resolution of about 20-25 nm, which is slightly less than the distance separating consecutive triplets in centrioles. The two techniques combined thus allowed me to distinguish triplets from centrioles as well as, in some cases, the chirality of the structure (Figure 24).

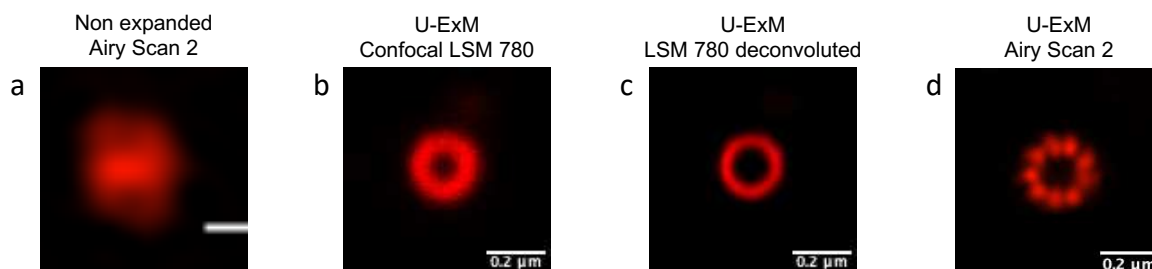


Figure 24: Comparison of centriole images obtained by confocal or AiryScan 2 microscopy, with or without expansion. Centrioles were stained for acetylated α -tubulin. Scale bar, 200 nm, rescaled to account for expansion in (b-d). (a) Unexpanded centriole, longitudinal view acquired by the LSM 980 AiryScan 2 (Zeiss), the cylinder shape is barely discernible. (b) Centriole expanded by U-ExM and imaged on a LSM 780 confocal microscope (Zeiss), in cross section. The lumen of the centriole is clearly visible, and the wall appears as a continuous ring. (c) Same image as in (b) after deconvolution with Huygens software. The deconvolution generates a more focused image but does not allow to distinguish the individual triplets. (d) Cross section of a centriole in proximal view, expanded by U-ExM and acquired with an LSM 980 AiryScan 2.

Evolutionary conservation of centriole rotational asymmetry in the human centrosome

Noémie Gaudin ¹, Paula Martin Gil ¹, Meriem Boumendjel ¹, Dmitry Ershov ^{2,3}, Catherine Pioche-Durieu ¹, Manon Bouix ¹, Quentin Delobelle ¹, Lucia Maniscalco ¹, Thanh Bich Ngan Phan ¹, Vincent Heyer ^{4,5,6,7}, Bernardo Reina-San-Martin ^{4,5,6,7} and Juliette Azimzadeh ^{1,8}.

¹ Université de Paris, CNRS, Institut Jacques Monod, 75006, Paris, France.

² Image Analysis Hub, C2RT, Institut Pasteur, Paris, France.

³ Hub de Bioinformatique et Biostatistique – Département Biologie Computationnelle, Institut Pasteur, USR 3756 CNRS, Paris, France.

⁴ Institut de Génétique et de Biologie Moléculaire et Cellulaire (IGBMC), Illkirch, France.

⁵ Institut National de la Santé et de la Recherche Médicale (INSERM), U1258, Illkirch, France.

⁶ Centre National de la Recherche Scientifique (CNRS), UMR7104, Illkirch, France.

⁷ Université de Strasbourg, Illkirch, France.

⁸ Author for correspondence: juliette.azimzadeh@ijm.fr

Keywords: centriole, centrosome, LRRCC1, VFL1, C2CD3, Joubert syndrome, asymmetry.

Abbreviations:

DA: distal appendage; JBTS: Joubert syndrome; MCC: multiciliated cell; PCM: pericentriolar material; SAG: SMOOTHENED agonist; SMO: SMOOTHENED; TZ: transition zone.

Abstract

Centrioles are formed by microtubule triplets in a nine-fold symmetric arrangement. In flagellated protists and in multiciliated cells, accessory structures tethered to specific triplets render the centrioles rotationally asymmetric, a property that is key to cytoskeletal and cellular organization in these contexts. In contrast, centrioles within the centrosome of animal cells display no conspicuous rotational asymmetry. Here, we uncover rotationally asymmetric molecular features in human centrioles. Using ultrastructure expansion microscopy, we show that LRRCC1, the ortholog of a protein originally characterized in flagellate green algae, associates preferentially to two consecutive triplets in the distal lumen of human centrioles. LRRCC1 partially co-localizes and affects the recruitment of another distal component, C2CD3, which also has an asymmetric localization pattern in the centriole lumen. Together, LRRCC1 and C2CD3 delineate a structure reminiscent of a filamentous density observed by electron microscopy in flagellates, termed the ‘acorn’. Functionally, the depletion of LRRCC1 in human cells induced defects in centriole structure, ciliary assembly and ciliary signaling, supporting that LRRCC1 cooperates with C2CD3 to organizing the distal region of centrioles. Since a mutation in the *LRRCCI* gene has been identified in Joubert syndrome patients, this finding is relevant in the context of human ciliopathies. Taken together, our results demonstrate that rotational asymmetry is a conserved ancient property of centrioles. Our work also reveals that asymmetrically localized proteins are key for primary ciliogenesis and ciliary signaling in human cells.

Introduction

Centrioles are cylindrical structures with a characteristic ninefold symmetry, which results from the arrangement of their constituent microtubule triplets (LeGuennec et al., 2021). In animal cells, centrioles are essential for the assembly of centrosomes and cilia. The centrosome, composed of two centrioles embedded in a pericentriolar material (PCM), is the main organizer of the microtubule cytoskeleton. In addition, most vertebrate cells possess a primary cilium, a sensory organelle that assembles from the oldest centriole within the centrosome, called mother centriole (Kumar and Reiter, 2021).

Centrioles within the centrosome show no apparent rotational asymmetry, *i.e.*, no structural asymmetry of the microtubule triplets. In vertebrates, the mother centriole carries distal appendages (DAs) and subdistal appendages arranged in a symmetric manner around the centriole cylinder (Kumar and Reiter, 2021). In contrast, the centriole/basal body complex of flagellates, to which the animal centrosome is evolutionary related, is characterized by marked rotational asymmetries (Azimzadeh, 2021; Yubuki and Leander, 2013). In flagellates, an array of fibers and microtubules anchored asymmetrically at centrioles controls the spatial organization of the cell (Feldman et al., 2007; Yubuki and Leander, 2013). The asymmetric attachment of cytoskeletal elements appears to rely on molecular differences between microtubule triplets. In the green alga *Chlamydomonas reinhardtii*, Vfl1p (Variable Flagella number 1 protein) localizes principally at two triplets near the attachment site of a striated fiber connecting the centrioles (Silflow et al., 2001). This fiber is absent or mispositioned in the *vfl1* mutant, leading to defects in centriole position and number, and overall cytoskeleton disorganization (Adams et al., 1985; Feldman et al., 2007). In the same region, a rotationally asymmetric structure termed the ‘acorn’ was observed in the centriole lumen by transmission

electron microscopy. The acorn appears as a filament connecting five successive triplets and is in part colocalized with Vfl1p (Geimer and Melkonian, 2005, 2004).

We recently established that Vfl1p function is conserved in the multiciliated cells (MCCs) of planarian flatworms, which was later confirmed in xenopus (Basquin *et al.*, 2019; Nommick *et al.*, 2021). MCCs assemble large numbers of centriole that are polarized in the plane of the plasma membrane to enable the directional beating of the cilia (Meunier and Azimzadeh, 2016), like in *C. reinhardtii*. The planarian ortholog of Vfl1p is required for the assembly of two appendages that decorate MCC centrioles asymmetrically, the basal foot and the ciliary rootlet (Basquin *et al.*, 2019). Depleting Vfl1p orthologs in planarian or xenopus MCCs alters centriole rotational polarity, reminiscent of the *vfl1* phenotype in *C. reinhardtii* (Adams *et al.*, 1985; Basquin *et al.*, 2019; Nommick *et al.*, 2021). Intriguingly, the human ortholog of Vfl1p, called LRRCC1 (Leucine Rich Repeat and Coiled Coil containing 1) localizes at the centrosome despite the lack of rotationally asymmetric appendage in this organelle (Andersen *et al.*, 2003; Muto *et al.*, 2008). Furthermore, a homozygous mutation in the *LRRCC1* gene was identified in two siblings affected by a ciliopathy called Joubert syndrome (JBTS), suggesting that LRRCC1 might somehow affect the function of non-motile cilia (Shaheen *et al.*, 2016).

Here, we show that LRRCC1 localizes in a rotationally asymmetric manner in the centrioles of the human centrosome. We further establish that LRRCC1 is required for proper ciliary assembly and signaling, which likely explains its implication in JBTS. LRRCC1 affects the recruitment at centrioles of another ciliopathy protein called C2CD3 (C2 domain containing 3), which we found to also localize in a rotationally asymmetric manner, forming a pattern reminiscent of the acorn described in flagellates. Our findings uncover the unanticipated rotational asymmetry of centrioles in the human centrosome and show that this property is connected to the assembly and function of primary cilia.

Results

LRRCC1 localizes asymmetrically at the distal end of centrioles

To investigate a potential role of LRRCC1 at the centrosome, we first sought to determine its precise localization at the centrosome. We raised antibodies against two different fragments within the long C-terminal coiled-coil domain of LRRCC1 (Ab1, 2), which both stained the centrosome region in human Retinal Pigmented Epithelial (RPE1) cells (Fig. 1a; Supplemental Fig. S1b), as previously reported (Muto *et al.*, 2008). Labeling intensity was decreased in LRRCC1-depleted cells for both antibodies, supporting their specificity (Fig. 4a; Supplemental Fig. S1c, e, f, h). LRRCC1 punctate labelling in the centrosomal region indicated that it is present within centriolar satellites, confirming a previous finding that LRRCC1 interacts with the satellite component PCM1 (Gupta *et al.*, 2015). Importantly, following nocodazole treatment to depolymerize microtubules, the satellites were dispersed but a fraction of LRRCC1 was retained at the centrioles (Fig. 1a; Supplemental Fig. S1b, e), supporting that LRRCC1 is a core centriole component.

To determine LRRCC1 localization more precisely within the centriolar structure, we used ultrastructure expansion microscopy (U-ExM) (Gambarotto *et al.*, 2019) combined with imaging on a Zeiss Airyscan 2 confocal microscope, thereby increasing the resolution by a factor of ~ 8 compared to conventional confocal microscopy. We found that LRRCC1 localizes at the distal end of centrioles as well as of procentrioles (Fig. 1b). Strikingly, and unlike any other known centriole components, LRRCC1 decorated the distal end of centrioles in a rotationally asymmetric manner. Indeed, LRRCC1 was detected close to the triplet blades and towards the lumen of the centriole (Fig. 1c). The staining was often associated with two or more consecutive triplets, one of them being usually more brightly labelled than the others. In addition, a fainter staining was consistently detected along the entire length of all triplets (Fig.

1b, see brighter exposure). This pattern was observed in both RPE1 and HEK 293 cells and was obtained with both anti-LRRCC1 antibodies (Supplemental Fig. S1g), supporting its specificity. There was some variability in the distal pattern, particularly in the distance between LRRCC1 and the centriole wall (Fig. 1c), which possibly resulted from the fact that the centrioles were not perfectly orthogonal to the imaging plan. To obtain a more accurate picture of LRRCC1 localization, we generated 3D reconstructions that we realigned, first along the vertical axis, then with respect to one another using the most intense region of the LRRCC1 labelling as a reference point (Fig. 1d; Supplemental Fig. S2a-c). An average 3D reconstruction was then generated (Fig. 1e) and revealed that in transverse view, LRRCC1 was mainly associated to one triplet, and to a lesser extent to its direct neighbor counterclockwise, on their luminal side. A longitudinal view confirmed that LRRCC1 is principally located at the distal end of centrioles.

Together, our results show that LRRCC1 is localized asymmetrically within the distal centriole lumen, establishing that centrioles within the human centrosome are rotationally asymmetric.

The localization pattern of LRRCC1 is similar at the centrosome and in mouse MCCs

LRRCC1 orthologs are required for establishing centriole rotational polarity in planarian and xenopus MCCs, like in *C. reinhardtii* (Basquin et al., 2019; Nommick et al., 2021; Silflow et al., 2001). It is therefore plausible that LRRCC1-related proteins localize asymmetrically in MCC centrioles, and indeed, *Lrrcc1* was recently found associated to the ciliary rootlet in xenopus MCCs (Nommick et al., 2021). To determine whether LRRCC1 also localizes at the distal end of MCC centrioles in addition to its rootlet localization, and if so, whether LRRCC1 localization pattern resembles that observed at the centrosome, we analyzed mouse ependymal and tracheal cells by U-ExM. In *in vitro* differentiated ependymal cells, the labelling generated

by the anti-LRRCC1 antibody was consistent with our observations in human culture cells. Mouse *Lrrcc1* localized asymmetrically at the distal end of centrioles, opposite to the side where the basal foot is attached (Fig. 2a), as determined by staining the basal foot marker γ -tubulin (Clare et al., 2014). *Lrrcc1* was also present at the distal end of procentrioles forming via either the centriolar or acentriolar pathways (*i.e.*, around parent centrioles or deuterosomes, respectively) (Fig. 2b). We also examined tracheal explants, in which centrioles were docked and polarized at the apical membrane in higher proportions (Fig. 2c). We obtained an average image of *Lrrcc1* labelling from 35 individual centrioles aligned using the position of the basal foot as a reference point. This revealed that *Lrrcc1* is principally located in the vicinity of 3 triplets located opposite the basal foot, to the right of basal foot main axis (triplet number 9, 1 and 2 on the diagram in Fig. 2d). *Lrrcc1* was located farther away from the triplet wall than in centrioles of the centrosome, but this was likely an effect of a deformation of the centrioles (Fig. 2c, d) caused by the incomplete expansion of the underlying cartilage layer in tracheal explants. In agreement, *Lrrcc1* was located close to the triplets in ependymal cell monolayers, which expand isometrically. Besides the distal centriole staining, we found no evidence that *Lrrcc1* is associated to the ciliary rootlet in mouse MCCs, unlike in xenopus. The *Lrrcc1* pattern in mouse MCCs was thus similar to the pattern observed at the human centrosome.

Together, these results show that LRRCC1 asymmetric localization is a conserved feature of mammalian centrioles, presumably linked to the control of centriole rotational polarity and ciliary beat direction in MCCs.

Centriole rotational asymmetry is not linked to stereotypical patterns of procentriole position and orientation during centriole duplication

In *C. reinhardtii*, centriole rotational polarity and flagellar beat direction depend on the position and orientation at which new centrioles arise during cell division. Reflecting the stereotypical

organization of centrioles and procentrioles in this species, Vfl1p is recruited early and at a fixed position at the distal end of procentrioles (Fig.3a) (Geimer and Melkonian, 2004; Silflow et al., 2001). We therefore wondered whether this mechanism might be somewhat conserved in human cells, which could then explain the persistence of LRRCC1 asymmetric localization despite the lack of asymmetric appendages or ciliary motility in these cells. We first analyzed the timing of LRRCC1 incorporation into procentrioles. LRRCC1 was already present at an early stage of centriole assembly, when the procentrioles were only about 100 nm in length and 70 nm in diameter (Fig. 3b, c). LRRCC1 was then detected during successive stages of procentriole elongation, always localizing asymmetrically and distally (Fig. 3c), like in *C. reinhardtii*. We then examined LRRCC1 localization in duplicating centrosomes by generating 3D-reconstructions of diplosomes (*i.e.*, orthogonal centriole pairs) from RPE1 and HEK 293 cells processed by U-ExM (Fig. 3d). We analyzed two parameters: the angle between LRRCC1 in the procentriole and the long axis of the parent centriole used as reference (Fig. 3d, LRRCC1 localization in procentrioles), and the angle between procentriole position and LRRCC1 in the parent centriole (Fig. 3d, Procentriole position with respect to centriolar LRRCC1). We found that LRRCC1 localization in procentrioles was more often aligned with the long axis of the parent centriole in RPE1 cells (Fig. 3d, top left panel, quadrants Q1 and Q3, respectively), but less so in HEK 293 cells (top right panel), in which the distribution was closer to a random distribution. Thus, human procentrioles do not arise in a fixed orientation, unlike in flagellates. Next, we analyzed the position of procentrioles with respect to centriolar LRRCC1 (bottom panels). Based on current models, procentriole assembly is expected to occur at a random position around parent centrioles in animal cells (Takao et al., 2019). Identification of LRRCC1 provided the first opportunity to directly test this model. In diplosomes from both RPE1 and HEK 293 cells, the position of procentrioles with respect to LRRCC1 location in the parent centriole was variable, confirming that the position at which procentrioles assemble is not

precisely controlled in human cells. Interestingly, however, the procentrioles were not distributed in a completely random fashion either. Procentrioles were found in quadrant Q2 (45-135 degrees clockwise from LRRCC1 centroid) on average 4 times less often than in the other quadrants, both in RPE1 and HEK 293 cells, suggesting that rotational polarity of the parent centriole somehow impacts procentriole assembly.

Overall, these results nevertheless suggest that the conservation of centriole rotational asymmetry in human cells is likely not linked to a role in centriole duplication.

LRRCC1 is required for primary cilium assembly and ciliary signaling

A previous report identified a homozygous mutation in a splice acceptor site of the *LRRCC1* gene in two siblings diagnosed with JBTS (Shaheen et al., 2016), but how disruption of *LRRCC1* expression affects ciliary assembly and signaling has never been investigated. To address this, we generated RPE1 cell lines deficient in *LRRCC1* using two different CRISPR/Cas9 strategies and targeting two different regions of the *LRRCC1* locus. We could not recover null clones despite repeated attempts in RPE1 - both wild type and *p53*^{-/-} (Izquierdo et al., 2014), HEK 293 and U2-OS cells, suggesting that a complete lack of *LRRCC1* is possibly deleterious. Nevertheless, we obtained partially depleted mutant clones, including three RPE1 clones targeted in either exons 11-12 (clone 1.1) or exons 8-9 (clones 1.2 and 1.9). We could not evaluate the overall decrease in *LRRCC1* levels since the endogenous *LRRCC1* protein was not detected by Western blot (Supplemental Fig. S1a). However, we confirmed the decrease in centrosomal *LRRCC1* levels by immunofluorescence using the two different anti-*LRRCC1* antibodies, as well as by quantitative RT-PCR (Fig. 4a; Supplemental Fig. S1c-e).

Following induction of ciliogenesis, the proportion of ciliated cells was decreased in all three mutant clones compared to control cells (Fig. 4b). We were unable to obtain stable RPE1 cell lines expressing myc- or GFP-tagged versions of *LRRCC1*, and transient overexpression

of LRRCC1 in wild-type cells led to a decrease in the proportion of ciliated cells, making phenotype rescue experiments difficult to interpret. We therefore used RNAi as an independent method to verify the specificity of ciliary defects observed in CRISPR clones. Targeting LRRCC1 expression using two different siRNAs, we obtained a comparable decrease in LRRCC1 levels and in the proportion of ciliated cells as in the CRISPR clones (Fig. 4c; Supplemental Fig. S1f). Sensory ciliopathies like JBTS result to a large extent from defective Hedgehog signaling (Romani et al., 2013). We determined the effect of LRRCC1-depletion on Hedgehog signaling by measuring the ciliary accumulation of the activator SMOOTHENED (SMO) upon induction of the pathway (Rohatgi et al., 2007). Depletion of LRRCC1 by either CRISPR editing or RNAi led to a drastic decrease in SMO accumulation at the primary cilium following induction of the Hedgehog pathway by SMO-agonist (SAG) (Fig. 4d, e), and reduced expression of the target gene *PTCH1* (Supplemental Fig. S1g) (Goodrich et al., 1996).

Taken together, our results demonstrate that LRRCC1 is required for proper ciliary assembly and signaling in human cells, further establishing its implication in JBTS.

Depletion of LRRCC1 induces defects in centriole structure

Mutations in distal centriole components can alter centriole length regulation or the assembly of DAs, which both result in defective ciliogenesis (Reiter and Leroux, 2017; Sharma et al., 2021). We used U-ExM to search for possible defects in centriole structure in LRRCC1-depleted RPE1 cells. We measured centriole length in the two RPE1 CRISPR clones that express the lowest levels of LRRCC1 (1.1 and 1.9). Centrioles were co-stained with anti-acetylated tubulin and an antibody against the DA component CEP164 to differentiate mother and daughter centrioles. We observed an increase in centriole length in clone 1.9 (Fig. 5a), which expresses the lowest levels of LRRCC1, compared to control cells (483 ± 53 nm for mother and 372 ± 55 nm for daughter centrioles in clone 1.9; 427 ± 56 nm for mother and 320

± 46 nm for daughter centrioles in control cells; mean \pm SD). Although on a limited sample size, we also observed abnormally long centrioles by transmission electron microscopy in this clone (494 ± 73 nm in clone 1.9, N = 9; 429 ± 52 nm in control cells, N = 3; mean \pm SD) (Fig. 5b). However, clone 1.1 was not significantly different from control cells by U-ExM, suggesting that this phenotype is not fully penetrant at the remaining levels of LRRCC1 expression observed in the CRISPR clones. We next used U-ExM to analyze the structure of DAs labelled with anti-CEP164 antibody (Fig. 5c-e). In RPE1 control cells, 80 ± 14 % of mother centriole had 9 properly shaped DAs, but this proportion fell to 57 ± 16 % and 44 ± 17 % (mean \pm SD) in clones 1.1 and 1.9, respectively (Fig. 5c, d). Mutant clones exhibited an increased proportion of centrioles with one or more abnormally shaped DAs (29 ± 17 % and 42 ± 18 % in clones 1.1 and 1.9, respectively, compared to 11 ± 11 % in control cells; mean \pm SD). We obtained similar results in a HEK 293 CRISPR clone expressing half the control levels of LRRCC1 (Fig. 5e; Supplemental Fig. S1h). LRRCC1-depletion did not affect overall CEP164 levels at mother centrioles in the CRISPR clones (Supplemental Fig. S3a, d), consistent with the relatively mild defect in DA morphology observed by U-ExM.

Together, these results show that a partial loss of LRRCC1 leads to abnormal DA morphology.

LRRCC1 and C2CD3 delineate a rotationally asymmetric structure in human centrioles

We next wanted to determine whether LRRCC1 cooperates with other distal centriole components. Proteins shown to be recruited early at procentriole distal end include CEP290 (Kim et al., 2008), OFD1 (Singla et al., 2010) and C2CD3 (Thauvin-Robinet et al., 2014). Of particular interest, OFD1 and C2CD3 are required for DA assembly and centriole length control, and mutations in these proteins have been implicated in sensory ciliopathies (Singla et al., 2010; Thauvin-Robinet et al., 2014; Tsai et al., 2019; Lei Wang et al., 2018). We first

determined whether depletion of LRRCC1 either by CRISPR editing or by RNAi led to modifications in the recruitment of these proteins within centrioles. We found no major differences in the centrosomal levels of OFD1 and CEP290 compared to control cells (Supplemental Fig. S3b, c, e, f). In contrast, C2CD3 levels were moderately increased in cells depleted from LRRCC1 either by CRISPR editing (clones 1.1 and 1.9) or by RNAi (Fig. 6a, b). We thus analyzed C2CD3 further by U-ExM. As described previously, C2CD3 localized principally at the distal extremity of centrioles (Fig. 6c) (Tsai et al., 2019; Yang et al., 2018). Strikingly, the C2CD3 labelling was also asymmetric, principally in terms of shape, often a C-shape, and to some extent in terms of position within the centriole lumen (Fig. 6d). After correcting the vertical alignment of centrioles as previously, we generated two different average 3D reconstructions of the C2CD3 pattern. For the first one, we used the central region of the C shape as reference in the xy plane point to superimpose individual centriole views (Fig. 6e, 'Shape'). For the second one, we used the region where the C2CD3 signal is closest to the centriole wall (after realignment along the vertical axis) as a reference point (Fig. 6e, 'Position'). The first method produced a robust C-shaped pattern positioned symmetrically in the centriole lumen. In the second average view, the C-shape was lost and instead a circular pattern of uneven intensity positioned asymmetrically within the centriole lumen was obtained. The fact that the first method generates a clear profile that more closely resembles the individual images suggests that the C-shape pattern is the most probable of the two. To determine whether the C2CD3 localization pattern is affected by LRRCC1-depletion, we analyzed C2CD3 in LRRCC1 CRISPR clones 1.1 and 1.9. The C2CD3 pattern was more variable than in control RPE1 cells, and was often abnormal in shape, position, or both (Fig. 6f). As a result, averaging the signal from 51 (1.1) or 20 (1.9) individual LRRCC1-depleted centrioles as previously produced aberrant patterns, most strikingly in the clone expressing

lower levels of LRRCC1 (clone 1.9; Fig. 6g). Thus, LRRCC1 is required for the proper assembly of the C2CD3-containing distal structure.

To determine whether LRRCC1 and C2CD3 might belong to a common structure, we next examined the respective positions of C2CD3 and LRRCC1 within the centriole. We co-stained centrioles with our anti-LRRCC1 antibody and a second anti-C2CD3 antibody produced in sheep (Table 1). We confirmed that LRRCC1 and C2CD3 are present in the same distal region of the centriole (Fig. 7a). In transverse views, the two proteins were usually not perfectly colocalized but found in close vicinity of one another near the microtubule wall (Fig. 6e). However, C2CD3 distal staining was consistently fainter than with the previous antibody, and we either could not observe a full C-shaped pattern, or we could not image it due to fluorescence bleaching. Neither anti-C2CD3 antibodies worked in mouse, so we were not able to compare C2cd3 and Lrrcc1 localization in MCCs. Nevertheless, the results obtained by individually labelling LRRCC1 and C2CD3 at the centrosome (Fig. 1e, 6e, g) together with the co-localization data (Fig. 7a) are consistent with the hypothesis that LRRCC1 is located somewhere along the C2CD3-containing, C-shaped structure (Fig. 7b). C2CD3 was not co-immunoprecipitated with a GFP-LRRCC1 fusion protein however, suggesting that LRRCC1 and C2CD3 do not directly interact (Supplemental Fig. S4).

Taken together, our results support that C2CD3 localizes asymmetrically in the distal lumen of human centrioles, a pattern that depends in part on LRRCC1.

Discussion

Here, we show that centrioles within the human centrosome are rotationally asymmetric despite the apparent nine-fold symmetry of their ultrastructure. This asymmetry is manifested by a specific enrichment in LRRCC1 near two consecutive triplets, and the asymmetric localization of C2CD3 within the centriole lumen. Depletion of LRRCC1 perturbed the recruitment of C2CD3 and induced defects in centriole structure, ciliogenesis and ciliary signaling, supporting that LRRCC1 contributes to organizing the distal centriole region together with C2CD3. LRRCC1 localizes like its *C. reinhardtii* ortholog Vfl1p, and C2CD3 delineates a filamentous structure reminiscent of the acorn described in this species (Geimer and Melkonian, 2005, 2004) and in *Trypanosoma brucei* (Vaughan and Gull, 2016). Collectively, our results support that rotational asymmetry is a conserved property of centrioles linked to ciliary assembly and signaling in humans.

LRRCC1 and C2CD3 belong to a conserved rotationally asymmetric structure

Our work identifies two proteins located asymmetrically in the distal centriole lumen of the human centrosome, each with a specific pattern. LRRCC1 localizes principally near two consecutive triplets, with the first triplet counterclockwise labelled approximately 50 % more than the next one. This pattern is highly reminiscent of the LRRCC1 ortholog Vfl1p, which localizes predominantly to the triplet facing the second centriole (referred to as triplet 1), and to a lesser extent to its immediate neighbor counterclockwise (triplet 2; Fig. 7b) (Silflow et al., 2001). In *C. reinhardtii*, triplets 1 and 2 are positioned directly opposite to the direction of flagellar beat, which is directed towards triplet 6 (Fig. 7b) (Lin et al., 2012). In mouse MCCs, Lrrcc1 is associated to triplets located not exactly opposite to the basal foot but with a clockwise shift of at least 20° from the basal foot axis. However, the beating direction was shown to be

also shifted approximately 20° clockwise relative to the position of the basal foot in bovine tracheal MCCs (Schneiter et al., 2021) (Fig. 2d). The position of Lrrcc1/Vfl1p-labelled triplets with respect to ciliary beat direction might thus be similar in *C. reinhardtii* and in animal MCCs. Overall, the specific localization pattern of Vfl1p-related proteins at the distal end of centrioles, and their requirement for centriole positioning and ciliary beat orientation when motile cilia are present, appear to be conserved between flagellates and animals.

The second protein conferring rotational asymmetry to human centrioles, C2CD3, likely delineates a C-shape positioned symmetrically in the distal lumen. Strikingly, this staining is reminiscent of a filament observed by electron microscopy, which is said to form an ‘incomplete circle’ in the distal lumen of human centrioles (Vorobjev and Chentsov, 1980). Several lines of evidence support the hypothesis that the C2CD3-containing structure is homologous to the acorn, a 10 nm-filament connecting five consecutive triplets along the centriole wall and across the lumen in *C. reinhardtii* (Fig. 7b) (Geimer and Melkonian, 2004; Vaughan and Gull, 2016). First, the C2CD3 labelling is consistent with a circular filament. Second, the C2CD3-containing structure is localized in close vicinity of several consecutive triplets. Third, C2CD3 is partially co-localized with LRRCC1 near the microtubule wall. And last, C2CD3 orthologs are found in a variety of flagellated unicellular eukaryotes, including the green alga *Micromonas pusilla* (Zhang and Aravind, 2012), suggesting an ancestral association to centrioles and cilia. The partial co-localization of Vfl1p and the acorn in *C. reinhardtii*, and the observation that both are already present at the distal end of procentrioles, led to propose that Vfl1p might also be a component of the acorn (Geimer and Melkonian, 2004). Consistent with this idea, both LRRCC1 and C2CD3 are recruited early at the distal end of human procentrioles, and LRRCC1 is required for the proper recruitment and/or positioning of the C2CD3-containing structure. C2CD3 recruitment at the centrioles also depends on the proteins CEP120 and Talpid3 (Tsai et al., 2019), which possibly explains why C2CD3

recruitment is not diminished, and is even increased in LRRCC1-depleted centrioles. Future work will help deciphering the relationships between these different proteins and characterize in more details the architecture of the rotationally asymmetric structure at the distal end of mammalian centrioles.

Rotationally asymmetric centriole components are required for ciliogenesis

Our results uncover a link between centriole rotational asymmetry and primary ciliogenesis in human cells. Mutations in C2CD3 have been involved in several sensory ciliopathies, including JBTS (Boczek et al., 2018; Cortés et al., 2016; Ooi, 2015; Thauvin-Robinet et al., 2014). The associated ciliary defects are likely caused by anomalies in the structure of centrioles, since depleting C2CD3 inhibits centriole elongation and DA assembly, whereas C2CD3 overexpression leads to centriole hyper-elongation (Thauvin-Robinet et al., 2014; Wang et al., 2018; Ye et al., 2014). We observed similar defects in LRRCC1-depleted cells, but of comparatively lesser extent. Defects in DA morphology were observed in all CRISPR clones analyzed, and centriole length was increased in the clone with the most severe phenotype. The fact that LRRCC1-depletion has a more limited impact on centriole assembly than perturbation of C2CD3 levels suggests that LRRCC1 might not be directly involved in centriole length control or DA formation, however. The defects observed in LRRCC1-depleted cells could instead result indirectly from the abnormal localization of C2CD3. Besides the defects in centriole structure, it is likely that LRRCC1-depletion also perturbs the organization of the ciliary gate, as LRRCC1-depleted cells exhibited a drastic reduction in Hedgehog signaling. Loss of ciliary gate integrity interferes with the accumulation of SMO in the cilium upon activation of the Hedgehog pathway and is a frequent consequence of ciliopathic mutations (Garcia-Gonzalo and Reiter, 2017). The ciliary gate consists of the TZ and the DA region, which both contribute to regulating protein trafficking in and out of the cilium (Garcia-Gonzalo

and Reiter, 2017; Nachury, 2018). The anomalies in DA morphology observed in LRRCC1-depleted cells could disrupt the organization of the so-called DA matrix (Yang et al., 2018), thus preventing SMO accumulation in the cilium. Another, non-mutually exclusive possibility is that the architecture of the TZ, which forms directly in contact with the distal end of the centriole, is altered by LRRCC1-depletion. In either case, our observations in RPE1 cells are consistent with the JBTS diagnosis in two siblings carrying a mutation in the *LRRCC1* gene (Shaheen et al., 2016), further establishing that *LRRCC1* is a novel ciliopathy gene. Besides signaling, ciliary gate integrity is required for axoneme extension and indeed, LRRCC1-depleted cells formed cilia at lower frequency than control cells – a defect that might also result from perturbed DA architecture. In the *vfl1* mutant of *C. reinhardtii*, both unanchored centrioles and centriole docked at the plasma membrane but lacking a flagellum were observed (Adams et al., 1985). This would support that LRRCC1/Vfl1p requirement for properly assembling the ciliary gate is a conserved functional aspect of this family of proteins (Fig. 7c).

Why is there a rotationally asymmetric structure at the base of primary cilia, and how does this structure form and contribute to the assembly of the DAs and the cilium remain open questions. In *C. reinhardtii* and in MCCs, LRRCC1 function is linked to the assembly of asymmetric appendages, which must be correctly positioned in relation to ciliary beat direction (Fig. 7c). An asymmetric structure present early during centriole assembly and ultimately located near the cilium appears well suited for this task. The conservation of such a structure at the base of the primary cilium could perhaps indicate that primary cilia also possess rotationally asymmetric features, which would open interesting new perspectives on ciliary roles in health and disease.

Other roles for centriole rotational assembly in human cells

Our finding that procentrioles do not form completely at random with respect to LRRCC1 location in the parent centriole suggests that centriole rotational polarity can influence centriole duplication in human cells. In *C. reinhardtii*, procentrioles are formed at fixed positions with respect to the parent centrioles, to which they are bound by a complex array of fibrous and microtubular roots (Fig. 7c) (Geimer and Melkonian, 2004; Yubuki and Leander, 2013). The process is likely different at the centrosome since the roots typical of flagellates are not conserved in animal cells (Azimzadeh, 2021; Yubuki and Leander, 2013). In mammalian cells, procentrioles form near the wall of the parent centriole following the recruitment of early centriole proteins directly to the PCM components CEP152 and CEP192 (Yamamoto and Kitagawa, 2021). It is nonetheless conceivable that an asymmetry in triplet composition could result in local changes in PCM composition, which in turn could negatively impact PLK4 activation in this region. For instance, our analyses in planarian MCCs led us to postulate that linkers might be tethered to one side of the centrioles in a VFL1-dependent manner and independently of centriole appendages (Basquin et al., 2019). Future work will allow deciphering how centriole rotational asymmetry influences centriole duplication, and whether it affects other aspects of centriole positioning and cellular organization.

Acknowledgements

The authors are deeply grateful to Marine Laporte, Virginie Hamel, Paul Guichard and Davide Gambarotto for teaching them the U-ExM procedure and for sharing antibodies; Arnaud Echard and Takashi Ochi for critical reading of the manuscript; Amélie-Rose Boudjema and Alice Meunier for providing mouse ependymal cells and Isabelle Le Parco for the tracheal tissue; Juliane Da Graça and Simon Herman for technical help; Rémi Le Borgne for help with transmission electron microscopy and for critical reading of the manuscript. We acknowledge

the core imaging facility of Institut Jacques Monod (ImagoSeine facility, member of the France BioImaging infrastructure supported by grant ANR-10-INBS-04 from the French National Research Agency). This work was supported by La Ligue Contre le Cancer and Fondation ARC pour la recherche sur le cancer funding to J.A. N.G. was recipient of a MESRI PhD fellowship from the French Government and a 4th year PhD fellowship from the Fondation pour la Recherche Médicale.

Declaration of interests

The authors declare no competing interests.

Material and Methods

Cell culture

RPE1 cells (hTERT-RPE1, RRID:CVCL_4388) were cultured in DMEM/F-12 medium (ThermoFisher Scientific) supplemented with 10 % fetal calf serum (ThermoFisher Scientific), 100 U/mL penicillin and 100 µg/mL streptomycin (ThermoFisher Scientific). Ciliogenesis was induced by culturing RPE1 cells in medium without serum during 48 hours. HEK 293 cells (kind gift from F. Causeret, Institut Imagine, Paris) were cultured in DMEM medium (ThermoFisher Scientific) supplemented with 10 % fetal calf serum and antibiotics as previously. All cells were kept at 37°C in the presence of 5 % CO₂.

Mouse ependymal cells and tracheal tissue

All experiments were performed in accordance with French Agricultural Ministry and European guidelines for the care and use of laboratory animals. *In vitro* differentiated ependymal cells were a kind gift from A.R. Boudjema and A. Meunier (IBENS, Paris). They were prepared as described previously (Delgehyr et al., 2015; Mercey et al., 2019) from Cen2GFP mice (CB6-Tg(CAG-EGFP/CETN2)3-4Jgg/J, The Jackson Laboratory). The fragment of trachea was obtained from a wild-type mouse of the Swiss background (kindly provided by I. Le Parco, Institut Jacques Monod).

CRISPR/Cas9 editing

LRRCC1 mutant clones were obtained by two different CRISPR/Cas9 strategies. First, RPE1 cells were co-transfected with plasmid px154-1 (U6p-gRNA#1_U6p-gRNA#2_CMVpnCas9-EGFP_SV40p-PuroR-pA with gRNA#1: 5'- AGA ATT CTA CCC TAC CTG CGG - 3' and gRNA#2: 5'- TAA GGT AGT GCT TCC TAC CGG -3') targeting the *LRRCC1* locus in exon

8, and px155-24 (U6p-gRNA#3_U6p-gRNA#4_CMVpnCas9-mCherry_SV40p-PuroR-pA; gRNA#1: 5' - ATC TAC TCG GAA AGC TGA CGG -3' and 5' - GCT TGA GGG CTC AAA TAC CGG - 3') targeting exon 9. Both constructs express the nickase mutant of Cas9 fused to either EGFP or mCherry. Two days after transfection, EGFP- and mCherry-positive cells were sorted by flow cytometry and grown at low concentration. Individual clones were picked after 2 weeks and analyzed by PCR to detect short insertions/deletions. A single clone was obtained (clone 1.1), which was further characterized by genomic sequencing. Both alleles of *LRRCC1* contained deletions (~ 0.6 kb deletion of exon 9 and a ~1.5 kb deletion of exon 8) leading to frameshifts. In a second approach, cells were co-transfected using a mix of 3 CRISPR/Cas9 Knockout Plasmids (sc-413781; Santa Cruz Biotechnology) targeting exons 11 (5' - CTT GTT CTC TTT CTC GAT GAA GG - 3' and 5' - ACT TCT TGC ATT GAA AGA ACA GG - 3') or 12 (5' - CGT GTT AAG CCA GCA GTA TAT GG - 3') of *LRRCC1*, together with the corresponding Homology Directed Repair plasmids carrying a puromycin-resistance cassette (sc-413781-HDR; Santa Cruz Biotechnology), following the recommendations of the manufacturer. Mutant clones were selected by addition of 2 µg/mL puromycin in the culture medium and further screened by immunofluorescence.

Inducible HEK 293 cell lines

LRRCC1 full-length coding sequence was amplified from cDNA clone IMAGE:5272572 (Genbank accession: BC070092.1), corresponding to the longest isoform of *LRRCC1* (NM_033402.5), after correction of a frameshift error by PCR mutagenesis. As N- and C-terminal GFP fusions were not targeted to the centrosome, we inserted the GFP tag within the *LRRCC1* sequence in disordered regions present between the leucine rich repeat and coiled-coil domains, either after amino acid 251 or 402. The fusions were cloned into the pCDNA-5FRT (ThermoFischer Scientific) vector using the Gibson assembly method (Gibson et al.,

2009) and then integrated into the Flp-In-293 cell line using the Flp-In system (ThermoFischer Scientific). Expression of the GFP-LRRCC1 fusions was induced by culturing the Flp-In-293 cell lines overnight in medium supplemented with 1 μ /mL doxycycline (ThermoFischer Scientific).

RNAi

Ready to use double-stranded siRNA LRRCC1-si1 (target sequence: 5'- AAG GAG AAA GAT GGA GAC GAT - 3') (Muto *et al.*, 2008), LRRCC1-si2 (target sequence: 5'- TTA GAT GAC CAA ATT CTA CAA - 3') and control siRNA (AllStars Negative Control) were purchased from Qiagen. siRNAs were delivered into cells using Lipofectamine RNAiMAX diluted in OptiMEM medium (ThermoFisher Scientific). Cells were fixed after 48 hours and processed for immunofluorescence. For RNAi-depletion of ciliated cells, RPE1 cells grown in complete culture medium were treated by RNAi, incubated for 2 days, then submitted to a second round of RNAi. After 8 hours, cells were washed 3 x in PBS then cultured during 24 hours in serum-free medium to induce ciliogenesis.

qRT-PCR

Total RNA extracts were obtained using the Nucleospin RNA kit (Macherey-Nagel) and cDNAs were synthesized using SuperScript III reverse transcriptase (Thermofisher Scientific). qPCR was performed with the GoTaq qPCR Master Mix (Promega) in a LightCycler 480 instrument (Roche) using the primers listed in Table 2. Quantification of relative mRNA levels was performed using CHMP2A and EMC7 as reference genes following the MIQE guidelines (Bustin *et al.*, 2009).

Antibodies

Fragments encoding either aa 671-805 (Ab1) or aa 961-1032 (Ab2) of LRRCC1 (NP_208325.3) were cloned in pGST-Parallel1 and expressed in *Escherichia coli*. The GST-fusion proteins were purified under native conditions using glutathione agarose (ThermoFisher Scientific) and the LRRCC1 fragments were recovered by Tev protease cleavage and dialyzed before rabbit immunization (Covalab). Antibodies were affinity-purified over the corresponding GST-LRRCC1 fusion bound to Affi-Gel 10 resin (Bio-Rad). Other primary and secondary antibodies used in this study are listed in Table 1.

Western blot

For whole-cell extracts, Flp-In-293 cell lines expressing the GFP-LRRCC1 fusions were induced overnight with doxycycline, collected by centrifugation, and resuspended in Western blot sample buffer prior to incubation at 95 °C for 5 minutes. For immunoprecipitation experiments, doxycycline-induced cells expressing LRRCC1 with a GFP inserted after aa 402 were resuspended in lysis buffer (50 mM Tris pH 8, 150 mM NaCl, 1 % NP-40, 0.5 % sodium deoxycholate, 0.1 % SDS) supplemented with 1 mM MgCl₂, 20 µg/mL DNase I (Roche) and a protease inhibitor cocktail (Complete mini, EDTA-free, Roche). After 30 minutes on ice, the lysates were centrifuged at 15 000 g for 10 minutes at 4°C. The supernatants were then incubated with Dynabeads M-280 sheep-anti rabbit magnetic beads (ThermoFischer Scientific) previously incubated with rabbit anti-IgGs, either anti-GFP or anti-HA tag for the control IP (Table 1), and rotated for 3 hours at 4°C. After 3 washes with lysis buffer, immunoprecipitated proteins were recovered by resuspending the beads in sample buffer and heating at 95 °C for 5 minutes. The samples were then run on 4-20% Mini-Protean TGX precast protein gels (Bio-Rad) and transferred onto PVDF membrane using the iBlot 2 blot system (ThermoFischer Scientific). The membranes were blocked and incubated with antibodies following standard

procedures, then visualized using Pierce ECL plus chemiluminescence reagents (ThermoFischer Scientific) on an ImageQuant LAS 4000 camera system (GE Healthcare Life Sciences).

Immunofluorescence

Cells were fixed in cold methanol for 5 minutes at $-20\text{ }^{\circ}\text{C}$, blocked 10 minutes with 3 % BSA (Sigma Aldrich) in PBS containing 0.05 % Tween-20 (PBST-0.05%), then incubated with primary antibodies diluted in PBST-0.05% containing 3 % BSA for 1 hour. After washing 3 x 1 minute in PBST-0.05%, cells were incubated 2 hours with secondary antibodies in PBST-0.05% containing 3 % BSA and 5 $\mu\text{g}/\text{mL}$ Hoechst 33342 (ThermoFischer Scientific), washed in PBST-0.05% as previously, and mounted using Fluorescence Mounting Medium (Agilent). For staining of primary cilia with anti-acetylated tubulin, cells were incubated 2 hours on ice prior to methanol fixation. For quantification of SMO accumulation within cilia, confluent cells cultured during 24 hours in serum-free medium were supplemented with 200 nM SAG (Sigma) diluted in DMSO, or DMSO alone for 24 hours. Cells were then co-stained for SMO and ARL13B to determine the position of the primary cilium. For all experiments involving induction of ciliogenesis by serum deprivation, we verified that cells were arrested in G0 by immunofluorescence staining of Ki67. To visualize centriolar LRRCC1, and to quantify CEP290 centrosomal levels, cells were treated during 1 hour with 5 μM nocodazole prior to fixation. Images were acquired using an Axio Observer Z.1 microscope (Zeiss) equipped with a sCMOS Orca Flash4 LT camera (Hamamatsu) and a 63x objective (Plan Apo, N.A. 1.4). The structured illumination microscopy (SIM) image was acquired on an ELYRA PS.1 (Zeiss) equipped with an EMCCD iXon 885 camera (Andor) and a 63x objective (Plan Apo, N.A. 1.4).

Ultrastructure expansion microscopy

We used the U-ExM protocol described in (Gambarotto et al., 2019) with slight modifications. Cells grown on glass coverslips were incubated in a fresh solution of 1 % acrylamide and 0.7 % formaldehyde diluted in PBS. After incubating 5 hours to overnight at 37 °C, the coverslips were washed with PBS and placed cells down on a drop of 35 µL monomer solution (19.3 % sodium acrylate, 10 % acrylamide, 0.1 % bis-acrylamide in PBS) to which 0.5 % TEMED and 0.1 % ammonium persulfate were added just before use. The coverslips were incubated 5 minutes on ice then 1 hour at 37°C, then transferred to denaturation buffer (200 mM SDS, 200 mM NaCl, 50 mM Tris pH9) for 15 minutes with agitation to detach the gels from the coverslips. The gels were then incubated in denaturation buffer 1.5 hours at 95 °C, washed 2 x 30 minutes in deionized water then incubated overnight in water at room temperature to allow expansion of the gel. The gels were measured at this step to determine the coefficient of expansion. After 2 x 10 minutes in PBS, the gels were cut into smaller pieces then incubated 3 hours at 37 °C with primary antibodies diluted in saturation buffer (3 % BSA, 0.05 % Tween-20 in PBS). The gel fragments were then washed 3 x 10 minutes in PBST-0.1%, incubated 3 h with secondary antibodies and washed in PBST-0.1% as previously. Finally, the gels were incubated 2 x 30 minutes in de-ionized water then left to expand overnight in de-ionized water to regain their maximum size. For U-ExM of mouse tracheal cells, a fragment of WT mouse trachea (kind gift from I. Le Parco, IJM, Paris) was adhered on a poly-lysine coated coverslip then processed as described above with the following modifications: for the first step, the fragment of trachea was incubated overnight to 48 hours in 1 % acrylamide and 0.7 % formaldehyde in PBS; they were placed 15 min on ice prior to the 1-hour incubation at 37 °C and the transfer to denaturation buffer. Note that GFP fluorescence was quenched during U-ExM processing, so the GFP-Cen2 construct expressed in ependymal cells was not detectable in final samples. Gels were imaged on Lab-Tek chamber slides (0.15 mm) coated with poly-

lysine (ThermoFisher Scientific). Images were acquired at room temperature using either a LSM780 confocal microscope (Zeiss) equipped with an oil 63x objective (Plan Apo, N.A. 1.4), or an LSM980 confocal microscope with Airyscan 2 (Zeiss) equipped with an oil 63x objective (Plan Apo, N.A. 1.4).

Image analysis

Protein levels were determined using ImageJ software (Schneider et al., 2012) by measuring the fluorescence intensity in the centrosome or cilium area and subtracting the cytoplasmic background in z-series taken at 0.5- μm interval.

To generate average images of LRRCC1 and C2CD3, U-ExM samples were systematically imaged using Airyscan 2. Only centrioles that were nearly perpendicular to the imaging plane were acquired in order to maximize the resolution in transverse views. Calculating the average image consisted of several steps: cropping out individual centrioles, aligning them, providing reference points, standardizing centrioles using the reference points, and averaging (Supplemental Fig. S2). The cropping was done in ImageJ, and for aligning and providing the reference points a graphical user interface was developed based on Napari (Sofroniew et al., 2020). Centriole alignment: the direction of centriole long axis was selected manually and used to position the centriole vertically. Providing the reference points: 9 points were manually selected to outline the circle of microtubules triplets and the location of the protein of interest. The centriole was also framed in Z dimension with a rectangle. Standardization: the reference points were used to calculate all necessary transformations (rotation, scaling and translation) to map the original image of a centriole to the standard image. Averaging: an average image was calculated for all the successive XY planes of the standardized image stacks. For alignment of tracheal cell centrioles, since the current version of the graphical user interface can only accommodate two channels, the position of the basal foot provided by the γ -tubulin channel

was reported manually in the acetylated tubulin channel using Image J. The images were then processed as before using the manual annotation as a reference point for the basal foot.

For analysis of procentriole position and LRRCC1 location in procentrioles, 3D-reconstructions of diplosomes processed for U-ExM were obtained using IMARIS software (Oxford Instruments).

Electron microscopy

RPE1 cells were grown at confluence before induction of ciliogenesis for 72 hours by serum deprivation. Cells were fixed 30 minutes in 2.5 % glutaraldehyde (Electron Microscopy Sciences), 2 % paraformaldehyde (Electron Microscopy Sciences), 1 mM CaCl₂ in PBS, then washed 3 x 5 minutes in PBS. Samples were then post-fixed during 30 minutes in 1 % Osmium tetroxide (Electron Microscopy Sciences), then washed 3 x 5 minutes in water. Dehydration was performed using graded series of ethanol in water for 5 minutes 30%, 50%, 70%, 90%, 100%, 100%. Resin infiltration was performed by incubating 30 minutes in an Agar low viscosity resin (Agar Scientific Ltd) and EtOH (1:2) mix, then 30 minutes in a resin and EtOH (2:1) mix followed by overnight incubation in pure resin. The resin was then changed and the samples further incubated during 1.5 hours prior to inclusion in gelatin capsules and overnight polymerization at 60 °C. 70 nm sections were obtained using an EM UC6 ultramicrotome (Leica), post-stained in 4 % aqueous uranyl acetate and lead citrate, and observed at 80 kV with a Tecnai12 transmission electron microscope (ThermoFischer Scientific) equipped with a 1K×1K Keen View camera (OSIS).

Statistical analysis

All statistical analyses were performed using the Prism7 for Mac OS X software (GraphPad Software, Inc.). All values are provided as mean ± SD. The number of experimental replicates

and the statistical test used are indicated in the figure legends, and the p values are included when statistically different.

References

- Adams GM, Wright RL, Jarvik JW. 1985. Defective temporal and spatial control of flagellar assembly in a mutant of *Chlamydomonas reinhardtii* with variable flagellar number. *J Cell Biol* **100**:955–964.
- Azimzadeh J. 2021. Evolution of the centrosome, from the periphery to the center. *Current Opinion in Structural Biology* **66**:96–103. doi:10.1016/j.sbi.2020.10.020
- Basquin C, Ershov D, Gaudin N, Vu HT, Louis B, Papon JF, Orfila AM, Mansour S, Rink JC, Azimzadeh J. 2019. Emergence of a Bilaterally Symmetric Pattern from Chiral Components in the Planarian Epidermis. *Dev Cell* **51**:516-525 e5. doi:10.1016/j.devcel.2019.10.021
- Boczek NJ, Hopp K, Benoit L, Kraft D, Cousin MA, Blackburn PR, Madsen CD, Oliver GR, Nair AA, Na J, Bianchi DW, Beek G, Harris PC, Pichurin P, Klee EW. 2018. Characterization of three ciliopathy pedigrees expands the phenotype associated with biallelic *C2CD3* variants. *European Journal of Human Genetics* **26**:1797–1809. doi:10.1038/s41431-018-0222-3
- Bustin SA, Benes V, Garson JA, Hellemans J, Huggett J, Kubista M, Mueller R, Nolan T, Pfaffl MW, Shipley GL, Vandesompele J, Wittwer CT. 2009. The MIQE guidelines: minimum information for publication of quantitative real-time PCR experiments. *Clin Chem* **55**:611–622. doi:10.1373/clinchem.2008.112797
- Clare DK, Magescas J, Piolot T, Dumoux M, Vesque C, Pichard E, Dang T, Duvauchelle B, Poirier F, Delacour D. 2014. Basal foot MTOC organizes pillar MTs required for coordination of beating cilia. *Nature communications* **5**:4888. doi:10.1038/ncomms5888
- Cortés CR, McInerney-Leo AM, Vogel I, Rondón Galeano MC, Leo PJ, Harris JE, Anderson LK, Keith PA, Brown MA, Ramsing M, Duncan EL, Zankl A, Wicking C. 2016.

- Mutations in human C2CD3 cause skeletal dysplasia and provide new insights into phenotypic and cellular consequences of altered C2CD3 function. *Scientific Reports* **6**. doi:10.1038/srep24083
- Delgehyr N, Meunier A, Faucourt M, Grau MB, Strehl L, Janke C, Spassky N. 2015. Ependymal cell differentiation, from monociliated to multiciliated cells. *Methods in Cell Biology* **127**:19–35. doi:10.1016/bs.mcb.2015.01.004
- Feldman JL, Geimer S, Marshall WF. 2007. The mother centriole plays an instructive role in defining cell geometry. *PLoS Biol* **5**:e149.
- Gambarotto D, Zwettler FU, le Guennec M, Schmidt-Cernohorska M, Fortun D, Borgers S, Heine J, Schloetel JG, Reuss M, Unser M, Boyden ES, Sauer M, Hamel V, Guichard P. 2019. Imaging cellular ultrastructures using expansion microscopy (U-ExM). *Nature Methods* **16**:71–74. doi:10.1038/s41592-018-0238-1
- Garcia-Gonzalo FR, Reiter JF. 2017. Open Sesame: How Transition Fibers and the Transition Zone Control Ciliary Composition. *Cold Spring Harb Perspect Biol* **9**. doi:10.1101/cshperspect.a028134
- Geimer S, Melkonian M. 2005. Centrin scaffold in *Chlamydomonas reinhardtii* revealed by immunoelectron microscopy. *Eukaryot Cell* **4**:1253–1263.
- Geimer S, Melkonian M. 2004. The ultrastructure of the *Chlamydomonas reinhardtii* basal apparatus: identification of an early marker of radial asymmetry inherent in the basal body. *J Cell Sci* **117**:2663–2674.
- Gibson DG, Young L, Chuang RY, Venter JC, Hutchison CA, Smith HO. 2009. Enzymatic assembly of DNA molecules up to several hundred kilobases. *Nature Methods* **6**:343–345. doi:10.1038/nmeth.1318

- Goodrich L v., Johnson RL, Milenkovic L, McMahon JA, Scott MP. 1996. Conservation of the hedgehog/patched signaling pathway from flies to mice: Induction of a mouse patched gene by Hedgehog. *Genes and Development* **10**:301–312. doi:10.1101/gad.10.3.301
- Gupta GD, Coyaud É, Gonçalves J, Mojarad BA, Liu Y, Wu Q, Gheiratmand L, Comartin D, Tkach JM, Cheung SWT, Bashkurov M, Hasegan M, Knight JD, Lin ZY, Schueler M, Hildebrandt F, Moffat J, Gingras AC, Raught B, Pelletier L. 2015. A Dynamic Protein Interaction Landscape of the Human Centrosome–Cilium Interface. *Cell* **163**:1484–1499. doi:10.1016/j.cell.2015.10.065
- Izquierdo D, Wang WJ, Uryu K, Tsou MF. 2014. Stabilization of cartwheel-less centrioles for duplication requires CEP295-mediated centriole-to-centrosome conversion. *Cell Rep* **8**:957–965. doi:10.1016/j.celrep.2014.07.022
- Kim J, Krishnaswami SR, Gleeson JG. 2008. CEP290 interacts with the centriolar satellite component PCM-1 and is required for Rab8 localization to the primary cilium. *Hum Mol Genet* **17**:3796–3805. doi:10.1093/hmg/ddn277
- Kumar D, Reiter J. 2021. How the centriole builds its cilium: of mothers, daughters, and the acquisition of appendages. *Current Opinion in Structural Biology*. doi:10.1016/j.sbi.2020.09.006
- LeGuennec M, Klena N, Aeschlimann G, Hamel V, Guichard P. 2021. Overview of the centriole architecture. *Current Opinion in Structural Biology* **66**:58–65. doi:10.1016/j.sbi.2020.09.015
- Lin J, Heuser T, Song K, Fu X, Nicastro D. 2012. One of the Nine Doublet Microtubules of Eukaryotic Flagella Exhibits Unique and Partially Conserved Structures. *PLoS ONE* **7**. doi:10.1371/journal.pone.0046494

- Mercey O, al Jord A, Rostaing P, Mahuzier A, Fortoul A, Boudjema AR, Faucourt M, Spassky N, Meunier A. 2019. Dynamics of centriole amplification in centrosome-depleted brain multiciliated progenitors. *Scientific Reports* **9**:1–11. doi:10.1038/s41598-019-49416-2
- Meunier A, Azimzadeh J. 2016. Multiciliated cells in animals. *Cold Spring Harbor Perspectives in Biology* **8**. doi:10.1101/cshperspect.a028233
- Muto Y, Yoshioka T, Kimura M, Matsunami M, Saya H, Okano Y. 2008. An evolutionarily conserved leucine-rich repeat protein CLERC is a centrosomal protein required for spindle pole integrity. *Cell Cycle* **7**:2738–2748.
- Nachury M v. 2018. The molecular machines that traffic signaling receptors into and out of cilia. *Current Opinion in Cell Biology*. doi:10.1016/j.ceb.2018.03.004
- Nommick A, Boutin C, Rosnet O, Bazellières E, Thomé V, Loiseau E, Viallat A, Kodjabachian L. 2021. Lrrcc1 and Ccdc61 are conserved effectors of multiciliated cell function. *bioRxiv* 2021.01.30.428946. doi:10.1101/2021.01.30.428946
- Ooi J. 2015. Mutations in C2CD3 cause oral-facial-digital syndrome through deregulation of centriole length. *Clinical Genetics* **87**:328–329. doi:10.1111/cge.12545
- Reiter JF, Leroux MR. 2017. Genes and molecular pathways underpinning ciliopathies. *Nat Rev Mol Cell Biol* **18**:533–547. doi:10.1038/nrm.2017.60
- Rohatgi R, Milenkovic L, Scott MP. 2007. Patched1 regulates hedgehog signaling at the primary cilium. *Science* **317**:372–376. doi:10.1126/science.1139740
- Romani M, Micalizzi A, Valente EM. 2013. Joubert syndrome: congenital cerebellar ataxia with the molar tooth. *Lancet neurology* **12**:894–905. doi:10.1016/S1474-4422(13)70136-4
- Schneiter M, Halm S, Odriozola A, Mogel H, Rička J, Stoffel MH, Zuber B, Frenz M, Tschanz SA. 2021. Multi-scale alignment of respiratory cilia and its relation to mucociliary function. *Journal of Structural Biology* **213**:107680. doi:10.1016/j.jsb.2020.107680

- Shaheen R, Szymanska K, Basu B, Patel N, Ewida N, Faqeih E, al Hashem A, Derar N, Alsharif H, Aldahmesh MA, Alazami AM, Hashem M, Ibrahim N, Abdulwahab FM, Sonbul R, Alkuraya H, Alnemer M, al Tala S, Al-Husain M, Morsy H, Seidahmed MZ, Meriki N, Al-Owain M, AlShahwan S, Tabarki B, Salih MA, Ciliopathy W, Faquih T, El-Kalioby M, Ueffing M, Boldt K, Logan C v, Parry DA, al Tassan N, Monies D, Megarbane A, Abouelhoda M, Halees A, Johnson CA, Alkuraya FS. 2016. Characterizing the morbid genome of ciliopathies. *Genome biology* **17**:242. doi:10.1186/s13059-016-1099-5
- Sharma A, Olieric N, Steinmetz MO. 2021. Centriole length control. *Current Opinion in Structural Biology* **66**:89–95. doi:10.1016/j.sbi.2020.10.011
- Silflow CD, LaVoie M, Tam LW, Tousey S, Sanders M, Wu W, Borodovsky M, Lefebvre PA. 2001. The Vfl1 Protein in *Chlamydomonas* localizes in a rotationally asymmetric pattern at the distal ends of the basal bodies. *J Cell Biol* **153**:63–74.
- Singla V, Romaguera-Ros M, Garcia-Verdugo JM, Reiter JF. 2010. *Odf1*, a human disease gene, regulates the length and distal structure of centrioles. *Dev Cell* **18**:410–424.
- Sofroniew N, Lambert T, Evans K, Nunez-Iglesias J, Yamauchi K, Solak AC, Bokota G, ziyangczi, Buckley G, Winston P, Tung T, Pop DD, Hector, Freeman J, Bussonnier M, Boone P, Royer L, Har-Gil H, Axelrod S, Rokem A, Bryant, Kiggins J, Huang M, Vemuri P, Dunham R, Manz T, jakirkham, Wood C, Siqueira A de, Chopra B. 2020. napari/napari: 0.3.8rc1. doi:10.5281/ZENODO.4046812
- Takao D, Yamamoto S, Kitagawa D. 2019. A theory of centriole duplication based on self-organized spatial pattern formation. *Journal of Cell Biology* **218**:3537–3547. doi:10.1083/JCB.201904156
- Thauvin-Robinet C, Lee JS, Lopez E, Herranz-Pérez V, Shida T, Franco B, Jegu L, Ye F, Pasquier L, Loget P, Gigot N, Aral B, Lopes CAM, St-Onge J, Bruel AL, Thevenon J, González-Granero S, Alby C, Munnich A, Vekemans M, Huet F, Fry AM, Saunier S,

- Rivière JB, Attié-Bitach T, Garcia-Verdugo JM, Faivre L, Mégarbané A, Nachury M v. 2014. The oral-facial-digital syndrome gene C2CD3 encodes a positive regulator of centriole elongation. *Nature Genetics* **46**:905–911. doi:10.1038/ng.3031
- Tsai JJ, Hsu W bin, Liu JH, Chang CW, Tang TK. 2019. CEP120 interacts with C2CD3 and Talpid3 and is required for centriole appendage assembly and ciliogenesis. *Scientific Reports* **9**. doi:10.1038/s41598-019-42577-0
- Vaughan S, Gull K. 2016. Basal body structure and cell cycle-dependent biogenesis in *Trypanosoma brucei*. *Cilia*. doi:10.1186/s13630-016-0023-7
- Vorobjev IA, Chentov YS. 1980. The ultrastructure of centriole in mammalian tissue culture cells. *Cell biology international reports* **4**:1037–1044. doi:10.1016/0309-1651(80)90177-
- Wang Lei, Failler M, Fu W, Dynlacht BD. 2018. A distal centriolar protein network controls organelle maturation and asymmetry. *Nature Communications* **9**. doi:10.1038/s41467-018-06286-y
- Wang L, Failler M, Fu W, Dynlacht BD. 2018. A distal centriolar protein network controls organelle maturation and asymmetry. *Nature communications* **9**:3938. doi:10.1038/s41467-018-06286-y
- Yamamoto S, Kitagawa D. 2021. Emerging insights into symmetry breaking in centriole duplication: updated view on centriole duplication theory. *Current Opinion in Structural Biology*. doi:10.1016/j.sbi.2020.08.005
- Yang TT, Chong WM, Wang WJ, Mazo G, Tanos B, Chen Z, Tran TMN, Chen Y de, Weng RR, Huang CE, Jane WN, Tsou MFB, Liao JC. 2018. Super-resolution architecture of mammalian centriole distal appendages reveals distinct blade and matrix functional components. *Nature Communications* **9**:1–11. doi:10.1038/s41467-018-04469-1
- Ye X, Zeng H, Ning G, Reiter JF, Liu A. 2014. C2cd3 is critical for centriolar distal appendage assembly and ciliary vesicle docking in mammals. *Proceedings of the National Academy*

of Sciences of the United States of America **111**:2164–2169.

doi:10.1073/pnas.1318737111

Yubuki N, Leander BS. 2013. Evolution of microtubule organizing centers across the tree of eukaryotes. *The Plant journal: for cell and molecular biology* **75**:230–244.

doi:10.1111/tpj.12145

Zhang D, Aravind L. 2012. Novel transglutaminase-like peptidase and C2 domains elucidate the structure, biogenesis and evolution of the ciliary compartment. *Cell Cycle* **11**:3861–

3875. doi:10.4161/cc.22068

Figure legends

Figure 1. LRRCC1 is localized in a rotationally asymmetric manner at the distal end of centrioles in the human centrosome. **a)** LRRCC1 localization in non-treated RPE1 cells (left) or in cells treated with nocodazole to disperse the pericentriolar satellites (right). LRRCC1 (Ab2, yellow), γ -tubulin (PCM, magenta) and DNA (cyan). Bar, 5 μm (insets, 2 μm). **b)** Longitudinal view of centrioles and procentrioles in the duplicating centrosome of an RPE1 cell analyzed by U-ExM. LRRCC1 (Ab2, yellow), acetylated tubulin (magenta). Bar, 0.5 μm . **c)** Centrioles from WT RPE1 cells as seen from the distal end. LRRCC1 (Ab2, yellow), acetylated tubulin (magenta). Bar, 0.2 μm . **d)** Workflow for calculating the average staining from 3D-reconstructed individual centrioles generated from confocal z-stacks. The brightest part of LRRCC1 signal was used as a reference point to align the centrioles. **e)** Average LRRCC1 staining obtained from 34 individual centrioles viewed from the distal end, in transverse and longitudinal views. A diagram representing the average pattern in transverse view is also included.

Figure 2. The LRRCC1 rotationally asymmetric pattern is conserved in mouse MCCs. **a)** Centrioles in the cytoplasm of mouse ependymal cells differentiating *in vitro* analyzed by U-ExM, in longitudinal and transverse view. *Lrrcc1* (Ab2, yellow), γ -tubulin (basal foot cap, cyan) and acetylated tubulin (magenta). Of note, γ -tubulin was also detected in the proximal lumen of centrioles. Bar, 0.2 μm . **b)** Procentrioles assembling via the centriolar (right) or the deuterosome pathway (left and center) in ependymal cells. *Lrrcc1* (Ab2, yellow), acetylated tubulin (magenta). Bar, 0.2 μm . **c)** Transverse view of centrioles docked at the apical membrane in fully differentiated mouse tracheal cells, viewed from the distal end. *Lrrcc1* (Ab2, yellow), γ -tubulin (cyan) and acetylated tubulin (magenta). Bar, 0.2 μm . **d)** Average image generated

from 35 individual centrioles from mouse trachea, viewed from the distal end, shown in transverse and longitudinal views. The position of the basal foot (cyan dotted line) stained with γ -tubulin was used as a reference point to align the centrioles. A diagram of the average pattern in transverse view is shown, in which the direction of ciliary beat (Schneiter et al., 2021) is represented by a dotted arrow and the basal foot axis by a green line. Triplets are numbered counterclockwise from the LRRCC1 signal.

Figure 3. The conservation of centriole rotational asymmetry in humans is not linked to stereotypical patterns of procentriole position and orientation. **a)** Early stage of procentriole assembly stained for LRRCC1 (Ab2, yellow), SAS-6 (cyan) and acetylated tubulin (magenta) in a HEK 293 cell. The brightness of the acetylated tubulin labelling was increased in the inserts. Bar, 0.1 μ m. **b)** Successive stages of centriole elongation in HEK 293 cells stained for LRRCC1 (Ab2, yellow) and acetylated tubulin (magenta). Bar, 0.1 μ m. **c)** Location of LRRCC1 in the procentrioles (top panels) and position of the procentriole relative to its parent centriole polarity (bottom panels), in RPE1 and HEK 293 centrioles analyzed by U-ExM. For each diplosome, the angle between LRRCC1 in the procentriole and the centriole long axis (top panels), or between the procentriole and LRRCC1 in the centriole (bottom panels) was measured. The number of diplosomes analyzed is indicated. p values are indicated when statistically different from a random distribution (χ^2 -test).

Figure 4. LRRCC1 is required for ciliary assembly and signaling. **a)** Left: LRRCC1 staining (Ab2) of WT or LRRCC1-deficient RPE1 cells obtained by CRISPR/Cas9 editing (clones 1.1, 1.2 and 1.9). Bar, 2 μ m. Right: quantification of fluorescence intensity. Bars, mean \pm SD, 3 independent experiments. p values are provided when statistically significant from the corresponding control (One-way ANOVA). **b)** Percentage of ciliated cells in WT or LRRCC1-

deficient serum-deprived cells. Bars, mean \pm SD, ≥ 331 cells from 4 independent experiments for each condition. p values are provided when statistically significant from the corresponding control (One-way ANOVA). **c**) Percentage of ciliated cells in serum deprived RPE1 cells treated with control or LRRCC1 siRNAs. Bars, mean \pm SD, ≥ 83 cells from 3 independent experiments for each condition. p values are provided when statistically significant from the corresponding control (One-way ANOVA). **d**) Left: SMO (yellow) accumulation at primary cilia (ARL13B, magenta) following SAG-induction of the Hedgehog pathway, in WT or CRISPR RPE1 cells. Bar, 2 μ m. Right: quantification of ciliary SMO expressed as a percentage of the SAG-treated WT mean. Bars, mean \pm SD, 3 independent experiments. p values are provided when statistically significant from the corresponding control (One-way ANOVA). **e**) Ciliary SMO expressed as a percentage of the SAG-induced WT mean in RPE1 cells treated with control or LRRCC1 siRNAs. Bars, mean \pm SD, 3 independent experiments. p values are provided when statistically significant from the corresponding control (One-way ANOVA).

Figure 5. Depleting LRRCC1 induces defects in centriole structure. **a**) Centriole length in mother (MC) and daughter (DC) centrioles analyzed by U-ExM in WT or LRRCC1-deficient clones (1.1 and 1.9). Left: Centrioles were stained for acetylated tubulin (magenta) and CEP164 (yellow) to measure centriole length (arrows). Bar, 0.5 μ m. Right: Quantification from 3 independent experiments. p values are provided when statistically significant from the corresponding control (One-way ANOVA). **b**) Transmission electron microscopy view of centrioles in WT and CRISPR (clone 1.9) RPE1 cells. Note that the two 1.9 centrioles are from the same cell. Bar, 0.5 μ m. **c**) Examples of normal DAs, DAs with abnormal morphology (white arrowhead: abnormal spacing between consecutive DAs; cyan arrowhead: abnormal DA shape) or missing DAs (grey arrowhead) analyzed by U-ExM. Bar, 1 μ m. **d**) Percentages of centrioles presenting DA defects in WT or CRISPR RPE1 cells. ≥ 87 centrioles from 8

independent experiments for each condition. p values are provided when statistically significant from the corresponding control (Two-way ANOVA). **e)** Percentages of centrioles presenting DA defects in WT or CRISPR HEK 293 (clone 21) cells. ≥ 40 centrioles from 4 independent experiments for each condition. p values are provided when statistically significant from the corresponding control (Two-way ANOVA).

Figure 6. C2CD3 localizes asymmetrically at the distal end of centrioles and is affected by LRRCC1-depletion. **a)** C2CD3 levels at the centrosome of WT or LRRCC1 CRISPR RPE1 clones. Bars, mean \pm SD, 3 independent experiments. p values are provided when statistically significant from the corresponding control (One-way ANOVA). **b)** C2CD3 levels at the centrosome in RPE1 cells treated with control or LRRCC1 siRNAs. Bars, mean \pm SD, 3 independent experiments. p values are provided when statistically significant from the corresponding control (One-way ANOVA). **c)** Longitudinal view of a centriole analyzed by U-ExM and stained for C2CD3 (yellow) and acetylated tubulin (magenta). Bar, 0.2 μ m. **d)** Centrioles from WT RPE1 cells as viewed from the distal end. C2CD3 (yellow), acetylated tubulin (magenta). Bar, 0.2 μ m. **e)** Average C2CD3 images obtained from 33 individual centrioles from WT RPE1 cells viewed from the distal end, in transverse views. These images were generated using either the central region of the C-shaped staining ('Shape') or the region where the C2CD3 signal is closest to the triplet wall after correction of centriole orientation ('Position') as a reference point to align the individual centrioles. **f)** Centrioles from LRRCC1-deficient cells (CRISPR clones 1.1 and 1.9) in transverse section as viewed from the distal end. C2CD3 (yellow), acetylated tubulin (magenta). Bar, 0.2 μ m. **g)** Average C2CD3 images obtained from 51 (clone 1.1) or 20 (clone 1.9) individual centrioles from LRRCC1-deficient RPE1 cells viewed from the distal end, in transverse views.

Figure 7. C2CD3 and LRRCC1 partially colocalize at the distal end of centrioles. **a)** RPE1 centrioles processed for U-ExM and stained for LRRCC1 (Ab2, yellow), C2CD3 (cyan) and acetylated tubulin (magenta). Bar, 0.1 μm . **b)** Model showing the possible location of LRRCC1 and C2CD3 relative to each other within human centrioles. Right panel: diagram showing the respective positions of the acorn (Geimer and Melkonian, 2004) and Vfl1p (Silflow et al., 2001) in *C. reinhardtii*. The direction of the flagellar beat is indicated by a dotted arrow, and the distal striated fiber is in grey. **c)** Evolution of the roles played by Vfl1p/LRRCC1 proteins and associated rotationally asymmetric centriolar substructures. In *C. reinhardtii*, Vfl1p is required for proper ciliary assembly (1), as well as for the formation of fibers and microtubular roots (2) that control the position of centrioles and procentrioles (3), and overall cellular organization (Adams et al., 1985; Silflow et al., 2001). In human cells, LRRCC1 and C2CD3 are required for primary cilium assembly (1) - this study and (Thauvin-Robinet et al., 2014; Ye et al., 2014) - and a role in asymmetric anchoring of centrosome or cytoskeletal components might also be conserved (2).

Supplemental material

Fig. S1 provides additional data on LRRCC1 expression in CRISPR clones and RNAi-treated cells. **Fig. S2** presents the image analysis pipeline for generating the average images of LRRCC1 and C2CD3 staining. **Fig. S3** shows the quantification of the DA component CEP164, and the distal centriole components CEP290 and OFD1, at the centrosome of RPE1 cells depleted from LRRCC1 by CRISPR or RNAi. **Fig. S4** shows that C2CD3 is not co-immunoprecipitated with GFP-LRRCC1.

Supplemental Figure Legends

Figure S1. Characterization of LRRCC1 expression in CRISPR or RNAi-treated cells. a) Western blot analysis of over-expressed GFP-LRRCC1 fusions using anti-LRRCC1 (Ab2) or anti-GFP antibodies. Cell lysates were obtained from HEK 293 cells induced (+ Dox) or not (- Dox) to express GFP-LRRCC1 fusions in which the GFP is inserted either after aa 251 or 402. The load represents the same number of cells for all conditions. The different samples were deposited in duplicate and the labeling with the two antibodies was performed in parallel and the exposed in the same way. Note that GFP fusions are already detected in the non-induced samples, whereas the endogenous protein (expected size ~120 kDa) is not. **b)** LRRCC1 localization in non-treated RPE1 cells (left), or in cells treated with nocodazole to disperse the pericentriolar satellites (right). Anti-LRRCC1 (Ab1, yellow), γ -tubulin (magenta) and DNA (cyan). Bar, 5 μ m (insets, 2 μ m). **c)** LRRCC1 centrosomal levels in CRISPR mutant cells stained with Ab1. Bars, mean \pm SD, 3 independent experiments. p values are provided when statistically significant from the corresponding control (One-way ANOVA). **d)** qRT-PCR analysis of *LRRCC1* expression in the CRISPR clones. mRNA levels are expressed as percentages of RPE1 control values. Bars, mean \pm SD, 3 independent experiments. p values are provided when statistically significant from the corresponding control (One-way ANOVA). **e)** LRRCC1 centrosomal levels in nocodazole-treated control or CRISPR mutant RPE1 cells stained with Ab2. Bars, mean \pm SD, 3 independent experiments. p values are provided when statistically significant from the corresponding control (One-way ANOVA). **f)** LRRCC1 centrosomal levels in RPE1 cells treated with either control or LRRCC1 siRNA and stained with Ab1. Bars, mean \pm SD, 3 independent experiments. p values are provided when statistically significant from the corresponding control (One-way ANOVA). **g)** qRT-PCR analysis of *PTCH1* expression in serum-deprived RPE1 cells treated with control or LRRCC1

siRNAs and with SAG or DMSO (expressed as percentages of the DMSO-treated control). Bars, mean \pm SD, 2 independent experiments. **h)** LRRCC1 centrosomal levels in control or CRISPR edited (clone 21) HEK 293 cells stained with Ab1. Bars, mean \pm SD, 3 independent experiments. p values are provided when statistically significant from the corresponding control (One-way ANOVA). **i)** Centriole and procentriole in a RPE1 cell processed for U-ExM and stained with anti-LRRCC1 (Ab1, yellow) and acetylated tubulin (magenta). Bar, 0.2 μ m.

Figure S2. Pipeline for generating average protein maps. a) Examples of verticalized and annotated centrioles (one centriole per row). (A, B): XY cross section taken at z-position, at which the XY reference points have been provided. (C, D): YZ cross section taken at x-position, at which the centriole center has been calculated (from XY reference points). The mentioned z-position and x-position are shown with blue lines; red lines in the right columns show the Z reference points: the top and the bottom of the provided rectangular frame. Note that the centrioles significantly differ in their diameters and lengths (in pixels), and that the protein of interest is not always positioned in the same manner. **b)** Examples of standardized images. (A, B): XY cross section taken at a fixed z-position slightly under the top of the Z reference rectangle (note that this position is slightly different from that at which the XY reference points were provided). (C, D): YZ cross section taken in the middle of the XY plane (the standardized centrioles are always placed with their centers in the middle of the image). The mentioned z-position and x-position are shown with blue lines; red shapes outline a cylinder with the target standard sizes: diameter 0.8 μ m (4 x expanded 0.2 μ m), length 3 μ m; image calibration 0.01 μ m/pixel (all three parameters are tunable). Note that in contrast to the centrioles in a), the diameter and the length of the standardized centrioles and the position of the protein of interest in the XY plane are very similar.

Figure S3. Quantification of DA or distal centriole components in LRRCC1-deficient cells. Centrosomal levels of CEP164 (a, d), CEP290 (b, e), and OFD1 (c, f) in (a-c) RPE1 CRISPR clones and (d-f) RNAi-treated RPE1 cells. Bars, mean \pm SD, 3 independent experiments. p values are provided when statistically significant from the corresponding control (One-way ANOVA).

Figure S4. LRRCC1 does not interact directly with GFP-C2CD3. Co-immunoprecipitation experiments from a lysate of HEK 293 cells expressing LRRCC1 with GFP inserted after aa 402. Anti-GFP or control (anti-HA tag) antibodies were used for immunoprecipitation, and Western blot was performed using either anti-GFP or anti-C2CD3 (RRID:AB_2718714) antibodies. Lys = lysate; SN = supernatant; IP = immunoprecipitation. The amount of lysate loaded on the gel represents 4% of the amount used for the immunoprecipitation.

Figure 1

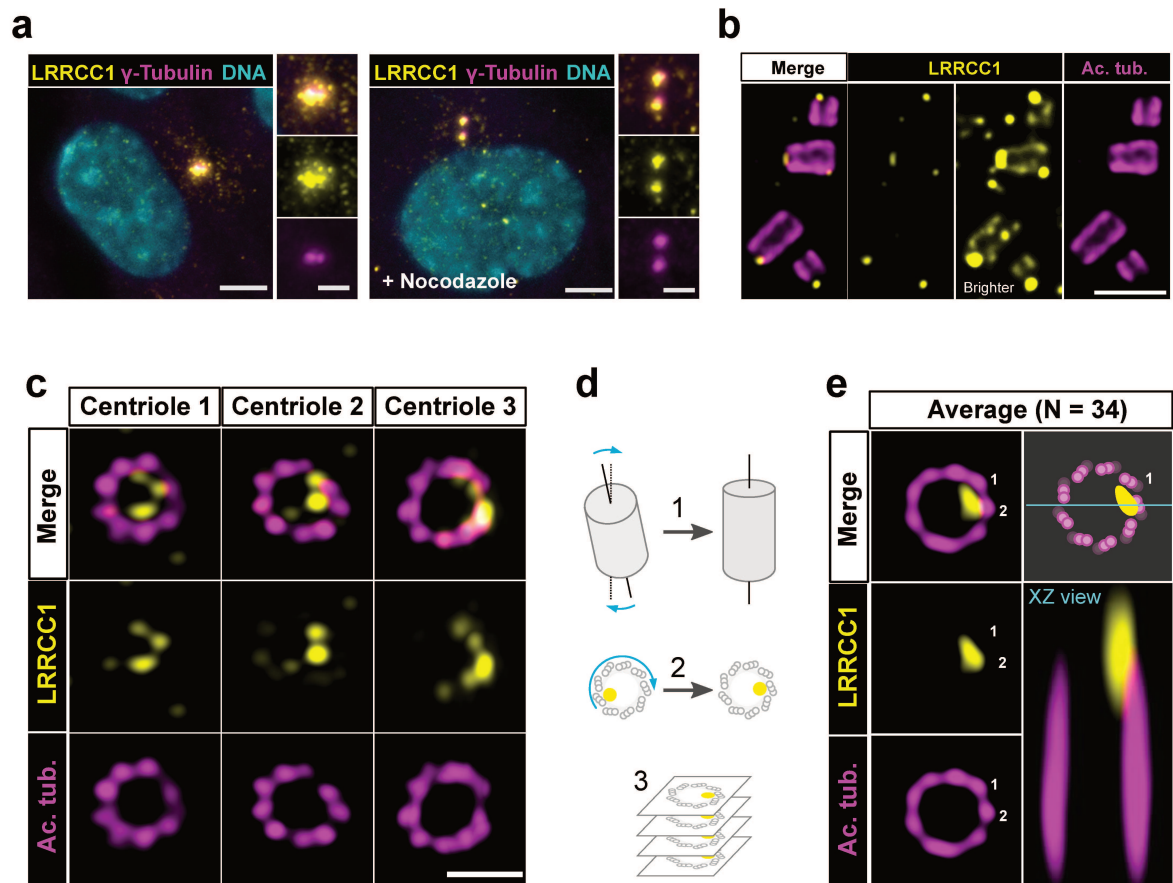


Figure 2

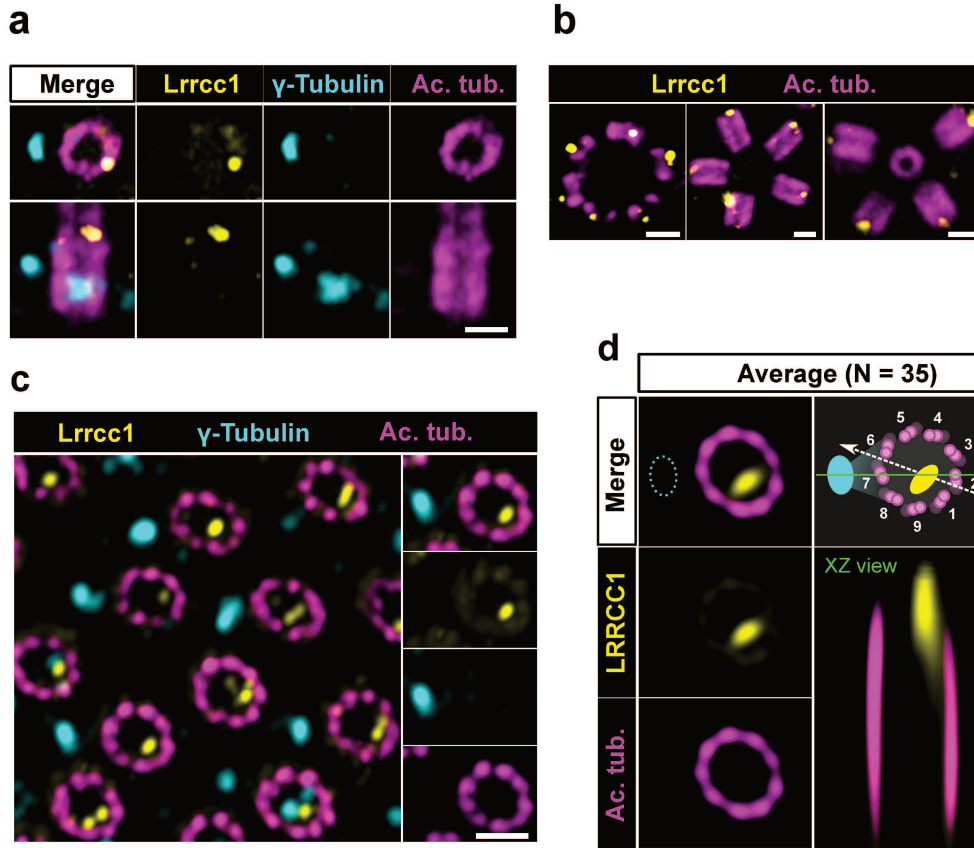


Figure 3

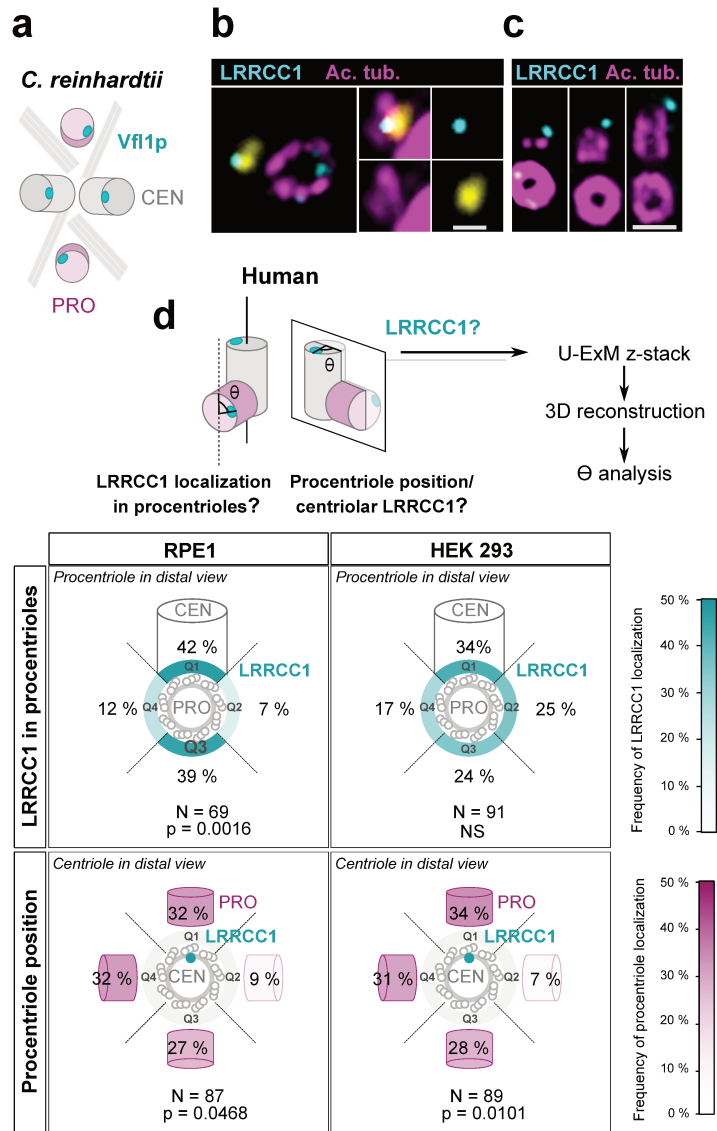


Figure 4

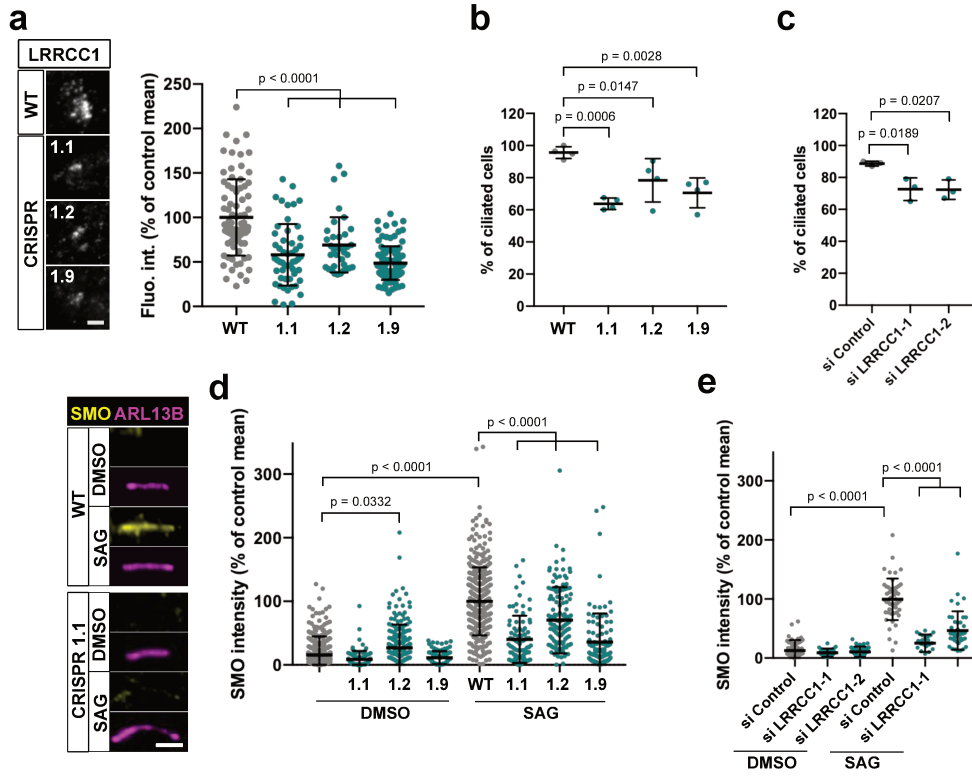


Figure 5

Gaudin *et al.*

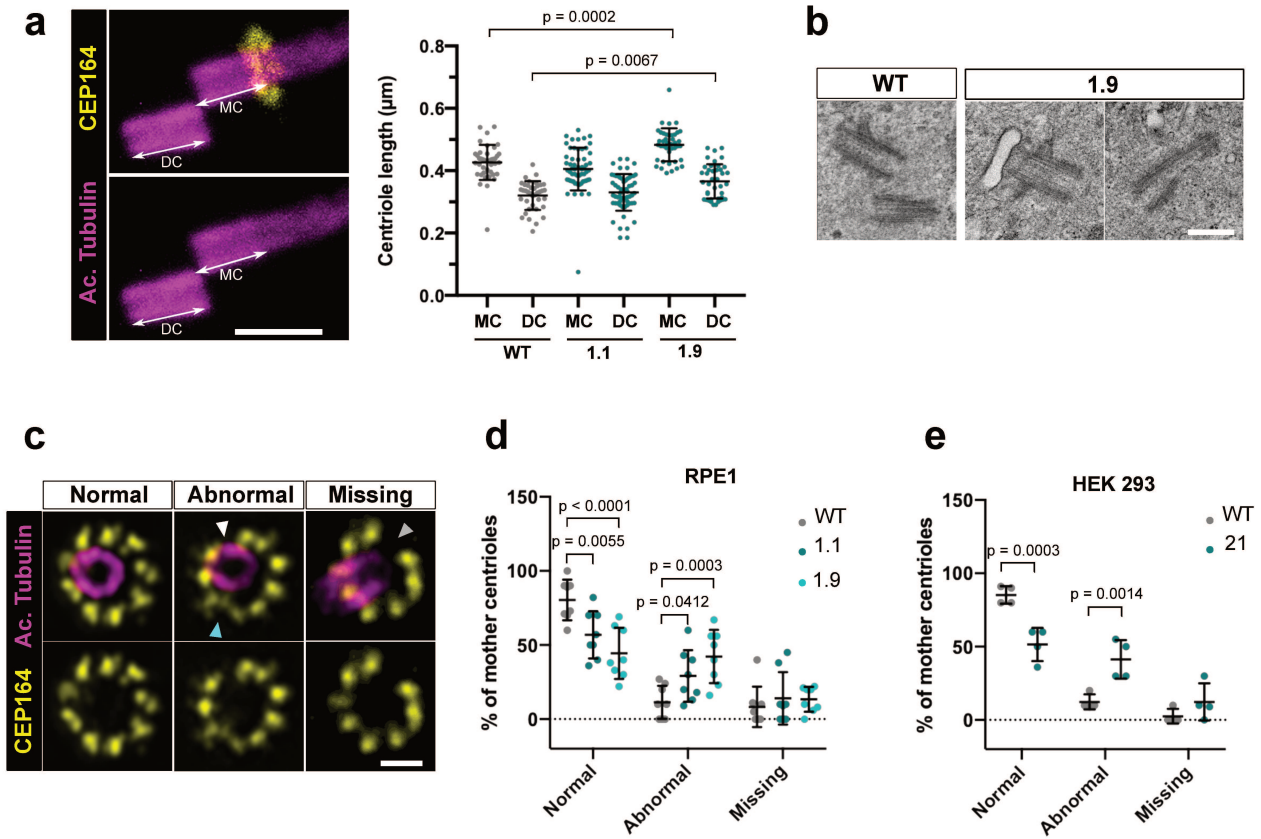


Figure 6

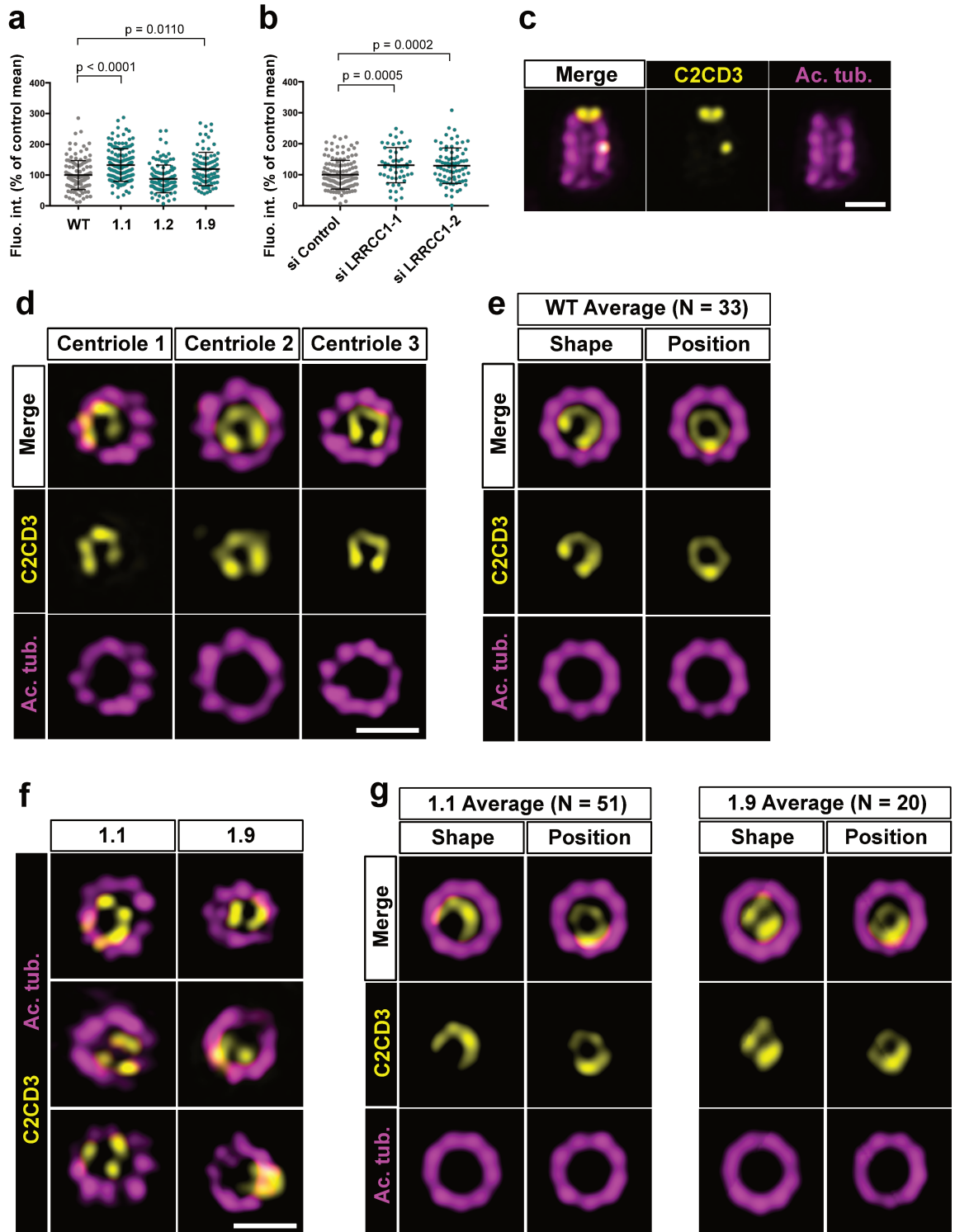


Figure 7

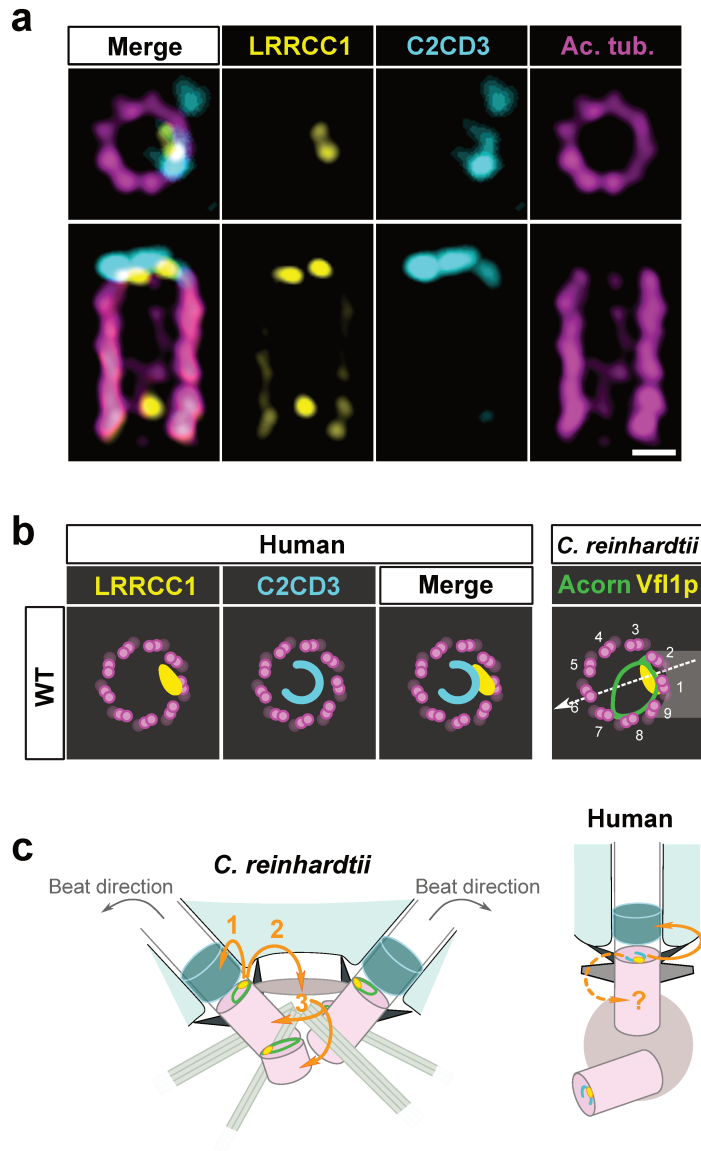


Figure S1

Gaudin *et al.*

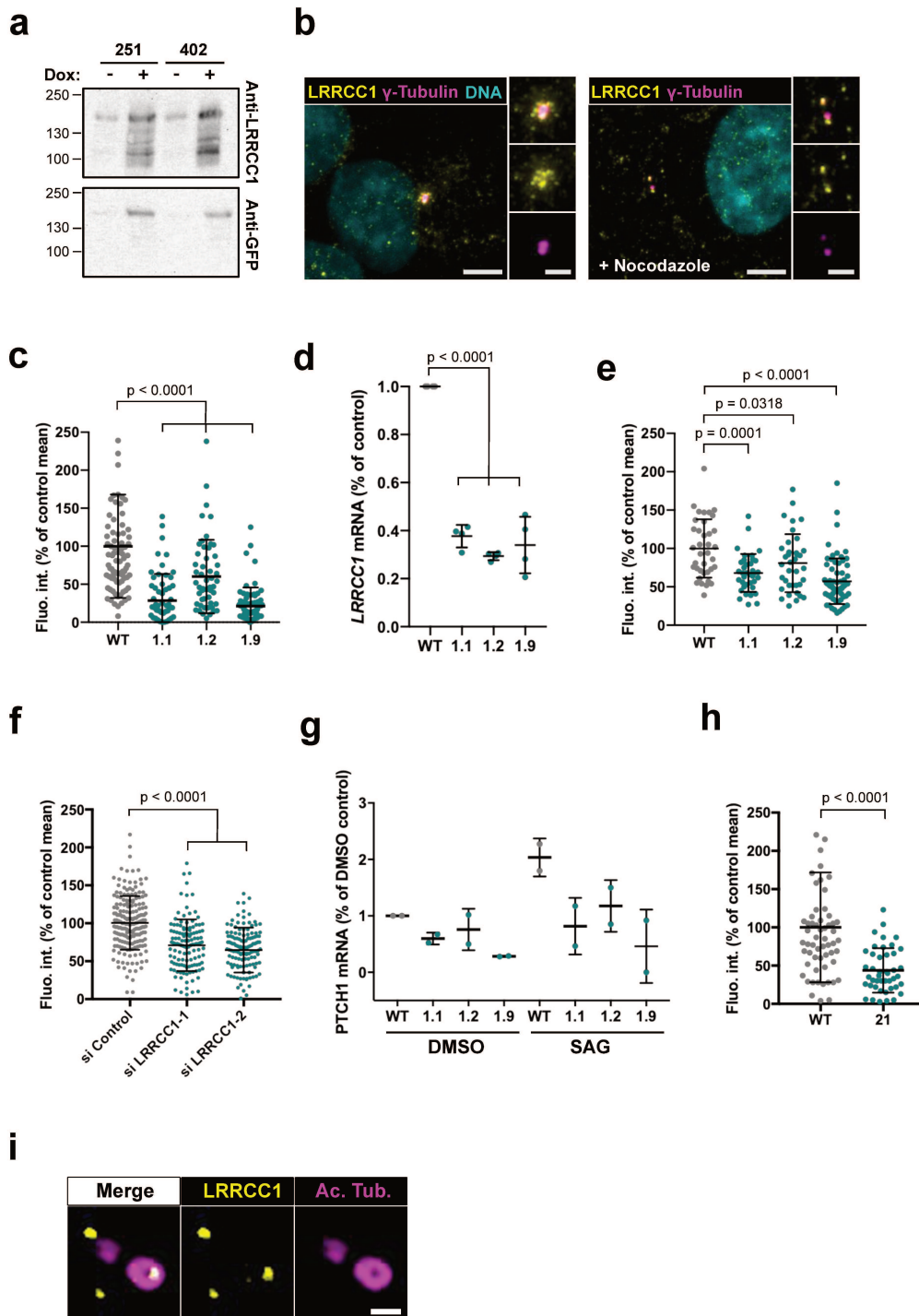
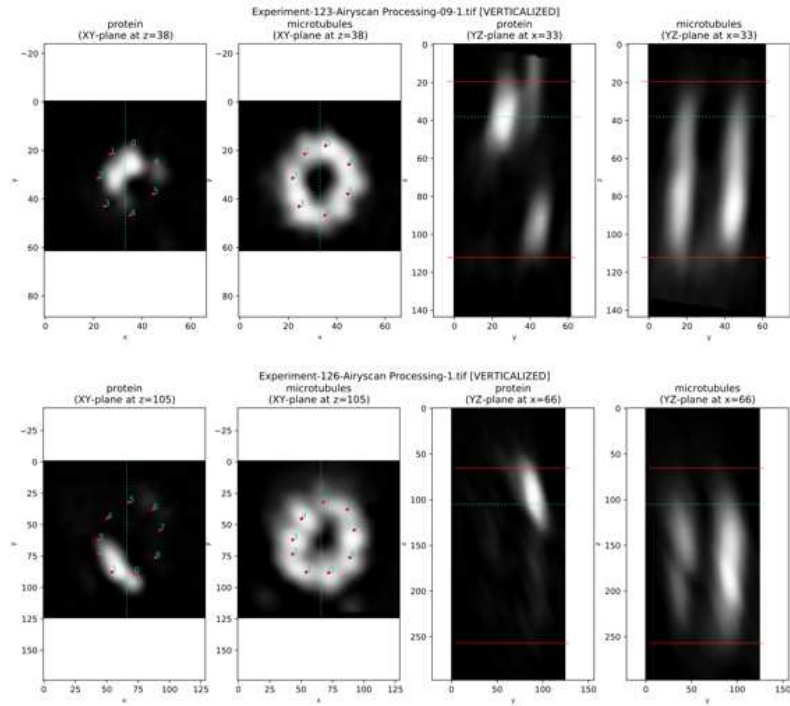


Figure S2

Gaudin *et al.*

a



b

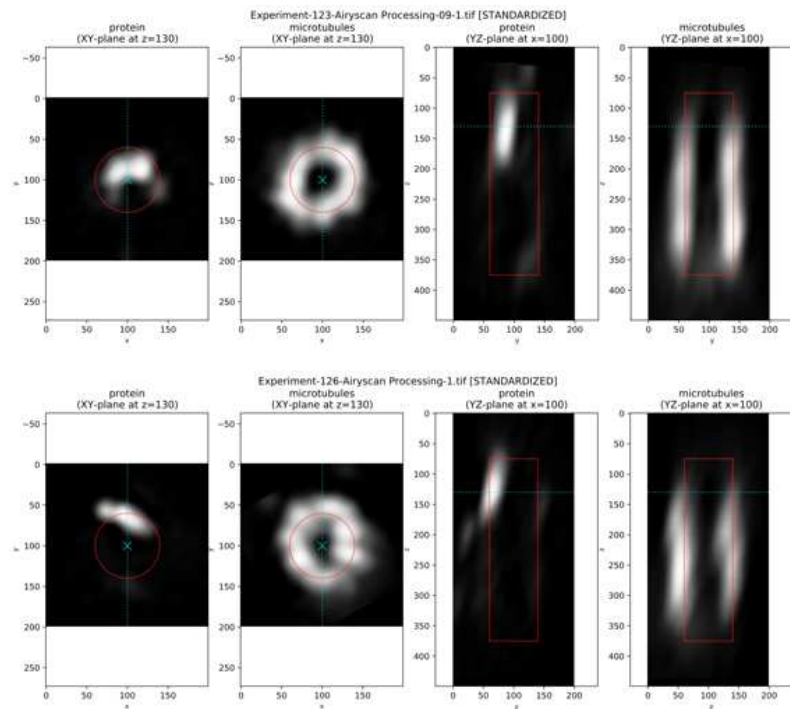


Figure S3

Gaudin *et al.*

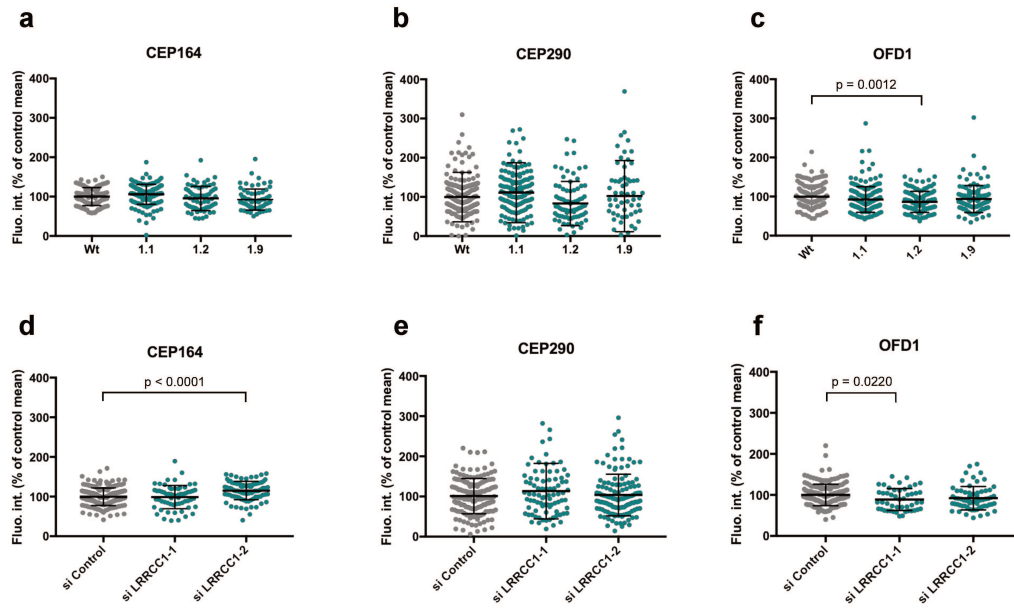


Figure S4

Gaudin *et al.*

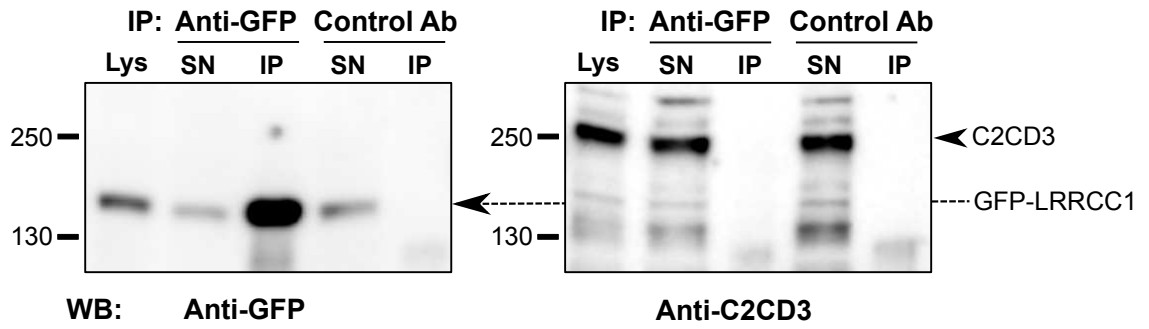


Table 1. Antibodies used in this study.

Antibody	Dilution IF	Dilution U-ExM	Dilution WB	RRID Identifier	Source	Reference
Primary antibodies						
Goat anti-ARL13B	1:100	/	/	RRID:AB_2058502	Santa Cruz Biotechnology	sc-102318
Guinea pig anti-alpha tubulin AA344 monobody	/	1:500	/		Geneva antibody facility	scFv-S11B
Guinea pig anti-beta tubulin AA345 monobody	/	1:500	/		Geneva antibody facility	scFv-F2C
Mouse anti-acetylated tubulin (6-11B-1)	1:1000	1:500	/	RRID:AB_628409	Santa Cruz Biotechnology	sc-23950
Mouse anti-CEP290 (B-7)	1:500	/	/	RRID:AB_2890036	Santa Cruz Biotechnology	sc-390462
Mouse anti-CBY (8-2)	1:500	/	/	RRID:AB_1561972	Santa Cruz Biotechnology	sc-101551
Mouse anti-gamma tubulin (GTU88)	1:2000	1:200	/	RRID:AB_532292	Sigma-Aldrich	T5326
Mouse anti-SAS-6	/	1:100	/	RRID:AB_1128357	Santa Cruz Biotechnology	sc-81431
Mouse anti-Smoothened	1:200	/	/	RRID:AB_1270802	Abcam	ab72130
Rabbit anti-ARL13B	1:500	/	/	RRID:AB_2060867	Proteintech	17711-1-AP
Rabbit anti-C2CD3	1:500	1:500	/	RRID:AB_10669542	Sigma-Aldrich	HPA038552
Rabbit anti-C2CD3	/	/	1:1000	RRID:AB_2718714	ThermoFisher Scientific	PA5-72860
Rabbit anti-CEP164	1:500	1:300	/	RRID:AB_2651175	Proteintech	22227-1-AP
Rabbit anti-GFP	/	/	1:1000	RRID:AB_591816	MBL International	598
Rabbit anti-HA	/	/	1:1000	RRID:AB_631618	Santa Cruz Biotechnology	sc-805
Rabbit anti-KI67	1:1000	/	/	RRID:AB_443209	Abcam	ab15580
Rabbit anti-LRRCC1 Ab1	1:500	1:200	/		This study	
Rabbit anti-LRRCC1 Ab2	1:500	1:300	1:1000		This study	
Rabbit anti-OFD1	1:500	/	/	RRID:AB_2890033.	Sigma-Aldrich	ABC961
Sheep anti-C2CD3	1:200	1:100	/	RRID:AB_10997138	R&D systems	AF7348
Secondary antibodies						
Donkey Anti-Goat IgG H&L (Alexa Fluor® 488)	1:500	1:500	/	RRID:AB_2687506	Abcam	ab150129
Donkey Anti-Goat IgG H&L (Alexa Fluor® 568)	1:500	1:500	/	RRID:AB_2636995	Abcam	ab175474
Donkey Anti-Goat IgG H&L (Alexa Fluor® 647)	1:500	1:100	/	RRID:AB_2732857	Abcam	ab150131
Donkey Anti-Mouse IgG H&L (Alexa Fluor® 488)	1:500	1:500	/	RRID:AB_2732856	Abcam	ab150105
Donkey Anti-Mouse IgG H&L (Alexa Fluor® 568)	1:500	1:500	/	RRID:AB_2636996	Abcam	ab175472
Donkey Anti-Mouse IgG H&L (Alexa Fluor® 647)	1:500	1:100	/	RRID:AB_2890037	Abcam	ab150107
Donkey Anti-Rabbit IgG H&L (Alexa Fluor® 488)	1:500	1:500	/	RRID:AB_2636877	Abcam	ab150073
Donkey Anti-Rabbit IgG H&L (Alexa Fluor® 647)	1:500	1:500	/	RRID:AB_2752244	Abcam	ab150075
Donkey Anti-Sheep IgG H&L (Alexa Fluor® 647)	/	1:100	/	RRID:AB_2884038	Abcam	ab150179
Goat Anti-Guinea Pig IgG (H+L) (Alexa Fluor 568)	/	1:100	/	RRID:AB_141954	ThermoFisher Scientific	A-11075
Goat Anti-Rabbit IgG (H+L) Horseradish Peroxidase Conjugate	/	/	1:1000	RRID:AB_2536530	ThermoFisher Scientific	G-21234

Table 2. PCR primers used in this study.

Primer	Sequence
LRRCC1-1_Fw	CAA CAA GGA TCT TCT CTA GCC CA
LRRCC1-1_Rv	AGT TTG GTC GTC TAT GAT TTT GCA
LRRCC1-2_Fw	GCA CAA CAA GGA TCT TCT CTA GC
LRRCC1-2_Rv	TCG CAG ACA TTC ATT CTC TCT AGA
PTCH1_Fw	CCC CTG TAC GAA GTG GAC ACT CTC
PTCH1_Rv	AAG GAA GAT CAC CAC TAC CTT GGC T
CHMP2A_Fw	ATG GGC ACC ATG AAC AGA CAG
CHMP2A_Rv	TCT CCT CTT CAT CTT CCT CAT CAC
EMC7_Fw	GTC AGA CTG CCC TAT CCT CTC C
EMC7_Rv	CAT GTC AGG ATC ACT TGT GTT GAC

2.2. hVFL3/CCDC61 is a component of mother centriole subdistal appendages required for centrosome cohesion and positioning (Article 2)

The highlights of this work are:

- hVFL3 co-localizes at SDAs and at centriole proximal ends with components of the MT-anchoring complex, and physically interacts with CEP170.
- Depletion of hVFL3 increased the distance between mother and daughter centrioles without affecting the assembly of the filamentous inter-centriolar linker. The disruption of the linker in hVFL3-depleted cells exacerbated centriole splitting, a phenotype observed following depletion of other SDA components.
- Centrosome positioning is perturbed in hVFL3-depleted interphase cells, supporting the conclusion that hVFL3 is required for SDA function.
- hVFL3 is a MT-binding protein.

My participation of this work includes:

Developing and testing the anti-hVFL3 antibody used in this article.

Designing, performing, and analyzing the micro-pattern experiments showing that hVFL3 affects centrosome positioning in interphase cells.

Training and supervising Marion Poteau and Roland Demdou (Master and Bachelor students) to perform the experiments described in this article.

hVFL3/CCDC61 is a component of mother centriole subdistal appendages required for centrosome cohesion and positioning

Véronique Pizon*, Noémie Gaudin*, Marion Poteau†, Carmen Cifuentes-Diaz‡, Roland Demdou*, Vincent Heyer§||#**, Bernardo Reina San Martín§||#** and Juliette Azimzadeh*¹ 

*Université de Paris, Institut Jacques Monod, 75013, Paris, France, †Institut Gustave Roussy, CNRS UMR 8200/Université Paris-Sud, 94 805, Villejuif, France, ‡Institut du Fer à Moulin, Inserm UMR-S U839/UPMC, 75005 Paris, France, §Institut de Génétique et de Biologie Moléculaire et Cellulaire (IGBMC), Illkirch, France, ||Institut National de la Santé et de la Recherche Médicale (INSERM), U1258, Illkirch, France, #Centre National de la Recherche Scientifique (CNRS), UMR7104, Illkirch, France, and **Université de Strasbourg, Illkirch, France

Background. The centrosome regulates cell spatial organisation by controlling the architecture of the microtubule (MT) cytoskeleton. Conversely, the position of the centrosome within the cell depends on cytoskeletal networks it helps organizing. In mammalian cells, centrosome positioning involves a population of MT stably anchored at centrioles, the core components of the centrosome. An MT-anchoring complex containing the proteins ninein and Cep170 is enriched at subdistal appendages (SAP) that decorate the older centriole (called mother centriole) and at centriole proximal ends. Here, we studied the role played at the centrosome by hVFL3/CCDC61, the human ortholog of proteins required for anchoring distinct sets of cytoskeletal fibres to centrioles in unicellular eukaryotes.

Results. We show that hVFL3 co-localises at SAP and at centriole proximal ends with components of the MT-anchoring complex, and physically interacts with Cep170. Depletion of hVFL3 increased the distance between mother and daughter centrioles without affecting the assembly of a filamentous linker that tethers the centrioles and contains the proteins rootletin and C-Nap1. When the linker was disrupted by inactivating C-Nap1, hVFL3-depletion exacerbated centriole splitting, a phenotype also observed following depletion of other SAP components. This supported that hVFL3 is required for SAP function, which we further established by showing that centrosome positioning is perturbed in hVFL3-depleted interphase cells. Finally, we found that hVFL3 is an MT-binding protein.

Conclusions and significance. Together, our results support that hVFL3 is required for anchoring MT at SAP during interphase and ensuring proper centrosome cohesion and positioning. The role of the VFL3 family of proteins thus appears to have been conserved in evolution despite the great variation in the shape of centriole appendages in different eukaryotic species.



Additional supporting information may be found online in the Supporting Information section at the end of the article.

¹To whom correspondence should be addressed (email juliette.azimzadeh@ijm.fr)

Key words: CCDC61, centriole, centrosome, subdistal appendage, VFL3.

Abbreviations: CCDC61, coiled coil domain containing 61; Cep131, centrosomal protein of 131 kDa; Cep170, centrosomal protein of 170 kDa; C-Nap1, centrosomal Nek2-associated protein 1; CTR, centrosome; hVFL3, human variable

flagella number 3; hVFL3^{-/-}, RPE1 cells with the CCDC61 gene knocked out by CRISPR/Cas9 editing; MT, microtubule; ODF2, outer dense fiber 2; PCM1, pericentriolar material 1; RPE1, human telomerase-immortalized retinal pigment epithelial (hTERT-RPE-1) cells; SAG, smoothed-agonist; SAP, subdistal appendage; SMO, smoothed.

Introduction

The centrosome is the main site of microtubule (MT) nucleation and organisation in most animal cells. It is composed of two centrioles surrounded by a pericentriolar matrix onto which MT-nucleating complexes dock. Many MT nucleated within the matrix are released within the cytoplasm, but a fraction of the MT remains tethered at the centrosome via their minus ends [Piel et al., 2000]. The older centriole, called mother centriole, carries nine subdistal appendages (SAP) that are known sites of MT anchorage. MT-anchorage at SAP involves a complex containing the proteins ninein and Cep170 that are recruited at the periphery of SAP via additional SAP components [Mogensen et al., 2000; Gromley et al., 2003; Delgehr et al., 2005; Guarguaglini et al., 2005; Ishikawa et al., 2005; Kodani et al., 2013; Veleri et al., 2014; Mazo et al., 2016; Huang et al., 2017]. In addition, the ninein complex is present at the proximal end of both centrioles where it is anchored by the protein C-Nap1 [Mogensen et al., 2000; Mazo et al., 2016].

MT-anchorage at SAP has several important functions. First, it is required for controlling the position of the centrosome within interphase cells. In cells lacking SAP due to ODF2 knockdown, centrosome positioning is less precise than in control cells, and this affects directional migration of cells, a process that requires centrosome repolarisation [Hung et al., 2016]. In addition, MT anchorage at SAP was shown to participate in centrosome cohesion [Mazo et al., 2016]. In mammalian cells, the mother and daughter centrioles are linked together by a fibrous linker containing the protein rootletin and several additional components, which dock at the proximal end of centrioles via the protein C-Nap1 [Mayor et al., 2000; Bahe et al., 2005; He et al., 2013; Fang et al., 2014; Mazo et al., 2016; Xia et al., 2018]. The centrosome linker is normally disorganised shortly prior to mitosis to allow centrosome separation and spindle organisation, and disruption of the linker by depletion of its individual components leads to premature centriole splitting [Mayor et al., 2000; Mayor et al., 2002; Bahe et al., 2005; He et al., 2013; Fang et al., 2014; Xia et al., 2018]. Remarkably, loss of SAP was shown to enhance the splitting phenotype caused by loss of the centrosome linker, a phenotype also observed following MT drug-induced depolymerisation [Panic et al., 2015; Mazo et al., 2016]. These studies

thus established that SAP play a role in maintaining centrosome cohesion, a role that likely involves their role as MT anchoring sites.

Centrioles are related to the basal bodies present at the base of cilia in many eukaryotic species. These structures share a nine-fold symmetrical arrangement of their constituting MT triplets and many of their components are conserved [Keller et al., 2005; Carvalho-Santos et al., 2010; Hodges et al., 2010; Azimzadeh et al., 2012]. However, centriole/basal bodies anchor appendages that are much more variable in shape and number. In *Chlamydomonas reinhardtii* and *Paramecium tetraurelia*, basal bodies anchor specific sets of MT rootlets and striated fibres that are distinct from what is observed in animal cells [Geimer and Melkonian, 2005; Tassin et al., 2015]. Despite the variability of shape, the function of these appendages is overall conserved: they control the position of the centrioles and ensure their cohesion. The VFL3 (Variable FLagella number 3) family of proteins is one of the few protein families involved in assembling centriole appendages that is evolutionary conserved in eukaryotes [Bengueddach et al., 2017]. Mutations in the *Chlamydomonas VFL3* gene leads to the disruption of striated fibres and MT ribbons attached to the basal bodies, which leads to defects in basal body segregation during mitosis [Wright et al., 1983; Hoops et al., 1984]. Downregulation of *Paramecium VFL3*-related genes also leads to defects in the assembly and position of centriole rootlets [Bengueddach et al., 2017]. Because the appendages that decorate mammalian centrioles are distinct from those seen in flagellated protists, we were intrigued that a VFL3 family member, encoded by the *CCDC61* (*Coiled Coil Domain Containing 61*) gene, was found in the proteome of the human centrosome [Andersen et al., 2003]. A recent study established that hVFL3/CCDC61 is a centrosome component required for mitotic spindle assembly and symmetry [Barenz et al., 2018]. hVFL3/CCDC61 is also present within centriolar satellites, which are non-membranous 70–100 nm cytoplasmic granules concentrated around the centrosome [Kubo et al., 1999; Dammermann and Merdes, 2002; Kubo and Tsukita, 2003; Barenz et al., 2018]. Furthermore, we recently showed that in multiciliated cells of planarian flatworms, a hVFL3 ortholog is involved in assembling the basal foot, a centriole appendage structurally and molecularly related to SAP [Basquin et al., 2019].

Here, we show that hVFL3 is a component of SAP of the mother centriole. We found that targeting hVFL3 expression perturbs centriole cohesion and centrosome positioning in interphase cells, supporting that hVFL3 is required for MT-anchorage at SAP. Finally, we show that hVFL3 can bind to both free tubulin and MT indicating that it might be directly involved in tethering MT at SAP.

Results

hVFL3 affects the distribution of centriolar satellites

To address the role of hVFL3, we established knock-out cell lines by disrupting both copies of the *CCDC61* gene in human telomerase-immortalised retinal pigment epithelial (hTERT-RPE-1; hereafter referred to as RPE1) cells by CRISPR/Cas9 editing. Three null clones were isolated and characterised by Western blot and immunofluorescence experiments using a polyclonal antibody we generated against the C-terminus of the protein (Figure S1A and B). Sequencing of genomic DNA confirmed the presence of insertions or deletions in both copies of the *CCDC61* gene for all three clones (Figure S2). These clones were undistinguishable at the phenotypic level (Figures S1B, S3A, and S8), and hence clone 28-1 (hereafter named hVFL3^{-/-} cells) was retained for further analysis. Wild-type control and hVFL3^{-/-} cell lines expressing different levels of a Myc-hVFL3 transgene were also established (Figure S1C). In all clones, the Myc-hVFL3 fusion protein localised as the endogenous protein both during interphase and upon serum starvation (Figure S1D). Among these, RPE1+Myc-hVFL3 clone 13 (hereafter named RPE1+Myc-hVFL3) and hVFL3^{-/-}+Myc-hVFL3 clone 8 (hereafter named hVFL3^{-/-}+Myc-hVFL3) expressed respectively 22 and 10 times more hVFL3 than the endogenous protein present in control cells (Figure S1C).

We examined the effect of hVFL3 depletion on the localisation of centriolar satellites co-labelled with anti-PCM1 and anti-Cep131 antibodies (Figure 1A; Figure S3A). In RPE1 cells, satellites loosely accumulated around the centrosome, both during interphase and in serum-starved cells. In hVFL3^{-/-} cells however, satellites appeared more scattered within the cytoplasm (Figure 1A; Figure S3A). In agreement with this, we observed a decrease in the amounts of PCM1

accumulated within a 2- μ m radius of the centrosome in hVFL3^{-/-} compared to RPE1 cells (Figure 1B). Western blot analysis confirmed that the levels of PCM1 protein remained similar in control and hVFL3^{-/-} cells, supporting that hVFL3-depletion affected PCM1 localisation rather than its expression (Figure S3B). In contrast, satellites accumulated around the centrosome in hVFL3^{-/-}+Myc-hVFL3 cells to a similar or higher extent than in RPE1 cells, supporting that expression of the Myc-hVFL3 construct complemented the scattering phenotype observed in hVFL3^{-/-} cells (Figure 1B). Co-staining of Myc-hVFL3-expressing cells with anti-PCM1, anti-Cep131 and anti-Myc antibodies revealed that all three proteins co-localised in a large proportion of centriolar satellites (Figure 1A, arrows). To further establish that hVFL3 is in complex with PCM1 and Cep131, we performed co-immunoprecipitation experiments. Using extracts from RPE1 cells co-transfected with Myc-hVFL3 and GFP-PCM1 or GFP-Cep131 constructs, we indeed detected interaction of hVFL3 with PCM1 and Cep131 (Figure 1C).

Together, these results support that hVFL3 is a component of centriolar satellites and that depletion of hVFL3 affects the distribution of satellites.

hVFL3 is not required for ciliary assembly

Because satellite organisation is essential for ciliogenesis [Wang et al., 2016], we next assessed the effects induced by perturbation of hVFL3 levels on primary cilium formation. Ciliogenesis was induced by serum-starvation in control RPE1, RPE1+Myc-hVFL3, hVFL3^{-/-} and hVFL3^{-/-}+Myc-hVFL3 cells. Labelling of the nuclear protein Ki67 confirmed that most cells were arrested in G0 after serum depletion in all cell lines, indicating that modifying hVFL3 levels does not impede cell cycle exit (not shown). RPE1 (91.6 \pm 7.1 %) and hVFL3^{-/-} (88.1 \pm 10.4 %) cells displayed the same proportion of ciliated cells (Figure 2A), supporting that hVFL3 is not required for ciliary assembly. In cells overexpressing hVFL3, the percentage of ciliated cells was decreased (69.3 \pm 6.7 % of RPE1+Myc-hVFL3 and 64.7 \pm 10.2 % of hVFL3^{-/-}+Myc-hVFL3 cells) but the differences were not significant based on three independent experiments (Figure 2A). However, the proportion of ciliated cells in hVFL3^{-/-}+Myc-hVFL3 clones negatively correlated with the level of hVFL3

Figure 1 | hVFL3 affects the localisation of centriolar satellite and interacts with PCM1 and Cep131

(A) Immunofluorescence staining of Cep131 (green) and PCM1 (red) in RPE1 and hVFL3^{-/-} cells (left panels, DNA is in blue) or Cep131 (green), PCM1 (red) and Myc (blue) in RPE1+Myc-hVFL3 cells and hVFL3^{-/-}+Myc-hVFL3 cells (right panels, DNA is in grey). Scale bar: 10 μm (1 μm for magnified views). **(B)** Mean fluorescence intensity of PCM1 staining within a radius of 2 μm from the centrosome after 48 h of serum-starvation in control, hVFL3^{-/-}, hVFL3^{-/-}+Myc-hVFL3 (clone 8) and RPE1+Myc-hVFL3 (clone 13), expressed as percentages of the control mean values. Three independent experiments were performed with *N* > 200 for each condition. Error bars represent SD. Asterisks indicate a significant difference to the corresponding control (Kruskal–Wallis test; *P* < 0.0001 for all except serum-starved hVFL3^{-/-}+Myc-hVFL3: *P* = 0.0035). **(C)** Co-immunoprecipitation experiments on RPE1 cells co-transfected with Myc-hVFL3 and either GFP-PCM1-Cter (left panel) or GFP-Cep131 (right panel) constructs. RPE1 cells transfected with a GFP construct were used as a control. Immunoprecipitation was performed using GFP antibodies. I = input; B = beads. *Indicates non-specific bands detected with the Myc antibody.

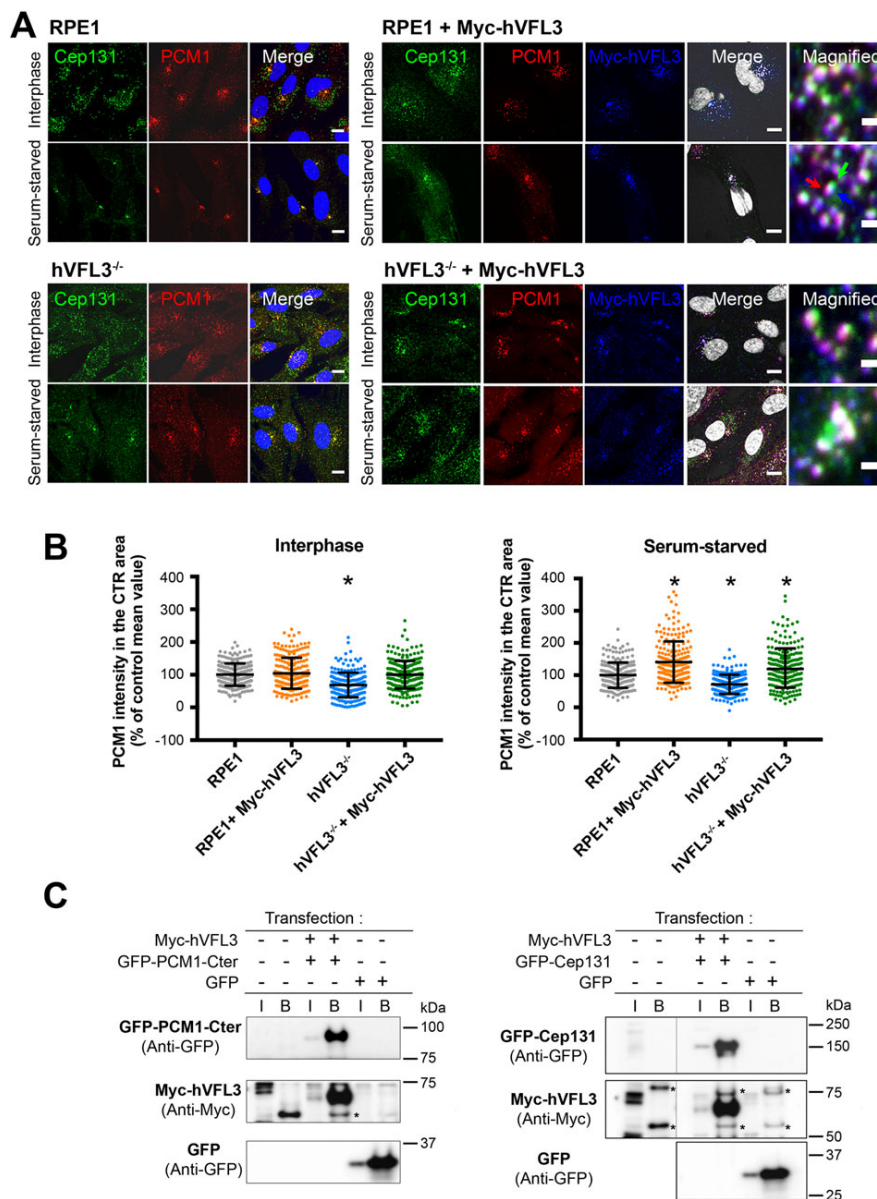
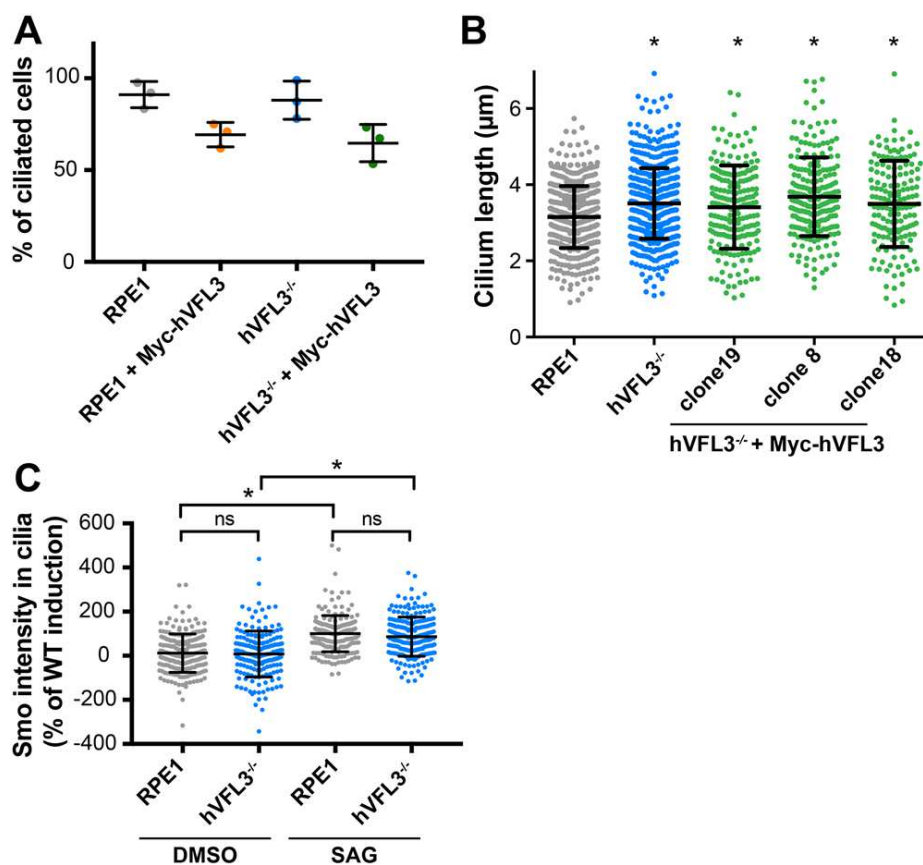


Figure 2 | Loss of hVFL3 does not affect ciliary assembly

(A) Percentage of ciliated cells after 48 h of serum-starvation and immunofluorescence staining with anti-acetylated-tubulin antibodies of control, hVFL3^{-/-}, hVFL3^{-/-}+Myc-hVFL3 (clone 8) and RPE1+Myc-hVFL3 (clone 13). Mean of three independent experiments are represented ($N > 190$ for each condition). Error bars represent SD between the three experiments. Differences are not significant (Kruskal–Wallis test). **(B)** Mean ciliary length in serum-starved cells stained with anti-acetylated tubulin antibodies. Four independent experiments were performed with $N > 159$ for each condition. Error bars represent SD. Asterisks indicate a significant difference from the control (Kruskal–Wallis test; $P < 0.0001$ for hVFL3^{-/-} and hVFL3^{-/-}+Myc-hVFL3 clone 8, < 0.001 for clone 18, < 0.01 for clone 19). **(C)** Mean fluorescence intensity of SMO at the primary cilium after a 24-h treatment with either 200 nM SAG or DMSO (percentage of the SAG-treated RPE1 mean value). Three independent experiments were performed with $N > 180$ for each condition. Error bars represent SD. Asterisk indicate a significant difference (Kruskal–Wallis test; $P < 0.0001$).



overexpression (Figure S4), suggesting that hVFL3 overexpression might interfere with ciliary assembly and/or stability. We also analysed ciliary length and observed that average length was slightly increased in hVFL3^{-/-} cells compared to control RPE1 cells (Figure 2B). In hVFL3^{-/-}+Myc-hVFL3 clones, a proportion of cells (around 15%) displayed a very short cilium – which also supports that hVFL3 overexpression affects ciliary assembly or stability – but the average length of other cilia was also slightly

increased compared to control cilia. Despite this limited effect on ciliary assembly, we wanted to determine whether ciliary function was affected by hVFL3-depletion. In vertebrates, Hedgehog signalling is dependent on ciliary assembly and integrity [Reiter and Leroux, 2017]. An early step of Hedgehog pathway activation corresponds to the accumulation of the transmembrane protein Smoothed (SMO) within the primary cilium [Anvarian et al., 2019]. Treating RPE1 cells with SMO-agonist (SAG) increased

SMO levels within cilia (Figure 2C), as expected. In hVFL3^{-/-} cells, SAG treatment enhanced the ciliary levels of SMO to a similar extent than in RPE1 cells, supporting that the Hedgehog pathway is still functional in mutant cells.

Together, these results support that loss of hVFL3 has a limited effect on ciliogenesis and ciliary signalling. However, hVFL3 overexpression possibly interferes with ciliary assembly or stability.

hVFL3 is a subdistal appendage component

We next sought to determine the precise localisation of hVFL3 within the centrosome. Because satellites are usually densely packed around the centrosome, we used nocodazole to disperse the satellites and better visualise centrosomal hVFL3. Although some satellites often remained in the vicinity of the centrosome in these conditions, we consistently observed a faint hVFL3-staining at the base of cilia that was reminiscent of mother centriole appendages (Figure 3A). hVFL3 appeared to co-localise with Cep170 and ninein, which decorate SAP and the proximal end of centrioles. To confirm these results, we used immunogold electron microscopy. Since the anti-hVFL3 antibody was not compatible with the electron microscopy protocol, RPE1+Myc-hVFL3 and hVFL3^{-/-}+Myc-hVFL3 cells were labelled with an anti-Myc antibody. In both cell lines, hVFL3 localised at SAP (two centrioles out of two for hVFL3^{-/-}+Myc-hVFL3 and three out of three for RPE1+Myc-hVFL3 cells) and to a lesser extent at the proximal end of centrioles (one centriole out of two for hVFL3^{-/-}+Myc-hVFL3 and three out of three for RPE1+Myc-hVFL3 cells; Figure 3B, arrows). This localisation was consistent with the recent identification of Cep170 as an interactor of hVFL3 by proximity biotinylation [Barenz et al., 2018]. We also identified Cep170 as a potential interactor by tandem-affinity purification coupled to mass spectrometry using a C-terminal fragment of hVFL3 that associates to the centrosome but not to satellites (Figure S5). We confirmed this interaction by co-immunoprecipitation assays on RPE1 cells expressing GFP-Cep170 and Myc-hVFL3 constructs (Figure 3C). Together, our results establish that hVFL3 is a SAP component and confirm its interaction with Cep170.

We next wondered whether loss of hVFL3 induced defects in the structure of SAP. The appearance or po-

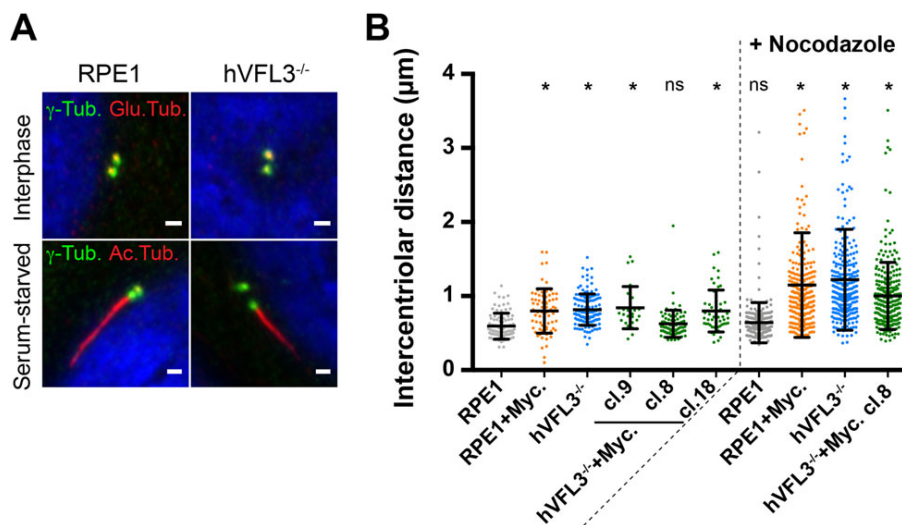
sition of SAP observed by electron microscopy in cells either depleted or overexpressing hVFL3 was similar to controls (Figure S6). Despite the lack of major structural changes in SAP morphology, hVFL3 could interfere with the recruitment of other SAP proteins. Therefore, we analysed the localisation of endogenous ninein, Cep170 and ODF2 in cells depleted from or overexpressing hVFL3. In all these cell lines, independently of hVFL3 levels, we did not detect any conspicuous change in the distribution of ninein, Cep170 or ODF2, or in the co-localisation of ninein and Cep170 (Figure 3D; Figure S7A). When we quantified their centrosomal levels, we found only a modest decrease in ninein levels and to a lesser extent in Cep170 levels in hVFL3^{-/-} compared to control cells (Figure 3E; Figure S7B). Because discrepancies between phenotypes resulting from genetic mutations or from knockdowns are known to occur [Hall et al., 2013; Rossi et al., 2015; Flanagan et al., 2017], we also analysed the effect of RNAi-depletion of hVFL3 on the localisation of other SAP components. After targeting hVFL3 using two different siRNAs that both strongly reduced its endogenous levels, we observed a modest decrease in centrosomal ninein after treatment with the most efficient siRNA (hVFL3-si1), whereas ODF2 levels were unaffected (Figure 3F and G; Figure S7C). In contrast, treatment with both hVFL3 siRNAs increased the levels of centrosomal Cep170 (Figure 3G). Thus, depletion of hVFL3 either by CRISPR/Cas9 editing or by RNAi overall had a limited impact on the recruitment of other SAP components, including its interaction partner Cep170. Altogether, these results demonstrate that hVFL3 is a SAP protein that interacts with Cep170 but is not essential for SAP assembly or the recruitment of the SAP components ninein, Cep170 and ODF2.

hVFL3 is implicated in centriole cohesion

We noticed that upon induction of ciliogenesis, the distance between the mother centriole (also called basal body in this context) and the daughter centriole was increased in hVFL3^{-/-} compared to control RPE1 cells (Figure 4A and B), from $0.50 \pm 0.10 \mu\text{m}$ in control RPE1 cells to $0.87 \pm 0.22 \mu\text{m}$ in hVFL3^{-/-} cells. Similar results were obtained for all three null clones (Figure S8). Surprisingly, the mean intercentriolar distance was also increased in RPE1+Myc-hVFL3 ($0.79 \pm 0.3 \mu\text{m}$) and

Figure 4 | hVFL3 is required for centriole cohesion

(A) Immunofluorescence staining of mother and daughter centrioles labelled with antibodies against gamma-tubulin (green) and glutamylated tubulin (interphase cells) or acetylated tubulin (serum-starved cells) (red) in RPE1 and hVFL3^{-/-} cells. Scale bar, 1 μm. **(B)** Mean intercentriolar distance in control, hVFL3^{-/-}, hVFL3^{-/-}+Myc-hVFL3 (clone 8) and RPE1+Myc-hVFL3 (clone 13) cells serum-starved during 24 h without further treatment or after treatment with 0.5 μM nocodazole to destabilise MT. Two independent experiments were performed with 27 < N < 134 for non-treated cells, three independent experiments with N > 250 for nocodazole-treated cells. Error bars represent SD. Asterisks indicate a significant difference from the untreated control (Kruskal–Wallis test; *P* < 0.0001 for all except hVFL3^{-/-}+Myc-hVFL3 clone 9: *P* = 0.0002 and clone 18: *P* = 0.0001).



hVFL3^{-/-}+Myc-hVFL3 clone 9 ($0.84 \pm 0.28 \mu\text{m}$) and clone 18 ($0.79 \pm 0.28 \mu\text{m}$) compared to control RPE1 cells ($0.59 \pm 0.17 \mu\text{m}$; Figure 4B). Thus, overexpression of hVFL3 like its depletion decreased centriole cohesion. However, intercentriolar distance was comparable to control values in hVFL3^{-/-}+Myc-hVFL3 clone 8 ($0.62 \pm 0.14 \mu\text{m}$), which expresses intermediate levels of Myc-hVFL3 (Figure S1C), supporting that expression of hVFL3 at definite levels can complement the centriole splitting phenotype observed in hVFL3^{-/-} cells. hVFL3 depletion or over-expression in interphase cells also increased intercentriolar distance in some of the cell lines, although to a lesser extent (Figure S8). In the presence of an intact centrosome linker, perturbing MT stability does not affect centrosome cohesion [Panic et al., 2015]. In agreement, intercentriolar distance was similar in RPE1 cells treated with a low dose of nocodazole and in non-treated cells (Figure 4B). In contrast, centriole-splitting was enhanced by nocodazole treatment in both hVFL3^{-/-} and overexpressing cells, further supporting that centriole cohesion is al-

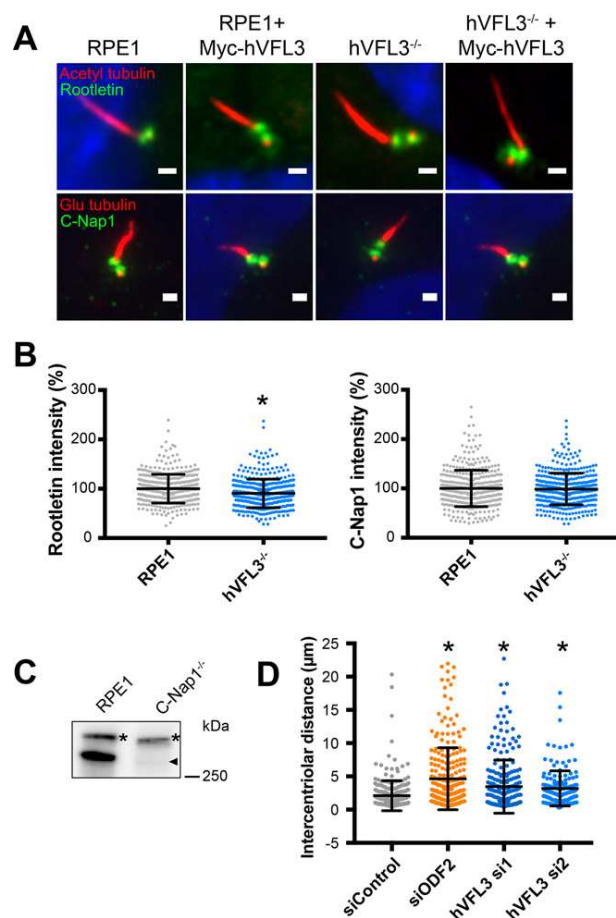
tered in these clones. Together, these results indicate that both depletion and overexpression of hVFL3 interfere with the regulation of intercentriolar distance, suggesting that hVFL3 participates in centrosome cohesion in a quantitatively regulated manner.

hVFL3 depletion exacerbates the centriole splitting phenotype induced by a disruption of the centrosome linker

In vertebrate cells, centriole cohesion relies on the linker components rootletin and C-Nap1 [Bahe et al., 2005; Agircan et al., 2014]. Since hVFL3 affects centriole cohesion and a fraction of hVFL3 localises at the proximal end of centrioles like C-Nap1, we examined the localisation of rootletin and C-Nap1 in ciliated cells depleted from or overexpressing hVFL3. Compared to RPE1 cells, neither depletion or overexpression of hVFL3 notably affected the recruitment of rootletin and C-Nap1 at the proximal end of centrioles (Figure 5A). Quantifying the levels of C-Nap1 and rootletin at the centrosome, we observed only a slight decrease in rootletin staining

Figure 5 | hVFL3 affects centriole cohesion via its function at SAP

(A) Immunofluorescence staining of rootletin or C-Nap1 (green) with either anti-acetylated tubulin or anti-glutamylated tubulin (red) in cells lacking or over-expressing hVFL3. Scale bar, 1 μ m. **(B)** Mean fluorescence intensity of rootletin or C-Nap1 staining at the centrosome in serum-starved control or hVFL3^{-/-} cells (percentage of control mean value). Three independent experiments were performed with $N > 400$ for each condition. Error bars represent SD. Asterisks indicate a significant difference (two-tailed Mann-Whitney test; $P < 0.0001$). **(C)** Western-blot analysis of C-Nap1 levels in control RPE1 or C-Nap1^{-/-} cells. Ten micrograms of total proteins were loaded for each sample. **(D)** Mean intercentriolar distance in C-Nap1^{-/-} cells treated with control, hVFL3 or ODF2 siRNAs. Three independent experiments were performed with $160 > N > 250$ for each condition. Error bars represent SD. Asterisks indicate a significant difference from the siControl condition (Kruskal-Wallis test; $P < 0.0001$ for siODF2 and hVFL3-si2, $P < 0.01$ for hVFL3-si1).



in hVFL3^{-/-} compared to control cells (90.5 ± 28.8 % in hVFL3^{-/-} vs. 100.0 ± 29.11 % in control cells; Figure 5B). Our results thus suggested that hVFL3 affects centriole cohesion independently of the C-Nap1/rootletin linker. In RPE1 cells, the centriole splitting phenotype induced by C-Nap1 depletion is strongly enhanced by simultaneous ablation of SAP components or by MT depolymerisation [Panic et al.,

2015; Mazo et al., 2016; Flanagan et al., 2017]. This supports that SAP play a role in maintaining centrosome cohesion, likely via their capacity to anchor MT. Since hVFL3 is a SAP component, we wondered whether it could also affect centriole cohesion by perturbing SAP function. We reasoned that in such case, simultaneous depletion of C-Nap1 and hVFL3 should exacerbate the splitting phenotype caused by C-Nap1

ablation. We disrupted both copies of the *CEP250* gene (encoding C-Nap1) by CRISPR editing in either control or hVFL3^{-/-} cells. Western blot analyses confirmed the loss of C-Nap1 expression in the different clones we isolated (Figure 5C; Figure S9A). We observed a very modest increase in intercentriolar distance in only two out of four hVFL3^{-/-}; C-Nap1^{-/-} clones (2.57 ± 1.96 and 2.38 ± 1.97 μm for clones 5–39 and 5–51, respectively) compared to C-Nap1^{-/-} cells (2.25 ± 2.17 μm ; Figure S9B). However, when we targeted hVFL3 expression by RNAi in C-Nap1^{-/-} cells, intercentriolar distance was markedly increased (3.45 ± 4.00 and 3.20 ± 2.64 μm for siRNA-1 and -2, respectively) compared to C-Nap1^{-/-} cells treated with a control siRNA (2.10 ± 2.27 μm ; Figure 5D). Thus, acute depletion of hVFL3 by RNAi could mimic the phenotype induced by depletion of other SAP components such as ODF2 in cells lacking the centrosome linker. The mean increase was about half of the one observed in C-Nap1^{-/-} cells treated with a siRNA against ODF2 (4.65 ± 4.67 μm) compared to a control siRNA, likely reflecting a milder impact of hVFL3-depletion on SAP function (Figure 5D). Altogether, our data support that hVFL3 affects centrosome cohesion by regulating MT-anchorage at SAP.

hVFL3 affects centrosome positioning in interphase cells

We next wondered whether depletion of hVFL3 would affect other SAP-related functions such as centrosome positioning. A powerful approach to study organelle positioning is to use adhesive micropatterns. In particular, seeding cells on crossbow-shaped micropatterns was found to induce centrosome relocation at a predictable position [Thery et al., 2006]. In contrast, centrosome position was more variable in cells depleted from the SAP component ODF2 [Hung et al., 2016]. We treated RPE1 cells with either control siRNA or with the most efficient hVFL3 siRNA (hVFL3-si1) during 48 h and then allowed the cells to attach and polarise on crossbow-shaped micropatterns. We then determined centrosome position relative to the pattern by co-labelling cells with anti-centrin and anti-ninein antibodies (Figure 6A). By measuring the distance separating the centrosome from the centroid of the pattern in both conditions, we found that the centrosome was on average more distant from the centroid in hVFL3-depleted than in

control cells (Figure 6A and B), suggesting that centrosome position is less precisely regulated in hVFL3-depleted cells. Thus, acute depletion of hVFL3 impacted centrosome positioning in interphase cells, which further indicates that hVFL3 is required for proper anchorage of MT at SAP.

hVFL3 is an MT-associated protein

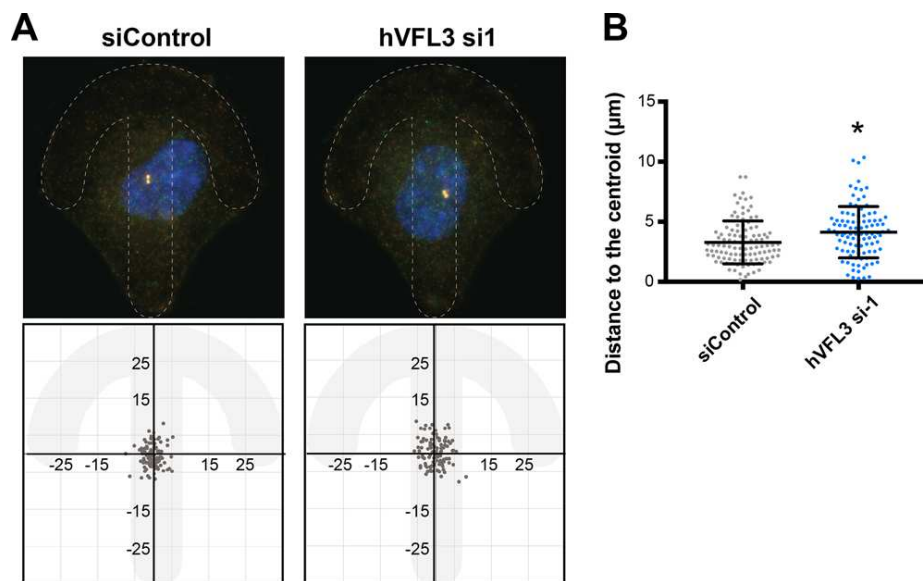
Our results supported that hVFL3 depletion affected MT anchorage without perturbing SAP morphology or the recruitment of the peripheral SAP components ninein, a key player in MT-anchorage at SAP [Mogensen et al., 2000; Delgehr et al., 2005; Kodani et al., 2013; Mazo et al., 2016] and Cep170, which can bind MT directly [Welburn and Cheeseman, 2012]. We thus wondered whether hVFL3 was itself required for binding MT, which could explain why SAP function was altered in hVFL3-depleted cells despite the presence at the centrosome of overall normal levels Cep170. In agreement with this, we observed that transient expression of Myc-hVFL3 or hVFL3-GFP fusion proteins both induced the formation of MT bundles. Depending on the level of over-expression, hVFL3 formed puncta or filaments co-localizing with MT (Figure 7A), suggesting that hVFL3 can bind to MT. To determine if hVFL3 could bind to tubulin, we performed co-immunoprecipitation experiments on RPE1 cells co-transfected with GFP-tubulin and Myc-hVFL3 constructs. We found that GFP-tubulin co-precipitated Myc-hVFL3 from cell extracts (Figure 7B), supporting that hVFL3 can bind to tubulin. Taken together, these results indicate that hVFL3 is a MT-binding protein.

Discussion

In the present work, we analysed the role played by the sole human member of the VFL3 family of proteins at the centrosome of interphase or G0 cells. We found that hVFL3 is present within centriolar satellites and is required for properly targeting the satellites to the centrosome region. Within the centrosome itself, hVFL3 is present at mother centriole SAP and at the proximal end of centrioles, where an MT-anchoring complex comprising ninein and Cep170 is localised. hVFL3 interacts with Cep170 but is not required for its recruitment at the centrosome

Figure 6 | hVFL3 is required for centrosome positioning in interphase cells

(A) Position of the centrosome in interphase RPE1 cells seeded on crossbow-shaped adhesive micropatterns after treatment with either control siRNA or hVFL3-si1. Upper panels: the position of the centrosome was determined by co-staining centrin (green) and ninein (red), DNA is in blue. Dotted lines delimit the contour of the micropattern. Lower panels: graphical representation of centrosome position. The x and y axes indicate the distance (in μm) to the centroid of the micropattern (shown in grey). Data were collected from two independent experiments. $N = 100$ (siControl) or 110 (hVFL3-si1). **(B)** Mean distance between the centrosome and the cell centroid for the data shown in (A). Error bars represent SD. The asterisk indicates a significant difference (Two-tailed Mann–Whitney test; $P = 0.0009$).



in RPE1 cells. Acute depletion of hVFL3 combined with disruption of the centrosome linker induced severe centriole splitting like in the case of other SAP components [Mazo et al., 2016], supporting that SAP function is altered in these conditions. Like depletion of ODF2, a protein essential for SAP assembly [Hung et al., 2016], hVFL3-depletion perturbed centrosome positioning in interphase cells, further establishing that hVFL3 affects MT-anchorage at SAP. In agreement, we found that hVFL3 is an MT-binding protein and thus might directly participate in anchoring MT at SAP.

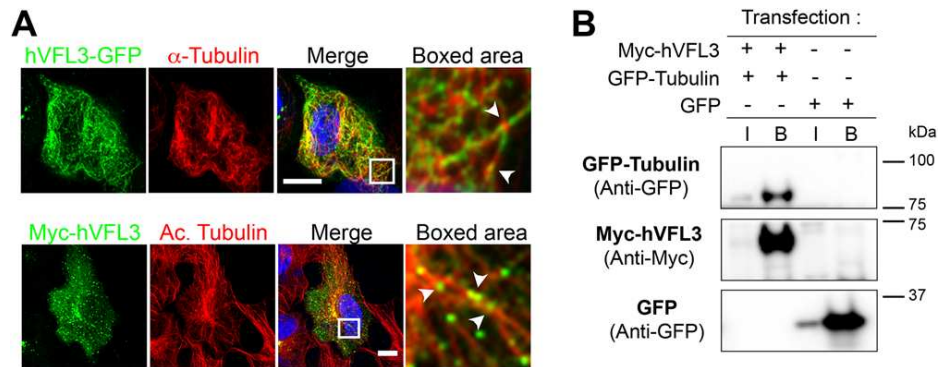
hVFL3 is a component of centriolar satellites

hVFL3 co-localises and interacts with the centriolar satellite components PCM1 and Cep131. In addition, loss of hVFL3 causes satellites to be mislocalised, a phenotype that can be rescued by re-expression of hVFL3. This is not unexpected, as depletion of many other satellite components causes loss or

mislocalisation of satellites [Tollenaere et al., 2015]. Loss of hVFL3 possibly induces the destabilisation of a subpopulation of satellites. Alternatively, hVFL3 could affect the transport of satellites towards the centrosome, which involves their interaction with dynein/dynactin motors. Satellite components such as BBS4 and Par6 α can directly bind the dynactin component p150^{glued} and their depletion cause satellite dispersion, indicating that they regulate the transport of satellites by dynein/dynactin [Kim et al., 2004; Kodani et al., 2010]. Loss of centrosome cohesion in cells lacking C-Nap1 also leads to dispersion of centriolar satellites [Panic et al., 2015; Flanagan et al., 2017]. This suggests that centriole cohesion somehow affects satellite localisation, which could also explain the scattering of satellites in hVFL3 null cells. Finally, hVFL3 deficiency might cause satellite dispersion by perturbing MT anchorage at SAP, which possibly impacts the transport of satellites towards the centrosome.

Figure 7 | hVFL3 interferes with the MT network and binds tubulin

(A) Immunofluorescence staining of RPE1 cells transfected with Myc-hVFL3 or hVFL3-GFP constructs using anti-hVFL3 antibodies (green) and anti-acetylated tubulin or anti- α tubulin antibodies (red). DNA is in blue. hVFL3 dots co-localised with MT are indicated by arrowheads (boxed area). Scale bar, 10 μ m. **(B)** Co-immunoprecipitation experiments on cells co-transfected with GFP-tubulin and Myc-hVFL3 constructs. GFP antibodies were used for immunoprecipitation and a GFP construct was used as a control. I = input; B = beads.

**hVFL3 localises at SAP and regulates their function**

Our results show that hVFL3 co-localises at SAP and centriole proximal ends with a MT-anchoring complex comprising ninein, Cep170, p150^{glued} and Kif2a [Mazo et al., 2016]. In agreement, we found that hVFL3 interacts with Cep170, as also described in a recent study [Barenz et al., 2018]. MT-anchorage at SAP is required for centrosome positioning and centrosome cohesion, and indeed we found that hVFL3-depletion affects both these processes. Our results support that hVFL3 is an MT-binding protein like Cep170 and p150^{glued} [Waterman-Storer et al., 1995; Welburn and Cheeseman, 2012], suggesting that these proteins might cooperate in tethering MT-minus ends at SAP.

We did not observe important modifications in the recruitment of SAP components upon depletion of hVFL3, including its binding partner Cep170. Genetic editing only slightly decreased Cep170 centrosomal levels, whereas acute depletion by RNAi increased these levels. Our results thus support that Cep170 can be anchored at SAP by additional interactors, and that hVFL3 can affect MT-anchorage independently of Cep170. These findings are in contrast with the work from Bärenz and colleagues who found that Cep170 is massively displaced from the centrosome when hVFL3 is absent in U2OS cells [Barenz et al., 2018]. Thus, some aspects of Cep170

recruitment might be cell type-specific, possibly owing to the presence of additional Cep170-interacting proteins in RPE1 but not U2OS cells. Alternatively, hVFL3 might affect the recruitment of Cep170 at SAP indirectly by influencing its transport or the transport of other Cep170-interacting proteins via centriolar satellites.

The observation that depleting hVFL3 by either RNAi or CRISPR/Cas9 editing had opposite effects on Cep170 centrosomal levels is intriguing. Discrepancies between RNAi and genetic mutant phenotypes have been documented for other genes, including the centrosome components Cep131 and C-Nap1 [Hall et al., 2013; Flanagan et al., 2017]. These differences are attributed to compensation in genetically modified cells, in particular changes in the level of expression of other players in the same pathway [Rossi et al., 2015]. Such a compensation could allow down-regulating centrosomal accumulation of Cep170 in hVFL3^{-/-} cells, or modify the levels of other centrosome proteins. How these differences in protein levels between RNAi-treated and CRISPR/Cas9-edited cells might affect SAP function is unclear, but they were nonetheless accompanied by additional phenotypic differences. Indeed, acute depletion of hVFL3 enhanced the splitting phenotype caused by disruption of the C-Nap1/rootletin linker – an indication that SAP function is altered, to a much greater extent than genetic ablation.

Direct analysis of MT anchorage at SAP is difficult because of the presence of many non-anchored MT in the close vicinity of the centrosome. In addition, some cell types including RPE1 cells can still form MT asters after perturbation of SAP assembly [Ishikawa et al., 2005; Mazo et al., 2016], indicating that other anchorage mechanisms are at play [Tu et al., 2018]. Nevertheless, characterisation of key specific SAP components such as ODF2 highlighted a role for SAP in regulating centrosome position and cohesion [Hung et al., 2016; Mazo et al., 2016], which is consistent with their role as MT-anchorage sites. Our observations that hVFL3 localises at SAP, that it interacts with both Cep170 and MT and that its depletion leads to defects in centrosome positioning and cohesion – the latter defect being enhanced when MT are destabilised by low doses of nocodazole – all support that hVFL3 is required for proper anchorage of MT at SAP in interphase and G0 cells.

The VFL3 family of proteins in evolution

hVFL3 is a member of an ancient family of centriole/basal body-associated proteins. In *Chlamydomonas* and in *Paramecium*, disruption of proteins of the VFL3 family leads to defects in the assembly and position of basal body-associated structures [Hoops et al., 1984; Bengueddach et al., 2017]. In planarian flatworms depleted from SMED-VFL3, about one third of centrioles lack a basal foot [Basquin et al., 2019]. We did not observe notable perturbations in the assembly of SAP or the rootletin linker in RPE1 cells. Nevertheless, the involvement of hVFL3 in MT-anchorage at mother centriole SAP is reminiscent of its ancestral function in connecting centriole/basal bodies to the cytoskeleton. In this respect, it is striking that despite the great evolutionary variation in the shape of appendages attached to centriole/basal bodies, some aspects of their molecular assembly are still conserved.

Material and methods

Cell culture

RPE1 (hTert-RPE-1) cells were cultured in DMEM/F-12 (ThermoFisher Scientific) supplemented with 10% foetal calf serum (ThermoFisher Scientific), 100 U/mL penicillin and 100 µg/mL streptomycin (ThermoFisher Scientific) and kept at 37°C in the presence of 5% CO₂.

Cloning

hVFL3 full-length coding sequence was amplified from cDNA clone IMAGE:4562394 (Genbank accession: BG325573.1),

cloned into the pENTR Gateway entry vector using the pENTR/D-TOPO cloning kit (ThermoFisher Scientific) and subcloned into pDEST47 using LR clonase (ThermoFisher Scientific) to generate a hVFL3-GFP fusion. For Myc-hVFL3 fusion, hVFL3 coding sequence was subcloned using ligation independent cloning (LIC) into pMyc-LIC, a mammalian expression vector derived from pEGFP-C1 vector (Clontech) by replacing the GFP coding sequence with Myc epitope sequence and the multiple cloning site with a LIC cassette. The full-length coding sequence of Cep131 was amplified from clone IMAGE:4634709 (Genbank accession: BC012130) after PCR mutagenesis to remove a partially retained intron, then cloned into pENTR and into pDEST53 (ThermoFisher Scientific) as described above. Full-length Cep170 and the central domain of PCM1 (aa. 714–1231), which localises at centriolar satellites [Dammermann and Merdes, 2002], were obtained by RT-PCR from RPE1 total RNA extracts using Superscript II Reverse-transcriptase (ThermoFisher Scientific) and cloned into pEGFP-LIC, a vector derived from pEGFP-C1 by insertion of a LIC cassette.

CRISPR/Cas9 editing

hVFL3^{-/-} cells were obtained by CRISPR/Cas9 editing. Briefly, RPE1 cells were co-transfected with two plasmids expressing two gRNAs targeting the *CCDC61* locus in exon 2 (target sequences: 5'-TGGTCCATGGCCAAGGTTGC-3' and 5'-GGACTACGTCTCCGGGGTG-3') or exon 4 (target sequences: 5'-GATGAGGATCAGGTAGCGCT-3' and 5'-CTCCGTGGAGTTTGACAGGT-3'), and co-expressing the nickase mutant of Cas9 fused to EGFP or mCherry, respectively. Two days after transfection, EGFP⁺ mCherry⁺ cells were sorted by fluorescence-activated cell sorting (FACS) based on GFP and mCherry expression, grown for 4 days, and plated at low concentration. Individual clones were picked after 2 wks and were selected based on the lack of hVFL3 expression as determined by Western blot analysis. Selected clones were subsequently characterised by PCR on genomic DNA followed by sequencing.

Antibodies

A fragment encoding hVFL3 aa. 367–512 was cloned in pGST-Parallel1 and expressed in *Escherichia coli*. The GST-hVFL3 fusion protein was purified under native conditions using glutathione agarose (ThermoFisher Scientific) and the hVFL3 fragment was recovered by Tev protease cleavage and dialysed before rabbit immunisation (Covalab). Antibodies were affinity-purified over the GST-hVFL3 fusion bound to Affi-Gel 10 resin (Bio-Rad). Rabbit polyclonal anti-Cep131 antibodies raised against aa. 567–767 of human Cep131 (NP_00136157) were obtained following the same procedure. Other antibodies include mouse monoclonal antibodies against acetylated tubulin (6-11B-1, Sigma), alpha-tubulin (DM1a, Sigma), gamma-tubulin (GTU-88, Sigma), actin (AC-40, Sigma), Cep170 (72-413-1, ThermoFisher Scientific), GFP (7.1+13.1, Roche), Myc (9E10, Santa Cruz Biotechnology), rootletin (C-2, Santa Cruz Biotechnology); SMO (E-5, Santa Cruz Biotechnology); rabbit polyclonal antibodies against C-Nap1 (Proteintech), detyrosinated tubulin (Glu-tubulin) (AB3201, Millipore), Myc (C3956, Sigma), ninein (ab52473, Abcam), ODF2 (ab43840, Abcam), ARL13B (17711-1-AP, Proteintech); goat polyclonal antibodies against PCM1 (D-19, Santa Cruz Biotechnology) and rootletin (C-20,

Santa Cruz Biotechnology). Donkey secondary antibodies coupled to DyLight 488/555 were purchased from Abcam.

Western blotting

Cells washed with cold PBS were lysed in the tissue culture dishes with lysis buffer containing 50 mM Tris, pH 8, 20 mM EDTA, 2% SDS, supplemented with protease inhibitor cocktail (Complete mini, EDTA-free, Roche) and heated 15 min at 95°C. Protein concentration was determined using the BCA protein assay kit according to the supplier's protocol (Pierce). For immunoblotting, 20 to 50 µg of lysate were run on NuPAGE novex 4–12% BisTris polyacrylamide gels (Novex, life technologies) and transferred onto Protran BA 83/85 nitrocellulose membranes (Whatman). Membranes blocked and incubated with antibodies following standard procedures were visualised with Immobilon chemiluminescence reagents (Millipore) using Image Reader LAS-400 (GE Healthcare Life Sciences). Protein quantification of Western blots was performed using ImageJ (National Institutes of Health, Bethesda, MD).

Immunoprecipitation

For immunoprecipitation, RPE1+Myc-hVFL3 cells were transfected with JetPEI (Polyplus) according to the manufacturer's instructions then lysed in RIPA extraction buffer (1% Triton X100, 1% sodium deoxycholate, 10 mM Tris pH 7.5, 150 mM NaCl, 5 mM EDTA, 0.1% SDS) with proteinase inhibitors and kept for 30 min on ice before sonication and centrifugation at 20 000 × *g* for 10 min at 4°C. Lysates were diluted in buffer containing 10 mM Tris pH 7.5, 150 mM NaCl and 5 mM EDTA and rotated for 3 h at 4°C with magnetic GFP-Trap_M (Chromotek). After 3 washes with wash buffer (10 mM Tris pH 7.5, 150 mM NaCl, 0.01 % NP40, 0.5 mM EDTA), immunoprecipitated proteins were isolated according to the manufacturer's instructions and used for Western blot analysis as previously indicated.

Tandem affinity purification

Full-length hVFL3 or a subdomain corresponding to aa. 331–521 (C-ter) were cloned in pEGFP-LAP-LIC, a mammalian expression vector derived from pEGFP-C1 vector (Clontech) by inserting a Tev protease cleavage site and an S-tag downstream of GFP. The C-ter domain of hVFL3 accumulated at the centrosome but not within centriolar satellites and was thus used in to identify proteins interacting specifically with hVFL3 at the centrosome. RPE1 cells stably expressing the fusion proteins were generated. Protein lysates obtained from these cells or control RPE1 cells were subjected to tandem-affinity purification as described previously [Cheeseman and Desai, 2005] using GFP-trap magnetic beads (Chromotek) and S-protein agarose (Novagen).

Immunofluorescence

Cells were fixed in cold methanol for 5 min at –20°C, blocked with 10% foetal bovine serum in PBS for 45 min then incubated with primary then secondary antibodies for 1 h each. In all experiments, Hoechst 33342 was used to stain DNA. For staining of primary cilia with anti-acetylated tubulin, cells were incubated on ice during 1 h prior to methanol fixation. For quantification of SMO accumulation within cilia, confluent cells cultured during 24 h in serum-free medium were supplemented with 200 nM SAG (Sigma) diluted in DMSO or DMSO alone during

24 h prior to fixation. Cells were then co-stained for SMO and ARL13B to determine the position of the primary cilium. To visualise centrosomal hVFL3, satellites were dispersed by treating the cells during 1 h with 5 µM nocodazole prior to fixation. For measuring the effect of MT destabilisation on intercentriolar distance, cells cultured during 24 h in serum-free medium were incubated during 1 h in serum-free medium containing 0.5 µM nocodazole prior to fixation. For micropattern analysis, CYTOOchips CW-M-A (Cytooo) were coated with bovine fibronectin (Sigma) prior to incubation with the cells following instructions from the manufacturer. RPE1 cells treated by RNAi during 48 h were detached using Versene solution and allowed to spread on adhesive micropatterns during 6–8 h before methanol fixation and immunostaining of centrosomes with anti-ninein antibodies.

Images were acquired using either a LSM780 confocal microscope (Zeiss) using an oil 63× objective (Plan Apo, N.A. 1.4) or a Axio Observer Z.1 microscope (Zeiss) equipped with a sCMOS Orca Flash4 LT camera (Hamamatsu) and a 63× objective (Plan Apo, N.A. 1.4).

Image analysis

All measurements of ciliary length, intercentriolar distance, and fluorescence intensity were executed using ImageJ software. For quantification of fluorescence intensity, the mean intensity in a ~0.25 µm² area centred on the centrosome was quantified on maximal intensity projections of *z*-series (0.5-µm interval).

Electron microscopy

For conventional transmission electron microscopy (TEM), cells were fixed for 1 h in 0.1 M Sorensen's phosphate buffer containing 4% paraformaldehyde and 2.5% glutaraldehyde. Following fixation, cells were post-fixed in 2% osmium tetroxide diluted in 0.2 M Palade's buffer. After osmication, cells were dehydrated using a graded ethanol series and flat embedded in epoxy resin (EPON 812, Polysciences). After resin polymerisation, small pieces were dissected from flat-embedded cultures, mounted in plastic stubs and sectioned. Ultrathin sections (70 nm) were stained with uranyl acetate and lead citrate. Sections were examined in a Philips CM100 electron microscope. Digital images were obtained with a CCD camera (Gatan Orius).

For Immunogold, cells were fixed with a solution containing 4% paraformaldehyde and 0.1% glutaraldehyde in 0.1 M phosphate buffer, pH 7.4 (PB) for 1 h. Samples were washed and incubated in the primary antibody diluted in PBS with 1% BSA-c (Aurion) for 12 h at 4°C. After washing in PBS with 0.1% BSA-c (washing solution), samples were incubated for 30 min in protein A-gold probe (5 nm; Center for Molecular Medicine, University of Utrecht, the Netherlands) diluted 1/50 in PBS with 1% BSA-c. Samples were then washed in washing solution then rinsed in PB and post-fixed with PB containing 2.5% glutaraldehyde for 20 min at 4°C. After washing in PB, cells were osmicated and treated as described for TEM. To test specificity of the immunostaining procedure, the primary antibody was omitted.

RNAi

Ready to use double-stranded siRNA hVFL3-si1 (target sequence: GCGGCTGACATGGCCGAAATA), hVFL3-si2 (target sequence: CAGCGAGCTGGCATTGTACAA), and control

siRNA (AllStars Negative Control) were purchased from Qiagen. siODF2 (ON-TARGETplus Human ODF2) was purchased from Dharmacon. siRNAs were delivered into cells using Lipofectamine RNAiMAX diluted in OptiMEM medium (ThermoFisher Scientific). Cells were fixed after 72 h and processed for immunofluorescence.

Statistical analysis

All statistical analyses were performed using the Prism7 for Mac OS X software (GraphPad Software, Inc.).

Author contribution

N.G. and M.P. contributed equally to this work. V.P. and J.A. conceptualised the study; V.P., N.M., M.P., C.C.-D., R.D. and J.A. performed the investigations; V.H. and B.R.S.M. provided resources; V.P. and J.A. were associated with the writing of the manuscript.

Funding

This work was supported by CNRS (ATIP-AVENIR), La Ligue Contre le Cancer (RS16/75-105) and ANR-15-CE13-0003 funding to J.A. and ANR-10-LABX-0030-INRT, a French state fund managed by ANR under the program “Investissements d’Avenir” labelled ANR-10-IDEX-0002-02 to B.R.S.M. N.G. was recipient of a MESRI Ph.D. fellowship from the French Government.

Acknowledgements

The authors would like to thank S. Kubanza, Q. Delobelle, C. Garcia and T. Léger for technical help, and C. Basquin for helpful discussions and critical reading of the manuscript. We acknowledge the core facilities of Institut Jacques Monod: ImagoSeine facility (member of the France BioImaging infrastructure supported by grant ANR-10-INSB-04 from the French National Research Agency) and Proteomics facility.

Conflict of interest

The authors have declared no conflict of interest.

References

Agircan, F.G., Schiebel, E. and Mardin, B.R. (2014) Separate to operate: control of centrosome positioning and separation. *Philos. R. Soc. Lond. B Biol. Sci.* **369**, 20130461.
Andersen, J.S., Wilkinson, C.J., Mayor, T., Mortensen, P., Nigg, E.A. and Mann, M. (2003) Proteomic characterization of the human centrosome by protein correlation profiling. *Nature* **426**, 570–574.

Anvarian, Z., Mykytyn, K., Mukhopadhyay, S., Pedersen, L.B. and Christensen, S.T. (2019) Cellular signalling by primary cilia in development, organ function and disease. *Nat. Rev. Nephrol.* **15**, 199–219.
Azimzadeh, J., Wong, M.L., Downhour, D.M., Sanchez Alvarado, A. and Marshall, W.F. (2012) Centrosome loss in the evolution of planarians. *Science* **335**, 461–463.
Bahe, S., Stierhof, Y.D., Wilkinson, C.J., Leiss, F. and Nigg, E.A. (2005) Rootletin forms centriole-associated filaments and functions in centrosome cohesion. *J. Cell Biol.* **171**, 27–33.
Barenz, F., Kschonsak, Y.T., Meyer, A., Jafarpour, A., Lorenz, H. and Hoffmann, I. (2018). Ccdc61 controls centrosomal localization of Cep170 and is required for spindle assembly and symmetry. *Mol. Biol. Cell* **29**, 3105–3118.
Basquin, C., Ershov, D., Gaudin, N., Vu, H.T.K., Louis, B., Papon, J.F., Orfila, A.M., Mansour, S., Rink, J.C. and Azimzadeh, J. (2019) Emergence of a bilaterally symmetric pattern from chiral components in the planarian epidermis. *Developmental Cell* **51(4)**: 516–525.
Bengueddach, H., Lemullois, M., Aubusson-Fleury, A. and Koll, F. (2017) Basal body positioning and anchoring in the multiciliated cell *Paramecium tetraurelia*: roles of OFD1 and VFL3. *Cilia* **6**, 6.
Carvalho-Santos, Z., Machado, P., Branco, P., Tavares-Cadete, F., Rodrigues-Martins, A., Pereira-Leal, J.B. and Bettencourt-Dias, M. (2010) Stepwise evolution of the centriole-assembly pathway. *J. Cell Sci.* **123**, 1414–1426.
Cheeseman, I.M. and Desai, A. (2005) A combined approach for the localization and tandem affinity purification of protein complexes from metazoans. *Sci. STKE* **2005**, pl1.
Dammermann, A. and Merdes, A. (2002) Assembly of centrosomal proteins and microtubule organization depends on PCM-1. *J. Cell Biol.* **159**, 255–266.
Delgehr, N., Sillibourne, J. and Bornens, M. (2005) Microtubule nucleation and anchoring at the centrosome are independent processes linked by ninein function. *J. Cell. Sci.* **118**, 1565–1575.
Fang, G., Zhang, D., Yin, H., Zheng, L., Bi, X. and Yuan, L. (2014) Centlein mediates an interaction between C-Nap1 and Cep68 to maintain centrosome cohesion. *J. Cell Sci.* **127**, 1631–1639.
Flanagan, A.M., Stavenschi, E., Basavaraju, S., Gaboriau, D., Hoey, D.A. and Morrison, C.G. (2017) Centriole splitting caused by loss of the centrosomal linker protein C-NAP1 reduces centriolar satellite density and impedes centrosome amplification. *Mol. Biol. Cell* **28**, 736–745.
Geimer, S. and Melkonian, M. (2005) Centrin scaffold in *Chlamydomonas reinhardtii* revealed by immunoelectron microscopy. *Eukaryot Cell* **4**, 1253–1263.
Gromley, A., Jurczyk, A., Sillibourne, J., Halilovic, E., Mogensen, M., Groisman, I., Blomberg, M. and Doxsey, S. (2003) A novel human protein of the maternal centriole is required for the final stages of cytokinesis and entry into S phase. *J. Cell Biol.* **161**, 535–545.
Guarguaglini, G., Duncan, P.I., Stierhof, Y.D., Holmstrom, T., Duensing, S. and Nigg, E.A. (2005) The forkhead-associated domain protein Cep170 interacts with Polo-like kinase 1 and serves as a marker for mature centrioles. *Mol. Biol. Cell* **16**, 1095–1107.
Hall, E.A., Keighren, M., Ford, M.J., Davey, T., Jarman, A.P., Smith, L.B., Jackson, I.J. and Mill, P. (2013) Acute versus chronic loss of mammalian Azi1/Cep131 results in distinct ciliary phenotypes. *PLoS Genet.* **9**, e1003928.
He, R., Huang, N., Bao, Y., Zhou, H., Teng, J. and Chen, J. (2013) LRRC45 is a centrosome linker component required for centrosome cohesion. *Cell Rep.* **4**, 1100–1107.
Hodges, M.E., Scheumann, N., Wickstead, B., Langdale, J.A. and Gull, K. (2010) Reconstructing the evolutionary history of the centriole from protein components. *J. Cell Sci.* **123**, 1407–1413.
Hoops, H.J., Wright, R.L., Jarvik, J.W. and Witman, G.B. (1984) Flagellar waveform and rotational orientation in a *Chlamydomonas* mutant lacking normal striated fibers. *J. Cell Biol.* **98**, 818–824.

- Huang, N., Xia, Y., Zhang, D., Wang, S., Bao, Y., He, R., Teng, J. and Chen, J. (2017) Hierarchical assembly of centriole subdistal appendages via centrosome binding proteins CCDC120 and CCDC68. *Nat. Commun.* **8**, 15057.
- Hung, H.F., Hehnlly, H. and Doxsey, S. (2016) The mother centriole appendage protein cenexin modulates lumen formation through spindle orientation. *Curr. Biol.* **26**, 793–801.
- Ishikawa, H., Kubo, A. and Tsukita, S. (2005) Odf2-deficient mother centrioles lack distal/subdistal appendages and the ability to generate primary cilia. *Nat. Cell Biol.* **7**, 517–524.
- Keller, L.C., Romijn, E.P., Zamora, I., Yates, J.R., 3rd and Marshall, W.F. (2005) Proteomic analysis of isolated *Chlamydomonas* centrioles reveals orthologs of ciliary-disease genes. *Curr. Biol.* **15**, 1090–1098.
- Kim, J.C., Badano, J.L., Sibold, S., Esmail, M.A., Hill, J., Hoskins, B.E., Leitch, C.C., Venner, K., Ansley, S.J., Ross, A.J., Leroux, M.R., Katsanis, N. and Beales, P.L. (2004) The Bardet-Biedl protein BBS4 targets cargo to the pericentriolar region and is required for microtubule anchoring and cell cycle progression. *Nat. Genet.* **36**, 462–470.
- Kodani, A., Salome Sirerol-Piquer, M., Seol, A., Garcia-Verdugo, J.M. and Reiter, J.F. (2013) Kif3a interacts with Dynactin subunit p150 Glued to organize centriole subdistal appendages. *EMBO J.* **32**, 597–607.
- Kodani, A., Tonthat, V., Wu, B. and Sutterlin, C. (2010) Par6 alpha interacts with the dynactin subunit p150 glued and is a critical regulator of centrosomal protein recruitment. *Mol. Biol. Cell* **21**, 3376–3385.
- Kubo, A., Sasaki, H., Yuba-Kubo, A., Tsukita, S. and Shiina, N. (1999) Centriolar satellites: molecular characterization, ATP-dependent movement toward centrioles and possible involvement in ciliogenesis. *J. Cell Biol.* **147**, 969–980.
- Kubo, A. and Tsukita, S. (2003) Non-membranous granular organelle consisting of PCM-1: subcellular distribution and cell-cycle-dependent assembly/disassembly. *J. Cell Sci.* **116**, 919–928.
- Mayor, T., Hacker, U., Stierhof, Y.D. and Nigg, E.A. (2002) The mechanism regulating the dissociation of the centrosomal protein C-Nap1 from mitotic spindle poles. *J. Cell. Sci.* **115**, 3275–3284.
- Mayor, T., Stierhof, Y.D., Tanaka, K., Fry, A.M. and Nigg, E.A. (2000) The centrosomal protein C-Nap1 is required for cell cycle-regulated centrosome cohesion. *J. Cell Biol.* **151**, 837–846.
- Mazo, G., Soplop, N., Wang, W.J., Uryu, K. and Tsou, M.B. (2016) Spatial control of primary ciliogenesis by subdistal appendages alters sensation-associated properties of cilia. *Dev. Cell* **39**, 424–437.
- Mogensen, M.M., Malik, A., Piel, M., Bouckson-Castaing, V. and Bornens, M. (2000) Microtubule minus-end anchorage at centrosomal and non-centrosomal sites: the role of ninein. *J. Cell Sci.* **113** (Pt 17), 3013–3023.
- Panic, M., Hata, S., Neuner, A. and Schiebel, E. (2015) The centrosomal linker and microtubules provide dual levels of spatial coordination of centrosomes. *PLoS Genet.* **11**, e1005243.
- Piel, M., Meyer, P., Khodjakov, A., Rieder, C.L. and Bornens, M. (2000) The respective contributions of the mother and daughter centrioles to centrosome activity and behavior in vertebrate cells. *J. Cell Biol.* **149**, 317–330.
- Reiter, J.F. and Leroux, M.R. (2017) Genes and molecular pathways underpinning ciliopathies. *Nat. Rev. Mol. Cell Biol.* **18**, 533–547.
- Rossi, A., Kontarakis, Z., Gerri, C., Nolte, H., Holper, S., Kruger, M. and Stainier, D.Y. (2015) Genetic compensation induced by deleterious mutations but not gene knockdowns. *Nature* **524**, 230–233.
- Tassin, A.M., Lemullois, M. and Aubusson-Fleury, A. (2015) *Paramecium tetraurelia* basal body structure. *Cilia* **5**, 6.
- Thery, M., Racine, V., Piel, M., Pepin, A., Dimitrov, A., Chen, Y., Sibarita, J.B. and Bornens, M. (2006) Anisotropy of cell adhesive microenvironment governs cell internal organization and orientation of polarity. *Proc. Natl. Acad. Sci. U. S. A.* **103**, 19771–19776.
- Tollenaere, M.A., Mailand, N. and Bekker-Jensen, S. (2015) Centriolar satellites: key mediators of centrosome functions. *Cell. Mol. Life Sci.* **72**, 11–23.
- Tu, H.Q., Qin, X.H., Liu, Z.B., Song, Z.Q., Hu, H.B., Zhang, Y.C., Chang, Y., Wu, M., Huang, Y., Bai, Y.F., Wang, G., Han, Q.Y., Li, A.L., Zhou, T., Liu, F., Zhang, X.M. and Li, H.Y. (2018) Microtubule asters anchored by FSD1 control axoneme assembly and ciliogenesis. *Nat. Commun.* **9**, 5277.
- Veleri, S., Manjunath, S.H., Fariss, R.N., May-Simera, H., Brooks, M., Foskett, T.A., Gao, C., Longo, T.A., Liu, P., Nagashima, K., Rachel, R.A., Li, T., Dong, L. and Swaroop, A. (2014) Ciliopathy-associated gene *Cc2d2a* promotes assembly of subdistal appendages on the mother centriole during cilia biogenesis. *Nat. Commun.* **5**, 4207.
- Wang, L., Lee, K., Malonis, R., Sanchez, I. and Dynlacht, B.D. (2016) Tethering of an E3 ligase by PCM1 regulates the abundance of centrosomal KIAA0586/Talpid3 and promotes ciliogenesis. *Elife* **5**, e12950.
- Waterman-Storer, C.M., Karki, S. and Holzbaur, E.L. (1995) The p150Glued component of the dynactin complex binds to both microtubules and the actin-related protein centractin (Arp-1). *Proc. Natl. Acad. Sci. U. S. A.* **92**, 1634–1638.
- Welburn, J.P. and Cheeseman, I.M. (2012) The microtubule-binding protein Cep170 promotes the targeting of the kinesin-13 depolymerase Kif2b to the mitotic spindle. *Mol. Biol. Cell* **23**, 4786–4795.
- Wright, R.L., Chojnacki, B. and Jarvik, J.W. (1983) Abnormal basal-body number, location and orientation in a striated fiber-defective mutant of *Chlamydomonas reinhardtii*. *J. Cell Biol.* **96**, 1697–1707.
- Xia, Y., Huang, N., Chen, Z., Li, F., Fan, G., Ma, D., Chen, J. and Teng, J. (2018) CCDC102B functions in centrosome linker assembly and centrosome cohesion. *J. Cell Sci.* **131**, jcs222901.

Received: 27 May 2019; Revised: 12 November 2019; Accepted: 15 November 2019; Accepted article online: 2 December 2019

2.3. Emergence of a bilaterally symmetric pattern from chiral components in Planarian epidermis (Article 3)

The highlights of this work are:

- Centrioles form a bilaterally symmetric pattern across the planarian epidermis.
- Within cells, centrioles are organized into a chiral asymmetric network.
- ODF2 and VFL1/3 help in establishing asymmetric connections between centrioles.
- Bilaterally symmetric patterns can emerge from chiral cellular structures.

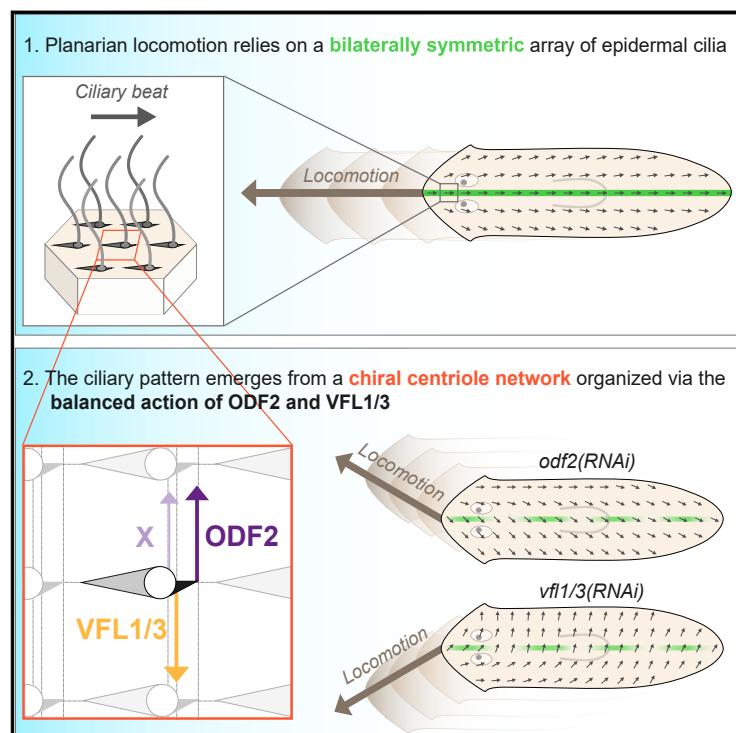
My participation of this work includes:

Developing and testing the anti-SMED-VFL1 and anti-SMED-ODF2 antibodies used in this article.

Developmental Cell

Emergence of a Bilaterally Symmetric Pattern from Chiral Components in the Planarian Epidermis

Graphical Abstract



Authors

Cyril Basquin, Dmitry Ershov, Noémie Gaudin, ..., Sarah Mansour, Jochen Christian Rink, Juliette Azimzadeh

Correspondence

juliette.azimzadeh@ijm.fr

In Brief

This study by Basquin et al. shows that bilaterally symmetric tissue patterns can emerge from chiral cellular structures. Using the planarian flatworm as a model, they describe how the intrinsic chirality of the cytoskeletal network that controls the orientation of epidermal cilia is compensated to achieve bilateral symmetry of the ciliary pattern.

Highlights

- Centrioles form a bilaterally symmetric pattern across the planarian epidermis
- Within cells, centrioles are organized into a chiral asymmetric network
- ODF2 and VFL1/3 help in establishing asymmetric connections between centrioles
- Bilaterally symmetric patterns can emerge from chiral cellular structures



Emergence of a Bilaterally Symmetric Pattern from Chiral Components in the Planarian Epidermis

Cyril Basquin,¹ Dmitry Ershov,² Noémie Gaudin,¹ Hanh Thi-Kim Vu,³ Bruno Louis,^{4,5,6} Jean-François Papon,^{4,5,7,8} Anne-Marie Orfila,¹ Sarah Mansour,³ Jochen Christian Rink,³ and Juliette Azimzadeh^{1,9,*}

¹Université de Paris, Institut Jacques Monod, CNRS UMR 7592, Paris 75013, France

²Institut Pasteur, Paris 75015, France

³Max Planck Institute for Molecular Cell Biology and Genetics, Dresden 01307, Germany

⁴INSERM U955, Créteil 94010, France

⁵CNRS ERL7240, Créteil 94010, France

⁶Faculté de Médecine, Université Paris-Est, Créteil 94010, France

⁷Hôpital Kremlin-Bicêtre, AP-HP, Le Kremlin-Bicêtre 94275, France

⁸Faculté de Médecine, Université Paris-Saclay, Le Kremlin-Bicêtre 94070, France

⁹Lead Contact

*Correspondence: juliette.azimzadeh@ijm.fr

<https://doi.org/10.1016/j.devcel.2019.10.021>

SUMMARY

Most animals exhibit mirror-symmetric body plans, yet the molecular constituents from which they are formed are often chiral. In planarian flatworms, centrioles are arranged in a bilaterally symmetric pattern across the ventral epidermis. Here, we found that this pattern is generated by a network of centrioles with prominent chiral asymmetric properties. We identify centriole components required for establishing asymmetric connections between centrioles and balancing their effects to align centrioles along polarity fields. SMED-ODF2, SMED-VFL1, and SMED-VFL3 affect the assembly of centriole appendages that tether cytoskeletal connectors to position the centrioles. We further show that the medio-lateral polarization of centrioles relies on mechanisms that are partly distinct on the left and right sides of the planarian body. Our findings shed light on how bilaterally symmetrical patterns can emerge from chiral cellular organizations.

INTRODUCTION

Animals with outwardly mirror-symmetric bodies, the so-called bilaterians, constitute the largest group of animals on earth. However, many of the molecular components that make up the mirror-symmetric bilaterians are intrinsically chiral, i.e., exhibit broken reflection symmetry. This raises a conceptual conundrum, as Euclidean geometry precludes the construction of a mirror-symmetric structure out of chiral components without the simultaneous use of their mirrored partners. One prominent example of a chiral cellular constituent is the centriole, the evolutionarily ancient nucleating center of the microtubule cytoskeleton (Azimzadeh, 2014). Centrioles consist of nine microtubule

triplets arranged in a circular arrangement. Their chirality results from the polar structure of the triplets and their placement at an angle with respect to their neighboring triplets. In many protozoa, this inherent chiral property is amplified by asymmetries between the different centriole triplets, which anchor distinct elements of the cytoskeleton and ultimately propagate the centriole chirality to chirality over the entire cell (Boyd et al., 2011; Marshall, 2012; Yubuki and Leander, 2013). The establishment of left-right asymmetry in vertebrates via the (chiral) clockwise rotation of cilia at the surface of the embryonic node—together with anterior-posterior asymmetric positioning of the nodal cilia, provides a further example of organismal asymmetry that ultimately has its roots in centriole chirality (Chen and Zhong, 2015; Hashimoto et al., 2010; Omori et al., 2017; Shinohara and Hamada, 2017). In this process, the centriole functions as the “F molecule” originally theorized by Brown and Wolpert, which specifies the orientation of the left-right axis by aligning along the two other embryonic axes (Brown and Wolpert, 1990).

However, not all centriole-nucleated structures display obvious chirality. For example, the cilia of multi-ciliated cells beat in a whip-like pattern and the polarization of all cilia along the polarity axes of the body plan thus allows directional mucus transport or whole animal translocation. In this case, centrioles carry two types of appendages that align with the axis of ciliary beat: the basal foot and the ciliary rootlet. These appendages in turn anchor cytoskeletal arrays that connect centrioles to each other and to the cellular junctions (Antoniades et al., 2014; Kunimoto et al., 2012; Vladar et al., 2012; Werner et al., 2011). Polarity proteins localized at the junctions and at the centrioles regulate cytoskeleton architecture to coordinate centriole rotational polarity with the planar polarity of the epithelium (Guirao et al., 2010; Park et al., 2008; Vladar et al., 2012). Recent work from our laboratories demonstrate the long-range polarization of ciliary rootlets in the planarian ventral epidermis along the head-tail axis that is mediated by the evolutionary conserved Wnt/planar cell polarity (Wnt/PCP) pathway, superimposed in the head region with a mirror-symmetric polarization component toward the body edge mediated by the Fat/Dachsous (Ft/Ds)



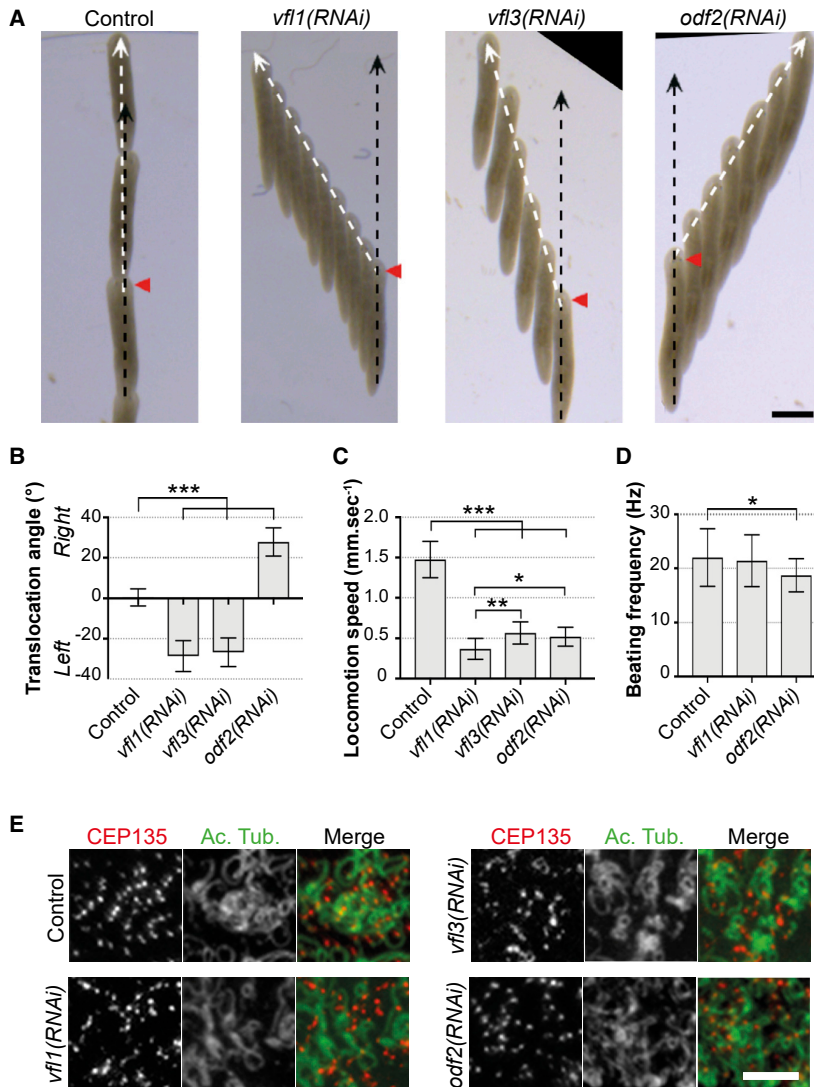


Figure 1. Depletion of SMED-ODF2 and SMED-VFL1/3 Affects the Direction of Locomotion in an Opposite Manner

(A) t-projection (2 s apart) of control planarians or animals depleted from VFL1/3 and ODF2. Black arrows: expected trajectory based on the initial orientation of the A/P axis; white arrows: observed trajectory. Red arrowheads: position of the head. Bar, 1 mm.

(B) Quantification of the angle between the translocation and head-tail vectors as shown in (A). 3 independent experiments, $62 \leq n \leq 344$ for each condition. Error bars represent SD. Asterisks indicate a significant difference from the control condition (Kruskal-Wallis test; *** $p < 0.001$).

(C) Locomotion speed of control and RNAi animals. 3 independent experiments, $41 \leq n \leq 120$ for each condition. Error bars represent SD. Asterisks indicate a significant difference from the control condition (Kruskal-Wallis test; * $p < 0.05$, ** $p < 0.01$, *** $p < 0.001$).

(D) Ciliary beat frequency in control and RNAi animals. $11 \leq n \leq 26$ independent measurements were performed on a total of 2 (control) or 3 (RNAi) different animals. Error bars represent SD. Asterisks indicate a significant difference from the control condition (Kruskal-Wallis test; * $p < 0.05$).

(E) Immunofluorescence views of the ventral epidermis of control and RNAi planarians. Centrioles were stained with an anti-SMED-CEP135 antibody (red) and cilia with an anti-acetylated tubulin (green). Bar, 5 μm . See also Figure S1; Videos S1 and S2.

pathway (Vu et al., 2019). Thus, in planarians and multi-ciliated epithelia in general, centrioles behave as bilaterally symmetric objects that align with the cardinal body axes of the bilaterian body plan.

Here, we demonstrate cryptic chirality underneath the apparent mirror-symmetry of planarian centriole alignment, which in wild-type animals is compensated by the opposing effects of the centriole components ODF2 and VFL1/VFL3. Our results provide insights into how animals can build bilaterally symmetric tissue patterns from chiral cellular constituents.

RESULTS

Centriole Components Affecting Planarian Locomotion in a Left-Right Asymmetric Manner

Previous results have established that paralysis, loss or gross misalignments of planarian cilia, all disrupt the smooth gliding motility of the animals and result in a secondary

phenotype (Azimzadeh et al., 2012; Reddien et al., 2005). Whereas in wild-type animals, the translocation vector (movement direction) was always in alignment with the head-tail vector (anterior-posterior [A/P] axis), RNAi animals displayed a striking misalignment between the two vectors (Figures 1A and S1; Video S1). Specifically, *vfl1*- and *vfl3(RNAi)* animals always translocated at an angle of $-29^\circ \pm 8^\circ$ and $-27^\circ \pm 7^\circ$ (counterclockwise) relative to the A-P axis, respectively, which resulted in a drift to the left. In contrast, *odf2(RNAi)* animals translocated at an angle of $28^\circ \pm 8^\circ$ (clockwise) and drifted to the right (Figure 1B). RNAi animals exhibited a drastic reduction in locomotion speed compared to controls, particularly in *vfl1(RNAi)* animals, but nevertheless retained gliding motility (Figure 1C; Video S1). In agreement with this, cilia were present across the ventral epidermis of RNAi animals like in control planarians (Figure 1E). High-speed imaging of cilia in live *odf2(RNAi)* and *vfl1(RNAi)* animals confirmed that cilia were motile and that beating frequency was overall

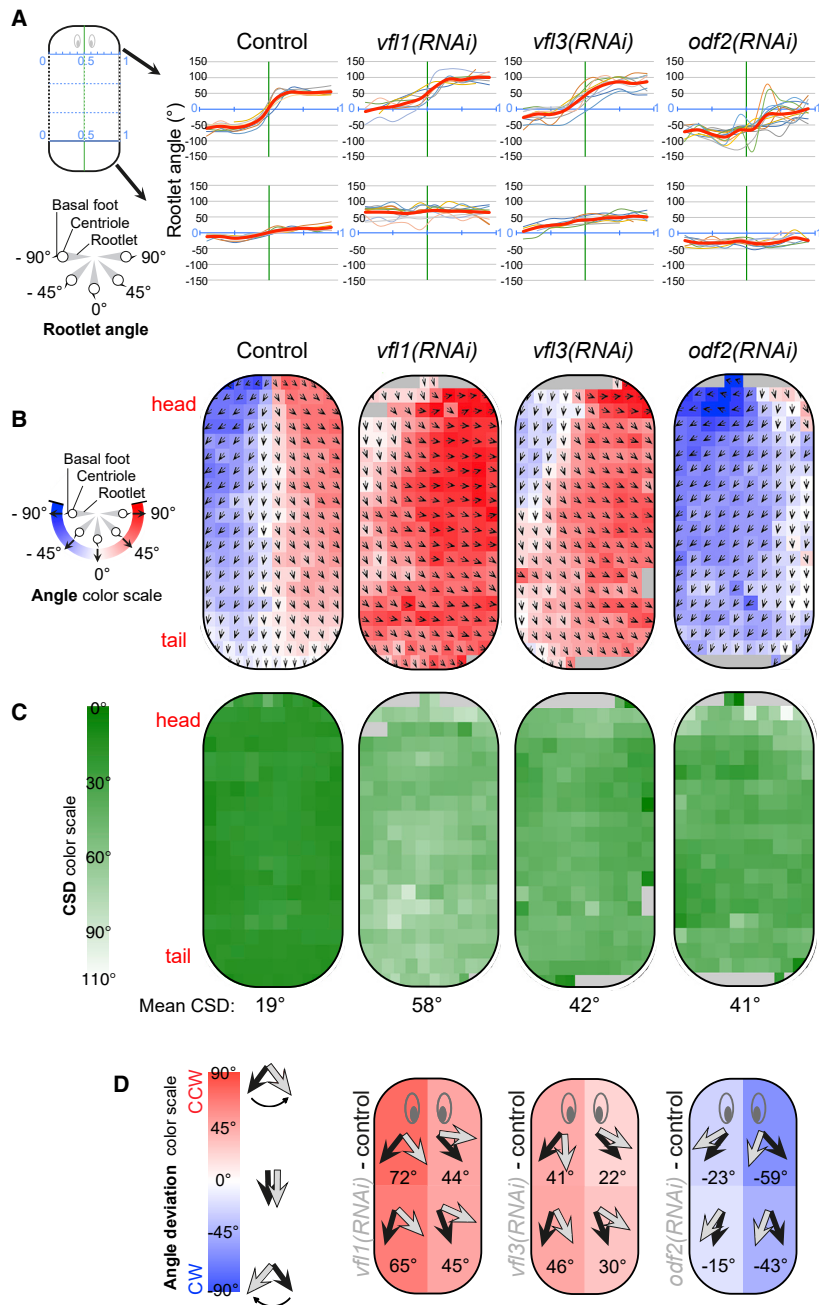


Figure 2. Sidewinder Locomotion Phenotypes Are Caused by Aberrant Centriole Rotational Polarity in the Ventral Epidermis

(A) Graphical representation of rootlet angle variation along the M/L axis in the anterior and posterior sides of control and RNAi planarians. Individual curves represent a single animal except the red curve that shows the mean.

(B) Centriole rotational polarity in the ventral epidermis of control or RNAi animals (viewed from above). Arrows show the orientation of the mean rootlet angle vector for each of 200 subdivisions of the epidermis. The color code highlights the CW (blue) or CCW (red) rotation of rootlets with respect to the A/P axis. $n \geq 6$ animals per condition.

(C) Heatmap of the local circular standard deviation (CSD) values associated to the mean rootlet angles represented in (B). The mean of all local CSD values is also indicated. $n \geq 6$ animals per condition.

(D) Schematic representation of angle deviations induced by depletion of VFL1/3 and ODF2. In each quadrant, arrows show the mean rootlet angle in control (black arrow) or RNAi-treated (gray arrow) planarians. Angle deviations are color-coded and the corresponding numeric values are indicated. See also Figures S1 and S3.

Sidewinder Phenotypes Are Caused by Defects in Centriole Rotational Polarity

To determine whether the observed locomotion defects were induced by anomalies in centriole positioning, we analyzed centriole rotational polarity in RNAi-treated animals. Using an antibody against ROOTLETIN1, a component of the ciliary rootlet (Vu et al., 2019), we measured the angle vector between individual rootlets and the A/P axis (Figures 2A, 2B, and S2). Depletion of all three genes decreased the homogeneity of rootlet polarity (i.e., increased the circular standard deviation or CSD) in all parts of the ventral epidermis, supporting that the entire tissue was affected (Figure 2C). Overall, the mean CSD (mean of CSD values determined for each subdivision of the epidermis) increased from 19° in control to 41° in

comparable to control values, with only a modest decrease in *odf2(RNAi)* animals (Figure 1D; Video S2). Cilia nevertheless appeared to beat less synchronously in RNAi animals, which likely contributed to the decrease in the locomotion speed that we observed (Video S2).

Thus, depleting the centriole components ODF2 and VFL1/3 induced left-right asymmetric locomotion phenotypes of opposite handedness. Furthermore, the persistence of gliding motility indicated maintained functionality and long-range alignment of epidermal cilia.

odf2(RNAi), 42° in *vfl3(RNAi)*, and up to 58° in *vfl1(RNAi)* animals. Decreased rootlet alignment likely contributed to the lower locomotion speed observed in RNAi animals, as coordination of ciliary beat orientation is critical for multi-ciliated cell function (Kunimoto et al., 2012; Park et al., 2008). In agreement, higher dispersion of rootlet angles in *vfl1(RNAi)* correlated with a stronger reduction in the locomotion speed (Figure 1C). Despite increased angle dispersion, we observed highly consistent patterns of orientation in RNAi animals (Figures 2A, 2B, and S3). Rootlets were pivoted counterclockwise

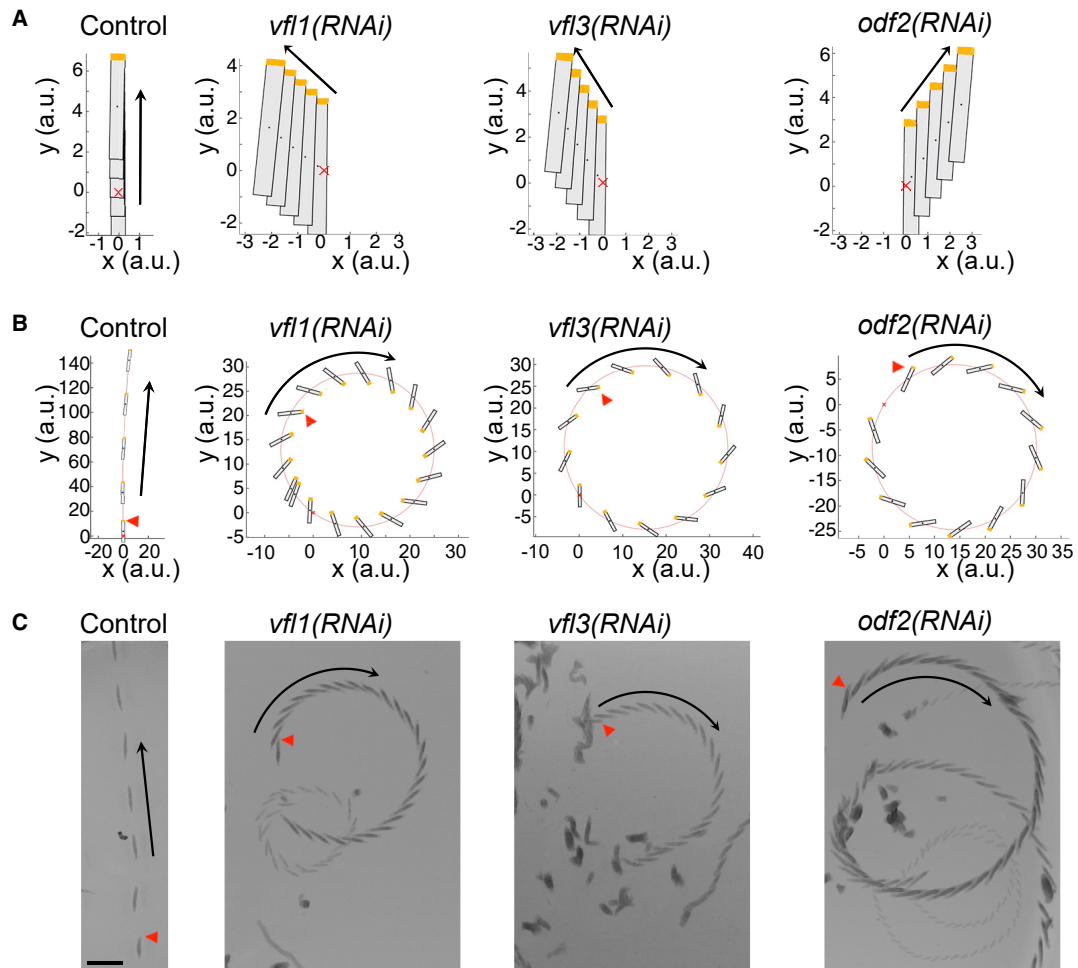


Figure 3. Rootlet Orientation Defects in RNAi Planarians Are Sufficient to Predict Sidewinder Locomotion

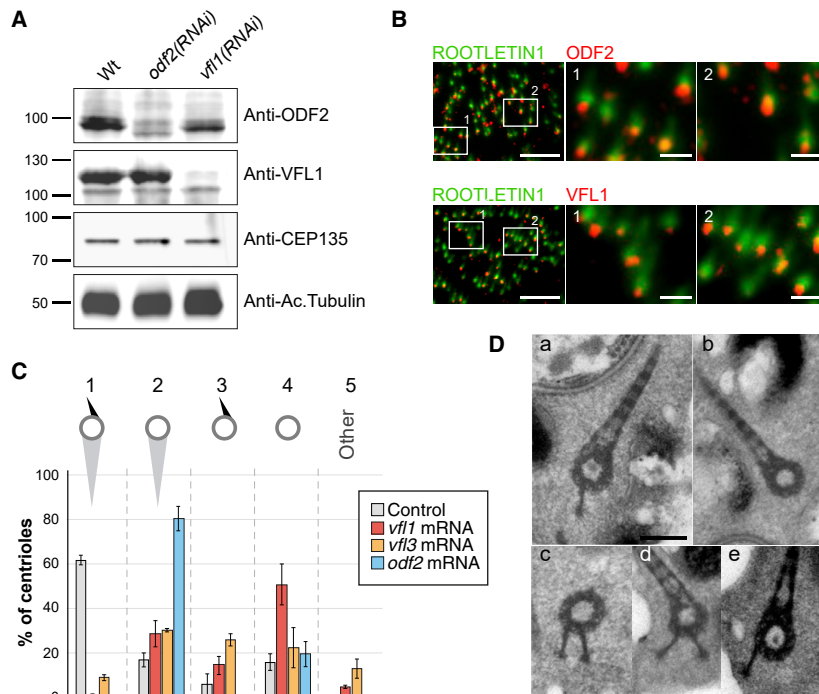
(A) Simulation of trajectories of control and RNAi planarians based on experimentally measured rootlet angles (see STAR Methods). The position of the head is in yellow. Red crosses at $x,y(0,0)$ indicate the starting point ($t = 0$) and black arrows show the direction of locomotion.

(B) Simulation of trajectories over longer time scales using experimental data obtained from *vfl1*⁻, *vfl3*⁻, *odf2*⁻, or control RNAi animals. The model predicts that depletion of VFL1, VFL3, and ODF2 will all result in a CW circular trajectory. For each graph, the anterior pole of the planarian is in yellow, the red cross at $x,y(0,0)$ indicates the starting point ($t = 0$), and the black arrow shows the direction of locomotion.

(C) Experimental observation of the CW circular trajectories of *vfl1*⁻, *vfl3*⁻, and *odf2*(RNAi) animals over longer time scales (~2 min). Each image corresponds to a t-projection of individual frames taken 5 s apart. Animals fortuitously crossing the field of acquisition (see Video S3) were manually erased for improved clarity. Red arrowheads indicate the head of the planarian at the beginning of the movie. Bar, 5 mm. See also Figure S4; Video S3.

in *vfl1*(RNAi) and *vfl3*(RNAi) and clockwise in *odf2*(RNAi) compared to control flatworms, confirming that centriole polarity is affected. Control animals display a bilaterally symmetric rootlet pattern characterized by a gradual increase in rootlet angles along the A/P and medio-lateral (M/L) axes (splay) (Vu et al., 2019) (Figures 2A, 2B, and 2D). Variation in rootlet angles along polarity axes still occurred in sidewinder animals despite the overall rotation of rootlet angles, which resulted in strikingly left-right asymmetric rootlet patterns across the ventral epidermis (Figures 2A, 2B, and 2D). To determine whether these complex patterns could explain the lateral translocation that characterizes the sidewinder phenotypes, we turned to computational modeling. We developed a model based on the assumption that the net flow generated by

beating cilia is locally aligned with the mean rootlet angle (Figure S4). Simulations recapitulated experimental trajectories, supporting that the observed defects in centriole rotational polarity are sufficient to cause the sidewinder phenotypes (Figure 3A). Interestingly, the model predicted that at longer time scales, all sidewinder animals would follow a clockwise circular trajectory, which we verified experimentally (Figures 3B and 3C; Video S3). Together, our data support that the sidewinder phenotypes are caused by the rotation of centrioles in the plane of the epidermis, either clockwise or counterclockwise. Thus, the sidewinder phenotypes are chirality phenotypes that uncover cryptic left-right asymmetries in centriole orientation underneath the bilateral symmetry of the wild-type pattern.



Planarian ODF2 and VFL1/3 Control the Assembly of Centriole Appendages

To gain further insights into the origin of these asymmetries, we characterized the function of planarian ODF2 and VFL1/3 proteins. SMED-ODF2 is the planarian ortholog of mouse ODF2/Cenexin, a component of the basal foot (Kunimoto et al., 2012). SMED-VFL1 and SMED-VFL3 are the orthologs of centriole proteins originally identified in unicellular models (Hoops et al., 1984; Silflow et al., 2001). We obtained antibodies against planarian VFL1 and ODF2 proteins and found that both stain centrioles across the ventral epidermis, confirming that they are centriole components in planarians (Figures 4A, 4B, and S5). We next analyzed the ultrastructure of centrioles in control and RNAi animals. In control samples, most centrioles exhibited a basal foot and a rootlet, although in a proportion of centrioles the basal foot (33% ± 7%) or the rootlet (22% ± 1%) was not included in the same electron microscopic section. In *odf2(RNAi)* animals, centrioles were systematically missing a basal foot, confirming data from mouse (Kunimoto et al., 2012), but rootlet assembly was unaffected (Figures 4C and 4D). In *vfl1(RNAi)* and *vfl3(RNAi)*, the assembly of both the basal foot and the rootlet were abnormal. In sections from *vfl1(RNAi)* animals, 80% ± 3% centrioles had no visible basal foot and 72% ± 6% no visible rootlet. Assuming that a similar fraction of basal feet and rootlets were not included in the same electron microscopic section as in controls indicated that about half of the centrioles lacked a basal foot and half lacked a rootlet. Similar results were obtained with *vfl3(RNAi)*, although the defects were less pronounced (52% ± 8% of centrioles without a basal foot and 48% ± 6% without a rootlet visible in the same section; ~ 1/3 of centrioles of each category considering the overestimation due to sectioning). In addition, centrioles with

anomalies in the number and/or respective positions of the appendages were observed (Figures 4C and 4D), suggesting that VFL1 and VFL3 affect the rotational asymmetry of centrioles. Thus, ODF2, VFL1, and VFL3 are centriole components required for appendage formation in the planarian epidermis. How is this related to the chirality of the sidewinder phenotypes? Strikingly, structural chirality is more conspicuous in planarians, in which the basal foot is asymmetric and positioned at an angle with respect to the beating axis (Figure 4D-a), unlike vertebrate basal feet that look more symmetric (Kunimoto et al., 2012; Mitchell et al., 2007). In addition, we noticed a strong left-right bias in cases where the respective positions of appendages were aberrant, as the basal foot was almost always found on the same side of the centriole with respect to the rootlet axis (31/32 of *vfl3(RNAi)* and 10/10 of *vfl1(RNAi)* centrioles were as in Figures 4D-d and 4D-e), suggesting that microtubule triplets on the left side possess specific characteristics. Thus, the basal foot and the centriole itself are chiral asymmetric, and these asymmetries depend in part on the ODF2 and VFL1 and VFL3 proteins.

ODF2 and VFL1/3 Allow Organizing a Chiral Asymmetric Centriole Network

One plausible model is that centriole chirality affects the architecture of cytoskeletal networks attached to the centrioles, possibly generating asymmetric forces. To better understand how ODF2 and VFL1/3 proteins affect the connections between centrioles, we studied their impact on centriole network organization. In planarians, large mucus granules (up to several microns in diameter) are secreted directly through the surface of the cells (Basquin et al., 2015; Hayes, 2017). Accordingly, we noticed that centrioles were irregularly distributed at the apical surface of control planarians, revealing the presence of “holes”

Figure 4. ODF2 and VFL1/3 Are Required for Proper Assembly of Centriole Appendages

(A) Assessment of anti-SMED-ODF2 and anti-SMED-VFL1 antibody specificity by western blot. Anti-SMED-CEP135 and anti-acetylated tubulin were used as loading controls. 50 μg total proteins (10 μg for acetylated tubulin) from control, *odf2(RNAi)*, and *vfl1(RNAi)* samples were analyzed.

(B) Immunofluorescence views of the ventral epidermis showing the respective localization of ODF2 (top) or VFL1 (bottom) in red and ROOTLETIN1 in green. Insets are magnified × 5. Bars, 5 μm (insets: 1 μm).

(C) Quantification of centriole ultrastructural defects in the ventral epidermis of control or RNAi animals. Percentages of centrioles with a basal foot and a rootlet at the correct position (1), no visible basal foot (2), no visible rootlet (3), no visible appendage (4), or appendages in abnormal number and/or relative positions (5) are shown. For each condition, 300–500 centrioles from 2–3 different animals were analyzed. Bars represent SD between different animals.

(D) Electron microscopic views of centrioles in epidermal cells in control (a), *odf2(RNAi)* (b), or *vfl3(RNAi)* (c–e) animals. Bar, 0.2 μm. See also Figure S5.

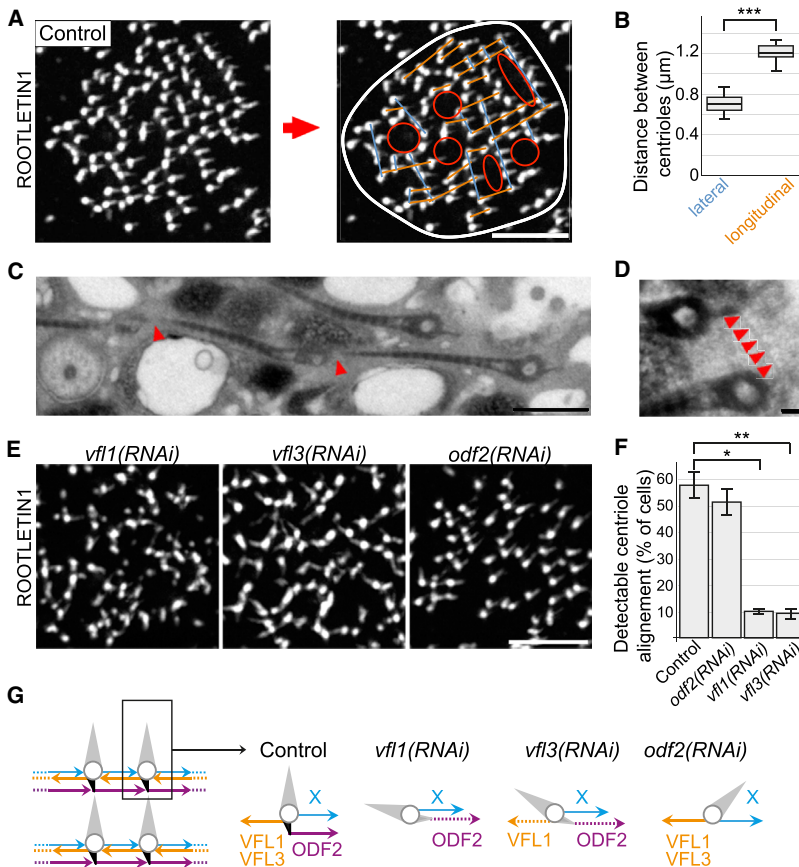


Figure 5. ODF2 and VFL1/3 Organize a Chiral Asymmetric Network of Centrioles

(A) ROOTLETIN1 staining of the ventral epidermis of a control animal. White line on the right panel: cell boundary; red circles: putative mucus secretion sites. Orange and blue lines: longitudinal and lateral rows of centrioles, respectively. Bar, 5 μm .

(B) Mean distance separating neighboring centrioles in lateral and longitudinal rows in control animals ($n \geq 700$ measurements from 17 different animals). Bars represent SD. Asterisks indicate a significant difference between the two variables (Mann-Whitney test; *** $p < 0.001$).

(C) Electron microscopic view of a control multi-ciliated cell showing a longitudinal row of centrioles. Red arrowheads point to rootlet tips. Bar, 0.5 μm .

(D) Electron microscopic view of an epidermal centriole. Arrowheads highlight a microtubule in the vicinity of two basal feet. Bar is 0.1 μm .

(E) ROOTLETIN1 staining of the ventral epidermis of RNAi animals. Bar, 5 μm .

(F) Percentage of epidermal cells displaying at least one rectangular arrangement of minimum four centrioles ($n \geq 500$ cells from 5 different animals analyzed per condition). Bars represent SD. Asterisks indicate a significant difference from the control condition (Kruskal-Wallis test; * $p < 0.05$, ** $p < 0.01$).

(G) Schematic model of the organization of centrioles in planarian multi-ciliated cells and the forces exerted on individual centrioles by elements of the cytoskeletal network via VFL1, VFL3, or ODF2 in control and RNAi-depleted planarians. The involvement of a component X is supported by results from the simultaneous inactivation of VFL1/3 and ODF2. The exact position where cytoskeletal elements bind to centrioles via VFL1/3- and X, and the notion that all forces are pulling forces, are hypothetical. See also Figures S1, S6, and S7; Video S4.

in the pattern that likely correspond to mucus secreting sites (Figure 5A). Outside of these regions, however, centrioles tended to align both laterally and along the beating direction, forming rows of up to 10 aligned centrioles (Figures 5A and S6). Within these rows, the distance separating consecutive centrioles along the two axes showed little variation (Figure 5B), suggesting the existence of structural constraints in centriole network organization. Ultrastructural analyses revealed that rootlets often terminate in the vicinity of a posteriorly positioned centriole and are on average $1.52 \pm 0.28 \mu\text{m}$ long ($n = 73$), close to the mean longitudinal distance determined by immunofluorescence (Figures 5B and 5C). Thus, rootlets appear to act as spacers between centriole rows along the beating axis. In addition, we observed microtubules attached to a basal foot and running perpendicular or oblique to the beating axis (Figure 5D), suggesting that microtubules are involved in the lateral alignment of centrioles. Hence, these data suggest that cytoskeletal connection between appendages connect neighboring centrioles to achieve proper spacing and alignment, as described in other systems (Kunimoto et al., 2012; Werner et al., 2011).

We next analyzed the impact of ODF2 and VFL1/3-depletion on centriole organization. In *odf2(RNAi)* animals, alignment of centrioles was still detected both longitudinally and laterally in most of the cells, although defects in centriole alignment and

polarity were widespread (Figures 5E and 5F). Thus, centrioles are aligned and spaced apart in a manner that is to a large extent independent from the basal foot, possibly via actin connectors as in *Xenopus* (Antoniades et al., 2014), although we could not observe actin with sufficient resolution in the planarian epidermis. This network induces a clockwise rotation of the centrioles that in control planarians is counteracted by cytoskeletal elements acting on the basal foot. In *vfl1(RNAi)* and *vfl3(RNAi)* animals, centriole alignment was strongly perturbed, indicating a more severe disorganization of the centriole network (Figures 5E and 5F). This is not unexpected as depletion of VFL1/3 impairs rootlet assembly, and rootlets seem to play a role in the longitudinal organization of centrioles. *vfl1(RNAi)* and *vfl3(RNAi)* animals are also partially defective in basal foot assembly, and hence, the counterclockwise rotation of rootlets observed in these conditions is unlikely to result solely from forces exerted via ODF2 and the basal foot. In agreement with this, the simultaneous depletion of VFL1/3 and ODF2 neither randomized, nor disrupted rootlet patterns (Figures S1, S3, and S7; Video S4), supporting the existence of additional attachment points between the cytoskeleton and the centrioles (component X in Figures 5G and S7).

Taken together, our results support that ODF2 and VFL1/3 are necessary for organizing the centriole network and

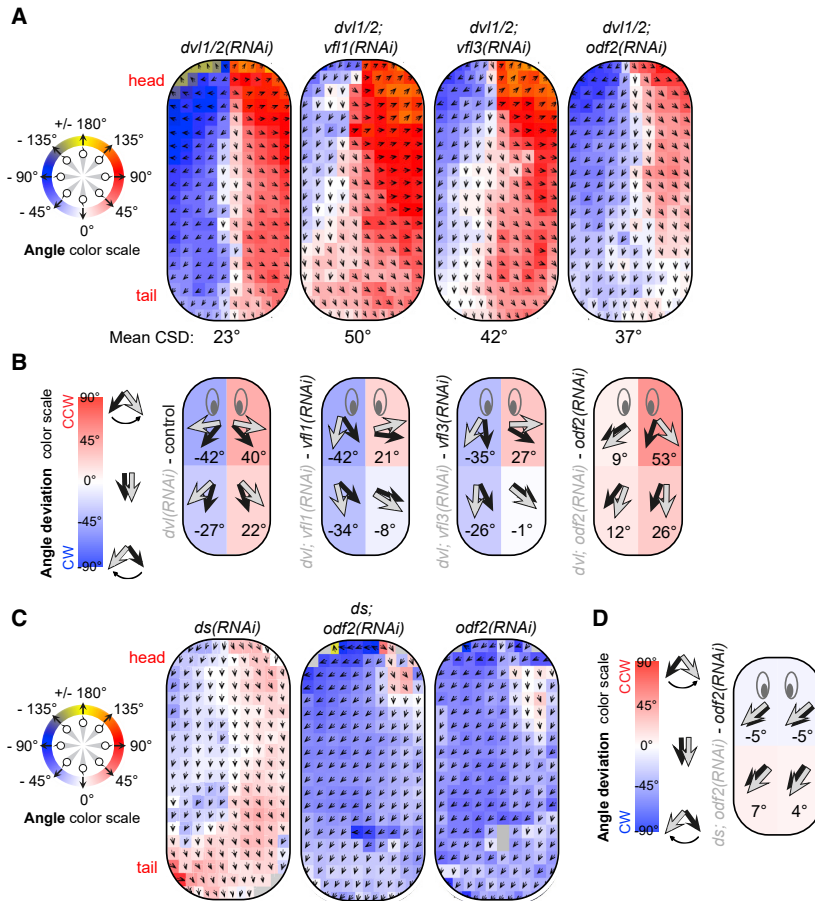


Figure 6. M/L Polarization of Centrioles Requires ODF2 and Additional Network Components

(A) Centriole rotational polarity in flatworms depleted from DVL1/2 only or in combination with depletion of VFL1, VFL3, or ODF2, represented as in Figure 2B ($n \geq 5$ animals analyzed per condition).

(B) Schematic representation of the shift resulting from DVL1/2 depletion in control and RNAi animals. Arrows: mean rootlet orientation in each quadrant in the presence of normal (black arrows) or decreased (gray arrows) levels of DVL1/2. Angle deviations between control and RNAi-treated animals are color-coded, and the corresponding numeric values are indicated.

(C) Centriole rotational polarity in *ds(RNAi)*, *odf2(RNAi)*, or *odf2;ds(RNAi)* planarians as in (A) ($n = 4$ for *ds(RNAi)*, 2 for *odf2(RNAi)*, and 6 for *odf2;ds(RNAi)*).

(D) Schematic representation of angle deviations resulting from Ds depletion in ODF2-depleted animals as in (B). See also Figures S1–S3; Video S5.

balancing opposite forces that likely result from an asymmetric attachment of the centrioles to the cytoskeletal network (Figure 5G).

M/L Polarization of Centrioles Involves Partially Distinct Mechanisms on the Left and Right Sides of the Body

Given the intrinsic chirality of the centriole network, how can planarians achieve the bilaterally symmetric rootlet pattern observed in wild-type animals? Our recent results demonstrate that the wild-type pattern emerges via the integration of Wnt/PCP and Ft/Ds planar cell polarity cues that act specifically along the A/P and M/L axes, respectively (Vu et al., 2019). Planar cell polarity pathways control the position of cellular structures by interacting with cytoskeletal networks (Devenport, 2014). We reasoned that if the Ft/Ds pathway acts via ODF2 or VFL1/3 to generate the splay observed in control animals, then the implementation of Ft/Ds cues should be hindered when ODF2 or VFL1/3 are missing. To test this, we downregulated the Wnt/PCP pathway in sidewinder animals. In wild-type planarians, depleting DVL1/2-induced rootlet reorientation toward the edges under the influence of the Ft/Ds pathway (Figures 6A, 6B, S1, and S3; Video S5) (Vu et al., 2019). Although DVL1/2 is involved in additional pathways, in particular the Wnt/ β -catenin pathway, this phenotype is most likely to result from a decrease in Wnt/PCP signaling (Vu et al., 2019).

In VFL1 and VFL3-depleted animals, Wnt/PCP downregulation induced rootlet reorientation like in control animals on the left side and to a lesser extent on the right side, suggesting that centrioles could still detect the Ft/Ds polarity field. In *odf2(RNAi)* animals, dampening Wnt/PCP activity induced a markedly asymmetric response: centrioles reoriented on the right side to a similar extent than in control planarians but failed to do so on the left side (Figures 6A, 6B, and S3). This suggested that on the left side the centriole network no longer aligned in the Ft/Ds polarity field, even when its relative influence was increased by Wnt/PCP inhibition. In contrast, repolarization on the right side of *odf2;dvl1/2(RNAi)* planarians indicated that Ft/Ds cues were still implemented, and hence the possibility that ODF2 is not required for rootlet splay on this side of the body. If this were the case, simultaneous depletion of ODF2 and the Ft/Ds pathway should produce a uniform rootlet orientation along the M/L axis. However, we found no significant difference between *odf2(RNAi)* and *odf2;ds(RNAi)* animals in this respect (Figures 6C, 6D, S1, and S3), suggesting that the response to Ft/Ds is impaired on both sides of the epidermis when ODF2 is missing. Together, these observations suggest that the rootlet pattern observed in *odf2(RNAi)* animals results from a defect in centriole network structure superimposed with a defect in the response to Ft/Ds cues. On the left side, the clockwise rotation of centrioles driven by VFL1/3-dependent connections is compensated by the lack of response to Ft/Ds, resulting in rootlet angles that are close to control values (Figures 2A–2C and S3). On the right side, the defects in network architecture and in the response to Ft/Ds, both induce a clockwise rotation of centrioles, leading to a strong deviation from control values. In addition, the data obtained after a simultaneous inhibition of DVL1/2 and ODF2 supports that a distinct

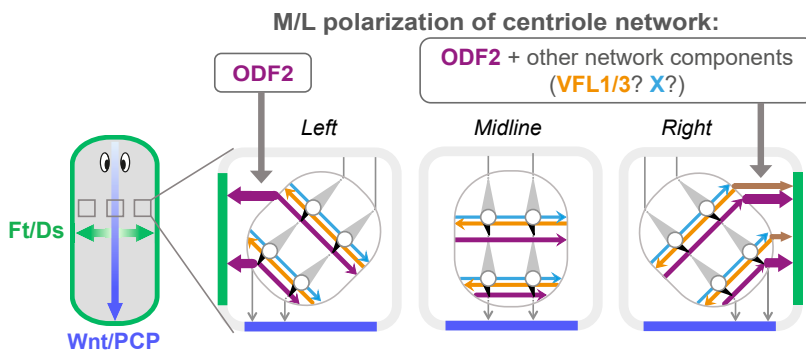


Figure 7. Proposed Model for M/L Polarization of Centrioles on Each Side of the Ventral Epidermis

The chiral asymmetric centriole network resulting from the balanced action of ODF2 and VFL1/3 (represented as in Figure 5G) is polarized by a mechanism that is executed in a differential manner on the left and right sides of the body: on the left side, polarization depends on ODF2, possibly acting downstream of the Ft/Ds pathway (in green), whereas on the right side it involves both ODF2 and other network components.

mechanism can drive centriole repolarization in response to Ft/Ds cues on the right side of the epidermis.

Altogether, our results support that ODF2 is required for the M/L polarization of centrioles in the planarian epidermis, most likely via its role in basal foot assembly. Additional components of the centriole network contribute specifically on the right side, supporting that the mechanism underlying M/L polarization is implemented differentially on each side of the midline (Figure 7).

DISCUSSION

This work illustrates how a bilaterally symmetric whole-tissue pattern can emerge from a prominently asymmetric cellular structure. In the multi-ciliated epidermis of planarian flatworms, centrioles are organized into an asymmetric mirror-imaged medio-lateral pattern, a property that likely derives from their intrinsic chirality. This network is polarized to generate a bilaterally symmetric pattern via a mechanism that is executed differentially on the left and right halves of the epidermis, reflecting the asymmetric nature of the network itself. We show that the centriole components ODF2, VFL1, and VFL3 are required for establishing chiral asymmetric connections between centrioles and balancing their effects. These proteins act in part by controlling the assembly of the basal foot, which in planarians has a structure that mirrors centriole chirality. Organizing chiral asymmetric cytoskeletal arrays is likely an ancestral property of centrioles (Yubuki and Leander, 2013), and this property is thus conserved in some metazoan species.

Functions of the ODF2 and VFL1/3 Proteins and Balance-of-Force Model of Centriole Orientation

The centriole network organized in part via ODF2 and VFL1/3 proteins is inherently asymmetric, independently of M/L polarity cues. This is best illustrated at the midline and the posterior end, where M/L polarity cues have a limited effect, but rootlets are nevertheless deviated from the A/P axis in RNAi animals. Network asymmetry likely stems from an asymmetric attachment of cytoskeletal elements to centrioles mediated by ODF2 and VFL1/3. Our results show that planarian ODF2 and VFL1/3 are required for building centriole appendages, which are known to organize cytoskeletal connectors necessary for positioning the centrioles in multi-ciliated cells (Antoniades et al., 2014; Clare et al., 2014; Kunimoto et al., 2012; Werner et al., 2011). ODF2 is necessary to basal foot assembly, consistent with results obtained in mouse (Kunimoto et al., 2012) thus establishing

the evolutionary conservation of this function. The roles of VFL1 and VFL3 appear more complex but these proteins also affect the assembly and position of the basal foot, as well as of the ciliary rootlet. These findings are reminiscent of studies in unicellular eukaryotes showing that VFL1/3 orthologs are required for building different sets of striated fibers and microtubule rootlets specific to each species (Adams et al., 1985; Bengueddach et al., 2017; Silflow et al., 2001; Wright et al., 1983). Hence, the functions of these proteins appear conserved despite important variations in the architecture of centriole-associated structures. In unicellular models, orthologs of VFL1 and VFL3 localize to specific microtubule triplets (Bengueddach et al., 2017; Silflow et al., 2001). In planarians, absence of VFL1 or VFL3 leads to basal feet assembling on the wrong triplets, most of the time shifting one triplet to the left. This suggests that VFL1/3 proteins might normally help restricting basal foot assembly to its proper site between the triplet facing the direction of the beating and the triplet placed immediately to its left. Moreover, the striking differences between the *vf1/3(RNAi)* and *odf2(RNAi)* phenotypes support that VFL1/3 proteins play an additional role beyond appendage assembly. When ODF2 was missing, VFL1/3-dependent forces rotated centrioles clockwise. In *Xenopus*, actin cables anchored in the vicinity of the basal foot connect centrioles laterally and contribute to centriole spacing (Antoniades et al., 2014). Centriole spacing is mostly unaffected in *odf2(RNAi)* but is perturbed in *vf1/3(RNAi)*, suggesting that VFL1/3 proteins might connect centrioles to the actin network. One possible model is that VFL1/3 anchor actin filaments in an asymmetric fashion to one or more triplets localized on the left of the basal foot. This would be consistent with the clockwise rotation of centrioles observed when ODF2 is missing. In the presence of ODF2, the rotation induced by VFL1/3-dependent connections is compensated, possibly by microtubules anchored at the basal foot and running perpendicular to the beating axis that we indeed observed. How these microtubules generate an asymmetric net force is unclear, but one possibility is that their orientation is biased along the M/L axis. The basal foot in planarians has an asymmetric shape, which might affect the polarity of microtubules attached to it. Beyond VFL1/3 and ODF2, additional players are also involved, as depletion of all three proteins is not sufficient to randomize centriole rotational polarity in this system (Figure 7). In wild-type planarians, the forces exerted by the different network components are balanced, thus compensating centriole chirality and masking the asymmetry of the network.

Interaction of the Centriole Network with M/L Polarity Cues to Generate Bilateral Symmetry

In addition to its role in organizing the network of centrioles, our analyses support that ODF2 is key to implementing the M/L polarity cues generated by the Ft/Ds pathway. Indeed, depletion of Ds produced no additive effect in *odf2(RNAi)* planarians, indicating that Ft/Ds pathway is already ineffective when ODF2 is downregulated. Microtubules anchored at the basal foot might orient centrioles toward the body edges (Figure 7), in line with the role played by the Ft/Ds pathway in polarizing microtubule networks in other systems (Matis et al., 2014). Further work is required to test this model and exclude alternative possibilities, for instance that Ft/Ds acts downstream or in parallel to ODF2. Analysis of *odf2;dvl1/2(RNAi)* animals nevertheless supports that M/L polarization can rely on additional network components on the right side of the body, as centriole re-polarized toward the right edge under the influence of M/L cues to a similar extent than in controls (Figure 7). Hence, the bilaterally symmetric pattern of centrioles observed in the planarian epidermis results from interactions between polarity cues and the cytoskeleton that are at least partly distinct on each side of the body. Why this did not result in a quantitative difference between the *odf2(RNAi)* and *odf2;ds(RNAi)* phenotypes is unclear, but one possibility is that the repolarization driven by ODF2-independent cytoskeletal arrays was enhanced by DVL1/2 downregulation and thus easier to detect in these conditions.

Biological Significance of Network Asymmetry

Our results support that centriole network asymmetry originates from asymmetries within the centrioles. Centrioles are intrinsically chiral structures, and this property is amplified in many unicellular eukaryotes by the presence of appendages that decorate specific microtubule triplets. In planarians, the basal foot is chiral asymmetric, and the *vfl1/3(RNAi)* phenotype points at additional asymmetries between microtubule triplets. Whether the polarization mechanism we uncovered is essentially required to compensate centriole chirality, or whether it allows generating larger-scale chirality remains an open question, however. Whole-cell chirality, which stems from inherent properties of the cytoskeleton, is widespread in animals (Kuroda et al., 2009; Wan et al., 2011; Xu et al., 2005). In some systems, whole-cell chirality has been linked to the establishment of left-right asymmetry of the body plan (Kuroda et al., 2009; Taniguchi et al., 2011). Planarians have no clear left-right asymmetry in this respect, but structural chirality in the epidermis might contribute generating the complex pattern of centrioles, reflecting the ancestral role of centrioles in shaping elaborate cell geometries. Future work will tell whether this mechanism evolved with the dual-axis control of planar polarity in planarians epidermis or whether it reflects a fundamental property of centriole networks.

STAR★METHODS

Detailed methods are provided in the online version of this paper and include the following:

- KEY RESOURCES TABLE
- LEAD CONTACT AND MATERIALS AVAILABILITY
- EXPERIMENTAL MODEL AND SUBJECT DETAILS

● METHODS DETAILS

- RNA Interference
- Antibodies
- Whole Mount Immunofluorescence
- qPCR
- Image Acquisition and Analysis
- Live Imaging
- Transmission Electron Microscopy
- Computational Modeling

● QUANTIFICATION AND STATISTICAL ANALYSIS

● DATA AND CODE AVAILABILITY

SUPPLEMENTAL INFORMATION

Supplemental Information can be found online at <https://doi.org/10.1016/j.devcel.2019.10.021>.

ACKNOWLEDGMENTS

The authors would like to thank L. Kodjabachian for critical reading of the manuscript and P. Le Gars and M.K. Nguyen for technical help. We acknowledge the ImagoSeine facility, member of the France Biolmaging infrastructure supported by grant ANR-10-INSB-04 from the French National Research Agency.

Funding: this work was supported by CNRS (ATIP-AVENIR) and ANR -15-CE13-0003 funding to J.A. N.G. was a recipient of a MESRI PhD fellowship from the French Government. D.E. was funded by the European Research Council (Cog forecaster n°647073).

AUTHORS CONTRIBUTIONS

Conceptualization, C.B., D.E., J.C.R., and J.A.; Methodology, C.B., D.E., B.L. and J.-F.P.; Investigation, C.B., D.E., H.T.V., B.L., J.-F.P., A.-M.O., and J.A.; Resources: N.G., S.M., H.T.V., and J.C.R.; Writing, C.B., J.C.R., and J.A.

DECLARATION OF INTERESTS

The authors declare no competing interests.

Received: October 15, 2018

Revised: September 6, 2019

Accepted: October 21, 2019

Published: November 18, 2019

REFERENCES

- Adams, G.M., Wright, R.L., and Jarvik, J.W. (1985). Defective temporal and spatial control of flagellar assembly in a mutant of *Chlamydomonas reinhardtii* with variable flagellar number. *J. Cell Biol.* 100, 955–964.
- Antoniades, I., Stylianou, P., and Skourides, P.A. (2014). Making the connection: ciliary adhesion complexes anchor basal bodies to the actin cytoskeleton. *Dev. Cell* 28, 70–80.
- Azimzadeh, J. (2014). Exploring the evolutionary history of centrosomes. *Philos. Trans. R. Soc. Lond. B Biol. Sci.* 369, 20130453.
- Azimzadeh, J., Wong, M.L., Downhour, D.M., Sánchez Alvarado, A., and Marshall, W.F. (2012). Centrosome loss in the evolution of planarians. *Science* 335, 461–463.
- Basquin, C., Orfila, A.M., and Azimzadeh, J. (2015). The planarian *Schmidtea mediterranea* as a model for studying motile cilia and multiciliated cells. *Methods Cell Biol.* 127, 243–262.
- Bengueddach, H., Lemullois, M., Aubusson-Fleury, A., and Koll, F. (2017). Basal body positioning and anchoring in the multiciliated cell *Paramecium tetraurelia*: roles of OFD1 and VFL3. *Cilia* 6, 6.
- Boyd, J.S., Gray, M.M., Thompson, M.D., Horst, C.J., and Dieckmann, C.L. (2011). The daughter four-membered microtubule rootlet determines

- anterior-posterior positioning of the eyespot in *Chlamydomonas reinhardtii*. *Cytoskeleton (Hoboken)* 68, 459–469.
- Brown, N.A., and Wolpert, L. (1990). The development of handedness in left/right asymmetry. *Development* 109, 1–9.
- Bustin, S.A., Benes, V., Garson, J.A., Hellems, J., Huggett, J., Kubista, M., Mueller, R., Nolan, T., Pfaffl, M.W., Shipley, G.L., et al. (2009). The MIQE guidelines: minimum information for publication of quantitative real-time PCR experiments. *ClinChem* 55, 611–622.
- Chen, D., and Zhong, Y. (2015). A computational model of dynein activation patterns that can explain nodal cilia rotation. *Biophys. J.* 109, 35–48.
- Clare, D.K., Magescas, J., Piolot, T., Dumoux, M., Vesque, C., Pichard, E., Dang, T., Duvauchelle, B., Poirier, F., and Delacour, D. (2014). Basal foot MTOC organizes pillar MTs required for coordination of beating cilia. *Nat. Commun.* 5, 4888.
- Devenport, D. (2014). The cell biology of planar cell polarity. *J. Cell Biol.* 207, 171–179.
- Guirao, B., Meunier, A., Mortaud, S., Aguilar, A., Corsi, J.M., Strehl, L., Hirota, Y., Desoeuvre, A., Boutin, C., Han, Y.G., et al. (2010). Coupling between hydrodynamic forces and planar cell polarity orients mammalian motile cilia. *Nat. Cell Biol.* 12, 341–350.
- Gurley, K.A., Rink, J.C., and Sánchez Alvarado, A. (2008). Beta-catenin defines head versus tail identity during planarian regeneration and homeostasis. *Science* 319, 323–327.
- Hashimoto, M., Shinohara, K., Wang, J., Ikeuchi, S., Yoshida, S., Meno, C., Nonaka, S., Takada, S., Hatta, K., Wynshaw-Boris, A., et al. (2010). Planar polarization of node cells determines the rotational axis of node cilia. *Nat. Cell Biol.* 12, 170–176.
- Hayes, M.J. (2017). Sulphated glycosaminoglycans support an assortment of planarian rhabdite structures. *Biol. Open* 6, 571–581.
- Hoops, H.J., Wright, R.L., Jarvik, J.W., and Witman, G.B. (1984). Flagellar waveform and rotational orientation in a *Chlamydomonas* mutant lacking normal striated fibers. *J. Cell Biol.* 98, 818–824.
- Kunimoto, K., Yamazaki, Y., Nishida, T., Shinohara, K., Ishikawa, H., Hasegawa, T., Okanou, T., Hamada, H., Noda, T., Tamura, A., et al. (2012). Coordinated ciliary beating requires Odf2-mediated polarization of basal bodies via basal feet. *Cell* 148, 189–200.
- Kuroda, R., Endo, B., Abe, M., and Shimizu, M. (2009). Chiral blastomere arrangement dictates zygotic left-right asymmetry pathway in snails. *Nature* 462, 790–794.
- Liu, S.Y., Selck, C., Friedrich, B., Lutz, R., Vila-Farré, M., Dahl, A., Brandl, H., Lakshmanaperumal, N., Henry, I., and Rink, J.C. (2013). Reactivating head regrowth in a regeneration-deficient planarian species. *Nature* 500, 81–84.
- Marshall, W.F. (2012). Centriole asymmetry determines algal cell geometry. *Curr. Opin. Plant Biol.* 15, 632–637.
- Matis, M., Russler-Germain, D.A., Hu, Q., Tomlin, C.J., and Axelrod, J.D. (2014). Microtubules provide directional information for core PCP function. *Elife* 3, e02893.
- Mitchell, B., Jacobs, R., Li, J., Chien, S., and Kintner, C. (2007). A positive feedback mechanism governs the polarity and motion of motile cilia. *Nature* 447, 97–101.
- Omori, T., Sugai, H., Imai, Y., and Ishikawa, T. (2017). Nodal cilia-driven flow: development of a computational model of the nodal cilia axoneme. *J. Biomech.* 61, 242–249.
- Papon, J.F., Bassinet, L., Cariou-Patron, G., Zerah-Lancner, F., Vojtek, A.M., Blanchon, S., Crestani, B., Amselem, S., Coste, A., Housset, B., et al. (2012). Quantitative analysis of ciliary beating in primary ciliary dyskinesia: a pilot study. *Orphanet J. Rare Dis.* 7, 78.
- Park, T.J., Mitchell, B.J., Abitua, P.B., Kintner, C., and Wallingford, J.B. (2008). Dishevelled controls apical docking and planar polarization of basal bodies in ciliated epithelial cells. *Nat. Genet.* 40, 871–879.
- Reddien, P.W., Bermange, A.L., Murfitt, K.J., Jennings, J.R., and Sánchez Alvarado, A. (2005). Identification of genes needed for regeneration, stem cell function, and tissue homeostasis by systematic gene perturbation in planaria. *Dev. Cell* 8, 635–649.
- Rink, J.C., Gurley, K.A., Elliott, S.A., and Sánchez Alvarado, A. (2009). Planarian Hh signaling regulates regeneration polarity and links Hh pathway evolution to cilia. *Science* 326, 1406–1410.
- Robb, S.M., Gotting, K., Ross, E., and Sánchez Alvarado, A. (2015). SmedGD 2.0: the *Schmidtea mediterranea* genome database. *Genesis* 53, 535–546.
- Sánchez Alvarado, A., Newmark, P.A., Robb, S.M., and Juste, R. (2002). The *Schmidtea mediterranea* database as a molecular resource for studying platyhelminthes, stem cells and regeneration. *Development* 129, 5659–5665.
- Schneider, C.A., Rasband, W.S., and Eliceiri, K.W. (2012). NIH Image to ImageJ: 25 years of image analysis. *Nat. Methods* 9, 671–675.
- Shinohara, K., and Hamada, H. (2017). Cilia in left-right symmetry breaking. *Cold Spring Harb. Perspect. Biol.* 9, a028282.
- Silflow, C.D., LaVoie, M., Tam, L.W., Tousey, S., Sanders, M., Wu, W., Borodovsky, M., and Lefebvre, P.A. (2001). The Vfl1 protein in *Chlamydomonas* localizes in a rotationally asymmetric pattern at the distal ends of the basal bodies. *J. Cell Biol.* 153, 63–74.
- Taniguchi, K., Maeda, R., Ando, T., Okumura, T., Nakazawa, N., Hatori, R., Nakamura, M., Hozumi, S., Fujiwara, H., and Matsuno, K. (2011). Chirality in planar cell shape contributes to left-right asymmetric epithelial morphogenesis. *Science* 333, 339–341.
- Timmons, L., Court, D.L., and Fire, A. (2001). Ingestion of bacterially expressed dsRNAs can produce specific and potent genetic interference in *Caenorhabditis elegans*. *Gene* 263, 103–112.
- Vischer, N.O., Verheul, J., Postma, M., van den Berg van Saparoea, B., Galli, E., Natale, P., Gerdes, K., Luijck, J., Vollmer, W., Vicente, M., et al. (2015). Cell age dependent concentration of *Escherichia coli* divisome proteins analyzed with ImageJ and ObjectJ. *Front. Microbiol.* 6, 586.
- Vladar, E.K., Bayly, R.D., Sangoram, A.M., Scott, M.P., and Axelrod, J.D. (2012). Microtubules enable the planar cell polarity of airway cilia. *Curr. Biol.* 22, 2203–2212.
- Vu, H.T., Mansour, S., Kücken, M., Blasse, C., Basquin, C., Azimzadeh, J., Myers, E.W., Bruschi, L., and Rink, J.C. (2019). Dynamic polarization of the multi-ciliated planarian epidermis between body plan landmarks. *Dev. Cell*. Published online November 18, 2019. <https://doi.org/10.1016/j.devcel.2019.10.022>.
- Vu, H.T., Rink, J.C., McKinney, S.A., McClain, M., Lakshmanaperumal, N., Alexander, R., and Sanchez Alvarado, A. (2015). Stem cells and fluid flow drive cyst formation in an invertebrate excretory organ. *eLife* 4, 07405.
- Wan, L.Q., Ronaldson, K., Park, M., Taylor, G., Zhang, Y., Gimble, J.M., and Vunjak-Novakovic, G. (2011). Micropatterned mammalian cells exhibit phenotype-specific left-right asymmetry. *Proc. Natl. Acad. Sci. USA* 108, 12295–12300.
- Werner, M.E., Hwang, P., Huisman, F., Taborek, P., Yu, C.C., and Mitchell, B.J. (2011). Actin and microtubules drive differential aspects of planar cell polarity in multiciliated cells. *J. Cell Biol.* 195, 19–26.
- Wright, R.L., Chojnacki, B., and Jarvik, J.W. (1983). Abnormal basal-body number, location, and orientation in a striated fiber-defective mutant of *Chlamydomonas reinhardtii*. *J. Cell Biol.* 96, 1697–1707.
- Xu, J., Wang, F., Van Keymeulen, A., Rentel, M., and Bourne, H.R. (2005). Neutrophil microtubules suppress polarity and enhance directional migration. *Proc. Natl. Acad. Sci. USA* 102, 6884–6889.
- Yubuki, N., and Leander, B.S. (2013). Evolution of microtubule organizing centers across the tree of eukaryotes. *Plant J.* 75, 230–244.
- Zayas, R.M., Cebrià, F., Guo, T., Feng, J., and Newmark, P.A. (2010). The use of lectins as markers for differentiated secretory cells in planarians. *Dev. Dyn.* 239, 2888–2897.

STAR★METHODS

KEY RESOURCES TABLE

REAGENT or RESOURCE	SOURCE	IDENTIFIER
Antibodies		
Mouse monoclonal anti-SMED-ROOTLETIN1	Vu et al., 2019	N/A
Rabbit polyclonal anti-SMED-CEP135	Azimzadeh et al., 2012	N/A
Mouse monoclonal anti-acetylated α -tubulin	Sigma-Aldrich	Cat#T6793, RRID: AB_477585
Rabbit polyclonal anti-SMED-VFL1	This paper	N/A
Rabbit polyclonal anti-SMED-ODF2	This paper	N/A
Donkey polyclonal Anti-Mouse DyLight 550	Thermo Fisher Scientific	Cat#SA5-10167, RRID: AB_2556747
Donkey Polyclonal Anti-Rabbit DyLight 488	Thermo Fisher Scientific	Cat#SA5-10038, RRID: AB_2556618
Bacterial and Virus Strains		
<i>Escherichia coli</i> : strain HT115(DE3)	Timmons et al., 2001	N/A
Chemicals, Peptides, and Recombinant Proteins		
Tri-reagent	Molecular Research Center	Cat#TR118
Critical Commercial Assays		
SuperScript III First-Strand Synthesis System	Thermo Fisher Scientific	Cat#18080093
Experimental Models: Organisms/Strains		
Planarian: <i>Schmidtea mediterranea</i> , asexual CIW4 strain	Sánchez Alvarado et al., 2002	N/A
Oligonucleotides		
Primers for qPCR, see Table S1	This paper	N/A
Recombinant DNA		
pPR-T4P vector	Liu et al., 2013	N/A
Software and Algorithms		
ImageJ v1.50h	Schneider et al., 2012	https://imagek.net/ , RRID: SCR_003070
ImageJ plugin: ObjectJ v1.03q	Vischer et al., 2015	https://sils.fnwi.uva.nl/bcb/objectj/
Oriana	Kovach Computing	https://www.kovcomp.co.uk/oriana/
MATLAB	MathWorks	RRID:SCR_001622
Code for computational modelling of planarian locomotion	This paper; GitHub	https://github.com/dershoff/simulation-of-planarian-movement
Other		
Canon Powershot SX230 HS camera	Canon	N/A

LEAD CONTACT AND MATERIALS AVAILABILITY

Further information and requests for resources and reagents should be directed to and will be fulfilled by the Lead Contact, Juliette Azimzadeh (juliette.azimzadeh@ijm.fr). All unique reagents generated in this study are available from the Lead Contact with a completed Materials Transfer Agreement.

EXPERIMENTAL MODEL AND SUBJECT DETAILS

Asexual *Schmidtea mediterranea* (strain CIW4) ([Sánchez Alvarado et al., 2002](#)) were maintained in the dark at 20°C in plastic containers filled with 1 X Monjuic water (1.6 mM NaCl, 1 mM CaCl₂, 1 mM MgSO₄, 0.1 mM MgCl₂, 0.1 mM KCl, 1.2 mM NaHCO₃, pH 7.2) and fed weekly with calf liver homogenate ([Basquin et al., 2015](#)). Animals were starved one week prior to experiments.

METHODS DETAILS

RNA Interference

cDNAs coding for ODF2 (SmedGD: SMU15005577), VFL1 (SmedGD: SMU15036303), VFL3 (SmedGD: SMU15004223) cloned in pPR-T4P were described in ([Azimzadeh et al., 2012](#)), DVL1 and DVL2 in ([Gurley et al., 2008](#)). *Caenorhabditis elegans* UNC22 cloned

in pPR-T4P (Liu et al., 2013) was used in all control experiments. Production and RNAi feeding was performed as described in (Basquin et al., 2015). Briefly, constructs were transformed into competent *Escherichia coli* strain HT115 (Timmons et al., 2001). Bacteria were grown in 2XYT medium, induced with 0.1 mM IPTG during 2 hours, pelleted and mixed with calf liver (1:0.66:1.34 bacteria: 1 X Montjuic water: calf liver homogenate). ~1-cm long animals were fed three times two days apart and amputated pre- and post-pharyngeally the day after the last feeding. Planarians were then fed once a week at least twice more before being processed for experiments. For simultaneous inactivation of 2 or 3 genes, bacteria/liver mixes for control or specific target genes were used at 1:1 or 1:1:1 ratios, respectively.

Antibodies

Rabbit polyclonal antibodies directed against SMED-VFL1 and SMED-ODF2 proteins were developed in the laboratory. Fragments corresponding ODF2 a.a. 599–769 (based on SmedGD: SMU15005577) (Robb et al., 2015) and VFL1 a.a. 575–703 (SmedGD: SMU15036303) were amplified by RT-PCR, cloned in pGST-Parallel1 and expressed in *Escherichia coli*. Bacterial pellets were solubilized in TNE buffer (50 mM Tris pH 7.5, 150 mM NaCl, 1 mM EDTA) containing 5 mM DTT, 20 mg/mL lysozyme, 0.25 % sodium deoxycholate, 250 U/mL DNase I, 5 mM MgCl₂ and protease inhibitor cocktail (Roche). The lysates were cleared out by centrifugation at 15,000g before incubation with glutathione agarose beads (ThermoFisher Scientific). The beads were washed 5 x with 50 mL TNE buffer containing 0.1 % Triton X-100, and the protein fragments were recovered by overnight incubation with 75- μ g tobacco etch virus protease in 1.5 mL TNE buffer supplemented with 5 mM DTT. The supernatants containing the cleaved protein fragments were then dialyzed against PBS before rabbit immunization (Covalab France). Antibodies were affinity-purified on the corresponding antigen immobilized on Affi-Gel 10 resin (Bio-Rad Laboratories). For this, 1–3 mg soluble antigen diluted in 0.1 M MOPS buffer pH 7.5 containing 0.1 M NaCl were incubated overnight at 4°C with 1.5 mL Affi-Gel 10 beads activated following the manufacturer's recommendations. The beads were then incubated with 5 mL rabbit antiserum diluted 5 x in PBS, transferred to a Poly-prep chromatography column (Bio-Rad) and washed with 80 mL PBS at 4°C. Immunoglobulins were recovered by elution with 0.1-M glycine pH 2.2 followed by neutralization with Tris base (100-mM final concentration), dialyzed against PBS buffer containing 50 % glycerol and stored at –20°C. The anti-SMED-ROOTLETIN1 was described in (Vu et al., 2019) and the anti-SMED-CEP135 antibody in (Azimzadeh et al., 2012).

Whole Mount Immunofluorescence

~ 0.1 - 0.3-cm long animals were euthanized in 1 % HCl during 1 min, fixed overnight at RT in methanol then rehydrated in graded series of methanol: 75%, 50%, 25% methanol in Montjuic water. Non-specific antibody binding sites were blocked 4 hours in PBS containing 2.5 % BSA and 0.5 % Tween-20 (PBST), and samples were incubated overnight at 4°C with primary antibodies at the following dilutions: anti-SMED-ROOTLETIN1 (1:500), anti-SMED-VFL1 (1:3000), anti-SMED-ODF2 (1:300) and anti-SMED-CEP135 antibody (1:500). DyLight488/550 secondary antibodies (ThermoFisher Scientific) were used at a dilution of 1:300. Samples were washed 4 x during 1 hours in PBST and incubated 4 hours at RT with secondary antibodies, concanavalin A coupled to AlexaFluor 647 (1:300; ThermoFisher Scientific) to label membranes (Zayas et al., 2010) and 5 μ g/mL hoechst 33342 to label nuclei. Samples were washed 4 x during 1 hours in PBST and mounted in Vectashield (Vector laboratories). For analysis of the *ds;odf2(RNAi)*, 0.8–1-cm long animals were used because the *ds(RNAi)* phenotype is more penetrant in larger animals. The flatworms were anesthetized in cold 0.2% chloretone in planarian water until completely stretched out, positioned on a filter paper on a cold block with their ventral side up and fixed with ice-cold methanol for at least 1 hours at - 20°C. The samples were then bleached in 6% H₂O₂ in methanol overnight under direct light, gradually rehydrated to PBS with 0.1 % Triton X-100 (PBSTw0.1%), transferred into reduction solution (1 % NP40, 50 mM DTT and 0.5 % SDS in PBS) for 10 minutes at 37°C, followed by 2 x 10 minute washes with PBSTw0.1%. The samples were then blocked for 1 hours in 10 % filtered horse serum in PBSTw0.1%, followed by primary antibody incubation in blocking solution (anti-SMED-ROOTLETIN-1 1:500, and anti-SMED-CEP135 1:500) overnight at 4°C. The samples were washed 6–8 times for 4 hours in PBSTw0.1%, and then incubated in secondary antibody in blocking solution (both secondary antibodies were used at 1:500) for 4 hours at room temperature (or overnight at 4°C). Stained samples were washed 4–6 times for 2 hours in PBSTw0.1%, and then mounted in 80 % glycerol (prepared in 10 mM Tris pH 8.5).

qPCR

Total RNA extracts were obtained using TRI-Reagent (Molecular Research Center) and cDNAs were synthesized using SuperScript III reverse transcriptase (ThermoFisher Scientific). qPCR was performed with GoTaq qPCR Master Mix (Promega, Southampton, UK) and the primers referenced in Table S1 in a LightCycler 480 instrument (Roche). Quantification of relative mRNA levels was performed using 3 reference genes (*smed-chmp2a*, *smed-emc7*, and *smed-ura4*) following the MIQE guidelines (Bustin et al., 2009).

Image Acquisition and Analysis

The ventral epidermis of planarians was imaged on an inverted Axio Observer Z.1 microscope (Zeiss) equipped with a sCMOS Orca Flash4 LT camera (Hamamatsu) using an air 10x objective (Plan Apo, N.A. 0.45) or an oil 63x objective (Plan Apo, N.A. 1.4). For rootlet analysis, optical sections were acquired at a 0.24- μ m interval using the 63 x objective and tiled images were stitched using ZEN software (Zeiss). Signal was enhanced using Subtract Background plugin and z-stacks were submitted to maximum intensity projection using ImageJ software (Schneider et al., 2012). To obtain rootlet polarity and position, vectors were drawn manually for each rootlet from the centriole-attachment side (bright end) to the tip of the comet using ObjectJ Plugin (Vischer et al., 2015). The contour of

planarians was determined on images acquired with the 10 x objective and the midline was positioned at equal distances of the lateral boundaries. The position of each rootlet relative to the M/L and A/P axes was determined. Planarians were segmented in 2 or 10 M/L and 2, 5 or 20 A/P segments, then mean rootlet orientation and circular standard deviation were calculated for each subdivision. For analysis of the *ds;odf2(RNAi)*, we used the automatic pipeline described in (Vu et al., 2019) because large specimens are difficult to analyze manually. *odf2(RNAi)* animals were re-analyzed in parallel to verify that it produces similar results as manual analysis of smaller specimens. *ds(RNAi)* planarians were also analyzed in the same experiment to confirm the efficiency of Ds-depletion.

Live Imaging

Live animals were imaged at $10 \text{ frame} \cdot \text{sec}^{-1}$ using a M205C stereomicroscope equipped with a 0.63 x objective (PlanApo) and DFC450 camera (Leica), or a PowerShot SX 230 HS camera (Canon) for analysis at longer time scales. The direction of locomotion was determined using ImageJ software by measuring the angle between the planarian A/P axis and the trajectory of the planarians (measured between the photoreceptors). Time sequences (≥ 2 seconds) during which the planarian body remained straight were used for this analysis. To better visualize the trajectories of the planarians shown in Figure 3, animals fortuitously passing in the field were erased manually before projecting consecutive time frames on a single image. For high speed imaging of ciliary beat, live planarians were mounted in a chamber obtained by cutting a $\sim 2 \times 2 \text{ mm}$ square from a Parafilm spacer placed between a microscopy slide and an $18 \times 18 \text{ mm}$ coverslip (Basquin et al., 2015), and were observed on an Axiovert 200 inverted microscope (Zeiss) using an oil immersion $\times 100$ objective. The beating of cilia located at the anterior margin were recorded with a digital camera (PixelINK A741) at a rate of 355 frames per second as described previously (Papon et al., 2012).

Transmission Electron Microscopy

Planarians were dissected in 4 % paraformaldehyde, 2 % glutaraldehyde in 0.1 M cacodylate pH 7.4 and fixed 4×1 minute in a Model 3450 Microwave Oven (Ted Pella Inc.) at 150 W, then incubated 48 hours at 4°C in 3 % glutaraldehyde in cacodylate buffer. The specimens were next fixed in 1 % OsO₄ in cacodylate buffer in the microwave (2×1 minute at 150 W, then 6×20 seconds at 450 W) and incubated during 1 hours at room temperature. *En bloc* staining was performed by incubating the samples in 0.5 % uranyl acetate overnight at 4°C . Dehydration was performed using graded series of 35, 50, 75, 80, 95, 100 % ethanol in water. Samples were rinsed in acetone and infiltration was performed using graded series of 10 %–100 % epon/araldite resin (Ted Pella Inc.) in acetone with 10 % increments, 4×1 minute in the microwave at 350 W for each concentration. Samples were incubated overnight in 100 % resin and then 4 hours in resin with accelerant before embedding. Ultrathin sections were obtained using an EM UC6 Ultracut microtome (Leica), stained with uranyl acetate and lead citrate, and examined in a Tecnai 12 transmission electron microscope (ThermoFisher Scientific).

Computational Modeling

To test the hypothesis that orientation of the cilia can ultimately determine the movement phenotype of a planarian as a whole, we devised a simple model that can predict planarian movement based on experimentally observed spatial and angular distributions of cilia within planarians using MATLAB (MathWorks).

We simulate a planarian as a solid body, meaning that there is no deformation of the body (*i.e.* no stretching or bending): the body is translated and rotated as one solid unscalable entity. A body has a rectangular shape and is divided, as in our experiments, into segments; the head and the tail have the same geometry (Figure S4A). We can arbitrarily set the length (L), the width (W) and the mass (M) of the whole body; the number of segments along L and W, from which the mass and the size of a single segment is then calculated. Each segment comprises a number of nodes (red circles in Figure S4A) that represent rootlets of cilia, and with each node cilia a beating force is associated during simulations. The number of nodes N in each segment is drawn randomly from a normal distribution, the mean and the standard deviation of which we control (N_m , N_s in Figure S4A). Spatial distribution of these N nodes within a segment is uniform: there is no spatial bias and a node can be placed anywhere inside the segment with the same probability. The parameters described above (planarian mass, length, width; segment mass, length, width, number; nodes numbers and spatial distribution) are fixed during generation of a planarian and do not change during simulation runs. Ideally, one segment should represent one cell with its unique spatial configuration of nodes. In our simulations, we construct a planarian so that its segments conform to our experimental planarian segmentation: 5 segments along the A/P axis and 10 segments along the M/L axis. However, this is absolutely not necessary to reproduce our simulation results. During each simulation iteration nodes in all segments individually generate a force due to cilia beating; these forces vary in direction and magnitude. Therefore, we associate with each node the angle of the beating force and its absolute magnitude f ; their values will be drawn from normal distributions, the mean and the standard deviation of which we control (Figure S4B). The angle is counted clock-wise from the Tail-Head axis for positive angles and counter clock wise for negative. We also introduce notation of incoherency in cilia beating: at any given iteration, there is only a fraction of segment's nodes (ϕ_{on} , varies from 0 to 1) that have beating cilia and thus are "on" ($s = 1$, red nodes), whereas the other segment's nodes ($1 - \phi_{on}$) have resting cilia and are "off" ($s = 0$, blue nodes). Thus, when $\phi_{on} = 1$, cilia beating is fully coherent and all cilia beat together during an iteration. The fraction of nodes with beating cilia ϕ_{on} is drawn from a normal distribution, the mean and the standard deviation of which we control (Figure S4B). These three normal distributions (α , f , and ϕ_{on}) are constructed during generation of a planarian, apply to all segments within this planarian and do not change during simulation runs. During new iteration, each segment acquires a new configuration of beating cilia by drawing randomly parameters α , f , and s for each node from these distributions; each node is first set to "off" state and then turned "on" with the probability of ϕ_{on} . Some parameters can be found experimentally: the planarian

sizes (L, W); normal distributions for drawing the number of nodes per segment (N) and the angular distribution of beating forces (α) (may be found experimentally in each segment as in Figure 2B). Some we set arbitrarily: the planarian mass (M), the magnitude distribution of the beating force (f) and the probability of on-off state (ϕ) are set arbitrarily.

We define planarian movement as a combination of translation of the whole body and rotation around its center of mass M (Figure S4D). To find the translation, we first calculate the total force \vec{F} generated by all beating cilia in the planarian (in all segments at each node); since the planarian is modeled as a rigid body, all cilia beating forces may directly be applied to the center of mass M. We then model the experimentally observed constant speed movement of planarians as follows. We assume that during each infinitesimal time span Δt the planarian speed starts from 0, accelerates due to action of \vec{F} and decelerates back to 0 due to action of counterforces (e.g.). More specifically, in the first half (from 0 to $\Delta t/2$) acceleration is $a = F/M$ (according to second Newton's law), and during the second half (from $\Delta t/2$ to Δt) deceleration is $a = -F/M$ (we use symmetric evolution of the speed for simplicity of calculations). Such periodic movement can be approximated as movement with constant speed $V = F\Delta t/4M$. Thus, we can calculate the translation from old position p_0 to new position p during iteration time Δt as

$$\vec{p} = \vec{p}_0 + \frac{\vec{F}}{4M}\Delta t^2 \quad (\text{Equation 1})$$

To find the rotation, we calculate for each i_{th} segment the net force \vec{F}_i arising from all its beating cilia and the torque $\vec{T}_i = \vec{r}_i \times \vec{F}_i$ about the planarian's center of mass M that \vec{F}_i generates (Figure S4C). The total torque of the planarian \vec{T} is then calculated as the sum of all \vec{T}_i . According to Euler's second law: $\Delta\omega/\Delta t = \vec{T}/I$, where $\Delta\omega/\Delta t$ is the angular acceleration, $\omega = \theta/\Delta t$ is the angular speed, $I = \sum_i r_i^2 m_i$ is the moment of inertia of the planarian body with r_i and m_i is the position and the mass of the i_{th} planarian segment. Following the same considerations as in the case of translation, we can approximate planarian's rotation as rotation with constant angular speed $\omega = T\Delta t/4I$. Thus, we can calculate the rotation from old angle θ_0 to new angle θ during iteration time Δt as

$$\theta = \theta_0 \pm \frac{T}{4I}\Delta t^2 \quad (\text{Equation 2})$$

where the sign depends on the direction of the torque.

In each new iteration, all segments acquire new cilia beating configuration, after this new total force \vec{F} and total torque \vec{T} are calculated; then using Equations 1 and 2 new position and new body orientation (\vec{p} , θ) are calculated.

Order of events in the simulation

- Planarian generation. Parameters of the planarian:
 - body mass (M), length (L) and width (W), initial orientation (in Figure S4 orientation is 90 degrees).
 - segment numbers along body length and width NL, NW.
 - node number bias; mean and standard deviation (Nm, N σ).
 - cilia beating angle bias; mean and standard deviation (αm , $\alpha\sigma$).
 - cilia beating force strength bias; mean and standard deviation (fm, f σ).
 - cilia beating coherency bias; mean and standard deviation (ϕm , $\phi\sigma$).
 - segment mass is calculated, node positions are set, cilia beating angles and forces are set, on/off state of each node is set.
- Simulation starts.
 - Iteration starts. Node positions never change.
 - cilia beating angle changes randomly within the given bias.
 - cilia beating force changes randomly within the given bias.
 - cilia beating coherency is used to set randomly a fraction of nodes in off state.
 - in each segment the total cilia beating force and torque is calculated.
 - total force and torque acting on the whole planarian body is calculated
 - the whole body is moved according to the calculated force.
 - the whole body is rotated according to the calculated torque.
 - repeat the iteration.

To test the simulation framework and see whether the results are qualitatively consistent, we run several simple tests. First, we generate two planarians: one is biased to rotate left (Figure S4E, planarian 2, with orange segment) and the other is biased to rotate right (planarian 1, with blue segment). All their segments have nodes generating force straight forward (grey segments), except for the colored two that have directional bias. Their trajectories are, as expected, mirrored, as shown with trajectory evolution and body orientation in Figure S4E. Second, we generate several planarians with the same shape parameters, but one without noise and the rest with random noise; their trajectory evolution and body orientation (Figure S4F) show the effect of noise. Varying and even opposite direction of rotation is caused by random asymmetrical distribution of nodes throughout the planarian body (which is fixed after a planarian has been generated), whereas the noise (visible in body orientation curves) comes from random cilia beating direction, force and on/off state. Next, we generate planarians with exactly the same angular bias of cilia per segment as in the experimentally observed RNAi-treated animals and run simulations on them. Our framework allows us qualitatively reproduce both linear translation on short time scale and circular movement on longer time scale (Figure 3); the direction of translation and rotation are

properly captured as well. Interestingly, even though these mutants translate in opposite directions, they both circle (rotate) in the same direction. However, it is not possible to quantitatively reproduce the speed of rotation or the speed of translation with simple model; it allows only qualitative translation of experimentally observed angular distributions into trajectories.

QUANTIFICATION AND STATISTICAL ANALYSIS

Statistical analysis was performed using Oriana 3 (Kovach Computing Services) for comparison of local rootlet angle variation. Significance was determined using Watson-Williams test and was defined as $p \geq 0.05$. All the other analyses were done with Prism 7.0.d (GraphPad). Significance was determined using Kruskal-Wallis test followed by Dunn's multiple comparisons test or with Mann-Whitney test. Statistical details can be found in the legends. Significance was defined as $p \leq 0.05$ (* $p < 0.05$, ** $p < 0.01$, *** $p < 0.001$). n numbers are biological repeats and measurements are represented as mean \pm SD.

DATA AND CODE AVAILABILITY

The code for computational modeling of planarian locomotion generated during this study is available from the GitHub source-code hosting facility (<https://github.com/dershoff/simulation-of-planarian-movement>).

2.4. hVFL1 impacts microtubules organization in mitosis and interphase

2.4.1. Introduction

As presented earlier, we have shown that the ortholog of VFL1, as well as the orthologs of VFL3 and ODF2, are involved in the control of BB rotational polarity in *S. mediterranea*. Rotational polarity is deeply linked to the anchoring of the cytoskeleton to the centriole, and our work has indeed confirmed the involvement of SMED-VFL1, -VFL3 and -ODF2 in the establishment of asymmetric connections between BBs. These connections involve MTs, as well as probably actin. Our study showed that all three proteins are required for properly forming the basal foot, an appendage necessary for MT anchoring that has similarities with SDAs (Article 2). We therefore hypothesized that the function of hVFL1 might also be related to the assembly or function of SDAs in the mother centriole, as it is the case for ODF2 and hVFL3. I therefore explored the role of hVFL1 in anchoring MTs to the centrosome. To do so, I analyzed the impact of hVFL1 depletion on processes that involve the anchoring of MTs to the centrosome: centrosome positioning in interphase, and spindle orientation in mitosis. I also analyzed MT network organization more directly in hVFL1-deficient cells. For this purpose, I performed regrowth experiments on interphase cells, and analyzed the number and length of astral MTs in mitosis. For all these phenotypes, I detected abnormalities in hVFL1-deficient compared to the control cells (Hung et al., 2016) (C.-T. Chen et al., 2014) (Delgehyr et al., 2005) (Piel et al., 2000).

On crossbow-shaped micropatterns, cells polarize in a stereotyped manner reminiscent of migrating cells. Under these conditions, the cells indeed rearrange their polarity axis to mimic migration, with the centriole at the front of the nucleus and the formation of a pseudo lamellipodium at the leading edge. The correct axis of polarization can be evidenced by the vector formed from the center of mass of the nucleus and the centrosome pointing forward in the direction of pseudo-migration. Under these conditions, the centrosome tends to be located approximately in the centroid of the pattern. Depletion of ODF2, a protein involved in the formation of SDAs and thus in the anchoring of MTs, leads to greater variability in centrosome

positioning (Hung et al., 2016). I thus analyzed the effect of depleting hVFL1 by RNAi on centrosome centering and cell polarization in cells grown on crossbow-shaped micropatterns.

I then studied the growth and release of MTs upon MT depolymerization in a regrowth experiment. During regrowth, MTs form an aster around the centrosome, which is the main MTOC. As they form, some of the MTs are released into the cytoplasm and some are anchored to the centrosome. The proportion of released and anchored MTs depends on the anchoring capacity of the centrosome. To quantify both populations, I measured the total fluorescence intensity of the MTs present in the cytoplasm and that of the aster after depolymerization followed by a short regrowth phase. The fluorescence intensity corresponding to the non-anchored MTs was obtained by subtracting the intensity of the aster from the total intensity.

To further investigate the involvement of hVFL1 in anchoring MTs to the centrosome, I analyzed it in the context of mitotic cells. During mitosis, SDAs rearrange the components present at their tips (Bowler et al., 2019). Nevertheless, anchoring of MTs still occurs under these conditions, probably via mechanisms partially different from those in interphase. In mitosis, the spindle is oriented through the anchoring of astral MTs to the cell cortex. Depletion of SDA components such as ODF2 induces spindle misorientation, which causes morphogenetic defects in acini obtained from 3D cultured MDCK cells (Hung et al., 2016). Under *in vitro* conditions, cells tend to orient their mitotic spindle parallel to the substrate. A greater variation in the angles formed by the spindle and the substrate is observed after depletion of ODF2. To test the effect of hVFL1 on MT anchoring, I therefore depleted hVFL1 on cells and measured spindle angle relative to the substrate. Astral MTs were then counted, and their length measured to investigate the origin of the spindle orientation defect I detected. The size of the spindle was also measured.

2.4.2. Methods

Cell culture:

RPE1 cells (hTERT-RPE1, RRID:CVCL_4388), and U2OS (RRID:CVCL_0042) were cultured in DMEM:F12 (1:1) and DMEM, respectively (Life Technologies). Both media were supplemented with 10% heat-inactivated fetal bovine serum and antibiotics (100 U/mL penicillin and 0,1 mg/mL streptomycin) (Life Technologies). Cells were kept at 37 °C in the presence of 5% CO₂. The CRISPR clones partially depleted from hVFL1 are the same than in Article 1.

RNA interference assay:

2,5 x 10⁴ cells/ml were seeded on glass coverslips in 24-well plates containing in 1 ml culture medium per well. Alternatively, for micropatterns, 2,5 x 10⁴ cells/ml were seeded in 6-well plates containing 4 ml of medium per well. The day after seeding, siRNAs were transfected using Lipofectamine RNAiMAX Reagent (Thermo Fisher Scientific) following recommendations of the manufacturer. The hVFL1-specific siRNA (sequence: 5'- AAG GAG AAA GAT GGA GAC GAT - 3') is the Si LRRCC1-1 used in article 1 (Muto et al., 2008). The ninein-specific siRNA (sequence: 5'- AAG AAG AAC TGG AAC GTT GTA -3') was purchase from Qiagen. AllStars negative control siRNA (Qiagen) was used as a control. Protein depletion was systematically verified by immunofluorescence using either an anti-hVFL1 antibody developed in the laboratory (Ab1 in Article 1) or an anti-Ninein antibody (Abcam, ab52473), together with an anti- γ tubulin antibody (Sigma, T5326).

Immunofluorescence:

Cells grown on coverslips were fixed in cold methanol for 5 minutes at -20°C. Coverslips were then incubated 10 minutes in saturation buffer, 0,5 % of Tween-20 and 3 % BSA (Sigma Aldrich) in PBS. Then primary antibodies diluted in blocking buffer were added to coverslips for 1 hour. Coverslips were washed 3 times for 1 minute in washing buffer (0,05% Tween-20 in PBS). Secondary antibodies diluted in blocking buffer were added to the coverslips for 1 hour. The following antibodies were used: Goat anti-mouse Alexa Fluor 488 (Invitrogen, A11001) and Goat anti-rabbit Alexa Fluor 555 (Invitrogen, A21428), both diluted 1/1000 in saturation buffer. Coverslips were then washed 3 times for 1 minute in washing buffer and mounted in

Fluoromount-G mounting medium (SouthernBiotech). Images were acquired in Z-series projections (at 0,5 μ m intervals) with either an Axio Imager Z1 widefield microscope (Zeiss) equipped with an AxioCam MRm camera (Zeiss), Plan-Apochromat 63x or 100x oil objectives with digital aperture 1,4, driven by the AxioVision software, or a Zeiss Apotome2 inverted widefield microscope Axio Observer Z1 (Zeiss) equipped with an sCMOS Orca Flash4 552 LT camera (Hamamatsu) and a 63x oil objective (Plan Apo, N.A. 1,4, Zeiss) driven by the Zen software.

Micropatterns:

10⁵ RPE1 cells per well were seeded in 6-well plates and RNAi interference was performed the next day. CYTOOchips CW-M-A (Cytoo) were coated with bovine fibronectin (Sigma) following instructions from the manufacturer. 48h after RNA interference, RPE1 cells were detached using Versene solution, seeded and allowed to spread on the adhesive micropatterns during 6–8h, following instructions of the manufacturer. Immunostaining was performed with primary antibodies anti-Ninein (Abcam, ab52473) and anti-Centrin (Milipore, 04-1624), both diluted 1/2000 and 5 μ g/mL Hoechst 33342 (ThermoFischer Scientific). Coordinates of the centrosome and the center of mass of the nucleus were determined relatively to the position of the micropattern. Nucleus-centrosome vectors were plotted using the Oriana software.

MT regrowth assays:

Cells were seeded in complete culture medium on 12 mm glass coverslips in a 24-well plate at a density of 25 000 cells/well. The day after, RNA interference was performed and 48h after transfection, cells were incubated in complete medium containing 2,5 μ M of nocodazole for 1h at 37°C and then 30 minutes at 4°C before regrowth. Prior to regrowth, cells were washed three times with cold medium. Regrowth time started with change to 37°C medium followed by incubation at 37°C during 5 min. Immediately after, cells were fixed and stained with anti- α tubulin (Abcam, ab7750) and anti-Ninein (Abcam, ab52473), both at 1/1000. The images were then analyzed with the image processing software ImageJ. α -tubulin fluorescence intensity was measured for MT asters or the whole cytoplasmic area and the background fluorescence intensity for each cell was subtracted to these values.

Spindle orientation analysis:

Cells were seeded in complete culture medium on 12 mm glass coverslips in a 24-well plate at a density of 80 000 cells/well and fixed the next day. For RNAi-treatment, cells were seeded and incubated with siRNAs during 48h as previously. Immunofluorescence was performed with anti-Ninein (Abcam, ab52473) and anti- γ tubulin (Sigma, T5326) or anti-EB1 (Santa Cruz, sc-398900), and 5 μ g/mL Hoechst 33342 (ThermoFischer Scientific). Metaphase cells identified by the presence of chromosomes aligned in a metaphase plate were imaged. Image analysis was performed using ImageJ software. Spindle orientation with respect to the coverslip was measured in the y-z axis following 3D reconstitution. Size was estimated in the different lines with cell area measurements. The length of growing MTs was estimated by measuring the distance between the centrosome and the EB1 signal.

2.4.3. Results

2.4.3.1. hVFL1 impacts microtubules during interphase

The centrosome, by controlling MT organization, plays an important role in the correct positioning of the different internal components of the cell. *In vitro*, the centrosome is positioned at the center of mass of the cell by pushing and pulling forces transmitted by the MTs. For MT forces to impact centrosome position, MTs need to be anchored at the centrosome. Changing MT stability or the nucleation capacity of the centrosome can also impact centrosome centering. To analyze centrosome centering in a reproducible and quantitative manner, we used crossbow-shaped adhesive micropatterns. Under these conditions, the cells are restricted in the shape of the micropatterns, and their internal components are positioned in a stereotyped fashion (Théry et al., 2006). Their polarization is reminiscent of migrating cells, with the centrosome positioned in front of the nucleus and near the center of the pattern. To determine whether hVFL1 has an impact on centrosome positioning, RPE1 cells depleted from hVFL1 by RNAi were polarized on crossbow-shaped micropatterns. Cells treated with control siRNA were used as a negative control, and cells depleted from Ninein were used as a positive control. Ninein is a component of SDAs that has been shown to be required for MT anchorage, and we thus expected a similar phenotype as the one observed following depletion of ODF2 (Hung et al., 2016). In cells depleted from Ninein, I observed as expected an increase in centrosome decentering compared to cells treated with control siRNA (Figure 25 A). In hVFL1-depleted cells, centrosome position was also more variable than in control cells and was comparable to what I observed for Ninein-depleted cells.

In control cells, the vector from the center of the nucleus to the centrosome usually points toward the front of the cell. In cells depleted from hVFL1 or Ninein, this vector was also globally oriented toward the front of the cell, indicating polarization respecting the pseudomigration axis (Figure 25 B). Nevertheless, the orientation of the vector was more variable than in control cells. These results therefore indicate that hVFL1 is important for controlling centrosome position in interphase cells as it is the case for Ninein or ODF2, which suggests that hVFL1 is involved in MT anchorage to the centrosome.

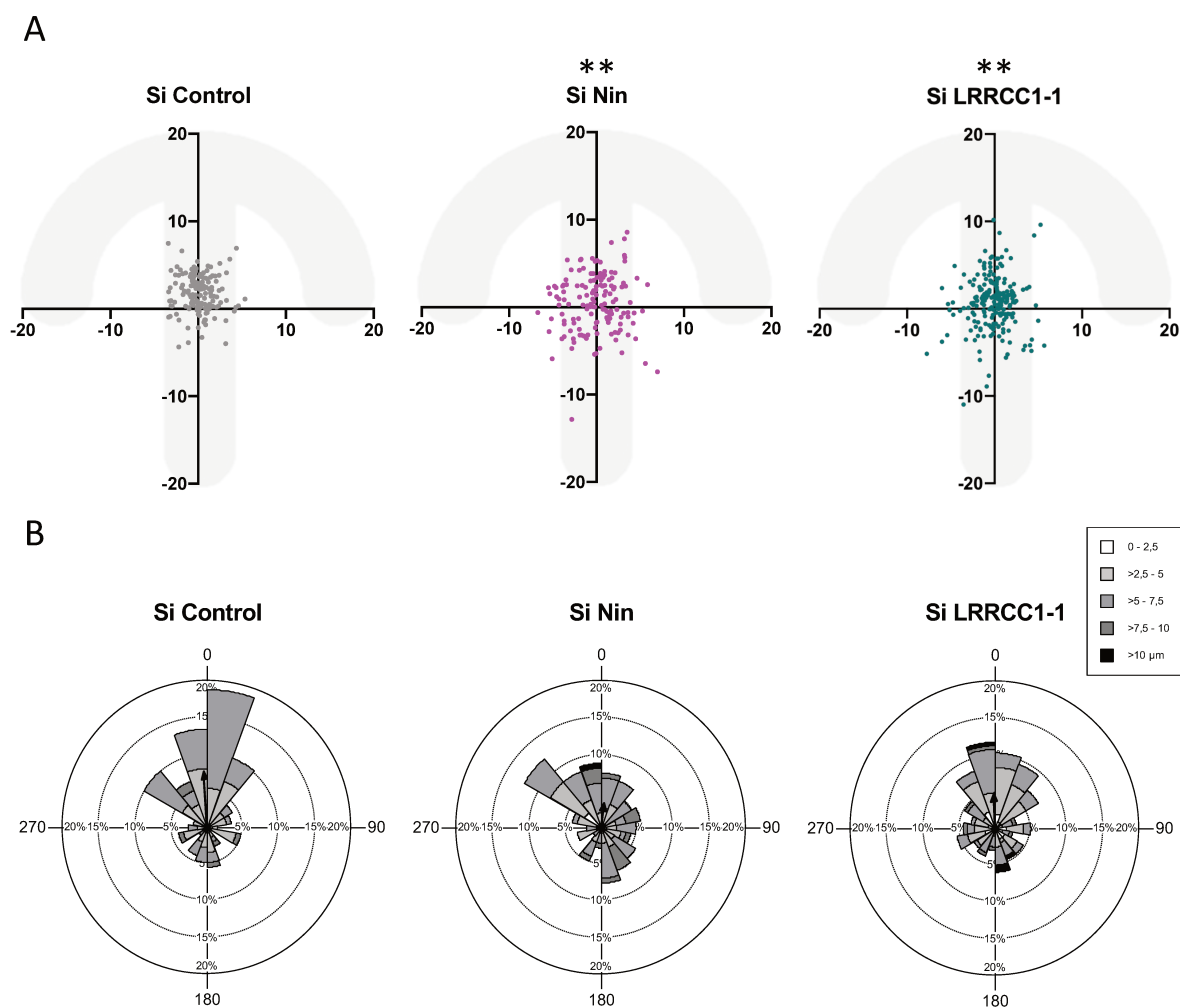


Figure 25: Analysis of centrosome position and nucleus-centrosome axis direction in RPE1 cells grown on crossbow-shaped micropatterns. (A) and (B) are from the same experiments. $N < 147$, ≥ 3 independents experiments. (A) Centrosome position with respect to the center of the micropattern. Si Nin and Si LRRCC1-1 coordinates are significantly different from Si Control coordinates, length is expressed in μm , (two-way ANOVA, P Value Si Control vs. Si Nin = 0.0014, P Value Si Control vs. Si LRRCC1-1 = 0.0018). (B) Distribution of the nucleus-centrosome vectors. Vector length is plotted as different shades of gray, length is expressed in μm . The black arrow indicates the mean vector for each condition. These results have been obtained with the help of Quentin Delobelle.

To further study the anchoring of interphase MTs and to measure it in a more direct way, I performed a MT regrowth experiment. The purpose of this experiment was to determine whether the ability of the centrosome to nucleate and anchor MTs was affected in cells depleted from hVFL1. For this, I used U2OS cells as in (Hung et al., 2016), because it was shown that MT anchorage in RPE1 cells is little affected by inactivation of ODF2 (Mazo et al., 2016), suggesting that other mechanisms can compensate for the absence of SDAs in this cell line. MTs were depolymerized then allowed to regrow for 2 minutes, a time short enough to avoid complete MT repolymerization. Under these conditions, an aster forms around the centrosome - localized by staining ninein - and some MTs are already present in the cytoplasm (Figure 26). I measured α -tubulin fluorescence intensity at the centrosome and in the cytoplasm of cells treated with hVFL1 or control siRNAs. Fluorescence intensity within asters was significantly decreased of about 20% in hVFL1-depleted compared to control cells (Figure 26 B). This decrease can be explained either by an increase in the proportion of MTs released into the cytoplasm or by a decrease in MT assembly. When I measured the MT intensity in the cytoplasm, I found a small but significant increase of about 10% in α -tubulin labeling in cells treated with hVFL1 siRNA. These results suggest that hVFL1 may play a role in the anchoring of interphase MTs. However, this experiment was performed only once, and these results are therefore too preliminary to conclude. These analyses will have to be repeated by including a second siRNA against hVFL1 and confirmed using CRISPR U2OS lines that I have generated during my thesis work.

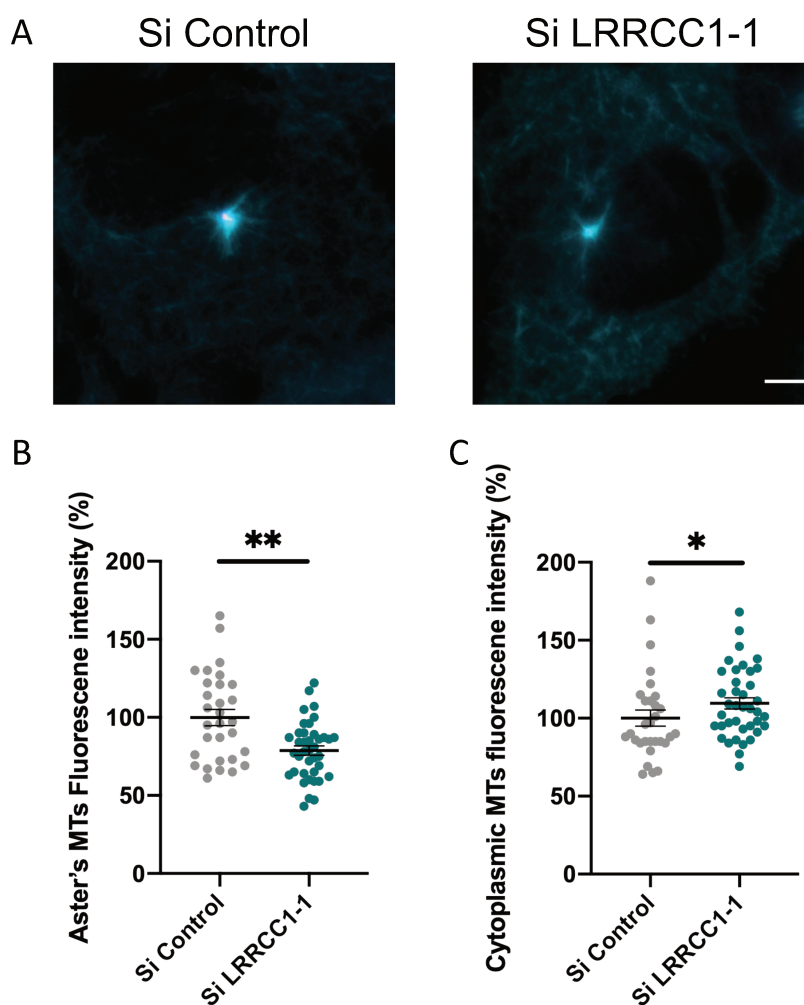


Figure 26: MT regrowth in U2OS cells depleted from hVFL1 by RNAi. (A) Immunofluorescence view of MT regrowth in control or hVFL1-depleted cells. Ninein in magenta, α -tubulin is in cyan. Bar, 5 μ m. (B)(C) Quantification of overall fluorescence intensity of α -tubulin in the aster (B) or in the cytoplasm (C), 1 experiment, $n \geq 30$ cells, Mean and Standard error, Mann-Whitney test, *: $P < 0,05$; **: $P < 0,01$. These results were obtained with the help of Thanh Bich Ngan Phan.

2.4.3.2. hVFL1 impacts microtubules during mitosis

MT anchoring is not trivial to analyze. Ideally, MTs should be observed in living cells to compare the dynamics of MTs in the vicinity of centrosomes, and to distinguish anchored MTs from released MTs. Unfortunately, these observations are made very difficult by the presence of a large number of MTs around the centrosome. Nevertheless, it is possible to test the effects of anchoring MTs in different ways to accumulate a body of evidence. During mitosis, SDAs are remodeled, and elements at the ends of SDAs are transiently relocated to the periphery of the parent centriole. It was therefore of interest to determine whether depletion of hVFL1 also has an effect on the organization mitotic MTs, as previously shown for ODF2. More specifically, ODF2 depletion induces a greater variability of spindle angle relative to the substrate, a phenotype explained by a modification of the number and stability of astral MTs (Hung et al., 2016).

I thus analysed spindle angle, deduced from the position of the centrosomes, by immunofluorescence in control or hVFL1-deficient RPE1 cells. For this purpose, centrosomes were labelled with anti-Ninein and anti- γ -tubulin antibodies, as well as a DNA stain to identify metaphase cells. With the help of Quentin Delobelle, I performed acquisitions in z-series in order to obtain 3D reconstructions and measure the spindle angle in the plane perpendicular to the acquisition axis. Under normal conditions, the centrosomes are positioned in a such way that the spindle is generally parallel to the substrate and perpendicular to the metaphase plate (Figure 27 A). The mean angle between the spindle and the substrate is therefore close to 0° . In contrast, a significant increase in spindle angle can be observed in the two hVFL1-deficient RPE1 CRISPR clones expressing the lowest levels of hVFL1 (clones 1.1 and 1.9). The slight increase for clone 1.2, which expresses the highest levels of residual hVFL1, is not significantly different from the control. To confirm the results obtained for clones 1.1 and 1.9, we used RNAi. We observed that spindle angle distribution was also significantly wider in hVFL1 siRNA-treated cells compared to control cells, confirming the results obtained with the CRISPR clones.

As the control of mitotic spindle orientation is dependent on the function of astral MTs, we next examined the impact of hVFL1 inactivation on these MTs. For this, we used an antibody against the EB1 protein, which only labels the growing plus end of MTs, as anti-tubulin produces dense labelling, making measurements of individual MTs impossible (Figure 27 B). Since astral MTs are dynamic structures, alternating very rapidly between polymerization and depolymerization

phases, the use of EB1 gives a good approximation of the behavior of all astral MTs (Hung et al., 2016). We measured the number of growing MTs either in the CRISPR clone 1.1, in RPE1 cells treated with hVFL1 siRNA, or in the corresponding controls. The average number of astral MTs per metaphase centrosome was significantly decreased upon hVFL1 depletion, both in the CRISPR clone 1.1 and in hVFL1 siRNA-treated cells compared to their respective control (Figure 27 B). For clone 1.1, an average of 85.2 ± 2.2 MTs per centrosome was counted compared to 110.6 ± 2.2 MTs/centrosome for wild-type RPE1 cells. In a comparable manner, cells depleted from hVFL1 by RNAi had an average of 87.7 ± 1.0 MTs/centrosome compared to 110.8 ± 1.3 MTs for cells treated with the control siRNA. The decrease in astral MT number in hVFL1-deficient cells thus probably contributes to increasing spindle angle distribution in these cells.

In parallel, we measured the length of astral MTs. We observed that the average length of growing astral MTs was significantly increased for clone 1.1 compared to WT cells (Figure 27 C). The same result is observed in RNAi-treated cells, confirming the effect of hVFL1 depletion on the length of astral MTs (Figure 27 C). We did not expect this result because depletion of ODF2 leads to a decrease in astral MT length (Hung et al., 2016). To determine whether the increase in astral MT length following hVFL1 depletion is accompanied by other changes in spindle architecture, we also analyzed mitotic spindle length, given by the distance between the two centrosomes, and cell area, given the surface of the mitotic cell in 2D. These measurements were performed on the same images used to measure the spindle angle. We observed differences in cell size between CRISPR clones. Cells in clones 1.2 and 1.9 were significantly larger than those in clone 1.1 and in WT (data not shown). This was not observed in RNAi-treated cells, and these differences did not correlate with the residual expression level of hVFL1 in CRISPR clones (WT>1.2>1.1 and 1.9). Thus, it is likely that the cell size increase in clones 1.2 and 1.9 is not related to hVFL1 depletion. We therefore compared the ratio of spindle length to cell area, normalized to the RPE1 WT condition, to determine the effect of hVFL1 loss on mitotic spindle size independent of cell size. We observed a significant decrease in mitotic spindle size in each of the CRISPR cell lines. We also observed a significant decrease in mitotic spindle size in hVFL1 siRNA-treated cells compared to control siRNA, but to a lesser extent than in CRISPR cells. Thus, loss of hVFL1 decreases mitotic spindle size in addition to increasing the length of astral MTs.

In conclusion, these results show that the loss of hVFL1 affects different aspects of the MT organization in metaphase. Astral MTs appear to be more stable and less numerous, which probably explains the misalignment of the metaphase spindle in these cells. As well, the mitotic spindle is shorter upon hVFL1 depletion. The latter aspect, as well as the reduction in the number of astral MTs, may be observed when the amount of γ -tubulin present at the centrosome is too low. However, we did not find a significant decrease in the amount of γ -tubulin present at the centrosome after inactivation of hVFL1 by RNAi or CRISPR (data not shown). Instead, our results are close to the phenotype caused by loss of ODF2, which disrupts spindle orientation and decreases the number of astral MTs (Hung et al., 2016). The hVFL1 protein thus appears to have a role in mitotic spindle formation, which seems to be related to the ability of centrosomes not to nucleate MTs, but to anchor and/or stabilize them.

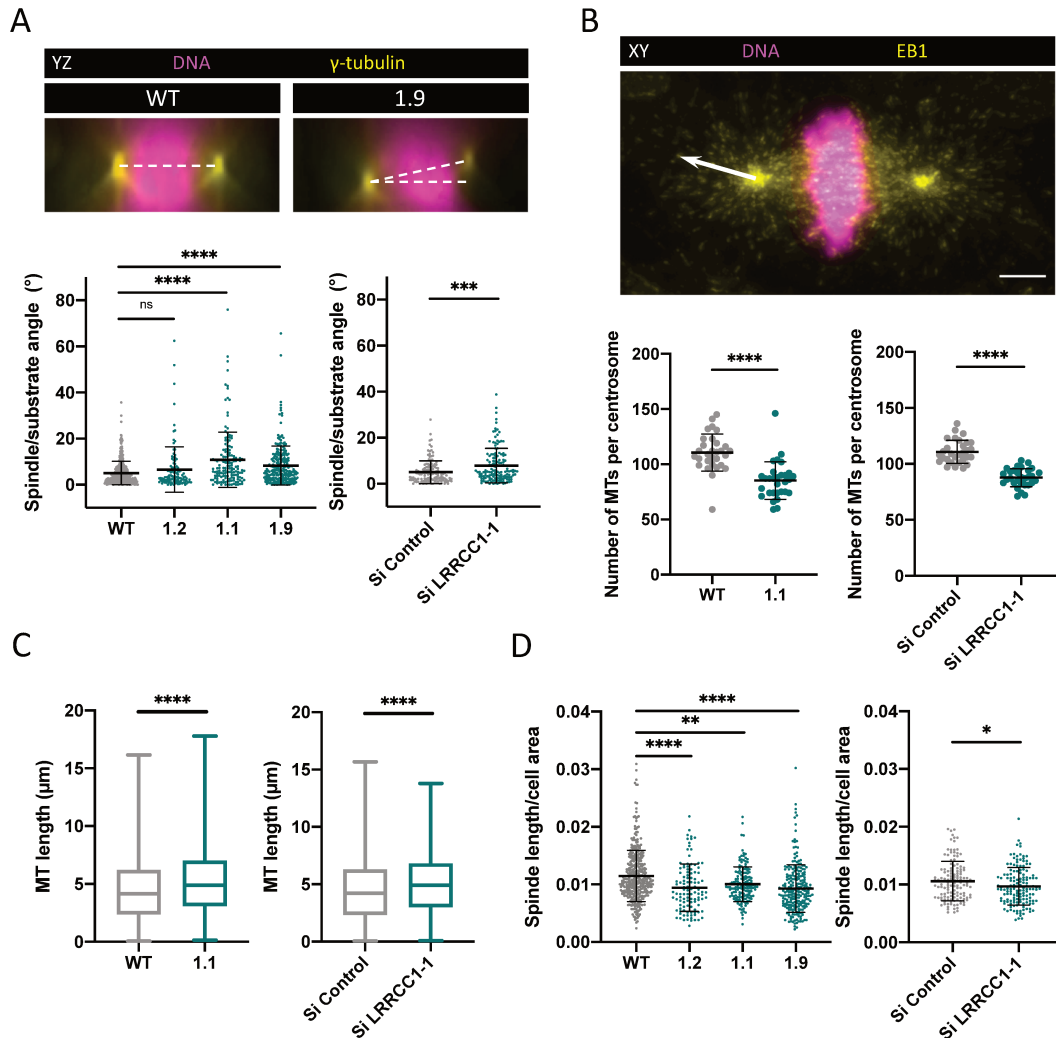


Figure 27: Analysis of spindle orientation and astral MT defects in hVFL1-depleted RPE1 cells. (A) Spindle orientation in cells depleted from hVFL1 by CRISPR or RNAi. Top panels: immunofluorescence views of mitotic spindles seen from the side (yz plane). The dotted lines show the angle formed by the long axis of the spindle given by the position of the two centrosomes, and the substrate; yellow: γ -tubulin; magenta: DNA. Bottom: quantification of spindle angles. CRISPR clones: $N \geq 111$, ≥ 3 independent experiments, Kruskal-Wallis test; RNAi-treated cells: $N \geq 131$, 3 independent experiments, Mann-Whitney test (B) Astral MT. Top panel: mitotic cell stained for EB1 (yellow) and DNA (magenta). The white arrow indicates how astral MT number and length was measured. Bar, 5 μm ; Bottom: quantification of MT number. CRISPR clones: $N = 30$, 3 independent experiments, Mann-Whitney test; RNAi: $N = 30$, 3 independent experiments, Mann-Whitney test. (C) Quantification of MT length. CRISPR: $N \geq 5098$, 3 independent experiments, Mann-Whitney test; RNAi: $N \geq 5286$, 3 independent experiments, Mann-Whitney test. (D) Quantification of spindle length over cell area. CRISPR: $N \geq 109$, 3 independent experiments, Kruskal-Wallis test; RNAi: $N \geq 131$, 3 independent experiments, Mann-Whitney test. For all panels: ns: $P > 0,05$; *: $P < 0,05$; **: $P < 0,01$; ***: $P < 0,001$; ****: $P < 0,0001$. These results were obtained with the help of Quentin Delobelle.

2.4.4. Preliminary conclusions and perspectives

hVFL1 depletion is thus influencing MT organization in three different manners:

- Centrosome centering is impaired in cells grown on micropatterns.
- Aster size is decreased and cytoplasmic MTs more numerous in MT regrowth assays.
- Spindle orientation is altered due to modifications of astral MTs.

These three phenotypes could be explained by a defect in MT anchoring to the centrosome. However, defective centrosome centering could also result from perturbations of other mechanisms than MT anchoring. For instance, MT nucleation and regulation of their dynamic properties is also important for centrosome centering. Similarly, the decrease in aster size in cells depleted from hVFL1 could be due to a defect in MT nucleation. Finally, the spindle position defect observed in hVFL1-depleted cells could result from an increase in MT stability, a decrease in MT nucleation, or a change in spindle size. Therefore, it will be important to further analyze these defects to better understand the role of hVFL1 in MT organization.

To test the hypothesis of a MT anchoring defect in cells lacking hVFL1, it would be interesting to verify the structural defects of SDAs by U-ExM. For example, we could label components of SDAs such as Ninein and CEP170, as well as ODF2, a protein common to SDAs and DAs, in interphase and mitosis. Possible defects observed after depletion of hVFL1 could then explain a defect in MT anchoring. Furthermore, abnormalities in MT anchoring could be observed directly by this approach to validate this hypothesis. The resolution provided by U-ExM could be used to directly observe the anchoring of MTs to SDAs, as it has already been done by super-resolution microscopy (Bowler et al., 2019). For U-ExM analysis, a specific fixation should be used to preserve the cytoplasmic MTs as previously described (Gambarotto et al., 2019). Under these conditions, interphase and mitotic anchoring could be measured at the centrosome.

An implication of hVFL1 in MT organization could also possibly explain why patients with a mutation in the gene encoding hVFL1 have progressive microcephaly. Indeed, mutations leading to an increase in the stability of interphase MTs have been described in patients with this pathology (Colin et al., 2014) (Pode-Shakked et al., 2017). However, progressive microcephaly is not well understood. A way to confirm the implication of hVFL1 in microcephaly would be to target its expression in an animal model like the zebrafish. This model has the advantage of being

very versatile and of allowing the inactivation of genes by different methods. Moreover, the zebrafish has already been established as a model not only for ciliopathies, but also for progressive microcephaly (Siekierska et al., 2019) (Song et al., 2016).

3. Discussion and Perspectives

Centrioles are structures based on a 9-fold symmetric arrangement of MTs that have been conserved since at least the last common ancestor of eukaryotes. These highly complex macromolecular ensembles are used by many organisms for different purposes. Much is still unknown about the structure of centrioles, their roles, and their diversity across eukaryotes. The studies presented here provide additional bits of information for understanding centrioles. We show that centrioles in the human centrosome are rotationally asymmetric despite their apparent symmetry. We found at least two markers of this asymmetry, hVFL1 (LRRCC1) which is specifically enriched near two consecutive triplets in the distal part of the centriole lumen, and C2CD3 which forms a C-shaped structure decentered towards the region of the centriole wall where hVFL1 is located. Depletion of hVFL1 disrupts C2CD3 localization and induces defects in centriole structure, ciliogenesis and ciliary signaling, indicating that hVFL1 is involved in the organization of the distal end of centrioles. Furthermore, we show that hVFL3 is localized to SDAs and to the proximal end of centrioles. hVFL3 interacts with CEP170 and depletion of hVFL3 impairs MT anchorage at SDAs. hVFL3 is a MT-binding protein that could be directly involved in MT anchoring to SDAs. In addition, we studied the multiciliated epidermis of *S. mediterranea* where centrioles are organized in a polarized network generating a bilaterally symmetric pattern. We showed that the centriole components SMED-ODF2, SMED-VFL1, and SMED-VFL3 are required to establish asymmetric chiral connections between centrioles and balance their effects. These proteins act in part by controlling the assembly of the basal foot, which in planarians has a structure that reflects the chirality of the centrioles. The organization of chiral asymmetric cytoskeletal network is probably an ancestral property of centrioles.

3.1. Centriole inherent asymmetry

My work shows that centrioles within the human centrosome have asymmetric constituents. This discovery could change the way we understand and study the function and structure of these centrioles. These findings suggest that an asymmetric structure is present in the lumen of human

centrioles that may be homologous to the acorn in *C. reinhardtii* centrioles. Confirmation of the existence of this structure by EM would be important to establish a parallel with the acorn. However, such a structure has never been clearly observed before despite numerous studies of vertebrate centrioles by EM. Some published electron micrographs nevertheless suggest the presence of an acorn-like filament in the distal lumen in different species including vertebrates, but it is not clear whether this structure has rotational asymmetry or not (Geimer & Melkonian, 2004). One reason why this structure could have escaped detection by EM so far could be its limited electron density. Indeed, the acorn described by Geimer *et al.* in 2004 and 2005 in *C. reinhardtii* is itself not very electron dense and has been observed only with difficulty even though the preservation of centriole fine structure is generally better in *C. reinhardtii* than in animal cells. The use of other techniques such as cryo-EM could help to resolve the structure of the “human acorn”. On the other hand, to attest that C2CD3 is indeed a component of a filamentous structure, immunogold labeling should be performed. It would also be important to analyze hVFL1 by the same approach to confirm the asymmetry of the proteins and their involvement in the same structure. In parallel, these analyses could be done by combining U-ExM with another super-resolution microscopy technique such as dSTORM, as recently described (Zwettler *et al.*, 2021).

C2CD3 has been studied in super resolution microscopy before but the rotational asymmetry of its localization pattern was not noted. This could be related to the fact that this asymmetry is less obvious than that of hVFL1 and can be mistaken for a slight misalignment of the centriole axis in z during image acquisition. Nevertheless, we observed that correcting the alignment of centriole long axis in z reinforces not only the positional asymmetry, but also the shape asymmetry of the C2CD3 labeling. In our study, C2CD3 forms a C-shaped motif in the centriole lumen, slightly closer to a portion of the centriole wall. However, the localization of C2CD3 observed in dSTORM by (Yang *et al.*, 2018) (Figure 28, A) also appears to be slightly asymmetric, which was not commented in this study, probably because it was interpreted as coming from uneven labeling efficiency across the structure. The C2CD3 marking in lateral view (Figure X, B) also appears tilted, perhaps indicating another form of asymmetry that went unnoticed. In another study (Tsai *et al.*, 2019), the authors examined C2CD3 by 3D-SIM. Of important note, the images of C2CD3 presented in the paper show that C2CD3 is not perfectly centered but the signal is closer to one side of the centriole wall (Figure 28, C and D).

Geimer *et al.* in their 2005 study described a V-shaped structure in *C. reinhardtii* centrioles (Figure 5) positioned at the same level as the acorn and co-localized with centrin. They also describe that centrin is found internally as a mesh in the central and proximal part of the centriole, and as a fine spike in the distal part. In the study by Le Guennec *et al.* in 2020, the authors precisely determine the localization of centrin in the centrioles of human cells. They describe that Centrin-2 is a component of the centriole scaffold that occupies the proximal and central part of the centriole. They also observe a Centrin-2 spike in the distal portion of centrioles (Figure 28, E and F). The centrin pattern presented by the authors appears to be slightly asymmetric in the distal part. In different study (Kashihara *et al.*, 2019), Centrin-3 appears off centered with respect to the localization of CEP128 seen by SIM. The authors did not comment on this off-centering of Centrin-3 and they do indicate at which position along centriole length Centrin-3 is localized (although it is clearly distal in the daughter centriole seen in lateral view, which corresponds to published data on Centrin-3 localization). Taking all of this into account, one can hypothesize that the acorn-associated, centrin-containing V-shaped filament observed in *C. reinhardtii* is conserved in human centrioles. To confirm this hypothesis, we would need to further examine the localization pattern of Centrin-2 and Centrin-3 in the distal part of the centriole with greater resolution, together with C2CD3 and hVFL1.

In addition to the problems inherent to the observation itself (*i.e.*, heterogeneity of immunofluorescence labeling, lack of resolution, X-Y color shifts, poor preservation of structures in EM or low electron density), the fact that the rotational asymmetry of the centrioles of the centrosome was not detected could be related to the fact that image averaging is often used to improve the quality of images. This can be done by combining multiple images, as I did, or by rotating the same image around centriole long axis to reinforce electron dense structures as it is done for EM data. If these operations are performed under the assumption that the centrioles are symmetrical, they will have the effect of erasing the asymmetries which will thus go unnoticed (Bowler *et al.*, 2019) (Shi *et al.*, 2017) (Le Guennec *et al.*, 2020) (Klena *et al.*, 2020). As so, many asymmetric differences can go undetected.

It is therefore not surprising that the rotational asymmetry of centrioles within the animal centrosome has escaped observation until now. Accumulating data and improved imaging techniques now allow us to identify some deviations from symmetry in the structure. For

example, SDAs are present in numbers less than 9 in some cell types (Figure 28, H-L). It would then be interesting to determine whether these asymmetries are in any way correlated with the asymmetric location of hVFL1 and C2CD3. Using the hVFL1 domain as a reference point for aligning the centrioles, we could determine whether this reinforces asymmetries in the distribution of SDAs or other centriole features. In our study in *S. mediterranea* (Article 3), we hypothesized that SMED-VFL1 and -VFL3 might specify certain triplets of the BB to position appendages (*i.e.*, the basal foot and ciliary rootlet), a hypothesis already proposed in previous work in *C. reinhardtii* and *P. tetraurelia* (Silflow et al., 2001) (Bengueddach et al., 2017). Such a mechanism could be conserved in humans, where the presence of hVFL1 on certain triplets could also influence the formation of SDAs.

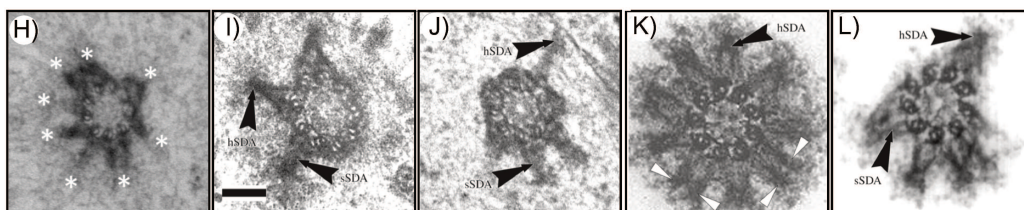
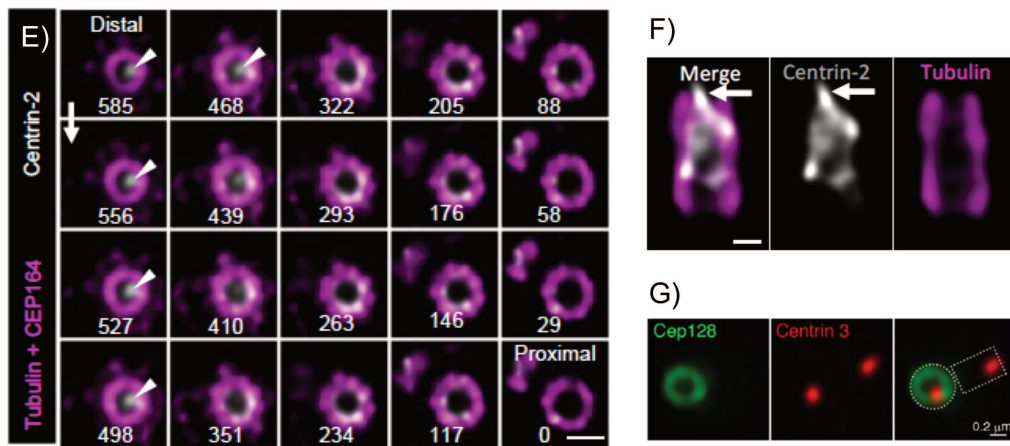
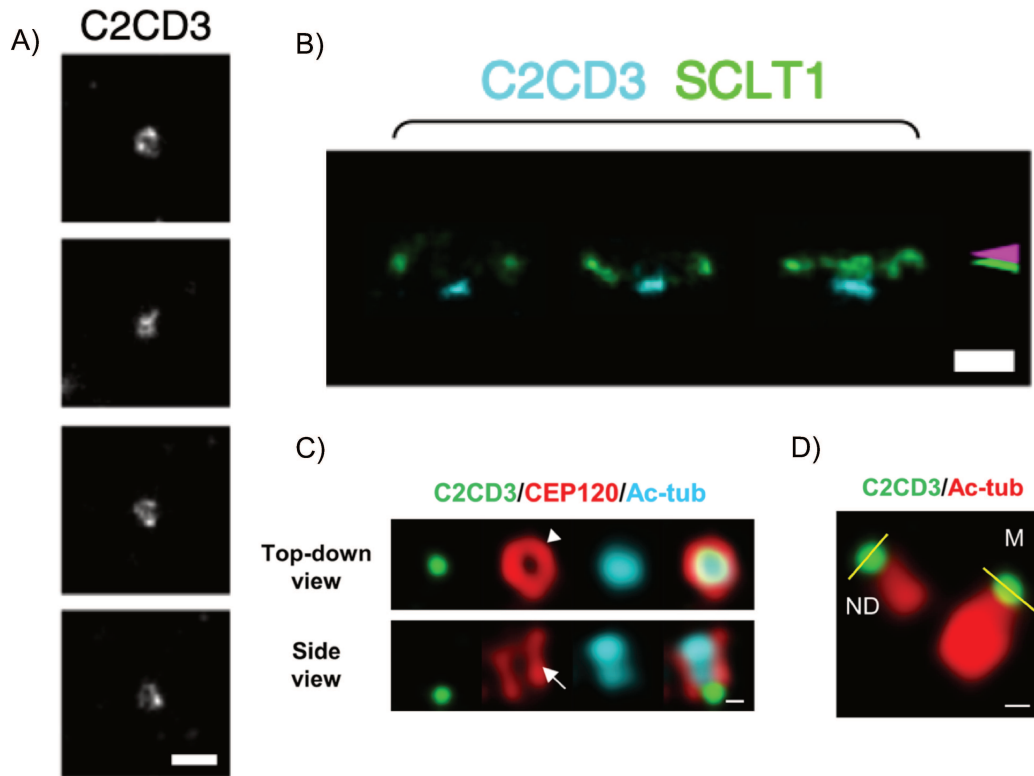


Figure 28: Images from the literature suggesting the existence of rotational asymmetries in centrioles of the centrosome. A) dSTORM super-resolution images showing the distribution patterns of C2CD3 proteins. From (Yang et al., 2018). B) Three representative dSTORM images of centrioles in lateral view illustrating the relative positions of C2CD3 (cyan) and SCLT1 (green). The green and pink arrowheads mark the positions of SCLT1 and FBF1, respectively. From (Yang et al., 2018). C) 3D-SIM analysis of the spatial localizations of C2CD3 and CEP120 at the distal ends of centrioles. RPE1 cells were synchronized in G2 phase and immunostained with the indicated antibodies. Scale bar, 100 nm. From (Tsai et al., 2019). D) Super-resolution (3D-SIM) microscopic analysis of centriole distal-end proteins. RPE1 cells were synchronized in G2 phase and immunostained with the indicated antibodies. From (Tsai et al., 2019). E) Top view 3D images of expanded mature human centrioles stained with tubulin and CEP164 (magenta) and Centrin-2 (gray). 3D volumes are shown as serial cross-sections through the centrioles, with Z-height indicated in each image. White arrowheads indicate an additional dot-like localization of Centrin-2 at the distal tip. Z-steps every 120 nm. Scale bar: 250 nm. Representative images from 3 independent experiments. From (Le Guennec et al., 2020). F) Representative Lightning confocal images of *in situ* expanded mature human centrioles (longitudinal views) co-stained for tubulin (magenta) and Centrin-2 (grey). White arrow indicates the additional distal localization of Centrin-2. Scale bar: 100 nm. From (Le Guennec et al., 2020) G) RPE1 cells transfected with GFP-CEP128 and stained for Centrin-3 (blue). Images were obtained by SR-SIM. Scale bars: 200 nm (centriole panels). From (Kashihara et al., 2019). H-L) EM sections of mother centrioles in different cell types. From (Chong et al., 2020) and (Uzbekov & Alieva, 2018) H) Centriole with an approximately nine-fold distribution of subdistal appendages (SDAs) in a RPE1 cell. I) Centriole with three SDAs in an epithelial pig kidney embryo cell. J) Centriole with four SDAs from a pig oviduct cell. (K, L) Centrioles with nine and six SDAs from KE-37 human cells. Scale bar, 100 nm.

Other centriole proteins could be asymmetrically localized. Because VFL3 and VFL1 appear to have a similar function in BB rotational polarity in *S. mediterranea*, I further examined the localization of hVFL3 by U-EXM. In Pizon *et al.*, (2020, Article 2), we found that by immun-EM a Myc-hVFL3 fusion localizes to SDAs and to a lesser extent to the proximal end of centrioles. Preliminary data presented in Figure 29 show the localization of the endogenous hVFL3 protein by U-ExM with α - and β -tubulin staining, as well as SAS6 in the right panel. Under these conditions, hVFL3 is localized in the proximal part of the centriole, asymmetrically, outside the centriole wall and associated with 1 to 3 triples. The staining of hVFL3 on SDAs is not visible by this method, which could reveal the existence of two pools of hVFL3, one stable associated with the proximal end of the centriole and the other more dynamic at SDAs. Indeed, the U-ExM protocol does not preserve cytoplasmic MTs, so it is possible that other structures less stable than the centrosome are not preserved by this method either. A change in the U-ExM protocol could help detect hVFL3 in SDAs. In any case, these preliminary experiments should be repeated. But the asymmetry of hVFL3 is further evidence that human centrioles in the

centrosome exhibit rotational asymmetries. Interestingly, hVFL3 does not stain procentrioles as does hVFL1, indicating a difference in the timing of integration of these proteins during centriole biogenesis. Future work will establish the relative position of hVFL1 and hVFL3 in centrioles of the centrosome and in oriented centrioles such as the BBs of multiciliated cells. Ochi *et al.* (2020) and Nommick *et al.* (2021) localized hVFL3 to the ciliary rootlet in xenopus multiciliated cells. It is likely that what they observe corresponds to the proximal localization of hVFL3 that we detect in human centrioles. Future work will determine how hVFL3 localizes with respect to components of the intercentriole linker, or with respect to the ciliary rootlet in multiciliated cells.

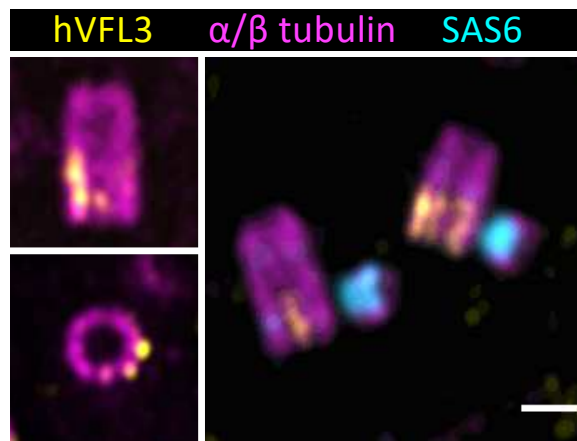


Figure 29: hVFL3 localization by U-ExM. α - and β -tubulin are in magenta, hVFL3 in yellow and SAS6 in cyan (right panel only). Scale bar, 200 nm. Top left panel, longitudinal view. Bottom left panel, transversal view of the proximal part. Right panel, longitudinal view of duplicating centrioles. hVFL3 signal is assymmetrically localized at the proximal end of centrioles, externally of centriole wall, on 1 to 3 triplets. We did not observe hVFL3 labeling at the subdistal appendages, contrary to what we found by conventional immunofluorescence microscopy (Pizon *et al.*, 2020) hVFL3 is also not present in procentrioles.

Thus, it appears that rotational asymmetry is more present in the ultrastructure of centrioles than we expected. Thus, it would be interesting to map centriolar proteins by super-resolution microscopy taking into account the orientation of the centriole. This would allow to detect possible other constituents that localize asymmetrically or show uneven accumulation around the circumference of the centriole. The evolutionary conservation of rotational asymmetry should also be exploited, as a multitude of organisms and cell types use centrioles for different purposes (motility, mucus removal, signaling, gradient formation...). For example, it would be interesting to inactivate the C2CD3 ortholog in *S. mediterranea* and to analyze the rotational polarity of

centrioles under these conditions to determine if it is altered as in VFL1-depleted animals. As well, it would be interesting to characterize C2CD3 orthologs in flagellates. We were unable to identify an ortholog of C2CD3 in the *C. reinhardtii* genome, although there is an ortholog in the closely related species *Micromonas pusilla*. This could be due to a gap in the genomic sequence, or too much divergence in the sequence of C2CD3. In contrast, an ortholog was identified in *P. tetraurelia* (Zhang & Aravind, 2012).

3.2. Centriole rotational asymmetry and the primary cilium

In *C. reinhardtii* and flatworms, hVFL1 orthologs are involved in the polarization of centrioles in the plane of the plasma membrane, which in turn determines the direction of the ciliary beat. According to (Schneider et al., 2010), primary cilia point in the direction of migration in mammalian cells. As the function of hVFL1 appears to be globally conserved, the mechanisms of centriole polarization could be similar to those described for motile cilia. Indeed, determining the localization of hVFL1 at the circumference of the mother centriole in migrating human ciliated cells could tell us whether centriole orientation plays a role in migration. Furthermore, there is no known asymmetry in the primary cilium, either structurally or in terms of intra-flagellar transport. IFT trains are large complexes, and they occupy considerable space in the cilium. How space is managed within the cilium is an open question. A previous study showed that bidirectional IFT is restricted to certain doublets of MTs in the cilium of *T. brucei*. In this organism, motile cilia are oriented and there is an asymmetric distribution of IFT (Bertiaux et al., 2018). Thus, it is possible that a mechanism restricting transport into specific doublets is conserved in primary cilia. It is conceivable that a cilium oriented towards specific ligands and spatially controlled intra-flagellar transport could be advantageous for signal transduction. Measuring such a phenomenon would involve resolving the ciliary superstructure in 3D in polarized cells to locate IFT trains within the cilia.

Furthermore, the acorns described in (Geimer & Melkonian, 2005) and (Vaughan & Gull, 2016) are of unknown composition and function. Since we found that C2CD3 delineates a filamentous structure reminiscent of an acorn and that hVFL1 localizes as its ortholog in *C. reinhardtii*, we hypothesize that together they could form a structure homologous to the acorn. In any case, it appears that there is a link between centriole rotational asymmetry and primary ciliogenesis in human cells. Perturbing the function of components of this structure induces sensory ciliopathies

in humans, as mutations in C2CD3 and hVFL1 have both been involved in such pathologies. Why this rotationally asymmetric structure is conserved at the base of primary cilia remains an open question. In *C. reinhardtii* and in MCCs, the function of VFL1 is related to the assembly of asymmetric appendages, which must be correctly positioned with respect to the direction of the ciliary beat. A rotationally asymmetric structure present early during centriole assembly and ultimately located near the cilium could coordinate centriole polarity, which might affect the organization of the surrounding cytoskeleton as in flagellates or MCCs, with asymmetric features within the primary cilium.

3.3. Rotational asymmetry in centriole duplication

Centriole rotational asymmetry could also play a role in centriole duplication, as it is the case in *C. reinhardtii*. Indeed, we found that the location of procentrioles is not completely random compared to the location of hVFL1 in the parent centriole. This result suggests that the rotational asymmetry of centrioles may somehow influence centriole duplication in human cells. In *C. reinhardtii*, procentriole formation is determined in relation to the parent centrioles, which are included in a complex structure called the basal apparatus (Fig 5A, page 16). This complex structure, which includes microtubular and fibrous roots in addition to centrioles and procentrioles, is not conserved in animal cells, in which procentrioles form near the wall of the parent centrioles. The site of formation is determined by the recruitment of PLK4 through the PCM components CEP152 and CEP192 (Yamamoto & Kitagawa, 2019). It is possible that a molecular asymmetry between triplets in the parent centriole could result in a local change in PCM composition, which in turn could impact PLK4 activation. Future work will need to elucidate how centriole rotational asymmetry influences centriole duplication. Since hVFL3 also localizes asymmetrically at the proximal part of the centriole, where procentrioles are formed, it would also be interesting to repeat this experiment using hVFL3 as a polarity marker - insofar as hVFL1 and hVFL3 are not consistently positioned relative to each other, which remains to be established.

hVFL1 is recruited early in centriole formation, like many distal proteins. Similarly, in *C. reinhardtii*, the acorn is also present very early in pbb, indicating that rotational polarity is constitutive of the centriole. Much remains to be discovered about centriole biogenesis, from the molecular to the structural chain of events. The difficulties in elucidating these mechanisms stem

from the small size of centrioles, and even more so procentrioles, and the large number of proteins that must be incorporated to form a complete centriole. One possible hypothesis would be that the incorporation of the different centriole elements would occur in a specific manner relative to this asymmetry. However, testing this hypothesis will require technologies not yet available to us - especially to achieve sufficient resolution in live cells. This would also allow to determine whether the localization of hVFL1 is constant around the circumference of the procentriole during centriole formation.

3.4. MT anchoring, polarity, development and cancer

Centriole asymmetry may also have a role to play in MT anchoring. I have shown that hVFL1 depletion impacts MT organization, likely through MT anchoring. Since hVFL1 depletion induces defects in DAs that are only quantifiable by U-ExM, it is possible that it also induces defects in SDAs that would not have been detected by conventional fluorescence microscopy. Thus, it would be necessary to study the defects in SDAs by U-ExM to determine whether the alteration in MT organization upon hVFL1 depletion is related to this. However, the SDAs often do not exhibit perfect 9-fold symmetry, so it will be more difficult than for the DAs to demonstrate a possible effect of hVFL1 depletion. A direct quantification of the number of MTs at the centriole by U-ExM would also help determining whether MT anchoring is affected in hVFL1-deficient cells. Anchoring has an important impact on cell migration and polarity. It would thus be also important to analyze cell migration to determine whether it is perturbed in cells depleted from hVFL1.

If centriole rotational polarity is regulated and plays a role in cell polarization, migration or signaling, it would be interesting to evaluate its possible involvement in cancer. For this, we could collect data from patients with hVFL1 mutations. It would also be possible to compare the rotational polarity of centrioles between cancer and non-transformed cell lines, as we have done for centriole duplication. A parallel could then be drawn with data on centriole polarity measured during normal development or in cancer. It also remains to be determined whether normal tissues with primary cilia have centrioles polarized with hVFL1 always in the same position. Such a pattern could explain the possible link between MT anchoring and centriole rotational asymmetry that I have uncovered in this work.

4. References

- Adams, G. M., Wright, R. L., & Jarvik, J. W. (1985). Defective temporal and spatial control of flagellar assembly in a mutant of *Chlamydomonas reinhardtii* with variable flagellar number. *The Journal of Cell Biology*, *100*(3), 955-964. <https://doi.org/10.1083/jcb.100.3.955>
- Agircan, F. G., Schiebel, E., & Mardin, B. R. (2014). Separate to operate : Control of centrosome positioning and separation. *Philosophical Transactions of the Royal Society B: Biological Sciences*, *369*(1650). <https://doi.org/10.1098/rstb.2013.0461>
- Andersen, J. S., Wilkinson, C. J., Mayor, T., Mortensen, P., Nigg, E. A., & Mann, M. (2003). Proteomic characterization of the human centrosome by protein correlation profiling. *Nature*, *426*(6966), 570-574. <https://doi.org/10.1038/nature02166>
- Azimzadeh, J. (2014). Exploring the evolutionary history of centrosomes. *Philosophical Transactions of the Royal Society of London. Series B, Biological Sciences*, *369*(1650). <https://doi.org/10.1098/rstb.2013.0453>
- Azimzadeh, J. (2021). Evolution of the centrosome, from the periphery to the center. *Current Opinion in Structural Biology*, *66*, 96-103. <https://doi.org/10.1016/j.sbi.2020.10.020>
- Azimzadeh, J., Hergert, P., Delouvé, A., Euteneuer, U., Formstecher, E., Khodjakov, A., & Bornens, M. (2009). HPOC5 is a centrin-binding protein required for assembly of full-length centrioles. *Journal of Cell Biology*, *185*(1), 101-114. <https://doi.org/10.1083/jcb.200808082>
- Azimzadeh, J., Wong, M. L., Downhour, D. M., Alvarado, A. S., & Marshall, W. F. (2012). Centrosome Loss in the Evolution of Planarians. *Science*, *335*(6067), 461-463. <https://doi.org/10.1126/science.1214457>
- Bärenz, F., Kschonsak, Y. T., Meyer, A., Jafarpour, A., Lorenz, H., & Hoffmann, I. (2018). Ccdc61 controls centrosomal localization of Cep170 and is required for spindle assembly and symmetry. *Molecular Biology of the Cell*, *29*(26), 3105-3118. <https://doi.org/10.1091/mbc.E18-02-0115>
- Barker, A. R., McIntosh, K. V., & Dawe, H. R. (2016). Centrosome positioning in non-dividing cells. *Protoplasma*, *253*(4), 1007-1021. <https://doi.org/10.1007/s00709-015-0883-5>
- Basquin, C., Orfila, A.-M., & Azimzadeh, J. (2015). The planarian *Schmidtea mediterranea* as a model for studying motile cilia and multiciliated cells. *Methods in Cell Biology*, *127*, 243-262. <https://doi.org/10.1016/bs.mcb.2015.01.009>
- Basto, R., Lau, J., Vinogradova, T., Gardiol, A., Woods, C. G., Khodjakov, A., & Raff, J. W. (2006). Flies without Centrioles. *Cell*, *125*(7), 1375-1386. <https://doi.org/10.1016/j.cell.2006.05.025>
- Bengueddach, H., Lemullois, M., Aubusson-Fleury, A., & Koll, F. (2017). Basal body positioning and anchoring in the multiciliated cell *Paramecium tetraurelia* : Roles of OFD1 and VFL3. *Cilia*, *6*(1), 6. <https://doi.org/10.1186/s13630-017-0050-z>
- Bertiaux, E., Mallet, A., Fort, C., Blisnick, T., Bonnefoy, S., Jung, J., Lemos, M., Marco, S., Vaughan, S., Trépout, S., Tinevez, J.-Y., & Bastin, P. (2018). Bidirectional intraflagellar transport is restricted to two sets of microtubule doublets in the trypanosome flagellum. *Journal of Cell Biology*, *217*(12), 4284-4297. <https://doi.org/10.1083/jcb.201805030>

- Bowler, M., Kong, D., Sun, S., Nanjundappa, R., Evans, L., Farmer, V., Holland, A., Mahjoub, M. R., Sui, H., & Loncarek, J. (2019). High-resolution characterization of centriole distal appendage morphology and dynamics by correlative STORM and electron microscopy. *Nature Communications*, *10*(1), 993. <https://doi.org/10.1038/s41467-018-08216-4>
- Breslow, D. K., Koslover, E. F., Seydel, F., Spakowitz, A. J., & Nachury, M. V. (2013). An in vitro assay for entry into cilia reveals unique properties of the soluble diffusion barrier. *Journal of Cell Biology*, *203*(1), 129-147. <https://doi.org/10.1083/jcb.201212024>
- Brooks, E. R., & Wallingford, J. B. (2014). Multiciliated Cells. *Current Biology*, *24*(19), R973-R982. <https://doi.org/10.1016/j.cub.2014.08.047>
- Buisson, J., Chenouard, N., Lagache, T., Blisnick, T., Olivo-Marin, J.-C., & Bastin, P. (2013). Intraflagellar transport proteins cycle between the flagellum and its base. *Journal of Cell Science*, *126*(Pt 1), 327-338. <https://doi.org/10.1242/jcs.117069>
- Burakov, A. V., & Nadezhdina, E. S. (2020). Centering and Shifting of Centrosomes in Cells. *Cells*, *9*(6), 1351. <https://doi.org/10.3390/cells9061351>
- Chen, C.-P. (2007). Meckel Syndrome : Genetics, Perinatal Findings, and Differential Diagnosis. *Taiwanese Journal of Obstetrics and Gynecology*, *46*(1), 9-14. [https://doi.org/10.1016/S1028-4559\(08\)60100-X](https://doi.org/10.1016/S1028-4559(08)60100-X)
- Chen, C.-T., Hehnlly, H., Yu, Q., Farkas, D., Zheng, G., Redick, S. D., Hung, H.-F., Samtani, R., Jurczyk, A., Akbarian, S., Wise, C., Jackson, A., Bober, M., Guo, Y., Lo, C., & Doxsey, S. (2014). A Unique Set of Centrosome Proteins Requires Pericentrin for Spindle-Pole Localization and Spindle Orientation. *Current Biology*, *24*(19), 2327-2334. <https://doi.org/10.1016/j.cub.2014.08.029>
- Choksi, S. P., Lauter, G., Swoboda, P., & Roy, S. (2014). Switching on cilia : Transcriptional networks regulating ciliogenesis. *Development*, *141*(7), 1427-1441. <https://doi.org/10.1242/dev.074666>
- Chong, W. M., Wang, W.-J., Lo, C.-H., Chiu, T.-Y., Chang, T.-J., Liu, Y.-P., Tanos, B., Mazo, G., Tsou, M.-F. B., Jane, W.-N., Yang, T. T., & Liao, J.-C. (2020). Super-resolution microscopy reveals coupling between mammalian centriole subdistal appendages and distal appendages. *eLife*, *9*, e53580. <https://doi.org/10.7554/eLife.53580>
- Colin, E., Huynh Cong, E., Mollet, G., Guichet, A., Gribouval, O., Arrondel, C., Boyer, O., Daniel, L., Gubler, M.-C., Ekinici, Z., Tsimaratos, M., Chabrol, B., Boddaert, N., Verloes, A., Chevrollier, A., Gueguen, N., Desquiere-Dumas, V., Ferré, M., Procaccio, V., ... Antignac, C. (2014). Loss-of-Function Mutations in WDR73 Are Responsible for Microcephaly and Steroid-Resistant Nephrotic Syndrome : Galloway-Mowat Syndrome. *The American Journal of Human Genetics*, *95*(6), 637-648. <https://doi.org/10.1016/j.ajhg.2014.10.011>
- Delgehyr, N., Sillibourne, J., & Bornens, M. (2005). Microtubule nucleation and anchoring at the centrosome are independent processes linked by ninein function. *Journal of Cell Science*, *118*(8), 1565-1575. <https://doi.org/10.1242/jcs.02302>
- Elric, J., & Etienne-Manneville, S. (2014). Centrosome positioning in polarized cells : Common themes and variations. *Experimental Cell Research*, *328*(2), 240-248. <https://doi.org/10.1016/j.yexcr.2014.09.004>

- Failler, M., Gee, H. Y., Krug, P., Joo, K., Halbritter, J., Belkacem, L., Filhol, E., Porath, J. D., Braun, D. A., Schueler, M., Frigo, A., Alibeu, O., Masson, C., Brochard, K., Hurault de Ligny, B., Novo, R., Pietrement, C., Kayserili, H., Salomon, R., ... Saunier, S. (2014). Mutations of CEP83 Cause Infantile Nephronophthisis and Intellectual Disability. *The American Journal of Human Genetics*, *94*(6), 905-914. <https://doi.org/10.1016/j.ajhg.2014.05.002>
- Fraser, A. M., & Davey, M. G. (2019). TALPID3 in Joubert syndrome and related ciliopathy disorders. *Current Opinion in Genetics & Development*, *56*, 41-48. <https://doi.org/10.1016/j.gde.2019.06.010>
- Fry, A. M., Sampson, J., Shak, C., & Shackleton, S. (2017). Recent advances in pericentriolar material organization: Ordered layers and scaffolding gels. *F1000Research*, *6*, 1622. <https://doi.org/10.12688/f1000research.11652.1>
- Gall, J. G. (2004). Early Studies on Centrioles and Centrosomes. In *Centrosomes in Development and Disease* (p. 1-15). John Wiley & Sons, Ltd. <https://onlinelibrary.wiley.com/doi/abs/10.1002/3527603808.ch1>
- Gambarotto, D., Zwettler, F. U., Le Guennec, M., Schmidt-Cernohorska, M., Fortun, D., Borgers, S., Heine, J., Schloetel, J.-G., Reuss, M., Unser, M., Boyden, E. S., Sauer, M., Hamel, V., & Guichard, P. (2019). Imaging cellular ultrastructures using expansion microscopy (U-ExM). *Nature Methods*, *16*(1), 71-74. <https://doi.org/10.1038/s41592-018-0238-1>
- Garcia, G., Raleigh, D. R., & Reiter, J. F. (2018). How the Ciliary Membrane Is Organized Inside-Out to Communicate Outside-In. *Current Biology: CB*, *28*(8), R421-R434. <https://doi.org/10.1016/j.cub.2018.03.010>
- Garcia-Gonzalo, F. R., & Reiter, J. F. (2017). Open Sesame: How Transition Fibers and the Transition Zone Control Ciliary Composition. *Cold Spring Harbor Perspectives in Biology*, *9*(2), a028134. <https://doi.org/10.1101/cshperspect.a028134>
- Geimer, S., & Melkonian, M. (2004). The ultrastructure of the *Chlamydomonas reinhardtii* basal apparatus: Identification of an early marker of radial asymmetry inherent in the basal body. *Journal of Cell Science*, *117*(13), 2663-2674. <https://doi.org/10.1242/jcs.01120>
- Geimer, S., & Melkonian, M. (2005). Centrin scaffold in *Chlamydomonas reinhardtii* revealed by immunoelectron microscopy. *Eukaryotic Cell*, *4*(7), 1253-1263. <https://doi.org/10.1128/EC.4.7.1253-1263.2005>
- Gonçalves, J., & Pelletier, L. (2017). The Ciliary Transition Zone: Finding the Pieces and Assembling the Gate. *Molecules and Cells*, *40*(4), 243-253. <https://doi.org/10.14348/molcells.2017.0054>
- Guichard, P., Chrétien, D., Marco, S., & Tassin, A.-M. (2010). Procentriole assembly revealed by cryo-electron tomography. *The EMBO Journal*, *29*(9), 1565-1572. <https://doi.org/10.1038/emboj.2010.45>
- Hamel, V., Steib, E., Hamelin, R., Armand, F., Borgers, S., Flückiger, I., Busso, C., Olieric, N., Sorzano, C. O. S., Steinmetz, M. O., Guichard, P., & Gönczy, P. (2017). Identification of *Chlamydomonas* Central Core Centriolar Proteins Reveals a Role for Human WDR90 in Ciliogenesis. *Current Biology*, *27*(16), 2486-2498.e6. <https://doi.org/10.1016/j.cub.2017.07.011>
- Hoops, H. J., Wright, R. L., Jarvik, J. W., & Witman, G. B. (1984). Flagellar waveform and

- rotational orientation in a *Chlamydomonas* mutant lacking normal striated fibers. *Journal of Cell Biology*, 98(3), 818-824. <https://doi.org/10.1083/jcb.98.3.818>
- Hori, A., & Toda, T. (2017). Regulation of centriolar satellite integrity and its physiology. *Cellular and Molecular Life Sciences: CMLS*, 74(2), 213-229. <https://doi.org/10.1007/s00018-016-2315-x>
- Hung, H.-F., Hehnlly, H., & Doxsey, S. (2016). The Mother Centriole Appendage Protein Cenexin Modulates Lumen Formation through Spindle Orientation. *Current Biology*, 26(6), 793-801. <https://doi.org/10.1016/j.cub.2016.01.025>
- Ishikawa, H., Kubo, A., Tsukita, S., & Tsukita, S. (2005). Odf2-deficient mother centrioles lack distal/subdistal appendages and the ability to generate primary cilia. *Nature Cell Biology*, 7(5), 517-524. <https://doi.org/10.1038/ncb1251>
- Joubert Syndrome—UW Hindbrain Malformation Research Program.* (s. d.). <https://depts.washington.edu/joubert/joubertsyndrome.php>
- Kashihara, H., Chiba, S., Kanno, S., Suzuki, K., Yano, T., & Tsukita, S. (2019). Cep128 associates with Odf2 to form the subdistal appendage of the centriole. *Genes to Cells*, 24(3), 231-243. <https://doi.org/10.1111/gtc.12668>
- Katoh, Y., Chiba, S., & Nakayama, K. (2020). Practical method for superresolution imaging of primary cilia and centrioles by expansion microscopy using an amplibody for fluorescence signal amplification. *Molecular Biology of the Cell*, 31(20), 2195-2206. <https://doi.org/10.1091/mbc.E20-04-0250>
- Kim, J., Krishnaswami, S. R., & Gleeson, J. G. (2008). CEP290 interacts with the centriolar satellite component PCM-1 and is required for Rab8 localization to the primary cilium. *Human Molecular Genetics*, 17(23), 3796-3805. <https://doi.org/10.1093/hmg/ddn277>
- Kitagawa, D., Vakonakis, I., Olieric, N., Hilbert, M., Keller, D., Olieric, V., Bortfeld, M., Erat, M. C., Flückiger, I., Gönczy, P., & Steinmetz, M. O. (2011). Structural basis of the 9-fold symmetry of centrioles. *Cell*, 144(3), 364-375. <https://doi.org/10.1016/j.cell.2011.01.008>
- Klena, N., Le Guennec, M., Tassin, A.-M., van den Hoek, H., Erdmann, P. S., Schaffer, M., Geimer, S., Aeschlimann, G., Kovacic, L., Sadian, Y., Goldie, K. N., Stahlberg, H., Engel, B. D., Hamel, V., & Guichard, P. (2020). Architecture of the centriole cartwheel-containing region revealed by cryo-electron tomography. *The EMBO Journal*, 39(22), e106246. <https://doi.org/10.15252/embj.2020106246>
- Kloc, M. (Éd.). (2019). *The Golgi Apparatus and Centriole : Functions, Interactions and Role in Disease*. Springer International Publishing. <https://doi.org/10.1007/978-3-030-23173-6>
- Kumar, D., & Reiter, J. (2021). How the centriole builds its cilium : Of mothers, daughters, and the acquisition of appendages. *Current Opinion in Structural Biology*, 66, 41-48. <https://doi.org/10.1016/j.sbi.2020.09.006>
- Le Guennec, M., Klena, N., Gambarotto, D., Laporte, M. H., Tassin, A.-M., van den Hoek, H., Erdmann, P. S., Schaffer, M., Kovacic, L., Borgers, S., Goldie, K. N., Stahlberg, H., Bornens, M., Azimzadeh, J., Engel, B. D., Hamel, V., & Guichard, P. (2020). A helical inner scaffold provides a structural basis for centriole cohesion. *Science Advances*, 6(7), eaaz4137. <https://doi.org/10.1126/sciadv.aaz4137>

- LeGuennec, M., Klena, N., Aeschlimann, G., Hamel, V., & Guichard, P. (2020). Overview of the centriole architecture. *Current Opinion in Structural Biology*, 66, 58-65. <https://doi.org/10.1016/j.sbi.2020.09.015>
- Loncarek, J., & Bettencourt-Dias, M. (2018). Building the right centriole for each cell type. *The Journal of Cell Biology*, 217(3), 823-835. <https://doi.org/10.1083/jcb.201704093>
- Mazo, G., Soplop, N., Wang, W.-J., Uryu, K., & Tsou, M. F. B. (2016). Spatial Control of Primary Ciliogenesis by Subdistal Appendages Alters Sensation-Associated Properties of Cilia. *Developmental Cell*, 39(4), 424-437. <https://doi.org/10.1016/j.devcel.2016.10.006>
- Meunier, A., & Azimzadeh, J. (2016). Multiciliated Cells in Animals. *Cold Spring Harbor Perspectives in Biology*, 8(12). <https://doi.org/10.1101/cshperspect.a028233>
- Mitchison, H. M., & Valente, E. M. (2017). Motile and non-motile cilia in human pathology : From function to phenotypes. *The Journal of Pathology*, 241(2), 294-309. <https://doi.org/10.1002/path.4843>
- Muto, Y., Yoshioka, T., Kimura, M., Matsunami, M., Saya, H., & Okano, Y. (2008). An evolutionarily conserved leucine-rich repeat protein CLERC is a centrosomal protein required for spindle pole integrity. *Cell Cycle*, 7(17), 2738-2748. <https://doi.org/10.4161/cc.7.17.6591>
- Nabais, C., Peneda, C., & Bettencourt-Dias, M. (2020). Evolution of centriole assembly. *Current Biology: CB*, 30(10), R494-R502. <https://doi.org/10.1016/j.cub.2020.02.036>
- Nakayama, T., Al-Maawali, A., El-Quessny, M., Rajab, A., Khalil, S., Stoler, J. M., Tan, W.-H., Nasir, R., Schmitz-Abe, K., Hill, R. S., Partlow, J. N., Al-Saffar, M., Servattalab, S., LaCoursiere, C. M., Tambunan, D. E., Coulter, M. E., Elhosary, P. C., Gorski, G., Barkovich, A. J., ... Mochida, G. H. (2015). Mutations in PYCR2, Encoding Pyrroline-5-Carboxylate Reductase 2, Cause Microcephaly and Hypomyelination. *The American Journal of Human Genetics*, 96(5), 709-719. <https://doi.org/10.1016/j.ajhg.2015.03.003>
- Nigg, E. A., & Holland, A. J. (2018). Once and only once : Mechanisms of centriole duplication and their deregulation in disease. *Nature reviews. Molecular cell biology*, 19(5), 297-312. <https://doi.org/10.1038/nrm.2017.127>
- Nigg, E. A., & Stearns, T. (2011). The centrosome cycle : Centriole biogenesis, duplication and inherent asymmetries. *Nature cell biology*, 13(10), 1154-1160. <https://doi.org/10.1038/ncb2345>
- Ochi, T., Quarantotti, V., Lin, H., Jullien, J., Rosa e Silva, I., Boselli, F., Barnabas, D. D., Johnson, C. M., McLaughlin, S. H., Freund, S. M. V., Blackford, A. N., Kimata, Y., Goldstein, R. E., Jackson, S. P., Blundell, T. L., Dutcher, S. K., Gergely, F., & van Breugel, M. (2020). CCDC61/VFL3 Is a Paralog of SAS6 and Promotes Ciliary Functions. *Structure*, 28(6), 674-689.e11. <https://doi.org/10.1016/j.str.2020.04.010>
- Pala, R., Alomari, N., & Nauli, S. M. (2017). Primary Cilium-Dependent Signaling Mechanisms. *International Journal of Molecular Sciences*, 18(11), 2272. <https://doi.org/10.3390/ijms18112272>
- Parisi, M., & Glass, I. (1993). Joubert Syndrome. In M. P. Adam, H. H. Ardinger, R. A. Pagon, S. E. Wallace, L. J. Bean, G. Mirzaa, & A. Amemiya (Éds.), *GeneReviews®*. University of Washington, Seattle. <http://www.ncbi.nlm.nih.gov/books/NBK1325/>
- Passemard, S., Kaindl, A. M., & Verloes, A. (2013). Microcephaly. *Handbook of Clinical Neurology*, 111, 129-141. <https://doi.org/10.1016/B978-0-444-52891-9.00013-0>

- Piel, M., Meyer, P., Khodjakov, A., Rieder, C. L., & Bornens, M. (2000). The Respective Contributions of the Mother and Daughter Centrioles to Centrosome Activity and Behavior in Vertebrate Cells. *Journal of Cell Biology*, *149*(2), 317-330. <https://doi.org/10.1083/jcb.149.2.317>
- Pizon, V., Gaudin, N., Poteau, M., Cifuentes-Diaz, C., Demdou, R., Heyer, V., Reina San Martin, B., & Azimzadeh, J. (2020). HVFL3/CCDC61 is a component of mother centriole subdistal appendages required for centrosome cohesion and positioning. *Biology of the Cell*, *112*(1), 22-37. <https://doi.org/10.1111/boc.201900038>
- Pode-Shakked, B., Barash, H., Ziv, L., Gripp, K. W., Flex, E., Barel, O., Carvalho, K. S., Scavina, M., Chillemi, G., Niceta, M., Eyal, E., Kol, N., Ben-Zeev, B., Bar-Yosef, O., Marek-Yagel, D., Bertini, E., Duker, A. L., Anikster, Y., Tartaglia, M., & Raas-Rothschild, A. (2017). Microcephaly, intractable seizures and developmental delay caused by biallelic variants in TBCD: Further delineation of a new chaperone-mediated tubulinopathy. *Clinical Genetics*, *91*(5), 725-738. <https://doi.org/10.1111/cge.12914>
- Prosser, S. L., & Pelletier, L. (2020). Centriolar satellite biogenesis and function in vertebrate cells. *Journal of Cell Science*, *133*(1). <https://doi.org/10.1242/jcs.239566>
- Reiter, J. F., & Leroux, M. R. (2017). Genes and molecular pathways underpinning ciliopathies. *Nature Reviews Molecular Cell Biology*, *18*(9), 533-547. <https://doi.org/10.1038/nrm.2017.60>
- Sakakibara, N., Morisada, N., Nozu, K., Nagatani, K., Ohta, T., Shimizu, J., Wada, T., Shima, Y., Yamamura, T., Minamikawa, S., Fujimura, J., Horinouchi, T., Nagano, C., Shono, A., Ye, M. J., Nozu, Y., Nakanishi, K., & Iijima, K. (2019). Clinical spectrum of male patients with OFD1 mutations. *Journal of Human Genetics*, *64*(1), 3-9. <https://doi.org/10.1038/s10038-018-0532-x>
- Schneider, L., Cammer, M., Lehman, J., Nielsen, S. K., Guerra, C. F., Veland, I. R., Stock, C., Hoffmann, E. K., Yoder, B. K., Schwab, A., Satir, P., & Christensen, S. T. (2010). Directional Cell Migration and Chemotaxis in Wound Healing Response to PDGF-AA are Coordinated by the Primary Cilium in Fibroblasts. *Cellular Physiology and Biochemistry*, *25*(2-3), 279-292. <https://doi.org/10.1159/000276562>
- Shaheen, R., Szymanska, K., Basu, B., Patel, N., Ewida, N., Faqeih, E., Al Hashem, A., Derar, N., Alsharif, H., Aldahmesh, M. A., Alazami, A. M., Hashem, M., Ibrahim, N., Abdulwahab, F. M., Sonbul, R., Alkuraya, H., Alnemer, M., Al Tala, S., Al-Husain, M., ... Alkuraya, F. S. (2016). Characterizing the morbid genome of ciliopathies. *Genome Biology*, *17*(1), 242. <https://doi.org/10.1186/s13059-016-1099-5>
- Shamseldin, H. E., Shaheen, R., Ewida, N., Bubshait, D. K., Alkuraya, H., Almardawi, E., Howaidi, A., Sabr, Y., Abdalla, E. M., Alfaifi, A. Y., Alghamdi, J. M., Alsagheir, A., Alfares, A., Morsy, H., Hussein, M. H., Al-Muhaizea, M. A., Shagrani, M., Al Sabban, E., Salih, M. A., ... Alkuraya, F. S. (2020). The morbid genome of ciliopathies: An update. *Genetics in Medicine*, *22*(6), 1051-1060. <https://doi.org/10.1038/s41436-020-0761-1>
- Sharma, A., Olieric, N., & Steinmetz, M. O. (2021). Centriole length control. *Current Opinion in Structural Biology*, *66*, 89-95. <https://doi.org/10.1016/j.sbi.2020.10.011>
- Shi, X., Garcia, G., Van De Weghe, J. C., McGorty, R., Pazour, G. J., Doherty, D., Huang, B., & Reiter, J. F. (2017). Super-resolution microscopy reveals that disruption of ciliary transition-zone architecture causes Joubert syndrome. *Nature Cell Biology*, *19*(10), 1178-1188. <https://doi.org/10.1038/ncb3599>

- Siekierska, A., Stamberger, H., Deconinck, T., Oprescu, S. N., Partoens, M., Zhang, Y., Sourbron, J., Adriaenssens, E., Mullen, P., Wiencek, P., Hardies, K., Lee, J.-S., Giong, H.-K., Distelmaier, F., Elpeleg, O., Helbig, K. L., Hersh, J., Isikay, S., Jordan, E., ... De Jonghe, P. (2019). Biallelic VARS variants cause developmental encephalopathy with microcephaly that is recapitulated in vars knockout zebrafish. *Nature Communications*, *10*(1), 708. <https://doi.org/10.1038/s41467-018-07953-w>
- Silflow, C. D., LaVoie, M., Tam, L.-W., Tousey, S., Sanders, M., Wu, W., Borodovsky, M., & Lefebvre, P. A. (2001). The Vfl1 Protein in Chlamydomonas Localizes in a Rotationally Asymmetric Pattern at the Distal Ends of the Basal Bodies. *The Journal of Cell Biology*, *153*(1), 63-74. <https://doi.org/10.1083/jcb.153.1.63>
- Sluder, G. (2014). One to only two: A short history of the centrosome and its duplication. *Philosophical Transactions of the Royal Society of London. Series B, Biological Sciences*, *369*(1650). <https://doi.org/10.1098/rstb.2013.0455>
- Soares, H., Carmona, B., Nolasco, S., Viseu Melo, L., & Gonçalves, J. (2019). Cilia Distal Domain: Diversity in Evolutionarily Conserved Structures. *Cells*, *8*(2). <https://doi.org/10.3390/cells8020160>
- Song, Z., Zhang, X., Jia, S., Yelick, P. C., & Zhao, C. (2016). Zebrafish as a Model for Human Ciliopathies. *Journal of Genetics and Genomics = Yi Chuan Xue Bao*, *43*(3), 107-120. <https://doi.org/10.1016/j.jgg.2016.02.001>
- Spassky, N., & Meunier, A. (2017). The development and functions of multiciliated epithelia. *Nature Reviews Molecular Cell Biology*, *18*(7), 423-436. <https://doi.org/10.1038/nrm.2017.21>
- Srsen, V., Gnad, N., Dammermann, A., & Merdes, A. (2006). Inhibition of centrosome protein assembly leads to p53-dependent exit from the cell cycle. *Journal of Cell Biology*, *174*(5), 625-630. <https://doi.org/10.1083/jcb.200606051>
- Stepanek, L., & Pigino, G. (2016). Microtubule doublets are double-track railways for intraflagellar transport trains. *Science*, *352*(6286), 721-724. <https://doi.org/10.1126/science.aaf4594>
- Sullenberger, C., Vasquez-Limeta, A., Kong, D., & Loncarek, J. (2020). With Age Comes Maturity: Biochemical and Structural Transformation of a Human Centriole in the Making. *Cells*, *9*(6), 1429. <https://doi.org/10.3390/cells9061429>
- Tajhya, R., & Delling, M. (2020). New insights into ion channel-dependent signalling during left-right patterning. *The Journal of Physiology*, *598*(9), 1741-1752. <https://doi.org/10.1113/JP277835>
- Takao, D., Yamamoto, S., & Kitagawa, D. (2019). A theory of centriole duplication based on self-organized spatial pattern formation. *The Journal of Cell Biology*, *218*(11), 3537-3547. <https://doi.org/10.1083/jcb.201904156>
- Taschner, M., & Lorentzen, E. (2016). The Intraflagellar Transport Machinery. *Cold Spring Harbor Perspectives in Biology*, *8*(10), a028092. <https://doi.org/10.1101/cshperspect.a028092>
- Thauvin-Robinet, C., Lee, J. S., Lopez, E., Herranz-Pérez, V., Shida, T., Franco, B., Jegou, L., Ye, F., Pasquier, L., Loget, P., Gigot, N., Aral, B., Lopes, C. A. M., St-Onge, J., Bruel, A.-L., Thevenon, J., González-Granero, S., Alby, C., Munnich, A., ... Nachury, M. V. (2014). The oral-facial-digital syndrome gene C2CD3 encodes a positive regulator of centriole elongation. *Nature*

- genetics*, 46(8), 905-911. <https://doi.org/10.1038/ng.3031>
- Théry, M., Racine, V., Piel, M., Pépin, A., Dimitrov, A., Chen, Y., Sibarita, J.-B., & Bornens, M. (2006). Anisotropy of cell adhesive microenvironment governs cell internal organization and orientation of polarity. *Proceedings of the National Academy of Sciences*, 103(52), 19771-19776. <https://doi.org/10.1073/pnas.0609267103>
- Tischer, J., Carden, S., & Gergely, F. (2020). Accessorizing the centrosome: New insights into centriolar appendages and satellites. *Current Opinion in Structural Biology*, 66, 148-155. <https://doi.org/10.1016/j.sbi.2020.10.021>
- Tovey, C. A., & Conduit, P. T. (2018). Microtubule nucleation by γ -tubulin complexes and beyond. *Essays in Biochemistry*, 62(6), 765-780. <https://doi.org/10.1042/EBC20180028>
- Tsai, J.-J., Hsu, W.-B., Liu, J.-H., Chang, C.-W., & Tang, T. K. (2019). CEP120 interacts with C2CD3 and Talpid3 and is required for centriole appendage assembly and ciliogenesis. *Scientific Reports*, 9(1), 6037. <https://doi.org/10.1038/s41598-019-42577-0>
- Uzbekov, R., & Alieva, I. (2018). Who are you, subdistal appendages of centriole? *Open Biology*, 8(7), 180062. <https://doi.org/10.1098/rsob.180062>
- Uzbekov R.E. & Alieva I.B. (2013). *Centrosome : History of Study and New Discoveries. From Cytoplasmic Granule to the Center of Intracellular Regulation* (Moscow University Press).
- van Breugel, M., Hirono, M., Andreeva, A., Yanagisawa, H., Yamaguchi, S., Nakazawa, Y., Morgner, N., Petrovich, M., Ebong, I.-O., Robinson, C. V., Johnson, C. M., Veprintsev, D., & Zuber, B. (2011). Structures of SAS-6 suggest its organization in centrioles. *Science (New York, N.Y.)*, 331(6021), 1196-1199. <https://doi.org/10.1126/science.1199325>
- Vaughan, S., & Gull, K. (2016). Basal body structure and cell cycle-dependent biogenesis in *Trypanosoma brucei*. *Cilia*, 5(1), 5. <https://doi.org/10.1186/s13630-016-0023-7>
- Vu, H. T.-K., Mansour, S., Kücken, M., Blasse, C., Basquin, C., Azimzadeh, J., Myers, E. W., Bruschi, L., & Rink, J. C. (2019). Dynamic Polarization of the Multiciliated Planarian Epidermis between Body Plan Landmarks. *Developmental Cell*, 51(4), 526-542.e6. <https://doi.org/10.1016/j.devcel.2019.10.022>
- Wang, G., Jiang, Q., & Zhang, C. (2014). The role of mitotic kinases in coupling the centrosome cycle with the assembly of the mitotic spindle. *Journal of Cell Science*, 127(19), 4111-4122. <https://doi.org/10.1242/jcs.151753>
- Wang, L., Failler, M., Fu, W., & Dynlacht, B. D. (2018). A distal centriolar protein network controls organelle maturation and asymmetry. *Nature Communications*, 9(1), 3938. <https://doi.org/10.1038/s41467-018-06286-y>
- Wiegering, A., Dildrop, R., Kalfhues, L., Spsychala, A., Kuschel, S., Lier, J. M., Zobel, T., Dahmen, S., Leu, T., Struchtrup, A., Legendre, F., Vesque, C., Schneider-Maunoury, S., Saunier, S., Rütter, U., & Gerhardt, C. (2018). Cell type-specific regulation of ciliary transition zone assembly in vertebrates. *The EMBO Journal*, 37(10), e97791. <https://doi.org/10.15252/embj.201797791>
- Winey, M., & O'Toole, E. (2014). Centriole structure. *Philosophical Transactions of the Royal Society B: Biological Sciences*, 369(1650). <https://doi.org/10.1098/rstb.2013.0457>

- Woodruff, J. B., Wueseke, O., & Hyman, A. A. (2014). Pericentriolar material structure and dynamics. *Philosophical Transactions of the Royal Society B: Biological Sciences*, 369(1650). <https://doi.org/10.1098/rstb.2013.0459>
- Wright, R. L., Chojnacki, B., & Jarvik, J. W. (1983). Abnormal basal-body number, location, and orientation in a striated fiber-defective mutant of *Chlamydomonas reinhardtii*. *Journal of Cell Biology*, 96(6), 1697-1707. <https://doi.org/10.1083/jcb.96.6.1697>
- Wu, J., & Akhmanova, A. (2017). Microtubule-Organizing Centers. *Annual Review of Cell and Developmental Biology*, 33, 51-75. <https://doi.org/10.1146/annurev-cellbio-100616-060615>
- Wu, Z., Pang, N., Zhang, Y., Chen, H., Peng, Y., Fu, J., & Wei, Q. (2020). CEP290 is essential for the initiation of ciliary transition zone assembly. *PLOS Biology*, 18(12), e3001034. <https://doi.org/10.1371/journal.pbio.3001034>
- Yamamoto, S., & Kitagawa, D. (2019). Self-organization of Plk4 regulates symmetry breaking in centriole duplication. *Nature Communications*, 10(1), 1810. <https://doi.org/10.1038/s41467-019-09847-x>
- Yamashita, Y. M., Yuan, H., Cheng, J., & Hunt, A. J. (2010). Polarity in Stem Cell Division : Asymmetric Stem Cell Division in Tissue Homeostasis. *Cold Spring Harbor Perspectives in Biology*, 2(1), a001313. <https://doi.org/10.1101/cshperspect.a001313>
- Yang, T. T., Chong, W. M., Wang, W.-J., Mazo, G., Tanos, B., Chen, Z., Tran, T. M. N., Chen, Y.-D., Weng, R. R., Huang, C.-E., Jane, W.-N., Tsou, M.-F. B., & Liao, J.-C. (2018). Super-resolution architecture of mammalian centriole distal appendages reveals distinct blade and matrix functional components. *Nature Communications*, 9. <https://doi.org/10.1038/s41467-018-04469-1>
- Yang, T. T., Su, J., Wang, W.-J., Craige, B., Witman, G. B., Tsou, M.-F. B., & Liao, J.-C. (2015). Superresolution Pattern Recognition Reveals the Architectural Map of the Ciliary Transition Zone. *Scientific Reports*, 5, 14096. <https://doi.org/10.1038/srep14096>
- Zhang, D., & Aravind, L. (2012). Novel transglutaminase-like peptidase and C2 domains elucidate the structure, biogenesis and evolution of the ciliary compartment. *Cell Cycle (Georgetown, Tex.)*, 11(20), 3861-3875. <https://doi.org/10.4161/cc.22068>
- Zwettler, F. U., Reinhard, S., & Sauer, M. (2021). Ex-dSTORM and automated quantitative image analysis of expanded filamentous structures. *Methods in Cell Biology*, 161, 317-340. <https://doi.org/10.1016/bs.mcb.2020.05.004>